

LASER POWDER BED FUSION OF ALUMINUM AND
ALUMINUM MATRIX COMPOSITES

Laser Powder Bed Fusion of Aluminum and Aluminum Matrix Composites

By

Ali Ghasemi, BSc., MSc.

A Thesis

Submitted to the School of Graduate Studies in Partial Fulfillment of the
Requirements for the Degree Doctor of Philosophy

McMaster University

© Copyright by Ali Ghasemi, April 2023 DOCTOR OF PHILOSOPHY (2023)

McMaster University

(Mechanical Engineering)

Hamilton, Ontario

TITLE: Laser Powder Bed Fusion of Aluminum and Aluminum
Matrix Composites

AUTHOR: Ali Ghasemi
B.Sc. in Materials Science and Engineering (Shiraz
University, Shiraz, Iran)
M.Sc. in Materials Science and Engineering-Welding
(Sharif University of Technology, Tehran, Iran)

SUPERVISOR: Dr. M. A. Elbestawi

CO-SUPERVISOR: Dr. Saeid Habibi

NUMBER OF PAGES: 298

Preface

This Ph.D. thesis is an integrated article thesis, also known as sandwich thesis, which is composed of five journal papers focusing on the laser powder bed fusion additive manufacturing of pure Aluminum, AlSi12 alloy, AlSi10Mg alloy and AlSi12-graphene composites. The followings list chapters in the order of the year:

Chapter 2 This chapter contains the previously published material in the “*Additive Manufacturing*” journal as “Role of powder particle size on laser powder bed fusion processability of AlSi10Mg alloy” by Mohamed Balbaa, Ali Ghasemi, Eskandar Fereiduni, Mohamed Elbestawi, Suraj Dinkar Jadhav, and Jean-Pierre Kruth.

Chapter 3 This chapter contains the previously published material in the “*Additive Manufacturing*” journal as “Influence of alloying elements on laser powder bed fusion processability of aluminum: A new insight into the oxidation tendency” by Ali Ghasemi, Eskandar Fereiduni, Mohamed Balbaa, Suraj Dinkar Jadhav, Mohamed Elbestawi, and Saeid Habibi.

Chapter 4 This chapter contains the previously published material in the “*Additive Manufacturing*” journal as “Unraveling the low thermal conductivity of the LPBF fabricated pure Al, AlSi12, and AlSi10Mg alloys through substrate preheating” by Ali Ghasemi, Eskandar Fereiduni, Mohamed Balbaa, Mohamed Elbestawi, and Saeid Habibi.

Chapter 5 The work presented in this chapter is currently under consideration for publication in the “*Powder Technology*” journal as “On the preparation and characterization of AlSi12-graphene powder for powder bed fusion additive manufacturing applications” by Ali Ghasemi, Eskandar Fereiduni, Mohamed Elbestawi, Jasmin Kathrin

Saewe, Niklas Hartke, Fran Adar, Kayvon Savadkouei, Yoshinori Fukushima, and Saeid Habibi.

Chapter 6 The work presented in this chapter is intended to be submitted to “*Additive Manufacturing*” journal as “Influence of the graphene incorporation on nanostructure and thermal properties of the laser powder bed fusion processed AlSi12 matrix composites” by Ali Ghasemi, Eskandar Fereiduni, Mohamed Elbestawi, Kayvon Savadkouei, Fran Adar, Jasmin Kathrin Saewe, Niklas Hartke, and Saeid Habibi.

I declare that this thesis is an original report of my research, has been written by me and has not been submitted for any previous degree.

Ali Ghasemi

April 2023

Abstract

Laser powder bed fusion (LPBF), one of the most promising additive manufacturing (AM) techniques, has enabled the production of previously impossible structures. This breakthrough in AM has not only facilitated the creation of new designs, but also the redesign of existing industrial and engineering components to produce lightweight and highly efficient dies and molds, biomaterial scaffolds, aircraft brackets, heat sink and heat exchangers. In many of the mentioned applications in industries such as automotive, aerospace, heat exchanger, and electronics, aluminum (Al), Al alloys, and Al matrix composites (AMCs) are considered potential candidates.

In the first phase of this study, the optimum powder particle size and size distribution of an Al alloy powder (i.e., AlSi10Mg) was determined with the aim being to achieve highest densification levels and dimensional accuracies. In the second phase, three materials with high thermal conductivities were selected, namely, pure Al, AlSi12 and AlSi10Mg alloys. Since Al/Al alloys are prone to oxidation, the LPBF process parameters were optimized not only in terms of the densification level but also oxygen content of the fabricated parts. It was found out that the rate of oxide diminishment for Al/Al alloys during the LPBF process is more than in-situ oxidation. Despite the efforts, the optimized LPBF fabricated samples showed lower thermal conductivity than their conventionally manufactured counterparts. To tackle the issue, two different potential solutions were put into test. In the third phase, the influence of preheating on thermal

properties of pure Al, AlSi12, and AlSi10Mg was investigated and a huge improvement in the thermal conductivity of the optimized as-built parts was obtained. In the fourth phase, the possibility of enhancing thermal conductivity of the LPBF fabricated Al/Al alloys in as-built condition through the incorporation of a second constituent with a higher thermal conductivity (i.e., graphene) was investigated.

*To my sister,
I owe you everything.*

Acknowledgments

Above all, I want to express my gratitude to Professor Mohamed Elbestawi, my supervisor, for his exceptional guidance and instruction. Your valuable comments and suggestions have taught me to refine my ideas and take my research to a superior level. I appreciate your encouragement, understanding, and patience throughout this four-year journey.

I would like to extend my sincere appreciation to Dr. Nabil Bassim and Dr. Philip Koshy, members of my supervisory committee, for their constructive feedback, valuable insights, and engaging discussions. I cannot express enough how grateful I am to have been part of the AMG group at McMaster University. I want to acknowledge my colleagues for the stimulating discussions, presentation preparations, and productive group meetings. In particular, I would like to express my gratitude to my dear friend, Eskandar Fereiduni, for his unwavering support, friendship, and willingness to share his expertise with me. I also want to thank Dr. J. E. Greedan and Evan Smith from the Department of Chemistry at McMaster University for providing access to the ball milling facility. Additionally, I would like to thank the following individuals and organizations for their invaluable contributions: (i) Dr. Zhilin Peng at the Center for Advanced Nuclear Systems (CANS) at McMaster University for providing and instructing me on the electron backscattered diffraction (EBSD) analysis facility, (ii) Erika Hahn at Linseis Messgeraete GmbH, Selb, Germany, where some of the thermal diffusivity measurements were conducted, (iii) Kayvon Savadkouei and Fran Adar from HORIBA Scientific for performing Raman spectroscopy and measuring the oxygen/nitrogen/hydrogen content of the samples, (iv) Ibrahim Aydin at the Welding Technology and NDT Center, and Cemil Hakan Gur at the Department of Metallurgical and Materials Engineering, both at Middle East Technical University,

Ankara, Turkey, for conducting the sound velocity measurements, (v) Westmoreland-Mechanical Testing & Research (WMT&R) Inc. for performing the DSC measurements, (vi) Canadian Center for Electron Microscopy (CCEM) at McMaster University for conducting Auger electron spectroscopy, TEM and STEM, and HRTEM imaging, (vii) Dr. Jean-Pierre Kruth at the Department of Mechanical Engineering and Dr. Suraj Dinkar Jadhav at the Department of Materials Engineering, KU Leuven, Belgium, for their valuable insights and expertise, and (viii) the anonymous reviewers for their constructive feedback, which significantly contributed to improving the quality of the published papers.

Finally, I would like to express my heartfelt appreciation to my parents for their unwavering support, timely motivation, and infinite patience throughout my journey. I am forever grateful to my parents for providing me with the opportunities and experiences that have shaped me into the person I am today. Their selfless encouragement has empowered me to explore new paths in life and pursue my aspirations. I owe this achievement to their tireless efforts and dedication, and I dedicate this milestone to them with deep gratitude.

1	Chapter 1 Introduction	1
1.1	Background	2
1.2	Motivations	6
1.3	Research objectives	7
1.4	Thesis outline	8
2	Chapter 1 Role of powder particle size on laser powder bed fusion processability of AlSi10Mg alloy	13
2.1	Introduction.....	15
2.2	Materials and Experimental Procedure.....	19
2.2.1	Powder characteristics (chemical composition, particle size distribution and morphology)	19
2.2.2	Powder behaviors (flowability, packing density and optical absorption)	22
2.2.3	L-PBF Processing	24
2.2.4	Characterization of L-PBF-fabricated parts (densification level, dimensional accuracy, surface quality, microstructure and microhardness)	25
2.3	Results and Discussion.....	27
2.3.1	Flowability and packing density	27
2.3.2	Laser absorptivity	28
2.3.3	Density-laser energy input relationship	30
2.3.4	Densification level	33
2.3.5	Top surface quality	39
2.3.6	Dimensional accuracy.....	44

2.3.6.1	X-Y plane	44
2.3.6.2	Building direction (Z-direction)	47
2.3.7	Microstructural characterization	50
2.3.8	Microhardness	54
2.4	Conclusions	56
3	Chapter 2 Influence of alloying elements on laser powder bed fusion processability of aluminum: A new insight into the oxidation tendency	64
3.1	Introduction	66
3.2	Materials and Experimental Procedure	70
3.3	Results and Discussion	74
3.3.1	Processability of Al/Al alloys	74
3.3.2	Influence of Powder attributes and laser absorptivity on the processability	79
3.3.3	Influence of the chemical composition on the oxidation tendency and processability	85
3.3.3.1	Nature of the oxide compounds in the starting powder	85
3.3.3.2	Oxygen content of the initial powders and printed parts	89
3.3.3.3	Oxide diminishment mechanism	93
3.3.3.4	Verifying the proposed oxide diminishment mechanism through microstructural observations	104
3.3.3.5	Rationalization of the lower oxygen content in the printed parts based on the proposed mechanism	108
3.3.4	Comments on the inability of decomposition and reduction reactions to decrease the oxygen content	111

3.4	Conclusions.....	113
4	Chapter 3 Unraveling the low thermal conductivity of the LPBF fabricated pure Al, AlSi12, and AlSi10Mg alloys through substrate preheating.....	120
4.1	Introduction.....	122
4.2	Materials and Experimental Procedure.....	125
4.3	Results.....	128
4.3.1	Thermal properties.....	128
4.3.1.1	Specific heat capacity (C_p).....	128
4.3.1.2	Density and thermal expansion.....	130
4.3.1.3	Thermal diffusivity.....	133
4.3.1.4	Thermal conductivity.....	135
4.3.2	Microstructure.....	137
4.3.2.1	Grain structure.....	138
4.3.2.2	Microstructure within grains.....	140
4.3.2.3	Identification of micro- and nano-constituents.....	142
4.4	Discussion.....	152
4.4.1	Electron mean free path at room temperature.....	152
4.4.2	Contribution of extrinsic scattering phenomena at room temperature	
	155	
4.4.3	Role of temperature in scattering phenomena and thermal properties	
	165	
4.5	Conclusion.....	170

5	Chapter 4 On the preparation and characterization of AlSi12-graphene powder for powder bed fusion additive manufacturing applications.....	177
5.1	Introduction.....	179
5.2	Experimental procedure.....	181
5.3	Results and Discussion.....	183
5.3.1	Powder attributes	184
5.3.1.1	Microscopical observations.....	184
5.3.1.2	Size and size distribution.....	190
5.3.1.3	Shape characteristics	193
5.3.2	Powder behaviors	196
5.3.2.1	Absorptivity.....	196
5.3.2.2	Packing density	197
5.3.2.3	Flowability	199
5.3.3	O/C/H content of the powders	208
5.3.4	Carbon quality and type: Raman spectroscopy	211
5.4	Conclusions.....	222
6	Chapter 5 Influence of the graphene incorporation on nanostructure and thermal properties of the laser powder bed fusion processed AlSi12 matrix composites.....	229
6.1	Introduction.....	231
6.2	Materials and experimental procedure.....	236
6.3	Results and Discussion.....	240
6.3.1	Processability of AlSi12-Gr composites.....	242
6.3.2	Microstructure	250

6.3.2.1	Investigation of the survival of Gr	252
6.3.2.2	Transformation of Gr to Al_4C_3	259
6.3.2.3	Influence of Al_4C_3 formation on the grain structure.....	265
6.3.3	Microstructure-thermal/electrical properties relationship	267
6.3.3.1	Specific heat capacity	267
6.3.3.2	Thermal expansion and density	269
6.3.3.3	Thermal diffusivity.....	272
6.3.3.4	Thermal conductivity	274
6.4	Conclusions.....	278
6.5	Supplementary materials	279
6.5.1	L-PBF Process parameters.....	279
6.5.2	Powder attributes and behaviors.....	280
7	Chapter 6 Summary, Application, and Future Work	290
7.1	Summary and Application	291
7.2	Future work.....	295

List of Figures

Figure 1.1. Particle size distribution (PSD) of coarse and fine AlSi10Mg powders used in this study.	20
Figure 1.2. SEM micrographs of: (a) coarse, and (c) fine AlSi10Mg powders. (b) and (d) are higher magnification micrographs of the coarse and fine powders shown in (a) and (c), respectively.	21
Figure 1.3. Schematic view of a single test cycle in the dynamic flow methodology of the FT4 Freeman powder rheometer test used to evaluate the powder flowability. The rotating impeller moves downward and then upward through a fixed volume of powder placed in a standard vessel.	23
Figure 1.4. Schematic of the employed stripe hatching pattern scanning strategy, alternating 90° between subsequent layers.	25
Figure 1.5. The variation in the reflectivity and the K-M absorption factor of fine and coarse AlSi10Mg powders as a function of the wavelength. The dashed vertical line (wavelength of 1070 nm) represents the laser wavelength of the L-PBF machine used in this study. .	30
Figure 1.6. (a) The variation in the density of L-PBF fabricated AlSi10Mg parts as a function of the volumetric energy density (EV). (b) and (c) Cross-sectional optical micrographs of parts with the optimum density obtained by L-PBF processing of coarse (P =335 W, v =1050 mm/s, h =0.15 mm and EV =21.9 J/mm ³) and fine (P =335 W, v =1050 mm/s, h =0.15 mm and EV =16.3 J/mm ³) AlSi10Mg powders, respectively.....	33
Figure 1.7. Cross-sectional non-etched optical micrographs of parts obtained by L-PBF processing of: (a)-(c) coarse and (d)-(f) fine AlSi10Mg powders. The employed hatch spacing and scanning speed are 0.15 mm and 1300 mm/s for all samples while the laser powder is: (a), (d) 300 W; (b), (e) 335 W and (c), (f) 370 W.	35
Figure 1.8. Cross-sectional non-etched optical micrographs of parts obtained by L-PBF processing of: (a)-(c) coarse and (d)-(f) fine AlSi10Mg powders. The employed hatch spacing and scanning speed are 0.19 mm and 800 mm/s for all samples while the laser powder is: (a), (d) 300 W, (b), (e)335 W, and (c), (f) 370 W.	38

Figure 1.9. SEM micrographs from the cross-section of part obtained by L-PBF processing of the fine AlSi10Mg powder employing laser power of 300 W, scanning speed of 1300 mm/s and hatch spacing of 0.19 mm ($EV=9.3\text{ J/mm}^3$). (b) Shows the higher magnification micrograph of the selected region in (a). 39

Figure 1.10. SEM micrographs of the top surface for parts manufactured by L-PBF processing of: (a), (c), (e) coarse and (b), (d), (f) fine AlSi10Mg powders. The parts have been processed by a fixed laser power of 335 W and a constant hatch spacing of 0.15 mm but varying scanning speeds of: (a) and (b) 800; (c) and (d) 1050; (e) and (f) 1300 mm/s. The arrows show the scanning direction..... 41

Figure 1.11. Color-3D images showing the top surface topography of parts produced by L-PBF processing of: (a), (c), (e) coarse and (b), (d), (f) fine AlSi10Mg powders. The roughness of the provided surfaces is also listed in the table. The parts have been processed by a laser power of 335 W and a hatch spacing of 0.15 mm but varying scanning speeds of: (a) and (b) 800; (c) and (d) 1050; (e) and (f) 1300 mm/s. 42

Figure 1.12. The oxygen concentration of parts obtained by L-PBF processing of coarse and fine AlSi10Mg powders using various laser powders. The measurement has been performed by EDS analysis. The employed scanning speed and hatch spacing were 800 mm/s and 0.15 mm, respectively. 44

Figure 1.13. The deviation in the area of the X-Y plane in the cubic samples fabricated by L-PBF processing of fine (F) and coarse (C) AlSi10Mg powders using various P/v ratios and two different hatch spacings of 0.16 and 0.19 mm. 45

Figure 1.14. SEM micrographs of the side surface corresponding to parts obtained by L-PBF processing of: (a), (b) coarse and (c), (d) fine AlSi10Mg powders using laser power of 335 W, scanning speed of 1300 mm/s and hatch spacing of 0.15 mm. The higher magnification micrograph of the selected region in (c) is provided in (d). The inset in (d) shows the magnified view of powder particles adhered to the surface. UM/PM refers to unmelted/partially melted. 46

Figure 1.15. The deviation from the nominal height of samples with the optimum density obtained by L-PBF processing of coarse ($P=335\text{ W}$, $v=1050\text{ mm/s}$, $h=0.15\text{ mm}$ and $EV=21.9\text{ J/mm}^3$) and fine ($P=335\text{ W}$, $v=1050\text{ mm/s}$, $h=0.15\text{ mm}$ and $EV=16.3\text{ J/mm}^3$)

AlSi10Mg powders. The nominal height refers to the height of samples after being cut off the build plate. The errors associated with measurements are 4.3 and 6.5 μm for coarse and fine powder cases, respectively..... 48

Figure 1.16. Cross-sectional optical micrographs of parts manufactured by L-PBF processing of: (a) coarse and (b) fine AlSi10Mg powders using laser power of 370 W, scanning speed of 1300 mm/s and hatch spacing of 0.19 mm. 50

Figure 1.17. Cross-sectional optical micrographs of parts fabricated by L-PBF processing of: (a), (b) coarse ($EV=21.9 \text{ J/mm}^3$) and (c), (d) fine ($EV=16.3 \text{ J/mm}^3$) AlSi10Mg powders using laser powder of 335 W, scanning speed of 1050 mm/s and hatch spacing of 0.15 mm. (b) and (d) are higher magnification micrographs of boxed regions in (a) and (c), respectively. 51

Figure 1.18. SEM microstructure for parts obtained by L-PBF processing of: (a), (c) coarse ($EV=21.9 \text{ J/mm}^3$) and (b), (d) fine ($EV=16.3 \text{ J/mm}^3$) AlSi10Mg powders using laser powder of 335 W, scanning speed of 1050 mm/s and hatch spacing of 0.15 mm. (a) and (b) show the variation in the microstructure adjacent to the melt pool boundaries. (c) and (d) are enclosed views of the MP-F regions shown in (a) and (b), respectively. MP-F, MP-C and HAZ refer to the melt pool-fine, melt pool-coarse, and heat-affected zone, respectively. 53

Figure 1.19. Typical SEM micrographs of parts achieved by L-PBF processing of: (a) coarse; and (b), (c) fine AlSi10Mg powders using laser powder of 335 W, scanning speed of 1050 mm/s and hatch spacing of 0.15 mm ($EV= 16.3 \text{ J/mm}^3$). (c) Enclosed view of micro-cracks existing in (b). 54

Figure 1.20. The variation in the microhardness of parts achieved by L-PBF processing of fine (F) and coarse (C) AlSi10Mg powders as a function of the employed P/v ratio for two different hatch spacings of 0.15 and 0.19 mm. 56

Figure 2.1. Schematic illustration of (a) LPBF process, (b) in-situ oxidation of aluminum/aluminum alloys during the formation of each track, and (c) breakdown of the oxides of the previous layer during the consolidation of the subsequent layer in the overlap regions. By deep etching of the printed samples, Louvis et al. [16] observed a continuous

oxide film between the laser scan tracks and concluded that the inter-track oxides do not break during the printing of the subsequent tracks. 68

Figure 2.2. The schematic view listing the analysis performed on: (a) powder, (b) single tracks, and (c) cubic coupons. 74

Figure 2.3. Relative density versus E_v of the LPBF-processed: (a) Pure Al, (e) AlSi12, and (i) AlSi10Mg. The density results are the average of two distinct measurements. The standard deviation from the average values was in the range of 0.04-0.98 for pure Al (a), 0.03-0.48 for AlSi12 (e), and 0.03-0.56 for AlSi10Mg (i). The zones designated in (a), (e), and (i) by the ovals with the dotted, dashed, and dash-dotted outlines represent the samples with large irregular pores (and delamination in (a)), highly-dense samples (with a relative density higher than 98.5%), and samples with large spherical pores, respectively. The region named as (1) in (a), (e), and (i) shows the samples having relative densities higher than 99%. The region named as (2) in (e) refers to the samples with relative densities between 98.5 and 99%. The optical micrographs in (b-d) show examples of pure Al samples with large irregular pores, delamination, and almost no defects (zone (1)), respectively. The optical micrographs in (f-h) show examples of AlSi12 samples with large irregular pores, almost no defects, and large spherical pores, respectively. The optical micrographs in (j-i) show examples of AlSi10Mg samples with large irregular pores, almost no defects, and large spherical pores, respectively. The process window for each material leading to relative densities higher than 99% is shown in (m). 78

Figure 2.4. (a) Particle size distribution and SEM micrographs, and (b) optical absorption versus wavelength of the pure Al, AlSi12, and AlSi10Mg powders. 81

Figure 2.5. The first-derivative Auger spectra for: (a) Pure Al, (b) AlSi12, and (c) AlSi10Mg powders. The reference spectra of Al_2O_3 , Al, SiO_2 , Si, MgO, and Mg, are provided in (d-i), respectively. The higher magnification of the designated colored box in each reference spectrum is shown in (j-r). 87

Figure 2.6. The oxygen content (mass ppm) of the starting powders as well as the pure Al, AlSi12, and AlSi10Mg parts fabricated by P=200 W ($v=2000$ mm/s) and P=300 W ($v=1400$ mm/s). The reported O concentrations for each powder or printed sample

represent the average of two distinct measurements. Error bars represent the standard deviation from the average values. 90

Figure 2.7. The schematic illustration of: (a) Al/Al alloy powder particles having an oxide shell, (b) melting of the core before its separation from the oxide shell caused by the non-equilibrium rapid heating of the powder particles, (c) oxide fracture and spallation through the core melting and pressure build-up mechanism, (d) buoyancy force and (e) Marangoni thermocapillary force in the melt pool causing the nano-sized oxide particles to concentrate on the surface of the melt pool, (f) evaporation of the oxides, especially in zone (I) as a result of their direct interaction with the laser beam, (g) the solidified melt pool and trapped oxides after the laser travels away, and (h) second chance of oxide evaporation during the printing of the subsequent tracks where the oxides in zone (II) of the previous track locate in zone (I) of the new track. 96

Figure 2.8. The size measurement results of pure Al single tracks: (a) scan track width, and (b) scan track depth as a function of v at different P . The reported values are the average of at least six distinct measurements, and the error bars are the standard deviations from the average values. The cross-sectional view of the tracks processed at high ($P = 370$ W, $v = 400$ mm/s), medium ($P = 370$ W, $v = 1600$ mm/s), and low ($P = 200$ W, $v = 1400$ mm/s) heat inputs are shown in (c-e), respectively. 102

Figure 2.9. The size measurement results of AlSi12 single tracks: (a) scan track width, and (b) scan track depth as a function of v at different P . The reported values are the average of at least six distinct measurements, and the error bars are the standard deviations from the average values. The cross-sectional view of the tracks processed at high ($P = 370$ W, $v = 800$ mm/s), medium ($P = 300$ W, $v = 1400$ mm/s), and low ($P = 200$ W, $v = 1600$ mm/s) heat inputs are shown in (c-e), respectively. 103

Figure 2.10. The size measurement results of AlSi10Mg single tracks: (a) scan track width, and (b) scan track depth as a function of v at different P . The reported values are the average of at least six distinct measurements, and the error bars are the standard deviations from the average values. The cross-sectional view of the tracks processed at high ($P = 370$ W, $v = 800$ mm/s), medium ($P = 300$ W, $v = 1400$ mm/s), and low ($P = 200$ W, $v = 1800$ mm/s) heat inputs are shown in (c-e), respectively. 104

Figure 2.11. Top surface SEM micrographs of pure Al samples processed using $v=1400$ mm/s and P of: (a) 200 W, (b) 250 W, (c) 300 W, and (d) 370 W. (e) and (f) Top surface of AlSi12 and AlSi10Mg samples processed using $v =1400$ mm/s and P of 250 W. There are two insets in each SEM micrograph, the top one is the EDS map showing the oxygen distribution on the top surface, and the bottom one shows the ESD map of oxygen distribution merged with the corresponding SEM micrograph.....	107
Figure 2.12. The hydrogen content in ppm (by mass) in the pure Al, AlSi12, and AlSi10Mg powders.....	113
Figure 3.1. Specific heat capacity (CP) versus temperature for (a) pure Al, (b) AlSi12, and (c) AlSi10Mg. The higher magnification of the designated colored box in (b) and (c) is shown in (d-f).....	130
Figure 3.2. XCT image of porosity distribution for (a) pure Al, (b) AlSi12, and (c) AlSi10Mg.....	131
Figure 3.3. The relative change in physical dimension (ΔLLO) versus temperature for (a) pure Al, (b) AlSi12, and (c) AlSi10Mg. The inset in (b) and (c) show the ΔLLO versus temperature in the cooling cycle. The higher magnification of the designated colored box in (b) and (c) is shown in (d) and (e), respectively. The variation of density with temperature is shown in (f) for all materials.	133
Figure 3.4. Thermal diffusivity versus temperature for (a) pure Al, (b) AlSi12 and (c) AlSi10Mg.....	135
Figure 3.5. Thermal conductivity results versus temperature for pure Al, AlSi12, and AlSi10Mg.....	137
Figure 3.6. Optical micrographs of cross-sections parallel to the building direction for (a) pure Al, (b) AlSi12, and (c) AlSi10Mg. The EBSD IPF-Z maps for the respective materials are shown in (d), (e), and (f).	139
Figure 3.7. SEM micrographs of (a,b) pure Al, (c,d) AlSi12, and (f,g) AlSi10Mg. The images provided in (b), (d), and (g) are the higher magnifications of regions designated by the dashed box in (a), (c), and (f), respectively. The Scheil Gulliver solidification modeling (SGSM) for AlSi12 and AlSi10Mg are shown in (e) and (h), respectively.	142

Figure 3.8. Pure Al samples: Bright-field TEM images showing (a) the TEM sample overview, (b) dislocations, and (c,d) oxides. The HAADF STEM image and EDS elemental mapping results for Al and O are shown in (e-g), respectively. (h) The size distribution of nano-size oxides observed in (c,d). (i,j) The EBSD grain boundary map and its corresponding geometrically necessary dislocation (GND) map..... 144

Figure 3.9. AlSi12 sample: Bright-field TEM images showing (a) TEM sample overview, (b,c) cells and cell boundaries, and (d) dislocations. The EDS elemental map analysis performed on HAADF image (e) showing the distribution of (f) Al, (g) Fe, (h) O, and (i) Si elements. (j,k) The point EDS analysis location and spectrum. (l,m) The EBSD grain boundary map and its corresponding geometrically necessary dislocation (GND) map.146

Figure 3.10. AlSi10Mg sample: Bright-field TEM images showing (a) TEM sample overview, (b,c) cell walls and phases within cells and (d) dislocations. The EDS elemental map analysis performed on the HAADF image in (e) showing the distribution of (f) Al, (g) Si, (h) Fe, (i) Mg, and (j) O elements. (k,l) The point EDS analysis location and spectrum. The EDS elemental map analysis performed on the HAADF image in (m) showing the distribution of (n) Al, (o) Si, and (p) Mg elements in the phases observed within cells. (q,r) The EBSD grain boundary map and its corresponding geometrically necessary dislocation (GND) map. 149

Figure 3.11. The oxygen content of pure Al, AlSi12, and AlSi10Mg samples. 152

Figure 3.12. XCT results used to measure the mean chord length for (a) pure Al, (b) AlSi12, and (c) AlSi10Mg. The range of grain size and/or cell size for (d) pure Al (e,g) AlSi12 and (f,h) AlSi10Mg..... 159

Figure 3.13. Contribution of intrinsic and different extrinsic scattering phenomena for the LPBF-fabricated: (a) Pure Al, (b) AlSi12, and (c) AlSi10Mg. Since being negligible, the contributions of pore and grain boundary are not shown for all materials. 161

Figure 4.1. SEM micrographs of different powders (a) AlSi12, (b) R4, (c) R6, (d,g) B1.5, (e,f,h) B2, and (i,j) ball milled unreinforced AlSi12..... 185

Figure 4.2. (a) SEM micrograph of carbonaceous powder with an inset showing the fine particles at higher magnification, and (b-k) SEM micrographs and their corresponding EDS mapping results showing the C distribution for the designated powders..... 188

Figure 4.3. SEM micrographs and their corresponding EDS mapping results showing the C distribution for (a-f) B1.5 and (g-l) B2 powders.	189
Figure 4.4. (a-e) Cumulative and relative frequency distributions of the designated powders, and (f) UI and span values for different powders.	192
Figure 4.5. (a-e) SPHT, (f-j) symmetry, and (k-o) b/l versus area mean diameter for the designated powders.	195
Figure 4.6. (a-e) Absorptivity versus wavelength for the designated powders and (f) average absorptivity values at the wavelength of 1070 nm.	197
Figure 4.7. Images captured from the powder in the rotating drum at the onset and after an avalanche for (a,b) AlSi12, (c,d) R4 and (e,f) B1.5 powders showing the avalanche angle and/or fractal surface.	201
Figure 4.8. (a-e) Avalanche angle, (e-j) avalanche energy, and (k-o) fractal dimension for the designated powders.	203
Figure 4.9. Schematic illustration of (a) two non-decorated host particles, (b) a guest-decorated particle with an undecorated one, and (c) two guest-decorated host particles and (d) relative humidity of different powders.	208
Figure 4.10. (a) Carbon, (b) oxygen and (c) hydrogen content of different powders.	211
Figure 4.11. Reference Raman spectra for (a,d,e) graphite [59], (b,f,g) graphene [60], (c,h,i) crystalline silicon [61], (j) nanographite [62], and (k) damaged graphene [63].	214
Figure 4.12. (a) Raman mapping results for three starting C particles, (b) Range of G, D and 2D positions detected for a C particle.	216
Figure 4.13. Raman mapping results for (a-g) B2 and (h) B1.5 samples. In the blue spectrum in (a) only the 2D ₂ peak is labeled.	217
Figure 4.14. Raman mapping results for R6 and R4 samples.	220
Figure 5.1. Schematic of the printed samples for thermal diffusivity measurement along and perpendicular to the building direction.	240

Figure 5.2. (a) SEM micrograph of AlSi12 powder, (b,c) SEM micrographs of carbonaceous powder, and (d-m) SEM micrographs and their corresponding EDS mapping results showing the C distribution for the designated powders.....	242
Figure 5.3. Relative density versus laser power and scanning speed for (a) AlSi12-0.25Gr and (b) AlSi12-0.5Gr samples printed at different hatch spacing. Optical micrographs of (c-e) AlSi12-0.25Gr and (f-h) AlSi12-0.5Gr samples at different level of energy densities (low, medium, and high) with sets of process parameters shown on the images.....	244
Figure 5.4. (a) Laser absorptivity versus wavelength of powders, (b) relative humidity of powders, (c) oxygen content, (d) carbon content, and (e) nitrogen content of the starting powders and printed parts. Sample 1,4 (optimum AlSi12-0.25Gr and AlSi12-0.5Gr), Sample 2,5 (300 W, 1200 mm/s, 100 μm , 30 μm), sample 3,6 (370 W, 2200 mm/s, 100 μm , and 30 μm). The absorptivity, relative humidity, oxygen and carbon content of the AlSi12 and AlSi12-0.5Gr powders were previously reported in [an under review paper].	249
Figure 5.5. AlSi12 sample: BF TEM images (a) overview, (b) cell and cell boundaries, and (c) dislocations. HAADF-STEM images and their corresponding EDS maps for cell structure (d,e) and Si particles at intercellular region (f-h).....	252
Figure 5.6. Overview of the wedge-shaped TEM images and their thickness profiles in the thick and thin sections obtained by EELS for (a-c) AlSi12-0.25Gr and (d-f) AlSi12-0.5Gr.	254
Figure 5.7. Thick section: HAADF-STEM images and their corresponding EDS maps for cell structure of (a,b) AlSi12-0.25Gr and (c,d) AlSi12-0.5Gr.	254
Figure 5.8. Thin section: HAADF-STEM images and their corresponding EDS maps for (a,b) AlSi12-0.25Gr and (c,d) AlSi12-0.5Gr. (e,f) HRTEM images of the carbonaceous nano-constituent phase detected in (c), (g) FFT pattern of the designated area in (f), and (h,i) inverse FFT of the yellow circles in (g) and the intensity-distance profile of the arrow in (h).....	256
Figure 5.9. Raman mapping results for (a-c) AlSi12-0.25Gr and (d-i) AlSi12-0.5Gr samples.....	258

Figure 5.10. Thin section: HAADF-STEM images and their corresponding EDS maps for (a-e) AlSi12-0.25Gr and (h-k) AlSi12-0.5Gr samples. (f,g) HRTEM images of Al4C3 at two different magnifications and their corresponding FFT patterns and inverse FFT for (f,g) AlSi12-0.25Gr and (l,m) AlSi12-0.5Gr samples.	260
Figure 5.11. (a) Binary equilibrium phase diagram of Al-C, (b) pseudo-binary equilibrium phase diagram of AlSi12-C, and (c-f) designated zones in (b).	263
Figure 5.12. IPF-Z EBSD maps for the designated samples (a-c) along the building direction, and (d-f) perpendicular to the building direction.	267
Figure 5.13. (a,c,e) C_p versus temperature for the labeled materials, and (b,d,f) higher magnification illustration of colored boxes shown in (a,c,e).	269
Figure 5.14. (a,c,e) relative change in physical dimensions versus temperature during heating cycle for the labeled materials, and (b,d,f) higher magnification illustration of colored boxes shown in (a,c,e). (g) relative change in physical dimensions versus temperature during cooling cycle, and (h) density versus temperature curves.	271
Figure 5.15. Thermal diffusivity versus temperature (a) along and (b) perpendicular to the building direction.	273
Figure 5.16. Thermal conductivity versus temperature (a) along and (b) perpendicular to the building direction.	275
Figure 5.17. SEM micrographs of the designated materials (a,c,e) along and (b,d,f) perpendicular to the building direction.	277

List of Tables

Table 1.1. Effect of powder particle size on the powder characteristics and/or the quality of the final printed parts in the literature.....	18
Table 1.2. Nominal chemical composition of powders.....	20
Table 1.3. The process parameters employed to fabricate parts.	25
Table 1.4. The results of Hall flowmeter and FT4 Freeman powder rheometer techniques presenting the flowability and density of powders.	28
Table 2.1. The nominal chemical composition of pure Al, AlSi12, and AlSi10Mg powders.	71
Table 2.2. Process parameters used for the fabrication of test coupons.....	72
Table 2.3. The apparent packing density of the powders measured by the Hall flowmeter funnel.	83
Table 2.4. Surface chemical composition of the pure Al, AlSi12, and AlSi10Mg powders	89
Table 3.1. Parameters used to calculate the electron mean free paths for the LPBF-fabricated pure Al, AlSi12, and AlSi10Mg and theoretical mean free paths for pure Al.	154
Table 3.2. Parameters used to calculate the electron mean free path in the presence of each extrinsic scattering site.....	159
Table 3.3. Parameters used to calculate the Debye temperature for the LPBF-fabricated pure Al, AlSi12, and AlSi10Mg	166
Table 4.1. sets of mixing parameters for optimum condition for regularly mixed and ball milled powders.....	182
Table 4.2. Apparent packing density, its standard deviation and relative density for different powders	199
Table 4.3. Hamaker constants and van der Waals attraction force ratios for B1.5 and B2 powder samples.....	207

Table 5.1. Range of process parameters used to print AlSi12-0.25Gr and AlSi12-0.5Gr samples.....	240
Table 5.2. Parameters used to calculate the critical velocity of the solidification front.	265
Table 5.3. Average grain size and percentage of different angle grain boundaries for different materials.	267

List of abbreviations and symbols

AM	Additive manufacturing
PBF	Powder bed fusion
DED	Directed energy deposition
L-PBF or LPBF	Laser powder bed fusion
SEM	Scanning electron microscopy
EDS	Energy dispersive X-ray spectroscopy
SVFR	Stable and Variable Flow Rate
BFE	Basic flow energy
SE	Specific energy
CBD	Conditioned bulk density
PSD	Particle size distribution
DRS	Diffuse reflectance spectroscopy
PMT	Photon Counting photomultiplier tubes
CMM	Coordinate measuring machine
OM	Optical microscopy
K-M	Kubelka-Munk absorption factor
MP-fine	Melt pool with a fine microstructure
MP-coarse	Melt pool with a coarse microstructure
HAZ	Heat affected zone
AES	Auger electron spectroscopy
IGA	Instrumental Gas Analyzer
XCT	X-ray computed tomography

PPM	Part per million (mass)
EV	Electric vehicle
LVDT	Linear voltage displacement transducer
EBSD	Electron backscatter diffraction
FESEM	Field-emission scanning electron microscopy
TEM	Transmission electron microscopy
FIB	Focused ion beam
STEM	Scanning transmission electron microscopy
TOF	Time of flight
LFA	Laser flash analyzer
DSC	Differential scanning calorimetry
IPF	Inverse pole figure
SGSM	Scheil-Gulliver solidification modeling
HAADF	High-angle annular dark-field
GND	Geometrically necessary dislocation
BF	Bright field
AMC	Aluminum matrix composite
UI	Uniformity index
SPHT	Sphericity
Symm	Symmetry
SD	Standard deviation

HRTEM	High resolution transmission electron microscopy
CNT	Carbon nanotube
BD	Build direction
EELS	Electron energy loss spectroscopy
FFT	Fast Fourier transform
PD	Perpendicular direction
D_{10}	Particle diameters at 10 vol% in the cumulative distribution
D_{50}	Particle diameters at 50% in the cumulative distribution
D_{90}	Particle diameters at 90% in the cumulative distribution
D_{ave}	
m_{split}	Mass of the powder after removing the excess powder from FT4 vessel
V_{split}	volume of powder after removing the excess powder from FT4 vessel
P	Laser power
V	Laser scanning speed
h	Hatch spacing
t	Powder layer thickness
t_{eff}	Effective powder layer thickness

S_a	Arithmetic mean surface roughness value
R	Reflectance of the powder
K or A	Absorption coefficient
S	Scattering coefficient
E_{need}	Energy required to melt a single powder particle
E_{av}	Average energy of the laser beam
r	Particle radius
ρ	Theoretical density or relative powder packing density
C or C_p	Specific heat capacity
ΔT_m	Temperature rise up to the melting point
L_m	Latent heat of fusion
I_0	Intensity of the laser beam
G	Thermal gradient
R	Solidification rate
μ	Electrical resistivity
λ	Wavelength of the laser beam
n_s	Absorptivity of the bulk material
f_o	Fraction of oxygen detected in powder
M	Molar mass
t_{oxide}	Oxide layer thickness

α	Coefficient of thermal expansion or thermal diffusivity
E	Young's modulus
σ_c	Circumferential stress
P_r	Pressure due to volume change
B	Bulk modulus
ε_v	Volume strain
σ_θ	Hoop stress
r_{ave}	Average particle radius
γ	Surface tension
T_m	Melting point of a particle
T_0	Bulk melting temperature
γ_{sv}	Solid/vapor surface energy
γ_{lv}	Liquid/vapor surface energy
ΔH_m	Latent heat of fusion
ρ_s	Density of solid material
A/V	Area-to-volume ratio of powder particles
T	Melt pool temperature
K (capital)	Thermal conductivity
k (small)	Boltzmann constant
r_0	Beam radius
r	Radial position in the melt pool
ρ_{RT}	Bulk density at ambient temperature

ΔL	Change in physical dimension
L_0	Initial sample length
ΔT	Solidification range
D_L	Solute diffusivity in the liquid material
l_e	Electron mean free path
V_F	Velocity of electrons above the Fermi level
τ	Average time between two subsequent electronic collisions
E_f	Fermi energy
m_e	Mass of an electron
ρ	Electrical resistivity
n	Number of atoms per volume
e	Electron charge
l_{pore}	Mean free path of electrons when scattering sites are porosities
l_{gb}	Mean free path of electrons when scattering sites are grain boundaries
l_{cb}	Mean free path of electrons when scattering sites are cell boundaries
l_{oxide}	Mean free path of electrons when scattering sites are oxides

l_{Si}	Mean free path of electrons when scattering sites are nano-size Si precipitates
l_{Mg_2Si}	Mean free path of electrons when scattering sites are nano-size Mg_2Si phase
l_{vac}	Mean free path of electrons when scattering sites are atomic vacancies
l_{dis}	Mean free path of electrons when scattering sites are dislocations
l_{ss}^{Si}	Mean free path of electrons when scattering sites are supersaturated Si atoms
n_v	Number of vacancies per unit volume
Q_v	Energy required to produce one mole of vacancies
R	Gas constant
σ_v	Cross-section for the scattering of the electrons by vacancies
n_d	Total length of dislocations per unit volume
σ_d	Scattering cross-section of the electrons per unit length of dislocations
$\Delta\rho_d^*$	Resistivity per unit dislocation density

n_{ss}	Number of solid solution Si atoms in the matrix per unit volume
σ_{ss}	Cross-section for the scattering of the electrons by solid solution atoms
θ_D	Debye temperature
n	Number of atoms per unit volume
h	Plank's constant
v	Sound velocity in the medium
v_T	Transverse sound velocity
v_L	Longitudinal sound velocity
$D(T_0)$	Diffusion coefficient of electrons at 295 K
b/l	Breadth-to-length ratio of particles
P	Perimeter of a particle projection
A	Measured area covered by a particle projection
$X_{C,min}$	Minimum chord length
$X_{Fe, max}$	Maximum Feret diameter
A_{hh}	Hamaker constant for the interacting host particles
A_{hg}	Hamaker constant for the interaction between host and guest particles
A_{gg}	Hamaker constant for the interaction between guest particles

D_h	Average Diameter of host powder particles
d	Diameter of guest particle
h_0	Atomic-scale separation between particles
$P_{\text{Non-decorated}}$	Van der Waals attraction force between two host particles
$P_{\text{Decorated}}$	Van der Waals attraction force between two guest decorated host particles
V_{cr}	Critical velocity of the solidification front
r	Radius of solid reinforcement
K_P	Thermal conductivity of reinforcement
K_L	Thermal conductivity of liquid
σ_{PS}	Reinforcement-interface surface energy
σ_{PL}	Reinforcement-liquid surface energy
σ_{SL}	Interface-liquid surface energy
η	Melt viscosity
d_0	Interatomic distance of the matrix alloy
V_{SL}	Velocity of the solidification front
θ	Angle between the scanning direction and the normal to the melt pool boundary

1 Chapter 1 Introduction

1.1 Background

What is additive manufacturing (AM)? Based on the ASTM terminology, AM is defined as "a process of joining materials to make objects from 3D model data, usually layer-upon-layer" [1]. "Rapid Manufacturing," "Rapid Prototyping," and "Layer Manufacturing" are other terminologies frequently used for AM. Initially, the computer-aided design (CAD) file of the part to be fabricated is sliced into several thin layers. Afterward, the sliced file is imported into the 3D printer's software, and by means of a heat source, the starting powder or wire feedstock turns into a consolidated 3D object in a layer-by-layer fashion [2]. Each consolidated layer represents one slice of the whole object that is to be printed. AM technology has been categorized into several distinct groups, two of which have been widely used to manufacture custom-designed metallic and metal matrix composite (MMC) parts, namely powder bed fusion (PBF) and directed energy deposition (DED) [3]. While the former enables the fabrication of relatively small components with complex geometries and intricate features, the latter provides the opportunity of manufacturing relatively large components with less complexity. Among the PBF-AM category, the laser PBF (L-PBF) process can be considered one of the most promising techniques for manufacturing fine features [4]. In this process, a uniform layer of powder feedstock is deposited on the build platform by a recoater unit. When subjected to the laser heat source, predefined regions of the deposited layer are melted and fused to the build platform, forming a single layer of the desired part. The powder bed is lowered by the downward movement of the build platform, and a new layer of powder is deposited. The extra powder during the deposition of each powder layer goes into the collection container. The newly deposited powder layer is then subjected to the heat source, melting specified regions, and their fusion into the previously

deposited material, followed by solidification. Repetition of powder deposition and melting procedures results in the fabrication of the part in a layer-by-layer manner [5].

Since there is no need for tools, molds, dies, or any other auxiliaries to manufacture a component, the L-PBF process gives designers a free hand to no longer be confined by the manufacturing processes but by their imagination [6]. On this account, the L-PBF process has greatly influenced different industries by changing the design concept from design-for-manufacturing to design-for-performance [7]. One of the industries that the L-PBF process has dramatically impacted is automotive due to the possibility of the L-PBF process in manufacturing tube/fin, plate/fin, finless tube micro-channels, pitot tube, and twisted tube heat exchangers [4]. Moreover, the L-PBF process has enabled the fabrication of heat sinks with lattice structures, cooling channels, and pins/fins with functionally graded geometries, resulting in significantly enhanced cooling efficiency [8]. Notwithstanding, full-scale implantation of such beneficial concepts might be hurdled by other determining factors such as fast heating/cooling rates (in the order of $\sim 10^5$ - 10^6 K/s) [9], development of non-equilibrium microstructures [10], in-situ oxidation [11], and defect formation during the L-PBF process [12]. Given that the structure-property relationships of materials are dictated by their manufacturing techniques, the physical/mechanical properties of the L-PBF fabricated structures have to be preeminently investigated before their reliable implementation.

In many automotive industry applications, aluminum (Al) and Al alloys are believed to be potential candidates owing to their high specific mechanical strength and thermal/electrical conductivity [13]. In the family of Al-based materials, AlSi12 and AlSi10Mg alloys are the most commonly used and studied materials due to their combination of high thermal conductivity and mechanical properties when produced by conventional manufacturing

processes. Based on the numerous research studies conducted on mechanical properties of the LPBF-processed AlSi10Mg and AlSi12 alloys, up to 40% improvement in yield and tensile strength for AlSi10Mg and up to 400 and 200% improvement in the corresponding values for AlSi12 alloy were reported [14-17]. However, from the thermal conductivity perspective, the literature suggests that the L-PBF fabricated pure Al, AlSi12, and AlSi10Mg alloys possess lower thermal conductivities in as-built conditions than their wrought counterparts [18]. According to a report published by EOS GmbH (L-PBF machine manufacturer), the application of post-build heat treatment (annealing at 300 °C/2h) is essential to achieve high thermal conductivities for the L-PBF fabricated AlSi10Mg parts. In light of the preceding, there is still a knowledge gap in understanding the underlying reasons for the observed inferior thermal behavior of most versatile L-PBF fabricated Al/Al alloys for thermal applications, which makes their industrial implementation as end-use products (without needing post-build heat treatment) rather challenging.

As discussed above, freedom in design is enabled by the capabilities of the L-PBF process. However, "design" does not exclusively refer to "geometric design." Materials with changing composition and microstructure through in-situ alloying and composite making are also feasible to be fabricated through the L-PBF process. The concept behind the addition of reinforcing particles into the aluminum metallic matrix is to have a material with a combination of the properties of the matrix and reinforcement [19]. Despite the DED processes, pre-processing powders prior to printing is an inseparable part of MMC production when employing PBF processes. This originates from the absence of different nozzles for feeding composite constituents in the L-PBF processes, requiring a composite powder feedstock as the starting material. In recent years, the emergence of cost-effective production

techniques for carbonaceous materials such as graphene has opened a new window toward their implementation as favorable reinforcements for Al/Al alloys [20]. The incorporation of the graphene into the Al matrix should not only lead to increased mechanical properties, which could be achieved by adding other families of reinforcements, but also may have the potential to (i) increase thermal and electrical conductivity, (ii) increase damping capacity, and (iii) decrease the wear rate and friction coefficient at the same time, improvements which are unique to carbonaceous over other reinforcements [21].

It is worth noting that the Al/Al alloys have performed adequately for several years in the automotive industry and electronic applications. However, the ever-growing demand for materials with higher specific thermal conductivity and mechanical properties necessitates the study of MMCs. The increase in the power level in many applications has made the thermal management of the systems rather challenging, a problem that may be solved by introducing a second constituent (i.e., graphene) with higher thermal conductivity to Al/Al alloy matrix and fabricating more complex architectures (e.g., lattice structures) with higher effective surface area to volume ratio through L-PBF process [22].

The present thesis sets out to investigate the processability of pure Al, AlSi12, and AlSi10Mg in the context of the L-PBF process. On this account, the following will be discussed in detail, (phase I) the role of powder particle size on the densification level, surface roughness, and dimensional accuracy of the fabricated parts, (Phase II) the oxidation behavior of Al/Al alloys during the L-PBF process and proving that the higher rate of oxide diminishment than any possible in-situ oxidation, (phase III) an easily attainable solution to end up with high thermal conductivities in the as-built condition (comparable to their conventionally manufactured counterparts) and eliminating the need for post-build heat treatments for the studied Al/Al

alloys, and (phase IV) the influence of graphene incorporation into an Al alloy on its thermal properties.

1.2 Motivations

Conventionally manufactured battery casings with simple designs are currently used in electric vehicles. The relatively low casing/battery contact area to volume ratio and the relatively high weight of such battery casings are their two major drawbacks. Moreover, active cooling of the batteries in conventional battery packs is essential to avoid fast degradation of the batteries. Adopting the L-PBF process to produce highly efficient electronic battery packs for electric devices/vehicles seems an interesting topic that has received scant attention. Yet there is a great deal of room in this field to manufacture battery packs with lattice structure casings to enhance the cooling efficiency of the battery packs during the operation of batteries and eliminate the need for active cooling, especially in the case of low-capacity packs (e.g., 1 kWh) with slow charging/discharging rates. Functional battery packs can be fabricated by the L-PBF process in which the lattice casing or solid casing with channels acts as a heat sink to cool down the batteries through passive cooling (rather than active cooling). These geometries are complex and are difficult to fabricate by conventional manufacturing processes. Highly conductive and lightweight materials such as pure Al, AlSi12, and AlSi10Mg are potential candidates for this application. However, it needs to be investigated whether or not the L-PBF-fabricated Al/Al alloy parts are highly conductive due to their non-equilibrium microstructure and the chance of in-situ oxidation. Due to the relatively large size of the battery casings, their heat treatment is rather tricky, time-consuming, and cost prohibitive. Therefore, it is highly desired to obtain end-use battery casings through the L-PBF process without using post-build heat treatment, which is one of the focus domains of this study. If the incorporation of Gr into

Al led to increased thermal conductivity, then the Al/Gr composite can also be a candidate for this application.

1.3 Research objectives

The core aim of the current research is to use the full scope of the L-PBF process in battery casing manufacturing in the automotive industry. Pure Al, AlSi12, and AlSi10Mg, as the most commonly used Al/Al alloys for thermal conductivity applications, will be the central focus of the current thesis. The objective of this work could be refined into the followings:

- 1) Studying the role of powder particle size and size distribution on the quality of the L-PBF fabricated Al/Al alloys through densification level, top and side surface roughness/waviness, in-plane and Z-direction dimensional accuracy investigations.
- 2) Investigation of the role of alloying elements such as Si and Mg on laser absorptivity, powder packing density, and flowability, nature of oxide layers on the surface of powder particles, and oxide diminishment during the L-PBF process; in a word, influence of alloying elements on the processability of aluminum.
- 3) Determining the processing window and optimum sets of process parameters to achieve highly dense pure Al, AlSi12, and AlSi10Mg parts with relative densities higher than 99%.
- 4) Developing a cost-effective and easily attainable solution to enhance the thermal conductivities of Al/Al alloys in as-built condition, eliminating the need for time-consuming and cost-prohibitive post-build heat treatments.
- 5) Incorporation of graphene into AlSi12 alloy and studying the process-microstructure-thermal properties relationship through density measurements, in-depth

microstructural characterizations, and specific heat capacity/coefficient of thermal expansion/ thermal diffusivity/thermal conductivity measurements.

1.4 Thesis outline

This Ph.D. thesis is an integrated article thesis, also known as a sandwich thesis, which is composed of 7 chapters focusing on the laser powder bed fusion additive manufacturing of pure Aluminum, AlSi12 alloy, AlSi10Mg alloy, and AlSi12-graphene composites. Chapters 2-6 correspond to articles published in reputable international journals or currently being reviewed for publication.

Chapter 1 introduces the background, motivation, and objectives of the research to frame the scope of the thesis.

Chapter 2 is focused on the influence of powder particle size on the densification level and dimensional accuracy of AlSi10Mg parts fabricated by the laser powder bed fusion process. This chapter contains the previously published material in the "Additive Manufacturing" journal as "Role of powder particle size on laser powder bed fusion processability of AlSi10Mg alloy" by Mohamed Balbaa, Ali Ghasemi, Eskandar Fereiduni, Mohamed Elbestawi, Suraj Dinkar Jadhav, and Jean-Pierre Kruth.

Chapter 3 deals with the influence of alloying elements on the processability, absorptivity, and oxidation tendency of Aluminum alloys during the laser powder bed fusion process. This chapter contains the previously published material in the "Additive Manufacturing" journal as "Influence of alloying elements on laser powder bed fusion processability of aluminum: A new insight into the oxidation tendency" by Ali Ghasemi, Eskandar Fereiduni, Mohamed Balbaa, Suraj Dinkar Jadhav, Mohamed Elbestawi, and Saeid Habibi.

Chapter 4 is concerned with proposing an easily attainable solution to obtain high thermal conductivities for the laser powder bed fusion fabricated pure Al, AlSi12, and AlSi10Mg in the as-built condition and eliminate the need for post-build heat treatments. This chapter contains the previously published material in the "Additive Manufacturing" journal as "Unraveling the low thermal conductivity of the LPBF fabricated pure Al, AlSi12, and AlSi10Mg alloys through substrate preheating" by Ali Ghasemi, Eskandar Fereiduni, Mohamed Balbaa, Mohamed Elbestawi, and Saeid Habibi.

Chapter 5 discusses the possibility of using dry mechanical mixing techniques to prepare ideal composite powders for laser powder bed fusion applications. The work presented in this chapter is currently under consideration for publication in the "Powder Technology" journal as "On the preparation and characterization of AlSi12-graphene powder for powder bed fusion additive manufacturing applications" by Ali Ghasemi, Eskandar Fereiduni, Mohamed Elbestawi, Jasmin Kathrin Saewe, Niklas Hartke, Fran Adar, Kayvon Savadkouei, Yoshinori Fukushima, and Saeid Habibi.

Chapter 6 explores the possibility of improving the thermal properties of the laser powder bed fusion fabricated AlSi12 alloy by incorporating graphene and provides an in-depth microstructural investigation of the graphene survival and its transformation into aluminum carbide. The work presented in this chapter is intended to be submitted to "Additive Manufacturing" journal as "Influence of the graphene incorporation on nanostructure and thermal properties of the laser powder bed fusion processed AlSi12 matrix composites" by Ali Ghasemi, Eskandar Fereiduni, Mohamed Elbestawi, Kayvon Savadkouei, Fran Adar, Jasmin Kathrin Saewe, Niklas Hartke, and Saeid Habibi.

Chapter 7 summarizes the main conclusions and contribution of the thesis and presents some suggestions for future work.

References

1. Standard, A., *F2792-12a*. Standard terminology for additive manufacturing technologies ASTM International, West Conshohocken, 2012.
2. Frazier, W.E., *Metal additive manufacturing: a review*. Journal of Materials Engineering and performance, 2014. **23**: p. 1917-1928.
3. DebRoy, T., et al., *Additive manufacturing of metallic components—process, structure and properties*. Progress in Materials Science, 2018. **92**: p. 112-224.
4. Balbaa, M., et al., *Role of powder particle size on laser powder bed fusion processability of AlSi10Mg alloy*. Additive Manufacturing, 2021. **37**: p. 101630.
5. Fereiduni, E., A. Ghasemi, and M. Elbestawi, *Selective laser melting of aluminum and titanium matrix composites: recent progress and potential applications in the aerospace industry*. Aerospace, 2020. **7**(6): p. 77.
6. Ghasemi, A., et al., *Unraveling the low thermal conductivity of the LPBF fabricated pure Al, AlSi12, and AlSi10Mg alloys through substrate preheating*. Additive Manufacturing, 2022. **59**: p. 103148.
7. Narvan, M., et al., *Laser powder bed fusion of functionally graded bi-materials: Role of VC on functionalizing AISI H13 tool steel*. Materials & Design, 2021. **201**: p. 109503.
8. Ghasemi, A., et al., *Influence of alloying elements on laser powder bed fusion processability of aluminum: A new insight into the oxidation tendency*. Additive Manufacturing, 2021. **46**: p. 102145.
9. Roberts, I.A., et al., *A three-dimensional finite element analysis of the temperature field during laser melting of metal powders in additive layer manufacturing*. International Journal of Machine Tools and Manufacture, 2009. **49**(12-13): p. 916-923.
10. Van Cauwenbergh, P., et al., *Unravelling the multi-scale structure–property relationship of laser powder bed fusion processed and heat-treated AlSi10Mg*. Scientific reports, 2021. **11**(1): p. 1-15.
11. Louvis, E., P. Fox, and C.J. Sutcliffe, *Selective laser melting of aluminium components*. Journal of Materials Processing Technology, 2011. **211**(2): p. 275-284.
12. Stugelmayer, E.J., *Characterization of process induced defects in laser powder bed fusion processed AlSi10Mg Alloy*. 2018, Montana Tech of The University of Montana.
13. Zhang, J., et al., *A review of selective laser melting of aluminum alloys: Processing, microstructure, property and developing trends*. Journal of Materials Science & Technology, 2019. **35**(2): p. 270-284.
14. Buchbinder, D., et al., *High power selective laser melting (HP SLM) of aluminum parts*. Physics Procedia, 2011. **12**: p. 271-278.

15. Read, N., et al., *Selective laser melting of AlSi10Mg alloy: Process optimisation and mechanical properties development*. *Materials & Design* (1980-2015), 2015. **65**: p. 417-424.
16. Yan, Q., B. Song, and Y. Shi, *Comparative study of performance comparison of AlSi10Mg alloy prepared by selective laser melting and casting*. *Journal of Materials Science & Technology*, 2020. **41**: p. 199-208.
17. Prashanth, K.G., et al., *Microstructure and mechanical properties of Al–12Si produced by selective laser melting: Effect of heat treatment*. *Materials Science and Engineering: A*, 2014. **590**: p. 153-160.
18. Yang, P., et al., *Microstructure evolution and thermal properties of an additively manufactured, solution treatable AlSi10Mg part*. *Journal of Materials Research*, 2018. **33**(23): p. 4040-4052.
19. Tjong, S.C., *Recent progress in the development and properties of novel metal matrix nanocomposites reinforced with carbon nanotubes and graphene nanosheets*. *Materials Science and Engineering: R: Reports*, 2013. **74**(10): p. 281-350.
20. Zhang, F., et al., *Recent Advances on Graphene: Synthesis, Properties, and Applications*. *Composites Part A: Applied Science and Manufacturing*, 2022: p. 107051.
21. Saboori, A., et al., *An overview of metal matrix nanocomposites reinforced with graphene nanoplatelets; mechanical, electrical and thermophysical properties*. *Metals*, 2018. **8**(6): p. 423.
22. Jafari, D. and W.W. Wits, *The utilization of selective laser melting technology on heat transfer devices for thermal energy conversion applications: A review*. *Renewable and Sustainable Energy Reviews*, 2018. **91**: p. 420-442.

2 Chapter 1 Role of powder particle size on laser powder bed fusion processability of AlSi10Mg alloy

Complete Citation:

Balbaa MA, Ghasemi A, Fereiduni E, Elbestawi MA, Jadhav SD, Kruth JP. Role of powder particle size on laser powder bed fusion processability of AlSi10mg alloy. Additive Manufacturing. 2021 Jan 1;37:101630.

Authorship contribution statement:

M.A. Balbaa: Conceptualization, Methodology, Investigation, Writing - original draft, Writing – review & editing. **A. Ghasemi:** Conceptualization, Methodology, Investigation, Writing - original draft, Writing – review & editing. **E. Fereiduni:** Conceptualization, Methodology, Investigation, Writing - original draft, Writing – review & editing. **M.A. Elbestawi:** Supervision, Writing – review & editing. **S.D. Jadhav:** Investigation, Writing – review & editing. **J.-P. Kruth:** Writing – review & editing.

***Role of Powder Particle Size on Laser Powder Bed Fusion
Processability of AlSi10Mg Alloy***

Abstract

Laser powder bed fusion (L-PBF) is one of the most promising additive manufacturing (AM) methods which provides an exceptional opportunity to improve the existing designs and move toward fabricating fine features and complex geometries with higher efficiencies. Considering the layer-wise nature of this technique, the possibility of fabricating fine features is tied to the ability to deposit thin powder layers in this process. Since the powder layer thickness is directly dictated by the powder particle size, finer powders are required to further enhance the ability of the L-PBF technique in manufacturing fine features and intricate geometries. Accordingly, this study aims at investigating the processability of fine AlSi10Mg powder ($D_{50} = 9 \mu\text{m}$) by using the L-PBF process. The densification level, surface quality and dimensional accuracy of the final parts are investigated in a wide range of process parameters and are compared to those manufactured by the commonly used AlSi10Mg powder (referred to as coarse powder with $D_{50} = 40 \mu\text{m}$). The underlying reasons behind the different processability of fine and coarse powders are explored from the density, surface quality, microhardness and dimensional accuracy viewpoints through analyzing the flowability, bed packing density and optical absorption of powders. Moreover, the process-microstructure-microhardness relationship is assessed in detail for both fine and coarse powders. This study reinforces the idea that the utilization of fine powders for L-PBF processing is rather challenging.

Keywords: Laser powder bed fusion (L-PBF); Particle size; Density; Laser absorptivity; Dimensional accuracy; Surface roughness.

2.1 Introduction

In recent years, the increase in the power level in many electronic applications has made the thermal management of the systems rather challenging, especially in microelectronic devices and miniaturized personal computers [1, 2]. Insufficient heat transfer of the excessive heat generated during the operation of these devices adversely affects their performance and may result in thermal failure [2]. To mitigate this concern, advanced manufacturing methods are required to produce more complicated architectures (e.g., lattice structures), which can increase the effective surface area of the heat exchangers by providing more channels for transportation of the coolant inside their volume [3-5]. In light of this scenario, additive manufacturing (AM) is the best choice for near-net-shape fabrication of these complex 3D components [6, 7]. Laser powder bed fusion (L-PBF) process is one of the most promising AM techniques in terms of fabricating fine features that are required in tube/fin, plate/fin, finless tube micro-channels, pitot tube and twisted tube heat exchangers [5]. Fabrication of these heat exchangers through the L-PBF process was reported to be successful using aluminum (Al) alloys, including AlSi10Mg and AlSi12, among others [8, 9]. However, there is still a great interest in decreasing the minimum achievable feature size in these devices to move towards more complicated designs having finer features and higher efficiencies.

In the L-PBF process, a focused laser beam directly creates a 3D part in a layer-wise manner based on a computer-aided design (CAD) model by selectively fusing regions of a powder bed [10-14]. For a given material (e.g., AlSi10Mg), the finest achievable feature is dictated by the laser beam diameter and the powder layer thickness. Laser spot sizes less than 40 μm are not common in the L-PBF process due to the limitations with the currently existing machines. However, there seems to be no limitation in decreasing the powder layer

thickness since it is a function of the powder particle size [15, 16]. For instance, for Al alloy powders with particles in the range of 15-50 μm , powder layer thicknesses less than 30 μm cannot be obtained. Nevertheless, finer micro-scale powder particles in the range of 1-20 μm and even submicron powders are also commercially available to further decrease the powder layer thickness and possibly provide the chance of printing finer features. Applying fine powder particles (less than 20 μm) in the L-PBF process seems to be beneficial not only in terms of fabricating finer features but also from the Al printability viewpoint. For example, the presence of fine powder particles enhances the consolidation kinetics due to the lower amount of heat required to melt the powder particles [17]. Moreover, the decrease in the powder particle size results in a higher specific surface area relative to volume, which in turn enhances the laser absorptivity [17, 18]. Due to the high laser reflectivity of Al-based alloys, the enhancement of their laser absorptivity is of utmost importance in L-PBF processing [19]. It has to be noted that Al is on the Special Health Hazard Substance List due to its flammability and high affinity to oxidation in the powder form (particle sizes less than 420 μm). Fine powders should be treated with more caution since they have lower minimum ignition energy as per standard ASTM E2019. For instance, by decreasing the mean particle size of Al powder from 32 to 9 μm , the minimum ignition energy declines from 10 to 4 mJ [20, 21].

Although the influence of process parameters and the scanning strategy on the quality of L-PBF processed Al alloys parts has been well investigated and documented in the literature [19, 22-26], this question has still remained unanswered that whether or not it is possible to fabricate sound Al-based parts with finer features using finer powder feedstocks.

Table 1 summarizes the research studies that have been conducted to analyze the effect of particle size on powder characteristics and/or quality of the final printed parts. Referring to Table 2.1, the following vacancies need to be fulfilled:

- **Flowability:** With a few exceptions [27], the literature appears to be devoid of investigating the role of the powder particle size on the powder flowability, which is of great importance in the L-PBF process. It is worth to mention that even when the flowability was concerned, the Hall flowmeter was utilized to measure the flowability. Although the Hall flowmeter is known to be closer to the AM process (especially the powder fed techniques) than other conventional powder flowability measurement techniques, it has major limitations with evaluating the flowability of cohesive powders which are still good enough for powder bed fusion additive manufacturing (PBF-AM) processes [28]. Among various techniques currently available for the powder flowability measurement, the FT4 Freeman powder rheometer technique has been recommended since the interaction of the precision blade with the powder resembles that of the recoater/powder in the L-PBF process [29].
- **Absorptivity:** The influence of the powder particle size on the laser absorptivity has not been reported through experimental measurements to the best knowledge of authors. By providing a larger specific surface area relative to volume for powder/laser interactions, finer powder particles are expected to have higher absorptivity and, therefore, higher kinetics of densification [17].
- **Printing samples:** Although powder characterization provides valuable information about the printability potential of fine powder particles, the literature lacks a systematic study correlating the powder behaviors (flowability, packing

density and absorptivity) to the densification level, surface quality, dimensional accuracy, microstructure and mechanical properties of the final parts.

Table 2.1. Effect of powder particle size on the powder characteristics and/or the quality of the final printed parts in the literature.

System	Powder particle size (μm)	Research focus	Reference
Ni-base alloy	150-200	Influence of powder particle size, and different coarse-to-fine powder ratios on the powder bed density by depositing a 500 μm thick powder layer using a metallic ruler as the recoater.	[30]
	100-150		
	50-75		
	25-40		
	<20		
SS316L	$D_{50}=15.05$	Effect of powder particle size on the relative powder density, effective powder layer thickness and the density of the L-PBF fabricated parts.	[31]
	28.19		
	37		
SS316L	$D_{50}=15.12$	Comparison between the density, surface quality and mechanical properties of parts fabricated by the L-PBF process using different powder sizes and size distributions.	[32]
	28.26		
	37.70		
IN718	$D_{ave}=7$	Influence of powder size on the powder bed packing density.	[33]
	21		
	70		
AlSi7Mg	$D_{50}=31$	Powders with different sizes were characterized in terms of flowability, powder bed packing density, particle segregation during recoating and particle cohesiveness.	[27]
	63		
	70		
Fe	$D_{50}=10$	The role of particle size on the microstructure of the printed parts (level of defects), surface morphology and particle bonding mechanism.	[17]
	26		
	41		
	51		
	68		
	104		
Ti	45-106	Influence of powder particle size on the flowability, apparent and tap density and the powder bed macro-surface profile.	[34]
	75-106		
	45-75		

This study discusses the possibility of fabricating sound parts using fine powder particles (less than 20 μm). AlSi10Mg powders with two different sizes (coarse: 15-70 μm and fine: 1-20 μm) were employed as a model to recognize the effect of the particle size on the quality of final parts in terms of density (level of defects), surface quality, dimensional accuracy, microstructure and microhardness. The fundamental reasons behind the

formation of defects, as well as the surface roughness trends and deviation from the nominal dimensions, were explored based on four key factors, namely, process parameters, powder flowability, powder bed packing density and powder laser absorptivity. In addition, the influence of powder particle size on the final microstructure was discussed in detail. To consider the physical properties of the material along with the process parameters in the energy density calculations, a modified volumetric energy density was proposed, considering the laser absorptivity and effective powder layer thickness of the powder feedstock. The lessons learned from this study can answer the question regarding the ability of fine powder particles to produce sound parts with finer features.

2.2 Materials and Experimental Procedure

2.2.1 Powder characteristics (chemical composition, particle size distribution and morphology)

The powders used in this study were fine and coarse AlSi10Mg alloy with the nominal chemical compositions provided in Table 2.2. The particle size distribution (PSD) of both fine and coarse powders was investigated by means of laser diffraction according to the ASTM B822-17 standard [35]. Figure 2.1 presents the particle size distribution (PSD) of coarse and fine AlSi10Mg powders. The D10, D50, and D90 of powders representing the particle diameters at 10, 50 and 90% in the cumulative distribution are also provided in Figure 2.1. As seen, the powders follow a Gaussian distribution with the mean particle size (D50) being ~9 and ~40 μm for fine and coarse powders, respectively.

Table 2.2. Nominal chemical composition of powders.

Powder	Elements (wt.%)					
	Al	Si	Mg	Fe	Cu	Other
Coarse AlSi10Mg	Bal.	9.76	0.21	0.07	0.08	1.5
Fine AlSi10Mg	Bal.	8.56	0.23	0.19	0.04	1.29

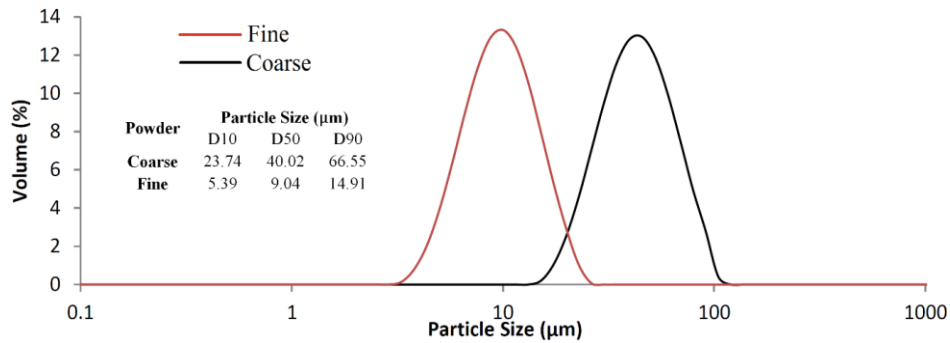


Figure 2.1. Particle size distribution (PSD) of coarse and fine AlSi10Mg powders used in this study.

The morphology of powders was observed using a Vega Tescan scanning electron microscopy (SEM) with an accelerating voltage of 20 kV. The SEM was equipped with an energy dispersive X-ray spectroscopy (EDS) detector for elemental analysis. Figure 2.2 shows the SEM micrographs of the gas atomized AlSi10Mg powders. As shown in Figure 2.2(a), a vast majority of particles in the coarse powder are almost spherical/quasi-spherical in shape. However, this powder contains particles which show some degrees of deviation from spherical to elongated shape (Figure 2.2(a) and (b)). Close observation of powder particles also reveals the presence of satellites on the surface of almost all particles (Figure 2.2(b)). These satellites are believed to form when the faster-solidified finer particles adhere to the molten or semi-solid surface of the coarser particles due to the in-flight collisions existing among the particles during the gas atomization process [36]. Morphological observation of the fine powder indicates that the particles are highly

spherical and satellite-free (Figure 2.2(c) and (d)). This can be attributed to the extremely high cooling rate of fine particles, which provides their full solidification before inter-particle collisions. As can be observed in Figure 2.2(d), fine powder particles show a high tendency to attach to each other and form agglomerates. However, the particles in the coarse powder do not show signs of agglomeration.

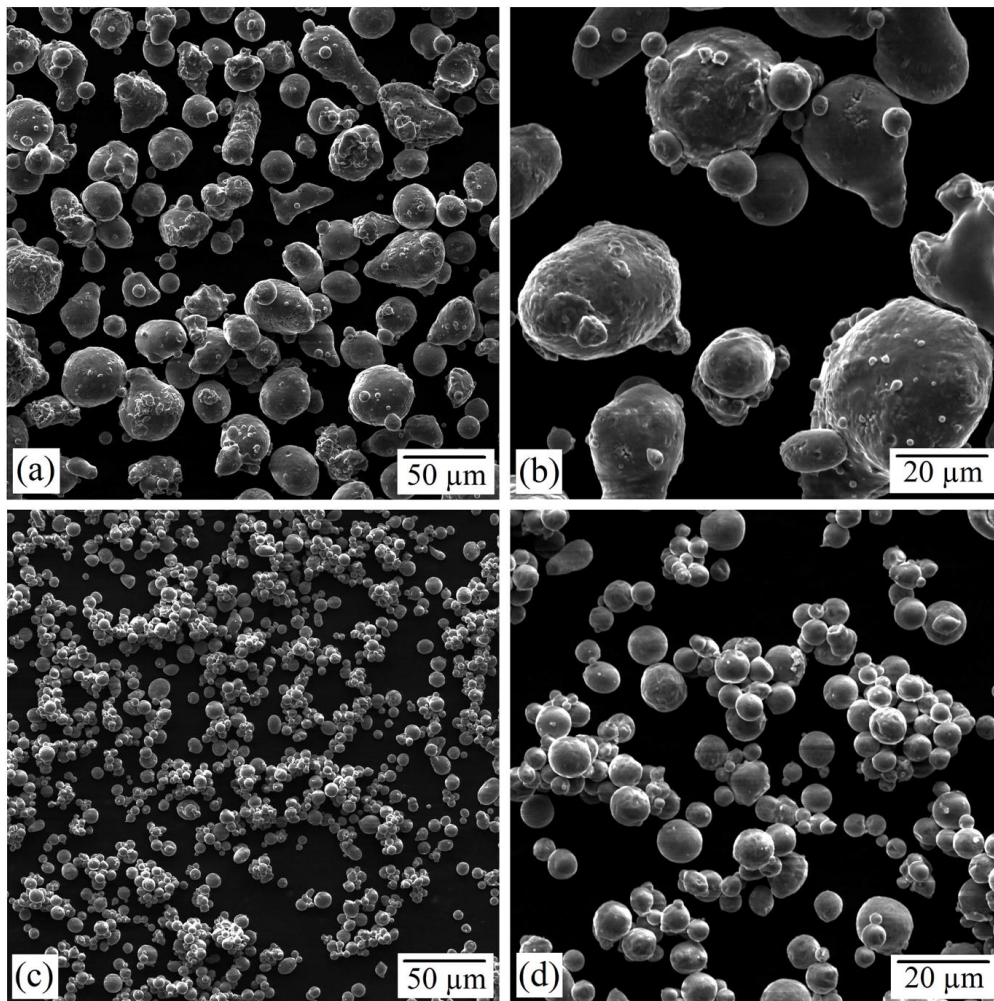


Figure 2.2. SEM micrographs of: (a) coarse, and (c) fine AlSi10Mg powders. (b) and (d) are higher magnification micrographs of the coarse and fine powders shown in (a) and (c), respectively.

2.2.2 Powder behaviors (flowability, packing density and optical absorption)

The flow behavior of powders was evaluated using three different methods, including Hall and Carney flowmeters (according to the ASTM B213-17 standard [37]) as well as the FT4 Freeman powder rheometer. In the Hall and Carney flowmeter techniques, the powder flowability refers to the time required for 50 g of powder to flow freely through a standard funnel. The larger diameter of the nozzle in the Carney method makes it possible to evaluate the flowability of powders, which might not flow through the nozzle of the Hall flowmeter. The dynamic flow methodology of the FT4 powder rheometer is of particular relevance to PBF-AM processes, where the powder spreading by the recoater is performed in a dynamic environment under a low-stress state [38]. This test is performed according to the standard "Stable and Variable Flow Rate (SVFR)" method, consisting of stable and variable zones. The stable zone has seven complete test cycles with the same tip speed. Following the stable zone, four complete test cycles with varying blade tip speeds are employed. As shown in Figure 2.3, each complete test cycle contains downward and then the upward movement of a precision blade in a standard vessel accommodating the powder. The details of the FT4 test procedure and process variables can be found in [29].

The flow behavior of samples was studied by analyzing the basic flow energy (BFE) and specific energy (SE). The BFE represents the ability of the powder to flow under the stressed condition and is defined as the energy required for the rotation of the blade during its downward movement in the 7th test cycle as:

$$BFE = E_{test\ 7,down} \quad \text{Eq.1}$$

The SE shows the energy required to establish a particular flow pattern in a precise volume of conditioned powder and is defined as the average energy of the upward blade rotation for the 7th and 8th test cycles, divided by the mass of powder remaining in the vessel (Eq.

2). By gently lifting the powder, the upward motion of the blade generates a low stress and unconfined flow mode in the powder.

$$SE = \frac{E_{test\ 7,up} + E_{test\ 8,up}}{2} \frac{1}{m_{split}} \quad \text{Eq.2}$$

where m_{split} is the mass of the powder after the excess powder is removed.

The conditioned bulk density (CBD) of powders was also measured by the FT4 powder rheometer according to the procedure reported in [29]. For each sample, three measurements were performed, and the average value was reported as the CBD based on

Eq. 3:

$$CBD = m_{split} / v_{split} \quad \text{Eq.3}$$

in which v_{split} signifies the volume of powder after removing the excess powder.

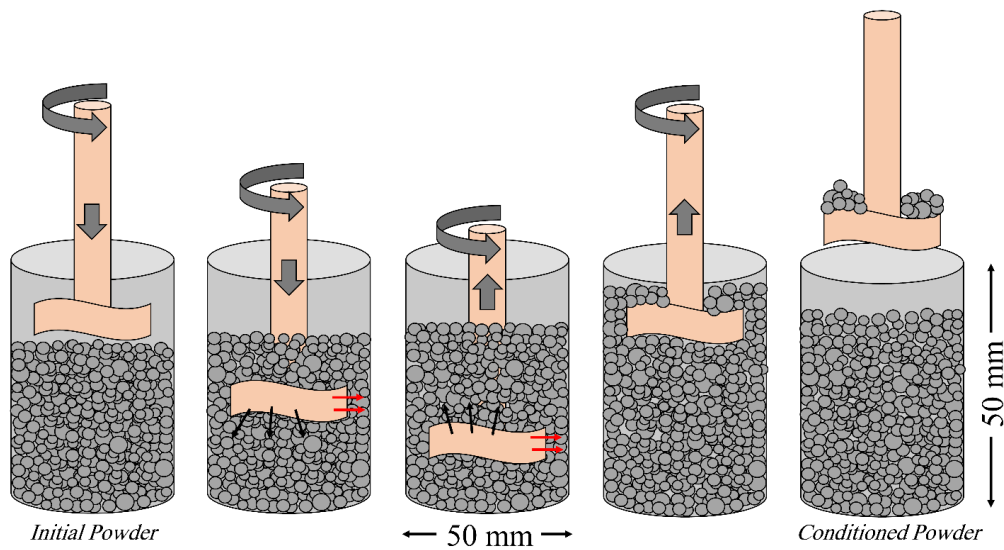


Figure 2.3. Schematic view of a single test cycle in the dynamic flow methodology of the FT4 Freeman powder rheometer test used to evaluate the powder flowability. The rotating impeller moves downward and then upward through a fixed volume of powder placed in a standard vessel.

The optical absorption of powders was measured by means of diffuse reflectance spectroscopy (DRS) in the wavelength range of 400-1400 nm using an UV-Visible-NIR LAMBDA 950 Perkin Elmer spectrophotometer equipped with a 150 mm diameter integrating sphere. The integrating sphere was coated with Spectralon with a spectral resolution of 1 nm. To remove the background and noise, Barium Sulfate powder with a reflectance of 100% was employed as reference. The powder samples were placed in a quartz cuvette and sealed prior to mounting on a Teflon sample holder for the DRS test. The light sources employed for the measurements had Deuterium (D2) and Tungsten with the wavelength ranges of 200-320 and 320-2500 nm, respectively. The employed detectors were Photon Counting *photomultiplier* tubes (*PMT*) and Lead Sulfide (PbS), applicable in the wavelength ranges of 200-860.8 and 861-2500 nm, respectively.

2.2.3 L-PBF Processing

The L-PBF machine used in this study was EOS M290 having a 400 W Yb fiber laser with a focus diameter of 100 μm . Two sets of samples, each containing 18 cubes with dimensions of $10 \times 10 \times 12 \text{ mm}^3$ were printed on an Al alloy build plate under the protection of a high-purity argon gas atmosphere to lower the oxygen content below 0.1% to minimize oxidation. The second set of samples was the replicate of the first set in terms of process parameters. The build plate was preheated to 200 °C to decrease the temperature difference along the building direction and reduce the residual stresses. As summarized in Table 2.3, using a fixed platform downward displacement of 30 μm (as recommended by the machine manufacturer for AlSi10Mg alloy), different laser powers, scanning speeds and hatch spacings were employed. As illustrated in Figure 2.4, the scanning of layers was conducted using a stripe hatching pattern, alternating 90° between subsequent layers. The stripe hatching pattern was employed to provide a more homogeneous distribution of residual

stress compared to the meander hatching pattern and higher building rate than the chessboard hatching pattern [39]. The main reason behind applying 90° rotation between subsequent layers was the ease of melt pool size and shape characterizations with higher accuracy. To reduce the chance of recoater jamming, the coupons were placed at a 20° angle to the recoating direction.

Table 2.3. The process parameters employed to fabricate parts.

Laser Power, P (W)	Scanning Speed, v (mm/s)	Hatch Spacing, h (mm)	Platform downward displacement (mm)
300, 335, 370	800, 1050, 1300	0.15, 0.19	0.03

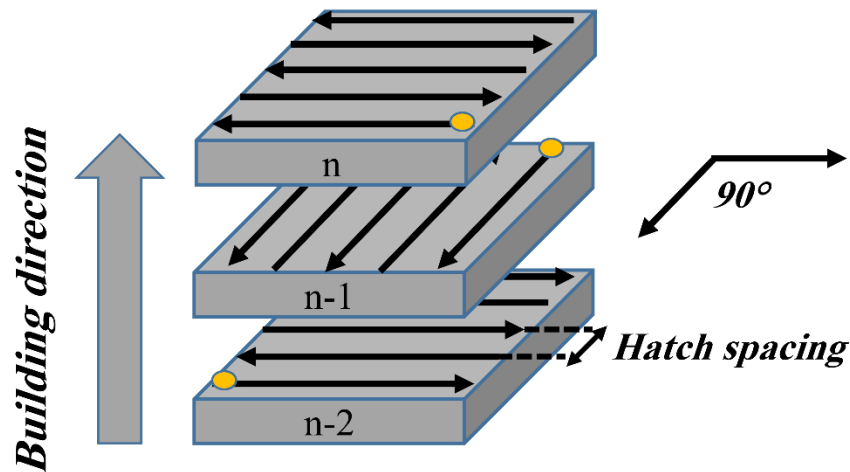


Figure 2.4. Schematic of the employed stripe hatching pattern scanning strategy, alternating 90° between subsequent layers.

2.2.4 Characterization of L-PBF-fabricated parts (densification level, dimensional accuracy, surface quality, microstructure and microhardness)

The densification level of L-PBF fabricated parts was measured using the Archimedes method in accordance with the ASTM B296-17 standard [40]. The reported relative density is the average of at least five measurements from different parts manufactured with the

same process parameters. The bulk density of AlSi10Mg parts was selected as 2.68 g/cm^3 [41, 42].

Dimensional accuracy and flatness of as-built coupons were measured using a coordinate measuring machine (CMM) having an accuracy of $0.1 \text{ }\mu\text{m}$. Measurements were done by recording 8 points on each surface of each coupon except the bottom surface to create planes. The distance between two parallel planes in X and Y directions is measured, respectively, along with the degree of flatness of each plane. The top surface of L-PBF fabricated parts was analyzed using SEM with an accelerating voltage of 20 kV as well as Alicona Infinite Focus G5 microscope (Alicona Manufacturing Inc., Bartlett, IL, USA) which generates real 3D surface images by varying the focus. While providing valuable information about the surface integrity, the surface roughness of the additively manufactured parts was also evaluated by employing the Alicona microscope. The surface roughness reported in this study is the arithmetic mean surface roughness value (S_a). The measurements were repeated five times for each part, and the mean value was reported as the surface roughness.

The defects were characterized by observing the front section of parts using a Nikon optical microscopy (OM). For this purpose, the front sections were ground and polished according to the standard metallography procedure. To observe the microstructural evolution in the L-PBF fabricated parts, the polished samples were etched chemically using Keller's Reagent and were characterized by OM as well as SEM operating at an accelerated voltage of 10 kV.

Microhardness measurements were performed by employing a Matsuzawa microhardness testing machine with a load of 200 g being applied for 10 s. The reported microhardness represents the average of at least 9 measurements for each specimen.

2.3 Results and Discussion

2.3.1 Flowability and packing density

The results of powder flowability measurements obtained by Hall flowmeters and FT4 powder rheometer are provided in Table 2.4. The fine AlSi10Mg powder flowed through the funnel neither in Hall nor in Carney flowmeter. However, the coarse AlSi10Mg powder experienced free flow even in the Hall flowmeter with a time of ~76 s for 50 g of powder. Based on the Hall and Carney flowmeter measurements, the coarse powder was found to be more flowable compared to the fine one. However, a quantitative comparison between the flowability of fine and coarse powder systems is only available by the FT4 powder rheometer method in which both powders can flow. The higher the BFE or SE in the FT4 test, the lower the powder flowability. The BFE and SE results derived from the FT4 test measurements were not in agreement in terms of introducing the powder with higher flowability. From the BFE index perspective, the fine powder showed a higher flowability. However, from the SE viewpoint, the coarse powder was found to be more flowable. Since the powder/blade interaction during the upward motion of the blade is closer to the powder/recoater interactions during the powder spreading stage in the L-PBF process, SE is a better representative of the powder flowability [29]. Based on the SE results provided in Table 2.4, the flowability of fine powder is 75% lower than that of the coarse one. This is attributed to the intensive cohesive forces existing among the fine powder particles with

significantly large specific surface area relative to volume, which results in noticeably high inter-particle friction and low powder flowability [43-45].

Table 2.4. The results of Hall flowmeter and FT4 Freeman powder rheometer techniques presenting the flowability and density of powders.

AlSi10Mg Powder	Powder Flowability			Powder Density
	Hall Flowmeter	FT4 Powder Rheometer		Conditioned Bulk Density-CBD (g/mL)
	Flow Time (sec)	Basic Flow Energy, BFE (mJ)	Specific Energy, SE (mJ/g)	
Coarse	76.54±0.6	234.2±10.08	2.606±0.068	1.424±0.003
Fine	No flow	99.85±3.27	4.568±0.193	1.019±0.027

The CBDs of the fine and coarse AlSi10Mg powders are also summarized in Table 2.4. The measurements revealed a major difference between the densities of fine and coarse powder systems. The coarse powder showed ~43% higher density compared to the fine powder due to the higher population of interstices, more inter-particle frictions, and the higher chance of agglomeration in the fine powder feedstock. The relative densities with respect to the bulk density of AlSi10Mg alloy (i.e., 2.68 g/mL) would be 53% and 38% for coarse and fine powders, respectively. Since the powder/blade interactions through the density measurement by the FT4 method resembles that of PBF-AM processes, the relative powder bed packing density is estimated to be around the same values as well [29].

2.3.2 Laser absorptivity

The reflectance results obtained by the DRS test were converted to the Kubelka-Munk (K-M) absorption factor to quantitatively compare the absorption behavior of powders using the K-M equation as [46]:

$$f(R) = K/S = (1 - R)^2 / 2R \quad \text{Eq. 4}$$

where R is the reflectance of the powder, K is the absorption coefficient, and S represents the scattering coefficient. Figure 2.5 shows the variation in the R and K-M absorption factor for both powders as a function of the wavelength. At the wavelength of 1070 nm, which is the wavelength for most of the commercially available L-PBF machines, including the EOS M290 employed in the present research, the R of the fine powder was ~2% lower than that of the coarse powder. Since the transmittance of the metallic powder as an opaque object is negligible, the absorption can be estimated as $(1 - R)$. Accordingly, the absorptance of the fine powder is ~2% higher than the coarse one (58% and 60% for coarse and fine powder systems, respectively). From the K-M absorption factor perspective, the fine powder was found to be ~13% more absorptive to the laser compared to the coarse powder. The higher absorption of the fine powder is due to the: (i) higher specific surface area relative to volume of powder particles and (ii) the entrance of more light and consequently more internal interaction caused by the lower packing density of the fine powder. However, based on the microstructural observations of powders provided in Figure 2.2(c) and (d), the agglomerates formed in the fine powder feedstock act to decrease the specific surface area relative to volume and consequently decline the absorption. In addition, the slightly higher (not significant) absorption of the fine powder can also be ascribed to the major dependence of the absorptivity on the material. The research studies have shown that the absorption of metallic materials with a relatively high laser absorptivity (e.g., AlSi10Mg alloy used in this study) is not highly dependent on the particle size distribution [47, 48].

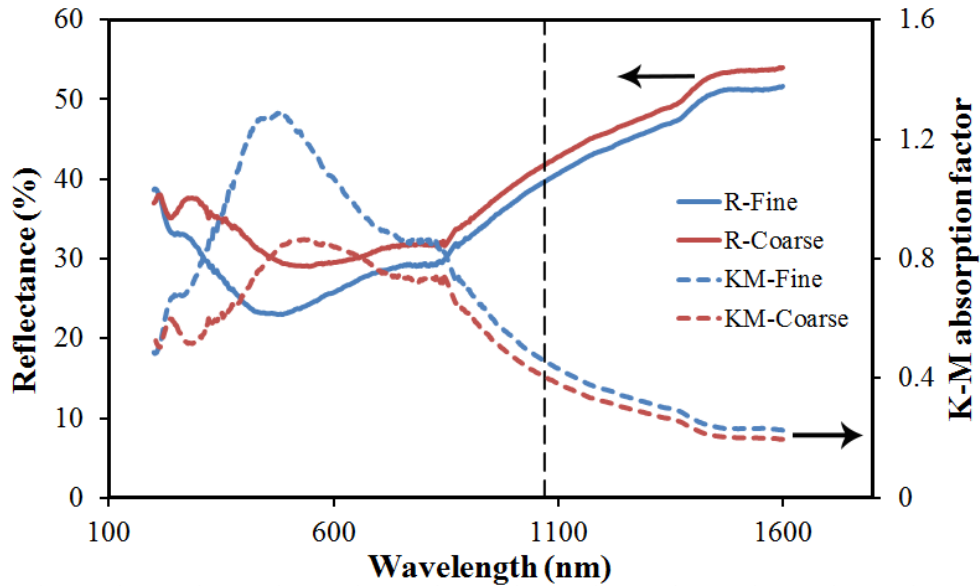


Figure 2.5. The variation in the reflectivity and the K-M absorption factor of fine and coarse AlSi10Mg powders as a function of the wavelength. The dashed vertical line (wavelength of 1070 nm) represents the laser wavelength of the L-PBF machine used in this study.

2.3.3 Density-laser energy input relationship

Energy density is usually used as a metric to compare the parts fabricated by the L-PBF process under different sets of process parameters. The volumetric energy density (e_V) is the most widely used energy density in the literature, which is defined as [10, 49]:

$$e_V = \frac{P}{vht} \quad \text{Eq. 5}$$

where P , v , h , and t denote the laser power, scanning speed, hatch spacing and powder layer thickness, respectively. The powder layer thickness is often mistaken for the platform downward displacement [50]. After the laser processing of the first deposited powder layer with the thickness of t , the consolidated layer is believed to have a lower thickness due to the presence of inter-particle pores within the powder bed. In other words, the molten material formed due to the powder/laser interaction fills the interstices and leads to a dense solidified layer with a thickness lower than t . Therefore, a gap is created between the top

surface of the consolidated layer and the tip of the recoater. Afterward, the platform moves downward for another t , and the recoater deposits the second powder layer. However, due to the presence of the free height formed as a result of the first layer consolidation, the thickness of the deposited powder in the second layer will be larger than t . It means that the thickness of the powder bed in the second layer is higher than the nominal value/platform displacement (t) considered as the powder layer thickness in Eq. 5. Further deviation from t occurs as the next powder layers are deposited and consolidated until the powder layer thickness approaches a constant value governed by the t and the powder bed packing density. The powder layer thickness in the steady-state condition is known as the "effective powder layer thickness (t_{eff})" which is larger than t [31]. To compensate the error associated with ignoring the actual powder layer thickness, t_{eff} should be substituted in Eq. 5. In addition, this equation assumes the laser absorptivity of the powder as 100%. However, since the laser absorptivity is dependent on the material and particle size, the laser absorptivity coefficient (K) needs to be involved in the volumetric energy density equation as well. By taking the t_{eff} and K into account, the energy input can be defined with a new perspective as:

$$E_V = \frac{KP}{vht_{eff}} \quad \text{Eq. 6}$$

This equation takes the effect of both the process parameters and the powder properties into account. In most of the research studies which have investigated the effect of process parameters on the densification of a single material with a fixed powder system, the application of this equation would only shift the energy input results to lower values. However, when it comes to the comparison between different materials or different powders of the same material, calculation of the energy density based on Eq. 5 would be

misleading. Therefore, to establish a correlation between the densification level of the L-PBF processed parts and the energy input, E_V (Eq. 6) was used in this study. By considering the platform displacement of 30 μm and relative powder bed packing densities of 53% and 38% (section 2.3.1), t_{eff} was calculated to be 56.3 and 78.8 μm for coarse and fine powder systems, respectively. By substituting the calculated t_{eff} and the measured K value (section 2.3.2) in Eq. 6, E_V would be 12.5-28.8 J/mm^3 and 9.3-21.3 J/mm^3 for the coarse and fine powder systems within the applied range of process parameters, respectively.

The results of relative density as a function of the E_V for parts fabricated by both fine and coarse powder systems are shown in Figure 2.6(a). The density measurement results are quite reliable, with a maximum coefficient of variation less than 1.3% for both powder systems. With one exception, the relative density is lower than 95% in the case of fine powder. However, highly dense samples with relative densities up to 99% are achieved in the case of coarse powder feedstock. In general, the relative density of the parts fabricated by the coarse powder was up to 4.6% higher than that of the fine powder case. Since the calculated standard deviations of the measured relative densities vary between 0.1-1.1% for both cases, the differences between relative densities of the fine and coarse powder cases are statistically significant. The optimum samples in terms of density for both coarse and fine powders are shown in Figure 2.6(b) and (c). Although their E_V are different, the laser power, scanning speed and hatch spacing of optimum samples are the same for both cases ($P=335$ W, $v=1050$ mm/s and $h=0.15$ mm). In the following section, the reasons behind the inferior densification levels in the case of the fine powder system are explored.

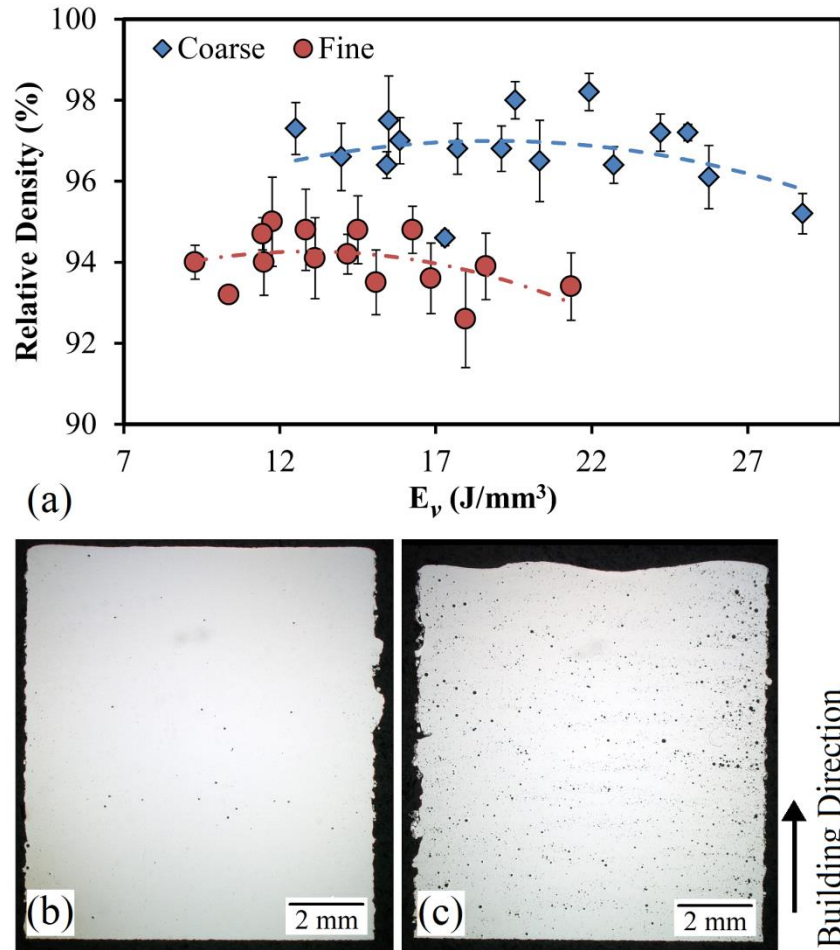


Figure 2.6. (a) The variation in the density of L-PBF fabricated AlSi10Mg parts as a function of the volumetric energy density (E_V). (b) and (c) Cross-sectional optical micrographs of parts with the optimum density obtained by L-PBF processing of coarse ($P=335$ W, $v=1050$ mm/s, $h=0.15$ mm and $E_V=21.9$ J/mm³) and fine ($P=335$ W, $v=1050$ mm/s, $h=0.15$ mm and $E_V=16.3$ J/mm³) AlSi10Mg powders, respectively.

2.3.4 Densification level

Referring to Figure 2.6, the fabrication of almost fully dense AlSi10Mg parts with fine powder feedstock seems to be impossible. Although the fine powder was expected to show higher kinetics of densification due to the smaller size and higher absorptivity, the results are suggesting otherwise. To understand the fundamental reasons behind the inferior

densification level of parts obtained by the fine powder, the factors dictating the density of L-PBF processed parts need to be investigated.

Powder bed packing density: *One of the most important factors affecting the part density in PBF-AM processes is the powder bed packing density [27]. Lower relative powder bed densities are accompanied by a higher volume fraction of pores within the powder bed. This consequently makes it rather challenging for the molten material to fill all of the interstices due to the rapid solidification nature of the L-PBF process [51]. Not only can the volume fraction of pores within the powder bed, but also their size can play a significant role in the densification level of the final printed part. While tiny inter-particle porosities can be easily filled by the molten material, the large pores have a lower chance of being filled, especially at high laser scanning speeds. Presence of large particle agglomerates which are not able to settle on the substrate (larger than t_{eff} in size) is believed to be one of the main sources for the formation of large voids within the powder bed. These agglomerates can also sweep the powder particles ahead of them and further influence the powder bed packing density [52]. Since the powder particles in the fine powder system tend to create agglomerates to alleviate their considerably high surface energy (Figure 2.2(c) and (d)), the existence of large voids within the powder bed of fine powder feedstock is highly probable [16]. Moreover, the significantly lower flowability of the fine powder feedstock compared to the coarse one (Table 2.4) can also generate large vacancies within the powder bed. According to the CBD measurement results, the relative powder bed density is 53% and 38% for coarse and fine powder systems, respectively. Accordingly, the volume fraction of pores in the bed of fine powder is 32% higher than that of the coarse one. This reveals that the filling of pores requires a significantly longer period during the processing of the fine powder, which is not available in the L-PBF process due to its rapid*

melting/solidification nature. Figure 2.7 shows optical micrographs of parts manufactured at a high scanning speed of 1300 mm/s and various laser powers. As it is evident, there is almost no defect in the case of the coarse powder system (Figure 2.7(a)-(c)). However, large pores which are free from un-melted/partially melted powder particles are visible in samples fabricated by the fine powder feedstock. The absence of un-melted/partially melted powder particles in most of these pores proves that they are formed due to the limited flow of the molten material to fill the large voids within the powder bed [53]. The fraction of these large pores shows a descending trend by increasing the laser power, which can be attributed to the larger melt pool, lower melt viscosity, lower cooling rate and higher chance of the molten material to fill the pores (Figure 2.7(d)-(f)) [54-56]. That is why the large pores are almost eliminated at the laser power of 370 W in the fine powder system (Figure 2.7(f)).

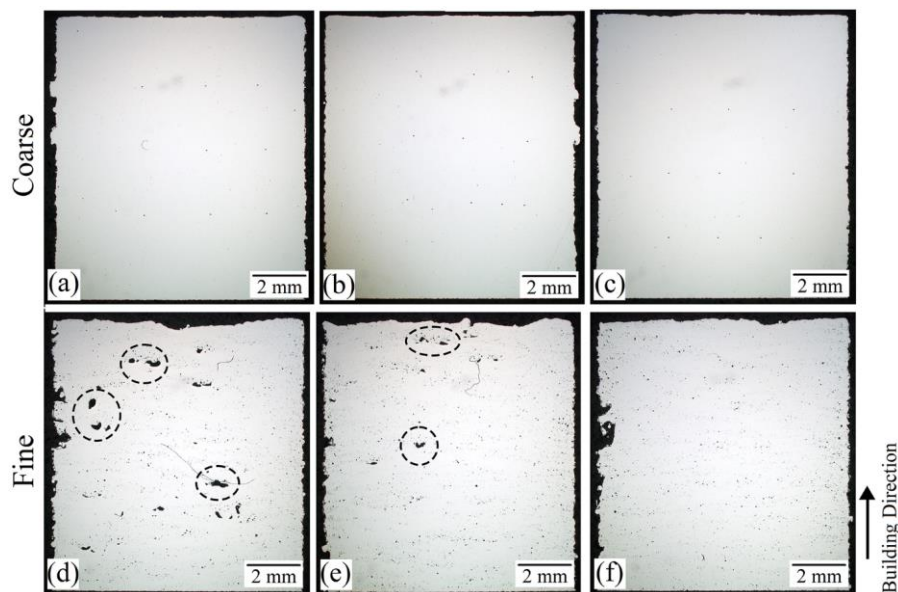


Figure 2.7. Cross-sectional non-etched optical micrographs of parts obtained by L-PBF processing of: (a)-(c) coarse and (d)-(f) fine AlSi10Mg powders. The employed hatch spacing and scanning speed are 0.15 mm and 1300 mm/s for all samples while the laser power is: (a), (d) 300 W; (b), (e) 335 W and (c), (f) 370 W.

Evaporation and oxygen content: Another factor which is mainly dominant at low scanning speeds is the material evaporation caused by the high E_V [54]. The evaporated AlSi10Mg and the entrapped oxygen gas would lead to the formation of spherical porosities in the final parts. Although the significantly higher t_{eff} of the fine powder favors lower E_V at the same process parameters, more evaporation is expected to take place when the fine powder is employed. This is due to the fact that the melting of individual powder particles and their evaporation is way easier in the fine powder system. The energy required to melt a single powder particle over the average energy of the laser beam can be calculated as [32]:

$$\frac{E_{need}}{E_{av}} = \frac{(\frac{4}{3}\pi r^3) \cdot \rho \cdot (c\Delta T_m + L_m)}{K \cdot I_0 \cdot \pi \cdot r^2} = r \cdot \frac{4\rho(c\Delta T_m + L_m)}{3KI_0} \quad \text{Eq. 7}$$

in which r , ρ , c , ΔT_m , L_m , K and I_0 denote the particle radius, density, specific heat capacity, temperature rise up to the melting point, latent heat of fusion, the absorption coefficient of the powder and the intensity of the laser beam, respectively. As it is evident, the finer the powder particle (smaller r) and the higher the absorption coefficient (K), the lower the energy required for melting and, therefore, evaporation. On the other hand, due to their higher specific surface area relative to volume, fine powders show a higher degree of contamination and are more prone to oxidation [57]. For instance, calculations for a portion of the powder bed with a volume of $10 \times 10 \times t_{eff}$ revealed that the number of particles and their surface area in the fine powder system are 88 and 4.5 times greater than those of the coarse powder feedstock, respectively. In this calculation, all of the powder particles in each system are assumed to have a diameter equal to their average powder particle size (9 and 40 μm for fine and coarse powders, respectively). It can be inferred from these calculations that the volume and, therefore, the mass fraction of the oxide layers existing on the surface of particles (e.g., MgAl_2O_5 detected on the surface of AlSi10Mg powder particles [58]) in the fine powder feedstock are 4.5 times greater than that of the

coarse powder. These oxide films usually have a melting point noticeably higher than that of metallic powders. However, they can be decomposed during the L-PBF process. Since the rapid solidification of the melt pool can hinder the generated oxygen/evaporated material to escape from the melt pool, the entrapped gas bubbles can lead to spherical porosities in the final part, which is more severe in the fine powder system due to its higher mass fraction of oxide layers. Figure 2.8 shows optical micrographs of parts manufactured at a low scanning speed of 800 mm/s and various laser powers. It can be seen that the dominant defects in these samples are spherical pores which are present in both samples fabricated by coarse and fine powder feedstocks. However, their volume fraction is higher in the case of the fine powder system (Figure 2.8(d)-(f)). The volume fraction of pores follows an ascending trend by increasing the laser power in both cases. This is attributed to the increased evaporation of the molten material and the intensified oxide decomposition caused by the increase in the E_V .

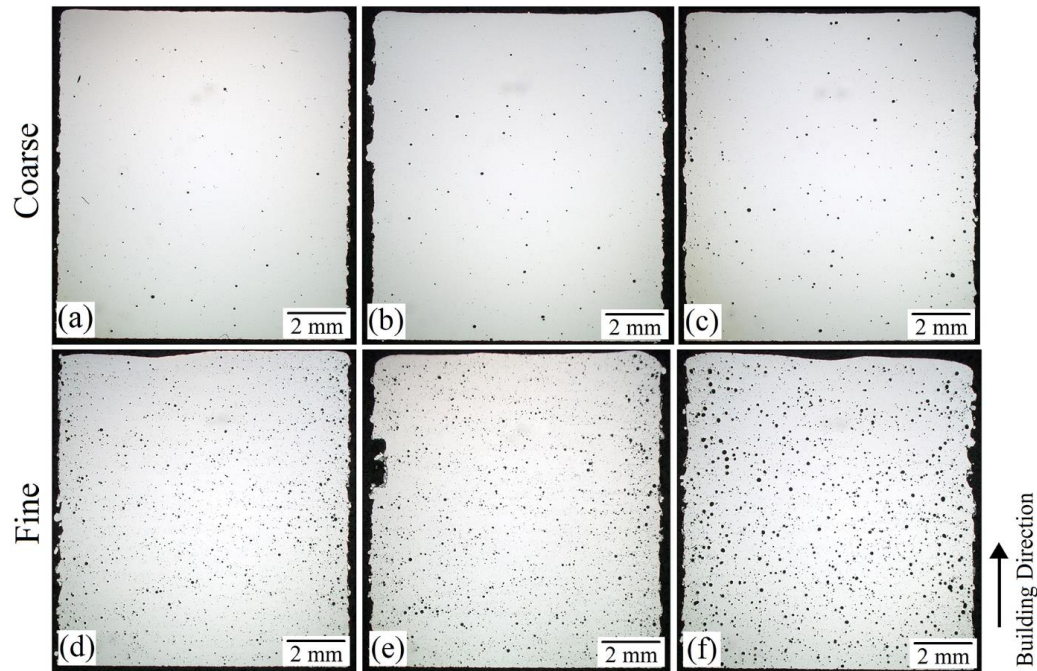


Figure 2.8. Cross-sectional non-etched optical micrographs of parts obtained by L-PBF processing of: (a)-(c) coarse and (d)-(f) fine AlSi10Mg powders. The employed hatch spacing and scanning speed are 0.19 mm and 800 mm/s for all samples while the laser power is: (a), (d) 300 W, (b), (e) 335 W, and (c), (f) 370 W.

Effective powder layer thickness (t_{eff}): Although rarely observed, un-melted or partially melted powder particles were also present in some of the parts fabricated by L-PBF processing of fine powder feedstock at low E_V . None of the parts had un-melted/partially melted powder particles within the applied range of process parameters when the coarse powder was used. This can be ascribed to the lower t_{eff} (56.3 μm) and the negligible tendency of coarse powder particles to form agglomerates. Figure 2.9 shows an irregular-shape defect which was formed due to the incomplete fusion of fine powder particles at $E_V=9.3 \text{ J/mm}^3$ (the minimum E_V in this study). Although the extremely large agglomerates cannot settle on the substrate during the spreading stage, clusters less than t_{eff} (78.5 μm) in size can be deposited. At low E_V , the laser cannot completely melt the deposited agglomerates, leading to the formation of defects which contain un-melted/partially melted

powder particles (Figure 2.9(b)). These particles seem to be sintered and fused together due to the thermal cycles induced during the processing of the adjacent tracks/next layers (Figure 2.9(b)).

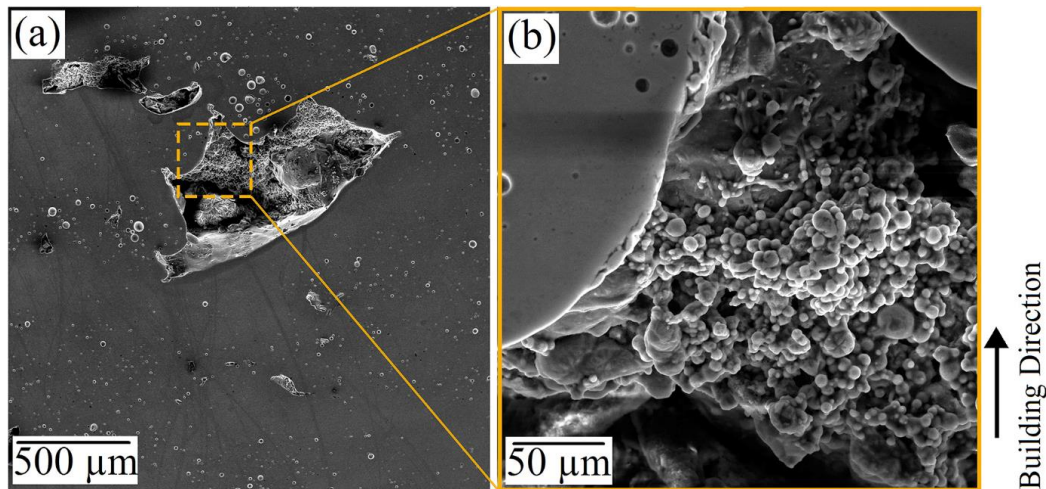


Figure 2.9. SEM micrographs from the cross-section of part obtained by L-PBF processing of the fine AlSi10Mg powder employing laser power of 300 W, scanning speed of 1300 mm/s and hatch spacing of 0.19 mm ($E_V = 9.3 \text{ J/mm}^3$). (b) Shows the higher magnification micrograph of the selected region in (a).

2.3.5 Top surface quality

Since in the L-PBF process, the components are fabricated through a layer-by-layer manner, the top surface of each consolidated layer acts as the substrate for the deposition of the next powder layer. Therefore, the top surface (not the side surface) quality of the consolidated layer plays a major role in the powder spreading process, powder bed packing density, and, consequently, the densification level of the next powder layer. Given the fact that the top surface of the last layer in the printed part resembles the top surface of every single consolidated layer during the process, its characterization provides valuable information about the quality of the final part. Figure 2.10 presents SEM micrographs of the top surface for parts manufactured by fine and coarse powders using various scanning

speeds. A qualitative comparison of the surfaces reveals the worsening of the surface quality by increasing the scanning speed. For the sake of quantitative analysis, top surfaces were also analyzed using 3D surface topography measurements. Figure 2.11 shows the effect of scanning speed on the surface topography of samples obtained by both fine and coarse powders as well as the S_a values corresponding to these surfaces. Within the applied range of process parameters, fine powder resulted in higher surface roughness compared to the coarse powder. Depending on the employed scanning speed, the difference between the S_a of fine and coarse powder cases was found to be 5-73%, with higher scanning speeds resulting in a larger difference in the S_a .

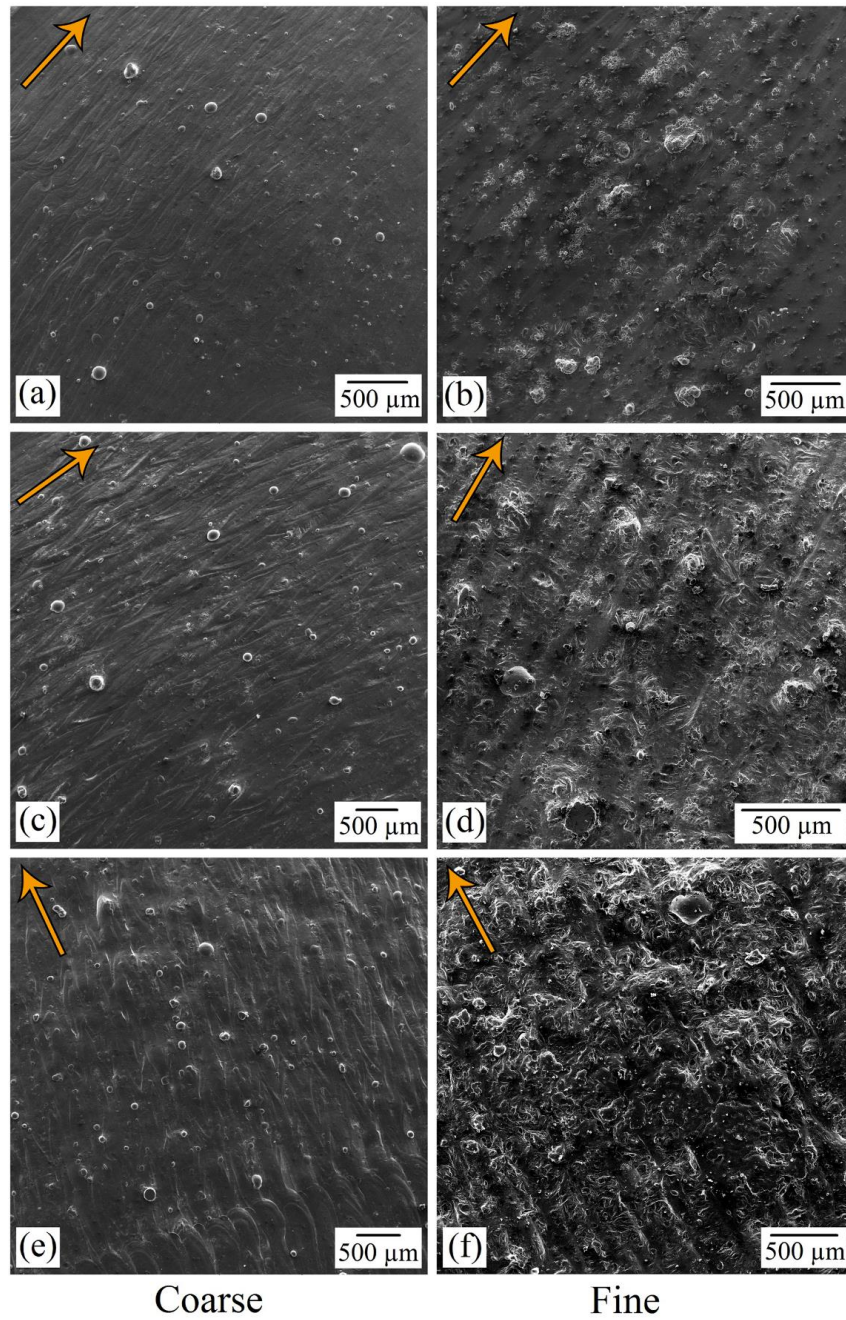
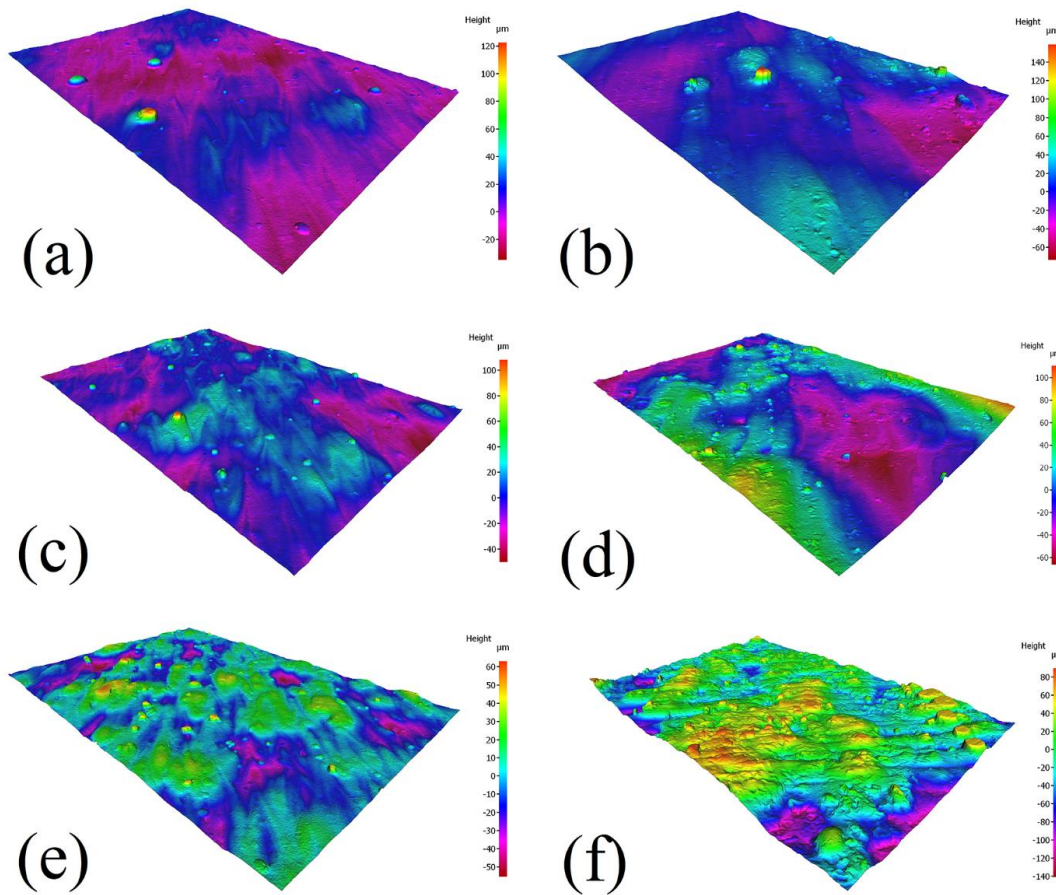


Figure 2.10. SEM micrographs of the top surface for parts manufactured by L-PBF processing of: (a), (c), (e) coarse and (b), (d), (f) fine AlSi10Mg powders. The parts have been processed by a fixed laser power of 335 W and a constant hatch spacing of 0.15 mm but varying scanning speeds of: (a) and (b) 800; (c) and (d) 1050; (e) and (f) 1300 mm/s. The arrows show the scanning direction.



Sample	Coarse powder			Fine powder		
	(a)	(c)	(e)	(b)	(d)	(f)
Sa (μm)	3.75	4.59	7.25	3.93	5.17	12.52

Figure 2.11. Color-3D images showing the top surface topography of parts produced by L-PBF processing of: (a), (c), (e) coarse and (b), (d), (f) fine AlSi10Mg powders. The roughness of the provided surfaces is also listed in the table. The parts have been processed by a laser power of 335 W and a hatch spacing of 0.15 mm but varying scanning speeds of: (a) and (b) 800; (c) and (d) 1050; (e) and (f) 1300 mm/s.

Although it has been reported in the literature that application of fine powders can lead to the fabrication of parts with the improved surface quality due to the decrease in the size of un-melted/partially melted particles on the surface [59, 60], the surface roughness obtained by the fine powder feedstock is lower than the coarse one regardless of the applied scanning

speed. Referring to Figure 2.10, the surface in both cases is almost free from unmelted/partially melted powder particles, suggesting that the variation in the surface roughness cannot be attributed to these particles. The reason behind the higher top surface roughness of samples fabricated by the fine powder can be unveiled through the analysis of the oxygen content. Figure 2.12 shows the oxygen concentration for the top surface of parts fabricated by fine and coarse powders with the same process parameters. As it is evident, the oxygen content in the case of fine powder is 2-7 times higher than that of the coarse powder system. The significantly higher specific surface area relative to volume of fine powder feedstock is the main reason behind its higher oxidation tendency, leading to the elevated oxygen content in the final part [57]. The presence of higher oxygen content in the melt pool results in the inward flow of the molten material due to the larger positive value of the surface tension gradient, encouraging the instability and discontinuity of the melt pool [61]. The locally disrupted tracks with the perturbed surface formed under such conditions lead to the higher top surface roughness. Moreover, higher content of oxygen is accompanied by the in-situ formation of oxides during the L-PBF process, which amplifies the surface roughness. It is also worth noting that some oxides existing in the fabricated parts may originate from the oxidation activated during the melting process [25].

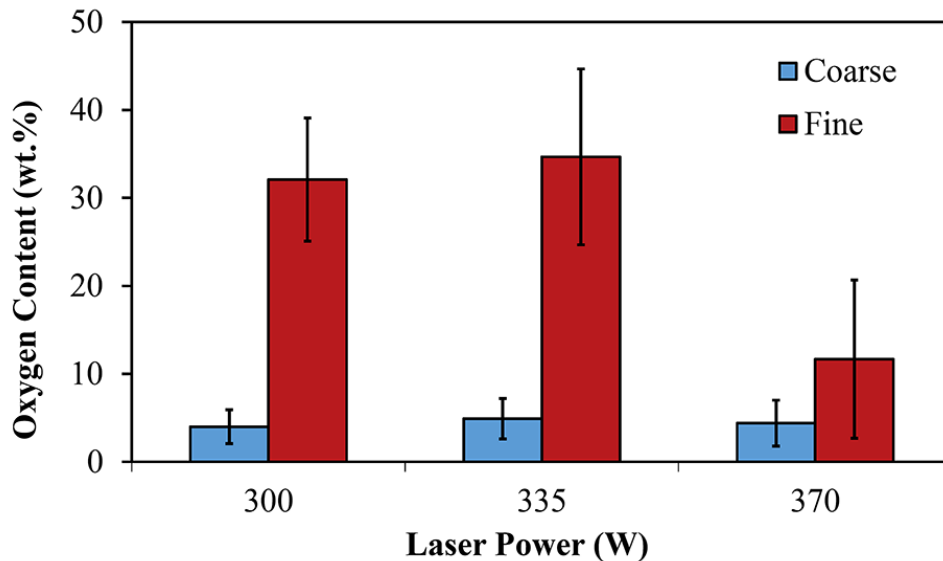


Figure 2.12. The oxygen concentration of parts obtained by L-PBF processing of coarse and fine AlSi10Mg powders using various laser powers. The measurement has been performed by EDS analysis. The employed scanning speed and hatch spacing were 800 mm/s and 0.15 mm, respectively.

It should be borne in mind that the surface quality is affected by not only the surface roughness but also the surface waviness of the fabricated parts. Based on the powder flowability results provided in Table 2.4, the fine powder system suffers from a poor flowability, originating from the enhanced inter-particle friction and cohesiveness. The deteriorated spreadability caused by inter-particle friction, as well as the higher tendency of agglomeration due to the high cohesiveness, leads to the deposition of non-uniform powder layers during the recoating process [62]. Consequently, the layer consolidated from the fine powder shows a surface texture that is wavier (Figure 2.11).

2.3.6 Dimensional accuracy

2.3.6.1 X-Y plane

Figure 2.13(a) illustrates the deviation in the area of X-Y plane (compared to the design dimensions of 10 mm×10 mm) for parts printed from the coarse and fine powders using

various linear laser energy densities (P/v) and two different hatch spacings of 0.15 and 0.19 mm. Compared to the case of coarse powder, the fine powder led to parts with higher deviations in the area within the employed range of P/v ratio and hatch spacing.

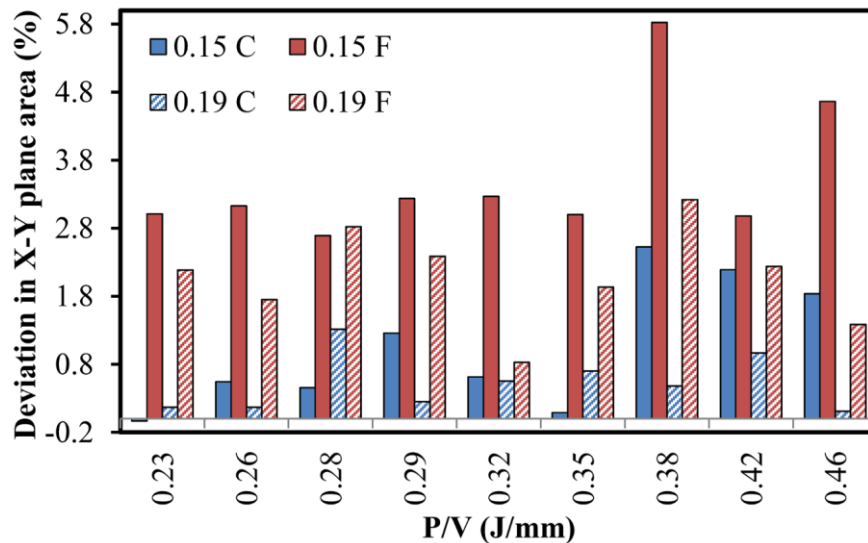


Figure 2.13. The deviation in the area of the X-Y plane in the cubic samples fabricated by L-PBF processing of fine (F) and coarse (C) AlSi10Mg powders using various P/v ratios and two different hatch spacings of 0.16 and 0.19 mm.

Microstructural observation of the side surface can provide valuable information regarding the in-plane dimensional accuracy. Figure 2.14 shows SEM micrographs of the side surface for parts obtained by L-PBF processing of coarse and fine powder feedstocks. The surface of the part processed from the coarse powder shows un-melted/partially melted powder particles and molten droplets attached to the surface (Figure 2.14(a) and (b)). Compared to the top surface of the same part provided in Figure 2.10(e), the side surface shows an inferior surface quality. The presence of un-melted/partially melted powder particles on the side surface is more significant in part produced by the fine powder (Figure 2.14). As shown in Figure 2.14(c) and (d), the side surface under this condition is noticeably rough and contains a large number of powder particles that seem to be attached to the molten

tracks during the L-PBF process. A close observation of these powder particles shows their agglomeration, which can be due to the sintering of fine powder particles adjacent to the melt pool caused by the thermal effects of the L-PBF process (Figure 2.14(d)). The intensified sinterability of fine powder particles arises from their noticeably higher specific surface area relative to volume compared to the coarse powder system [63, 64].

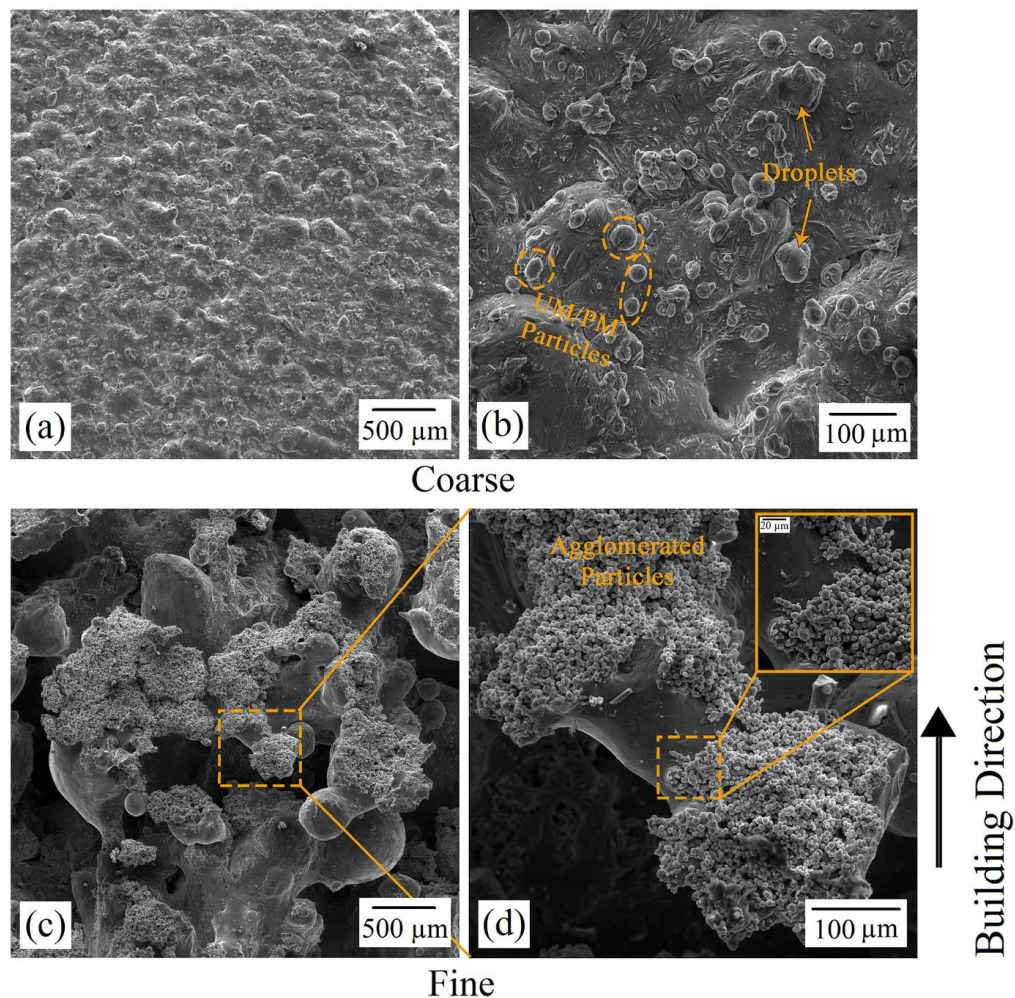


Figure 2.14. SEM micrographs of the side surface corresponding to parts obtained by L-PBF processing of: (a), (b) coarse and (c), (d) fine AlSi10Mg powders using laser power of 335 W, scanning speed of 1300 mm/s and hatch spacing of 0.15 mm. The higher magnification micrograph of the selected region in (c) is provided in (d). The inset in (d) shows the magnified view of powder particles adhered to the surface. UM/PM refers to un-melted/partially melted.

The X-Y plane dimensional accuracy was also found to be a function of the hatch spacing. As shown in Figure 2.13(a), the hatch spacing of 0.19 mm led to lower deviations in the area than that of 0.15 mm. This is almost valid for both fine and coarse powders within the applied range of P/v ratio. In general, the highest dimensional accuracy (the lowest deviation in the area) belongs to parts obtained by processing of the coarse powder with the hatch spacing of 0.19 mm. However, for almost the whole range of P/v ratio, L-PBF processing of the fine powder with the hatch spacing of 0.15 mm led to the worst dimensional accuracy in the X-Y plane. This may be attributed to the elevated heat input transferred to the surrounding powder media at lower hatch spacing. The dimensional accuracy measurement results suggest that the fabrication of sound parts with the fine powder feedstock is challenging not only from the densification level perspective but also from the dimensional accuracy viewpoint.

2.3.6.2 *Building direction (Z-direction)*

The dimensional accuracy along the Z direction (building direction) is shown in Figure 2.15 for the optimum samples of both the coarse and fine powder cases. The part obtained from the fine powder has a lower dimensional accuracy (higher percentage of deviation from the nominal height).

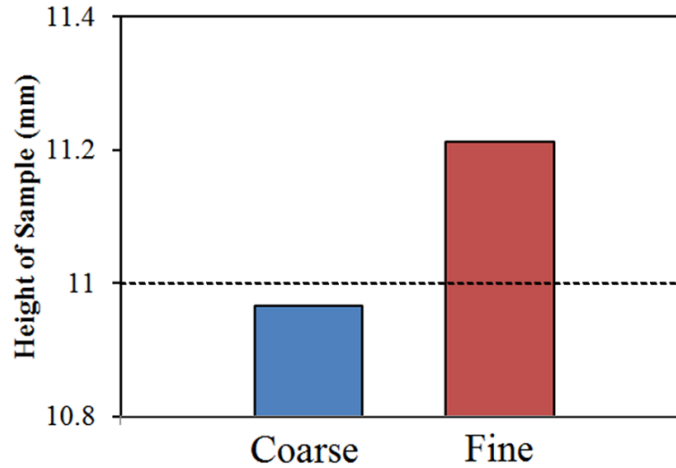


Figure 2.15. The deviation from the nominal height of samples with the optimum density obtained by L-PBF processing of coarse ($P=335$ W, $v=1050$ mm/s, $h=0.15$ mm and $E_V=21.9$ J/mm³) and fine ($P=335$ W, $v=1050$ mm/s, $h=0.15$ mm and $E_V=16.3$ J/mm³) AlSi10Mg powders. The nominal height refers to the height of samples after being cut off the build plate. The errors associated with measurements are 4.3 and 6.5 μm for coarse and fine powder cases, respectively.

This can be justified based on the higher cohesive forces existing among the particles of the fine powder system compared to the coarse one [16]. As mentioned before, the decrease in the size of powder particles is accompanied by an increase in the specific surface area relative to volume and, consequently, the inter-particle cohesive forces (e.g., van der Waals and electrostatic forces). Therefore, the fine powder system has a high tendency to form particle clusters to reduce the surface energy. Depending on their size, these agglomerates adversely affect the uniformity of the powder bed during the powder deposition stage through two different scenarios. If the agglomerates are larger than t_{eff} , they not only fail to settle on the substrate but also sweep the powder particles ahead of them, leading to the decreased overall powder bed packing density and uneven powder bed [50]. The clusters smaller than t_{eff} might be able to settle on the substrate. However, the size and population of particles deposited ahead, behind and on top of these agglomerates are completely different, resulting in local non-uniformities in the powder bed. Each of these two scenarios

leads to the formation of wavy surfaces in most of the parts obtained by L-PBF processing of fine powder feedstock (Figure 2.10(d) and (f), Figure 2.11(d) and (f), Figure 2.16(b)). Besides, the higher inter-particle friction in the fine powder system causes a poor powder flowability (higher SE provided in Table 2.4), which further decreases the dimensional accuracy in the Z direction. Lower flowability is believed to reduce the overall thickness of the powder bed and result in the deviation from the nominal height of the coupons [54]. As it is evident in Figure 2.16, the height of the part fabricated by the fine powder is lower than that of the coarse one, which is directly attributed to the poor flow behavior of the fine powder. It is of note that the higher volume fraction of defects in coupons fabricated by the fine powder system is another factor adversely affecting the dimensional accuracy in the Z direction (Figure 2.16). The defects formed in each layer influence not only the layer in which they are located but also the subsequent layer(s). In other words, the formation of a non-uniform consolidated layer jeopardizes the uniformity of the powder layer deposited on top of it and in turn hinders the creation of subsequent uniform layers.

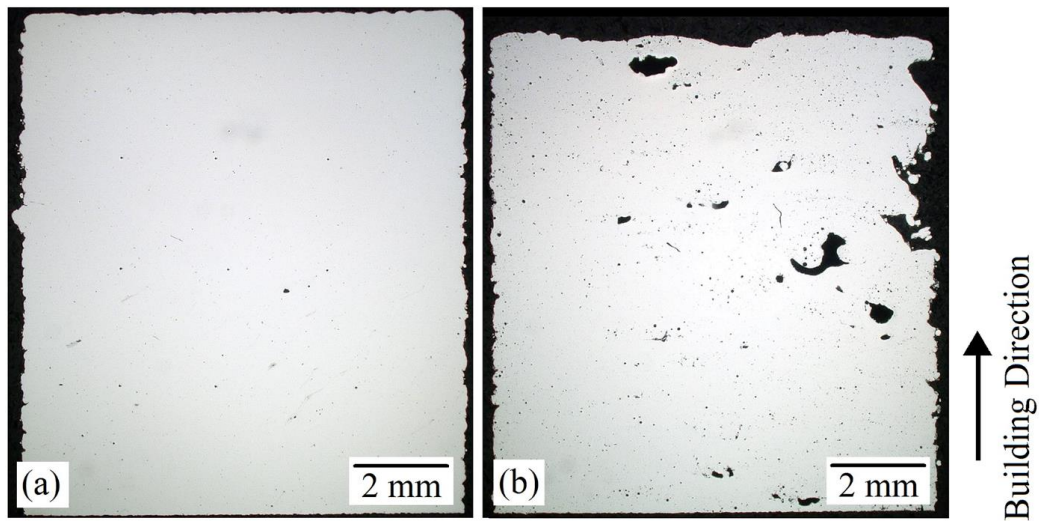


Figure 2.16. Cross-sectional optical micrographs of parts manufactured by L-PBF processing of: (a) coarse and (b) fine AlSi10Mg powders using laser power of 370 W, scanning speed of 1300 mm/s and hatch spacing of 0.19 mm.

2.3.7 Microstructural characterization

Figure 2.17 presents optical micrographs of the cross-sections for parts fabricated by L-PBF processing of coarse and fine powders using the same E_V . As being observed, cross-sections of the successive melt pools represent the layer-wise nature of the process. The typical semi-elliptical shape of the melt pool is evident in macrostructures due to the employed scanning strategy. The microstructures of parts processed by fine and coarse powders seem to show no considerable difference in the size of melt pools. Higher magnification micrographs provided in Figure 2.17(b) and (d) reveal the difference between the microstructure of the melt pool interiors and boundaries. This is why the melt pools can be observed in the L-PBF processed AlSi10Mg components.

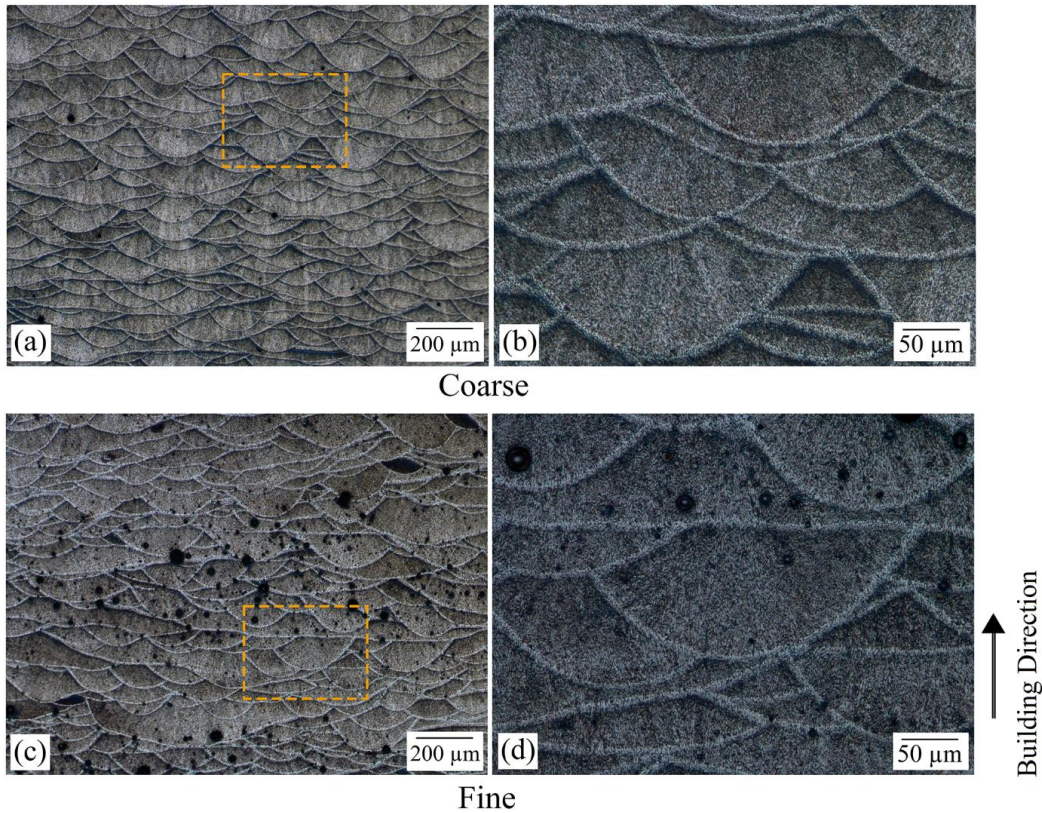


Figure 2.17. Cross-sectional optical micrographs of parts fabricated by L-PBF processing of: (a), (b) coarse ($E_V=21.9 \text{ J/mm}^3$) and (c), (d) fine ($E_V=16.3 \text{ J/mm}^3$) AlSi10Mg powders using laser powder of 335 W, scanning speed of 1050 mm/s and hatch spacing of 0.15 mm. (b) and (d) are higher magnification micrographs of boxed regions in (a) and (c), respectively.

To have a better understanding of the microstructural evolutions, SEM micrographs of the same samples provided in Figure 2.17 are shown in Figure 2.18. The microstructures presented in Figure 2.18(a) and (b) reveal a band structure of alternating coarse and fine structures in parts manufactured by either the fine or the coarse powder. Detailed microstructures of different regions presented in Figure 2.18(a) and (b) show that the obtained inhomogeneous microstructures can be divided into three distinct regions having different microstructural features; the core of melt pools with a fine microstructure (MP-fine), the boundary of melt pools with a coarse microstructure (MP-coarse) and the heat-affected zone (HAZ). Moving from layer n to layer $n+1$ along the boundary, HAZ, MP-

coarse and MP-fine regions are distinguishable. The HAZ is defined as the region in which the previous track/layer (layer n) experiences the thermal effects of the next track/layer (layer $n+1$) and may undergo microstructural changes. To analyze the microstructures developed inside the melt pools, the mode of solidification needs to be examined. The solidification mode of the melt pool is governed by the G/R ratio, in which G and R are the thermal gradient and solidification rate, respectively [65]. The micrographs shown in Figure 2.18 reveal the formation of a micro-cellular microstructure, in which fine α -Al cells are decorated by Si particles segregated at the cell boundaries. However, the size of cells varies from the boundary toward the center of the melt pool due to the variations in the $G \times R$, which governs the microstructural refinement [54, 65]. The finer microstructure of the MP-fine than the MP-coarse can be attributed to the higher $G \times R$ values induced in the center of the melt pool. The cellular microstructure also seems to be oriented mainly along the center of the melt pool. This directionality is known to be due the unidirectional heat flux occurring from center toward the boundaries of the melt pool in the welding and AM [54, 66, 67]. Such a thermal gradient allows preferential growth $\langle 100 \rangle$ direction in metals with cubic crystal structure such as Al) opposite to the heat flux vector, leading to the directional solidification [68-71].

The comparison of the melt pool interior microstructures (MP-fine) revealed a coarser microstructure (larger cells) for the sample obtained by L-PBF processing of the fine powder (Figure 2.18(c) and (d)). Based on the measurements performed on both powder cases using ImageJ Software, the cell size of the MP-F region was 1.04 ± 0.12 and 0.66 ± 0.14 for fine and coarse powder cases, respectively. This shows that the cell size of the part fabricated by the fine powder is 57% larger than that obtained by the coarse powder, suggesting a significant difference between their microstructural features. This

can be ascribed to the higher laser absorptivity of the fine powder, which may act to elevate the melt pool temperature or reduce the cooling rate (Figure 2.5).

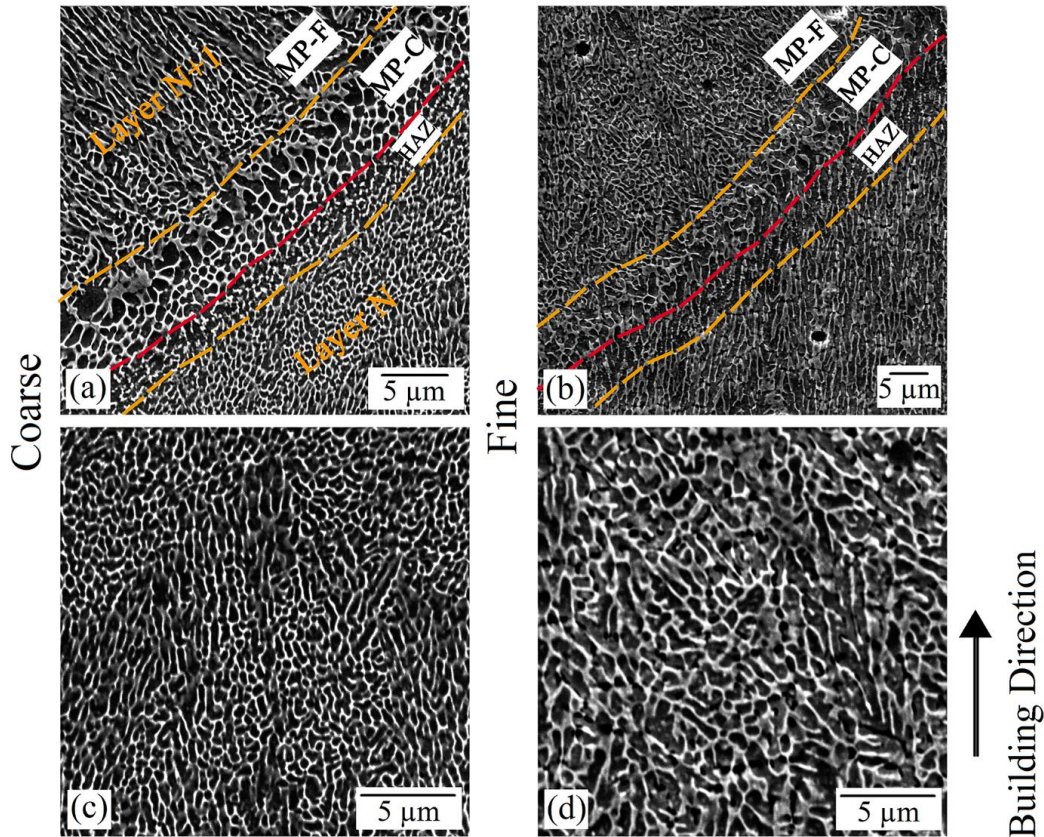


Figure 2.18. SEM microstructure for parts obtained by L-PBF processing of: (a), (c) coarse ($E_V=21.9 \text{ J/mm}^3$) and (b), (d) fine ($E_V=16.3 \text{ J/mm}^3$) AlSi10Mg powders using laser powder of 335 W, scanning speed of 1050 mm/s and hatch spacing of 0.15 mm. (a) and (b) show the variation in the microstructure adjacent to the melt pool boundaries. (c) and (d) are enclosed views of the MP-F regions shown in (a) and (b), respectively. MP-F, MP-C and HAZ refer to the melt pool-fine, melt pool-coarse, and heat-affected zone, respectively.

A close observation of the obtained microstructures unveils the existence of micro-cracks randomly distributed in the part fabricated by L-PBF processing of the fine powder (Figure 2.19(b), (c)). These micro-cracks were found throughout the part and seemed to be interconnected. The formation of these cracks may be attributed to the higher oxygen content of the fine powder system, which paves the way for the formation of Al oxide with poor

wettability by the Al melt during L-PBF processing. Despite the case of the fine powder, the part achieved by the coarse powder was almost free from these cracks (Figure 2.19(a)).

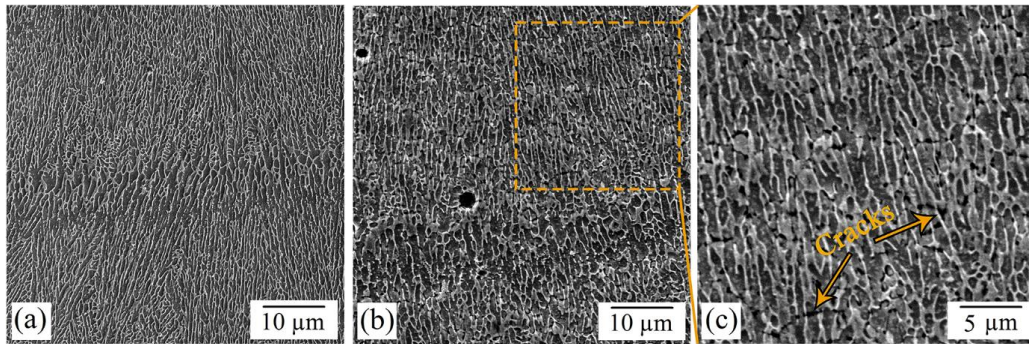


Figure 2.19. Typical SEM micrographs of parts achieved by L-PBF processing of: (a) coarse; and (b), (c) fine AlSi10Mg powders using laser power of 335 W, scanning speed of 1050 mm/s and hatch spacing of 0.15 mm ($E_V = 16.3 \text{ J/mm}^3$). (c) Enclosed view of micro-cracks existing in (b).

2.3.8 Microhardness

Microhardness measurement results are depicted in Figure 2.20 as a function of the P/v ratio and hatch spacing for both fine and coarse powder cases. The obtained microhardness data showed high accuracy and repeatability, with the maximum coefficient of variation less than 5% for both fine and coarse powder cases. It can be inferred that regardless of the P/v value and the employed hatch spacing, the coarse powder resulted in higher microhardness compared to the fine powder. The average microhardness of the samples fabricated by the coarse powder system is 3-15.5 HV higher than those for the fine powder feedstock, depending on the process parameters. This higher hardness can be traced back to two factors:

- I. Finer microstructure: As shown in Figure 2.18, the finer cellular microstructure in the case of the coarse powder can more efficiently resist the plastic deformation and consequently lead to the higher hardness and strength [72].

- II. Lower amount of micro-cracks: The micro-cracks existing in the part fabricated from the fine powder (Figure 2.19(b), (c)) can cause an easier collapse of the material underneath the indenter during the microhardness loading. Unlike the macro-hardness test, the microhardness measurement is not influenced by the porosities existing within the L-PBF processed parts since locally defect-free areas are typically selected by microstructural observations for indentation. Moreover, the indentation depth of the microhardness test is believed to be small enough to avoid any interactions with the sub-surface pores [10, 73]. However, the size of micro-cracks observed in the case of fine powder is considerably smaller than the indentation size, meaning that these cracks can play a role in decreasing the microhardness.

It is worth noting that for both the coarse and fine powder cases, the microhardness follows a decreasing trend when increasing the P/v ratio. Moreover, the results also reveal that for both powders, the hatch spacing of 0.15 mm leads to lower microhardness than that of 0.19 mm. Both of these findings can be ascribed to the microstructural coarsening caused by the elevated heat induced in the system by either increase in P/v ratio or decrease in the hatch spacing (Eq. 6). The coarser microstructure (larger cell size) associated with the lower cooling rate results in decreased hardness, as suggested by the well-known Hall-Petch equation. In other words, due to the significant role of grain boundaries on the movement of dislocations, the decreased fraction of cell boundaries obtained by the microstructure coarsening reduces the plastic deformation resistivity and consequently lowers the hardness of the material [74].

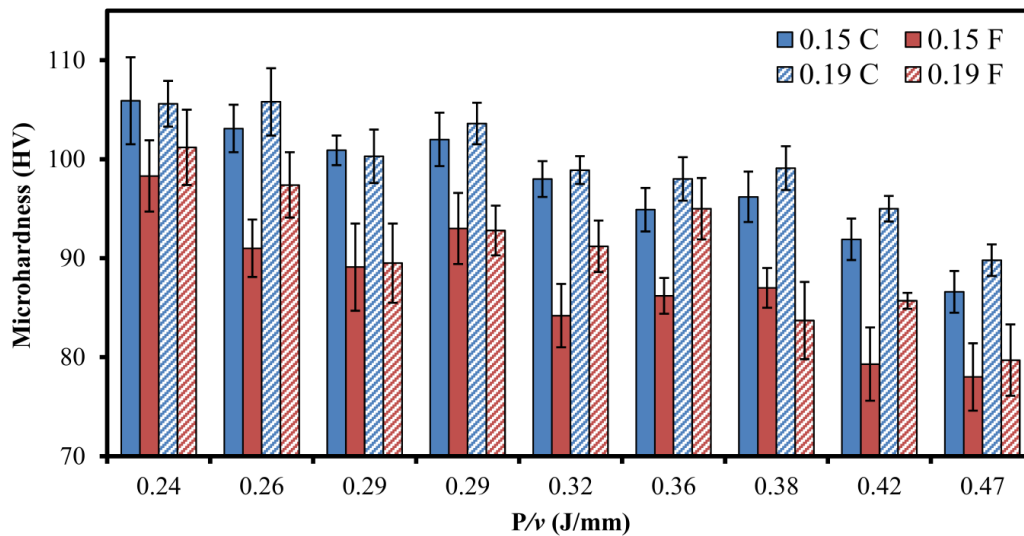


Figure 2.20. The variation in the microhardness of parts achieved by L-PBF processing of fine (F) and coarse (C) AlSi10Mg powders as a function of the employed P/v ratio for two different hatch spacings of 0.15 and 0.19 mm.

2.4 Conclusions

This study was aimed at investigating the role of powder particle size on the L-PBF processability of the AlSi10Mg alloy. For this purpose, two different powders with the mean particle sizes of 9 μm (fine) and 40 μm (coarse) were subjected to the L-PBF process to fabricate parts using various laser powers, scanning speeds and hatch spacings. A modified volumetric energy density was introduced to compare the parts, which takes the effects of the laser absorptivity and the effective powder layer thickness also into account. The influence of process parameters on the densification level, top and side surface integrity, dimensional accuracy, microstructural evolutions and microhardness was explored, and the parts obtained by L-PBF processing of the fine and coarse powders were compared. The main findings can be summarized as follows:

1. The flowability and packing density of the fine powder was 75% and ~30% lower than the coarse powder, respectively.

2. For both powders, the part density first raised and then declined by increasing the energy density. Within the applied range of energy density, inferior densification levels were achieved in the case of fine powder due to its lower powder bed packing density, higher oxygen content and higher effective powder layer thickness.
3. The maximum part densities were ~95 and ~99 for the fine and coarse powder cases, respectively.
4. The coarse powder led to a lower top surface roughness compared to the fine powder. Depending on the scanning speed, a difference of 5-73% between the S_a of parts obtained by the fine and coarse powder cases was attained.
5. The fine powder feedstock led to the lower dimensional accuracy in the X-Y plane, mainly due to the adherence of a noticeable volume of un-melted/partially melted powder particles to the side surfaces.
6. Due to its noticeably lower flowability and great tendency to form agglomerates, the parts fabricated by the fine powder had lower dimensional accuracy along the building direction (height).
7. The coarse powder resulted in finer cellular structure and, consequently, higher microhardness than the fine powder feedstock.

References

1. Schelling, P.K., L. Shi, and K.E. Goodson, *Managing heat for electronics*. Materials Today, 2005. **8**(6): p. 30-35.
2. Tjong, S.C., *Recent progress in the development and properties of novel metal matrix nanocomposites reinforced with carbon nanotubes and graphene nanosheets*. Materials Science and Engineering: R: Reports, 2013. **74**(10): p. 281-350.
3. Maloney, K.J., et al., *Multifunctional heat exchangers derived from three-dimensional micro-lattice structures*. International Journal of Heat and Mass Transfer, 2012. **55**(9-10): p. 2486-2493.
4. Wadley, H.N. and D.T. Queheillalt. *Thermal applications of cellular lattice structures*. in *Materials science forum*. 2007. Trans Tech Publ.
5. Jafari, D. and W.W. Wits, *The utilization of selective laser melting technology on heat transfer devices for thermal energy conversion applications: A review*. Renewable and Sustainable Energy Reviews, 2018. **91**: p. 420-442.
6. Fereiduni, E., A. Ghasemi, and M. Elbestawi, *Selective laser melting of aluminum and titanium matrix composites: recent progress and potential applications in the aerospace industry*. Aerospace, 2020. **7**(6): p. 77.
7. Balbaa, M., et al., *On selective laser melting of Inconel 718: Densification, surface roughness, and residual stresses*. Materials & Design, 2020: p. 108818.
8. Louvis, E., P. Fox, and C.J. Sutcliffe, *Selective laser melting of aluminium components*. Journal of Materials Processing Technology, 2011. **211**(2): p. 275-284.
9. Brandl, E., et al., *Additive manufactured AlSi10Mg samples using Selective Laser Melting (SLM): Microstructure, high cycle fatigue, and fracture behavior*. Materials & Design, 2012. **34**: p. 159-169.
10. Fereiduni, E., A. Ghasemi, and M. Elbestawi, *Selective laser melting of hybrid ex-situ/in-situ reinforced titanium matrix composites: Laser/powder interaction, reinforcement formation mechanism, and non-equilibrium microstructural evolutions*. Materials & Design, 2019. **184**: p. 108185.
11. Tiwari, J.K., et al., *Investigation of porosity, microstructure and mechanical properties of additively manufactured graphene reinforced AlSi10Mg composite*. Additive Manufacturing, 2020. **33**: p. 101095.
12. Astm, I., *ASTM52900-15 Standard Terminology for Additive Manufacturing—General Principles—Terminology*. ASTM International, West Conshohocken, PA, 2015. **3**(4): p. 5.

13. Sing, S.L., S. Huang, and W.Y. Yeong, *Effect of solution heat treatment on microstructure and mechanical properties of laser powder bed fusion produced cobalt-28chromium-6molybdenum*. Materials Science and Engineering: A, 2020. **769**: p. 138511.
14. Salmi, A. and E. Atzeni, *Residual stress analysis of thin AlSi10Mg parts produced by Laser Powder Bed Fusion*. Virtual and Physical Prototyping, 2020. **15**(1): p. 49-61.
15. Tiberto, D., et al., *Additive manufacturing of copper alloys: influence of process parameters and alloying elements*. Materials Science and Technology, 2019. **35**(8): p. 969-977.
16. Tan, J.H., W.L.E. Wong, and K.W. Dalgarno, *An overview of powder granulometry on feedstock and part performance in the selective laser melting process*. Additive Manufacturing, 2017. **18**: p. 228-255.
17. Simchi, A., *The role of particle size on the laser sintering of iron powder*. Metallurgical and Materials Transactions B, 2004. **35**(5): p. 937-948.
18. Niu, H. and I.H. CHANG, *Selective laser sintering of gas and water atomized high speed steel powders*. Scripta Materialia, 1999. **41**(1): p. 25-30.
19. Aboulkhair, N.T., et al., *Reducing porosity in AlSi10Mg parts processed by selective laser melting*. Additive Manufacturing, 2014. **1**: p. 77-86.
20. *Standard Test Method for Minimum Ignition Energy of a Dust Cloud in Air*.
21. Sheridan, W.D., *Reference Data Sheet for Aluminum*, in *Meridian Engineering and Technology*. 1996.
22. Kuo, C., et al., *Microstructure evolution and mechanical property response via 3D printing parameter development of Al–Sc alloy*. Virtual and Physical Prototyping, 2020. **15**(1): p. 120-129.
23. Yu, W., et al., *Influence of re-melting on surface roughness and porosity of AlSi10Mg parts fabricated by selective laser melting*. Journal of Alloys and Compounds, 2019. **792**: p. 574-581.
24. Aboulkhair, N.T., et al., *3D printing of Aluminium alloys: Additive Manufacturing of Aluminium alloys using selective laser melting*. Progress in Materials Science, 2019. **106**: p. 100578.
25. Tang, M. and P.C. Pistorius, *Oxides , porosity and fatigue performance of AlSi10Mg parts produced by selective laser melting*. International Journal of Fatigue, 2017. **94**: p. 192-201.
26. Beevers, E., et al., *Fatigue properties and material characteristics of additively manufactured AlSi10Mg–Effect of the contour parameter on the microstructure*,

- density, residual stress, roughness and mechanical properties*. International Journal of Fatigue, 2018. **117**: p. 148-162.
27. Muñoz-Lerma, J.A., et al., *A Comprehensive Approach to Powder Feedstock Characterization for Powder Bed Fusion Additive Manufacturing: A Case Study on AlSi7Mg*. Materials, 2018. **11**(12): p. 2386.
 28. Spierings, A.B., et al., *Powder flowability characterisation methodology for powder-bed-based metal additive manufacturing*. Progress in Additive Manufacturing, 2016. **1**(1-2): p. 9-20.
 29. Fereiduni, E., A. Ghasemi, and M. Elbestawi, *Characterization of composite powder feedstock from powder bed fusion additive manufacturing perspective*. Materials, 2019. **12**(22): p. 3673.
 30. Karapatis, N., et al. *Optimization of powder layer density in selective laser sintering*. in *1999 International Solid Freeform Fabrication Symposium*. 1999.
 31. Spierings, A.B. and G. Levy. *Comparison of density of stainless steel 316L parts produced with selective laser melting using different powder grades*. in *Proceedings of the Annual International Solid Freeform Fabrication Symposium*. 2009. Austin, TX.
 32. Bourell, D., et al., *Influence of the particle size distribution on surface quality and mechanical properties in AM steel parts*. Rapid Prototyping Journal, 2011.
 33. Elliott, A.M., et al., *A method for measuring powder bed density in binder jet additive manufacturing process and the powder feedstock characteristics influencing the powder bed density*. 2016, Oak Ridge National Lab.(ORNL), Oak Ridge, TN (United States). High
 34. Sun, Y., et al., *Manipulation and characterization of a novel titanium powder precursor for additive manufacturing applications*. Jom, 2015. **67**(3): p. 564-572.
 35. *Standard Test Method for Particle Size Distribution of Metal Powders and Related Compounds by Light Scattering*, in *ASTM B822-10*. 2010, ASTM International: West Conshohocken, PA.
 36. Özbilen, S., *Satellite formation mechanism in gas atomised powders*. Powder metallurgy, 1999. **42**(1): p. 70-78.
 37. *Standard Test Methods for Flow Rate of Metal Powders Using the Hall Flowmeter Funnel*, in *ASTM B213-17*. 2017, ASTM International: West Conshohocken, PA.
 38. van der Wiel, D., *ADVANCED POWDER CHARACTERIZATION FOR ADDITIVE MANUFACTURING*. ADVANCED MATERIALS & PROCESSES, 2019. **177**(5): p. 22-26.

39. Renishaw. *Meander stripe and chessboard hatchings pattern*. [cited 2020 July 7]; Available from: <https://resources.renishaw.com/en/details/--95492>.
40. *Standard Test Methods for Density of Compacted or Sintered Powder Metallurgy (PM) Products Using Archimedes' Principle*, in ASTM B962-17. 2017, ASTM International: West Conshohocken, PA.
41. Yan, C., et al., *Microstructure and mechanical properties of aluminium alloy cellular lattice structures manufactured by direct metal laser sintering*. Materials Science and Engineering: A, 2015. **628**: p. 238-246.
42. Kempen, K., et al., *Mechanical properties of AlSi10Mg produced by selective laser melting*. Physics Procedia, 2012. **39**: p. 439-446.
43. Leturia, M., et al., *Characterization of flow properties of cohesive powders: A comparative study of traditional and new testing methods*. Powder technology, 2014. **253**: p. 406-423.
44. Jallo, L.J., et al., *Prediction of inter-particle adhesion force from surface energy and surface roughness*. Journal of Adhesion Science and Technology, 2011. **25**(4-5): p. 367-384.
45. Dadbakhsh, S., et al., *Effect of powder size and shape on the SLS processability and mechanical properties of a TPU elastomer*. Physics Procedia, 2016. **83**: p. 971-980.
46. Li, X., et al., *Selective laser melting of nano-TiB₂ decorated AlSi10Mg alloy with high fracture strength and ductility*. Acta Materialia, 2017. **129**: p. 183-193.
47. Boley, C., S.A. Khairallah, and A.M. Rubenchik, *Calculation of laser absorption by metal powders in additive manufacturing*. Applied optics, 2015. **54**(9): p. 2477-2482.
48. Rubenchik, A., et al., *Direct measurements of temperature-dependent laser absorptivity of metal powders*. Applied optics, 2015. **54**(24): p. 7230-7233.
49. Thijs, L., et al., *A study of the microstructural evolution during selective laser melting of Ti-6Al-4V*. Acta Materialia, 2010. **58**(9): p. 3303-3312.
50. Mindt, H., et al., *Powder Bed Layer Characteristics: The Overseen First-Order Process Input*. Metallurgical and Materials Transactions A, 2016. **47**(8): p. 3811-3822.
51. Panwisawas, C., et al., *On the role of thermal fluid dynamics into the evolution of porosity during selective laser melting*. Scripta Materialia, 2015. **105**: p. 14-17.
52. Cordova, L., et al., *Measuring the spreadability of pre-treated and moisturized powders for laser powder bed fusion*. Additive Manufacturing, 2020. **32**: p. 101082.
53. Gu, D., M. Xia, and D. Dai, *On the role of powder flow behavior in fluid thermodynamics and laser processability of Ni-based composites by selective laser*

- melting*. International Journal of Machine Tools and Manufacture, 2019. **137**: p. 67-78.
54. DebRoy, T., et al., *Additive manufacturing of metallic components—process, structure and properties*. Progress in Materials Science, 2018. **92**: p. 112-224.
 55. Fereiduni, E. and M. Elbestawi, *Process-Structure-Property Relationships in Additively Manufactured Metal Matrix Composites*, in *Additive Manufacturing of Emerging Materials*. 2019, Springer. p. 111-177.
 56. Fereiduni, E., M. Yakout, and M. Elbestawi, *Laser-Based Additive Manufacturing of Lightweight Metal Matrix Composites*, in *Additive Manufacturing of Emerging Materials*. 2019, Springer. p. 55-109.
 57. Lowell, S., et al., *Characterization of porous solids and powders: surface area, pore size and density*. Vol. 16. 2012: Springer Science & Business Media.
 58. Maamoun, A.H., et al., *Thermal post-processing of AlSi10Mg parts produced by Selective Laser Melting using recycled powder*. Additive Manufacturing, 2018. **21**: p. 234-247.
 59. Spierings, A.B., N. Herres, and G. Levy, *Influence of the particle size distribution on surface quality and mechanical properties in AM steel parts*. Rapid Prototyping Journal, 2011. **17**(3): p. 195-202.
 60. Liu, B., et al., *Investigation the effect of particle size distribution on processing parameters optimisation in selective laser melting process*. Additive manufacturing research group, Loughborough University, 2011: p. 227-238.
 61. Rombouts, M., et al., *Fundamentals of selective laser melting of alloyed steel powders*. CIRP Annals-Manufacturing Technology, 2006. **55**(1): p. 187-192.
 62. Galy, C., et al., *Main defects observed in aluminum alloy parts produced by SLM: From causes to consequences*. Additive Manufacturing, 2018. **22**: p. 165-175.
 63. Ertugrul, O., et al., *Effect of particle size and heating rate in microwave sintering of 316L stainless steel*. Powder technology, 2014. **253**: p. 703-709.
 64. Lu, J., et al., *Influence of particle size on sinterability, crystallisation kinetics and flexural strength of wollastonite glass-ceramics from waste glass and fly ash*. Materials Chemistry and Physics, 2014. **148**(1-2): p. 449-456.
 65. Kou, S., *Welding metallurgy*. New Jersey, USA, 2003: p. 431-446.
 66. Lienert, T., et al., *Fundamentals of Weld Solidification*. 2011.
 67. Xiong, Z., et al., *Role of melt pool boundary condition in determining the mechanical properties of selective laser melting AlSi10Mg alloy*. Materials Science and Engineering: A, 2019. **740**: p. 148-156.

68. Simonelli, M., Y.Y. Tse, and C. Tuck, *On the texture formation of selective laser melted Ti-6Al-4V*. Metallurgical and materials transactions A, 2014. **45**(6): p. 2863-2872.
69. Thompson, S.M., et al., *An overview of Direct Laser Deposition for additive manufacturing; Part I: Transport phenomena, modeling and diagnostics*. Additive Manufacturing, 2015. **8**: p. 36-62.
70. Liu, X., et al., *Microstructure of selective laser melted AlSi10Mg alloy*. Materials & Design, 2019. **168**: p. 107677.
71. Jadhav, S.D., et al., *Influence of selective laser melting process parameters on texture evolution in pure copper*. Journal of Materials Processing Technology, 2019. **270**: p. 47-58.
72. Askeland, D.R., et al., *The science and engineering of materials*. 2003.
73. Zuback, J. and T. DebRoy, *The hardness of additively manufactured alloys*. Materials, 2018. **11**(11): p. 2070.
74. Hansen, N., *Hall–Petch relation and boundary strengthening*. Scripta Materialia, 2004. **51**(8): p. 801-806.

3 Chapter 2 Influence of alloying elements on laser powder bed fusion processability of aluminum: A new insight into the oxidation tendency

Complete Citation:

Ghasemi A, Fereiduni E, Balbaa M, Jadhav SD, Elbestawi M, Habibi S. Influence of alloying elements on laser powder bed fusion processability of aluminum: A new insight into the oxidation tendency. *Additive Manufacturing*. 2021 Oct 1;46:102145.

Authorship contribution statement:

Ali Ghasemi: Investigation, Conceptualization, Methodology, Writing - original draft.

Eskandar Fereiduni: Investigation, Conceptualization, Methodology, Writing - original draft. **Mohamed Balbaa:** Methodology, Conceptualization, Writing - original draft. **Suraj**

Dinkar Jadhav: Investigation, Writing - original draft. **Mohamed Elbestawi:** Supervision, Writing - review & editing. **Saeid Habibi:** Supervision, Writing - review & editing.

***Influence of Alloying Elements on Laser Powder Bed Fusion
Processability of Aluminum: A New Insight into the Oxidation
Tendency***

Abstract

This study focuses on the influence of alloying elements (Si and Mg) and the process parameters on the laser powder bed fusion (LPBF) processability of aluminum (Al). In this regard, pure Al, AlSi12, and AlSi10Mg parts with and without single tracks on their top surface were fabricated using a wide range of process parameters. The oxidation tendency, laser absorptivity, and powder attributes were evaluated to justify the densification level and the processing window of the fabricated parts. The starting powders were subjected to the Auger electron spectroscopy to characterize the nature of the oxide compounds participating in the melt pool. The measurement of the oxygen content in pure Al (2260 ppm), AlSi12 (1299 ppm), and AlSi10Mg (740 ppm) powders, as well as their printed parts (90, 220, and 130 ppm, respectively at laser power of 300 W), proved that the level of oxide removal overweighs any possible in-situ oxidation of the molten Al/Al alloys. A mechanism was proposed to explain the release of oxygen, confirmed by microstructural observations and oxygen elemental map analysis. This study indicates that neither the laser absorptivity of AlSi12 (58.4%) and AlSi10Mg (56.1%) alloys nor the high oxidation affinity of pure Al adversely affects their processability.

Keywords: Laser powder bed fusion (LPBF); Pure Al, AlSi12, and AlSi10Mg alloys; laser absorptivity; Oxygen content/Oxide nature; In-process oxide evaporation.

3.1 Introduction

Additive manufacturing (AM) is an exceptional manufacturing route in which industrial parts with complex geometries and intricate features can be easily produced in a single processing step without the need for expensive assemblies [1-4]. For instance, the laser powder bed fusion (LPBF) process, as one of the most promising AM techniques, has enabled the production of lattice structures [5, 6], which were not feasible to be produced before the emergence of AM. In other words, AM has changed the design concept from design-for-manufacturing to design-for-performance [7]. Breakthrough in the AM has been applied not only to generate new designs but also to redesign the existing industrial and engineering components. In recent years, topology optimization [8] and generative design [9] methods have been implemented to produce light and/or highly efficient dies and molds [10], biomaterial scaffolds [11], and aircraft brackets [12], while maintaining their overall initial size to meet the service requirements. In addition, the successful fabrication of heat exchangers and heat sinks with lattice structures [13], cooling channels [14], and pins/fins with functionally graded geometries [15] has significantly enhanced their cooling efficiency.

In many of the abovementioned applications in the automotive, aerospace, and heat exchanger industries, aluminum (Al) and Al alloys are believed to be potential candidates owing to their high specific mechanical strength and thermal/electrical conductivity [16, 17]. Given the fact that the manufacturing process directly influences the microstructure and hence the properties of the parts, microstructural characterization of the additively manufactured Al and Al alloys is essential prior to their reliable application. For Al and its alloys, their incredibly high oxidation tendency and relatively low laser absorptivity have been claimed to be the main obstacles to achieving sound oxide-free parts using the LPBF

process [16, 18]. Figure 3.1(a) shows the overview of the LPBF process in which a laser beam is directed onto the powder bed in specific regions to fuse the powder track-by-track and layer-by-layer [19]. In the case of Al/Al alloys, Louvis et al. [16] proposed that the consolidation of a track is accompanied by the formation of oxide layers since being highly prone to oxidation (Figure 3.1(b)). Given the fact that certain amounts of inter-track and inter-layer overlaps are required to ensure obtaining defect-free parts, the in-situ developed oxide layers on a track must break down during the printing of the subsequent tracks and layers (Figure 3.1(c)). Even if the oxide film's breakdown happens successfully during the LPBF process, the disrupted oxide inclusions will be trapped within the consolidated material. Therefore, the LPBF-processed Al/Al alloys should have higher oxygen concentrations and more oxide inclusions than their cast or wrought counterparts, originating from the stepwise nature of this manufacturing technique. If this is the case, parts with inferior mechanical and thermal properties are expected to be obtained. However, based on the numerous research studies conducted on mechanical properties [7, 20-22] and a few articles on thermal properties [23, 24] of the LPBF-processed Al/Al alloys, the former is superior (up to 40% improvement in yield and tensile strength for AlSi10Mg and up to 400 and 200% improvement in the corresponding values for AlSi12 alloy), and the latter is almost equal to that of the conventionally manufactured parts after heat treatment.

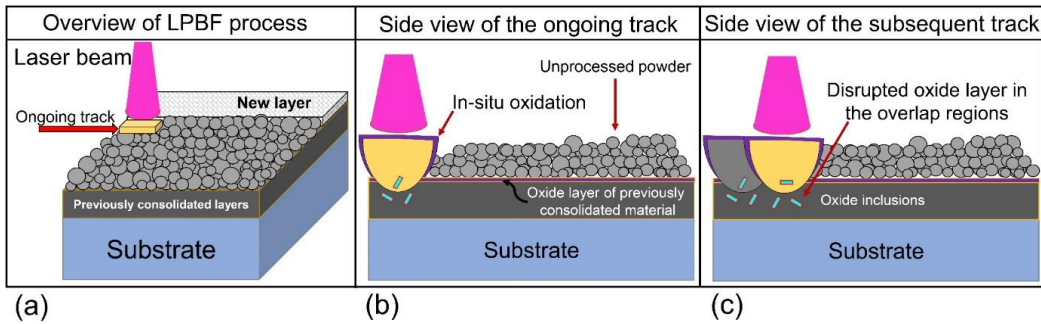


Figure 3.1. Schematic illustration of (a) LPBF process, (b) in-situ oxidation of aluminum/aluminum alloys during the formation of each track, and (c) breakdown of the oxides of the previous layer during the consolidation of the subsequent layer in the overlap regions. By deep etching of the printed samples, Louvis et al. [16] observed a continuous oxide film between the laser scan tracks and concluded that the inter-track oxides do not break during the printing of the subsequent tracks.

The Al/Al alloy oxidation investigation has not been renewed since 2010, when the abovementioned mechanism was proposed [16]. The current generation systems have two main differences with the old ones, which noticeably change the oxidation condition: (i) the output laser powers are increased from 50 W [16] (old systems) up to 1 kW [25], and (ii) the allowable oxygen content of the processing chamber during the printing of Al/Al alloys is reduced (from about 0.2 to less than 0.1 wt%). At relatively low laser powers, employment of relatively slow scan speeds was inevitable to produce dense parts. However, the possibility of applying relatively high laser powers in the new systems is accompanied by noticeably shorter scanning time [25], and therefore, the lower chance of in-situ oxidation. Moreover, it is expected that the lower oxygen content in the building chamber mitigates the oxidation reaction during the printing process. Therefore, it is essential to determine whether or not the in-situ oxidation of Al/Al alloys during the LPBF process is a serious issue under the processing condition of the current generation systems. It should be mentioned that for most of the materials, the optimization of process parameters has been done based on the densification level, surface roughness, and/or

mechanical properties [26-29]. However, for materials prone to oxidation (i.e., Al/Al alloys), the samples also need to be optimized in terms of the oxygen/oxide content. It is especially crucial for applications where fatigue [30] or thermal/electrical properties of the Al/Al alloys [31] are of interest. However, this vacancy in the literature has not been filled so far to the best of the author's knowledge.

In many of the research studies that targeted the challenges during the LPBF processing of Al and Al alloys, the in-situ oxidation of the molten material during this layer-wise manufacturing process has been acknowledged. Some examples of these studies can be found in [16-18, 30, 32]. They have referred to the work conducted by Louvis et al. [16], which was published at the early stages of the LPBF process, or cited articles that were published before the emergence of the LPBF process. On the other hand, owing to the complicated physics of the LPBF process with non-equilibrium melting and solidification nature, oxidation of melt pool has hitherto received only scant attention within the literature. This study calls into question the previously proposed mechanisms and proves that the level of the pre-existing oxygen in the starting powder can significantly decrease during the LPBF processing of Al/Al alloys under specific conditions. As will be discussed, neglecting the oxygen originating from the oxide layer of the starting powder has led to misleading conclusions in the literature. It should be borne in mind that the level of oxygen release is highly sensitive to the manufacturing process parameters. Nevertheless, any evolution related to the oxides in Al alloys is preeminently influenced by the chemistry of the alloy. The addition of alloying elements to Al can alter the nature of the oxide compounds and, therefore, their formation kinetics (i.e., the thickness of the oxide layer in the starting powder), evaporation temperature, and breakdown tendency; in a word, processability.

This study investigates the role of alloying elements (i.e., silicon (Si) and magnesium (Mg)) as well as the process parameters on the processability of Al. For this purpose, pure Al, binary Al-Si (AlSi12 alloy), and ternary Al-Si-Mg (AlSi10Mg alloy) were fabricated in a wide range of process parameters both in bulk and single track forms. Different contributing factors, namely, laser absorptivity of the powder, oxidation affinity, and powder characteristics, were thoroughly examined to justify the densification level and the processing window of the fabricated parts. The oxide compounds existing on the surface of the starting powders were characterized via Auger electron spectroscopy. The oxygen level was measured both in the starting powders and the final printed parts to understand whether or not in-situ oxidation occurs during the process. A mechanism governing the oxide diminishment during the LPBF process was proposed. By simultaneous consideration of the abovementioned contributing factors, the processability of pure Al, AlSi12, and AlSi10Mg was justified in detail, and the influence of Si and Mg alloying elements were scrutinized. Implications of the findings in this study are also essential for other Al alloys and materials with high oxidation affinity.

3.2 Materials and Experimental Procedure

EOSM280 and EOSM290 LPBF machines were utilized to build samples made of Al alloys (AlSi12 and AlSi10Mg) and pure Al, respectively. Both machines use a 400 W Yb-fiber laser with a nominal beam diameter of 100 μm and a nominal beam wavelength of 1070 nm. The nominal chemical composition of the powders is provided in Table 3.1. The AlSi12 and AlSi10Mg powders were supplied by LPW Technology Ltd. (a subsidiary of Carpenter Technology Corporation), and pure Al powder was provided by American Elements. All of the powders were manufactured by the gas atomization process. Three sets of samples were built for each material, with 36 cubic coupons per set corresponding

to 4 different laser powers and at each power, 9 different scan speeds. The other process parameters such as hatch spacing and nominal powder layer thickness (Platform displacement) were kept constant. The individual process parameters are shown in Table 3.2. Two subsets were replicas with dimensions of $10 \times 10 \times 10 \text{ mm}^3$ and one subset having samples dimensions of $10 \times 10 \times 4.2 \text{ mm}^3$. The shorter coupons had six single tracks printed on their top surface using the same process parameters. These single tracks were used to measure the melt pool dimensions. The employed process parameters spanned volumetric energy densities from 33.33 to 308.33 J/mm^3 . A stripe hatch pattern was used for in-layer exposure, while a 67° rotation was employed between subsequent layers. The build plate was preheated to 180°C to reduce residual stresses, and the build chamber was filled with argon gas to reduce the oxygen content to less than 0.1%.

Table 3.1. The nominal chemical composition of pure Al, AlSi12, and AlSi10Mg powders.

Powder	Elements [wt%]					
	Al	Si	Mg	Fe	Cu	Others
Pure Al	Bal.	-	-	-	-	1
AlSi12	Bal.	11-13	0.1	0.25	0.3	0.34
AlSi10Mg	Bal.	9-11	0.25-0.45	0.25	0.05	0.44

The apparent packing density of powders was measured using the Hall method. The optical absorption of powders was measured using the diffuse reflectance spectroscopy (DRS) technique as thoroughly explained in [33]. To determine the nature of the oxides existing in each powder system, Auger electron spectroscopy (AES) was utilized. Auger electron spectra in this study were acquired at 10 keV and $30 \text{ n}\text{\AA}$ with a JEOL JAMP-9500F Field Emission Auger Microprobe. The spectra were acquired from each powder particle using a slightly defocused beam and processed using the JEOL Spectra Investigator software.

The composition was determined by deconvolution of the acquired Auger spectra by curve fitting standard reference spectra of Al, Al₂O₃, Si, SiO₂, Mg, and MgO (Figure 3.2(a)).

Table 3.2. Process parameters used for the fabrication of test coupons.

<i>Laser power, P</i> [W]	<i>Scan speed, v</i> [mm/s]	<i>Hatch spacing, h</i> [mm]	<i>Nominal powder layer thickness, t</i> [mm]
200, 250, 300, 370	400, 600, 800, 1000, 1200, 1400, 1600, 1800, 2000	0.1	0.03

The density of LPBF-fabricated cubic samples was measured using the Archimedes method in accordance with the ASTM B296-17 standard. The theoretical bulk density was selected to be 2.7 g/cm³ for pure Al and 2.67 g/cm³ for both AlSi10Mg and AlSi12 alloys. For pure Al samples, the ImageJ software was also utilized to calculate the area fraction (volume fraction) of the porosities in the printed samples. For this purpose, 12 optical micrographs with a magnification of 50X and a field of view of 1.75×1.25 mm² were used. The reported relative densities (100 - Vol% porosities) achieved by the image analysis are the average of 12 distinct measurements. The top surface of the LPBF-fabricated parts was characterized using a Vega Tescan scanning electron microscope (SEM) equipped with energy-dispersive X-ray spectroscopy (EDS) analysis. The chemical composition of the top surface was also analyzed using EDS in the elemental mapping mode. To reveal the microstructures, the AlSi10Mg and AlSi12 samples were etched chemically using Keller's Reagent. For pure Al, a reagent containing 5 mL HNO₃, 5 mL HCl, 5 mL HF, and 95 mL distilled water was used to etch the samples chemically. The etched cross-sections of the laser scan tracks were observed by means of a Keyence (Osaka, Japan) VHX digital optical microscope as well as a Nikon LV100 optical microscope. The dimensions of the tracks were measured by analyzing the optical micrographs taken from the single tracks of each sample using the ImageJ software (Figure 3.2(b,c)). The reported dimensions are the

average of at least six distinct measurements. The depth of the melt pool is defined as the distance between the surface of the part and the root of the scan tracks. In other words, any section rise above the part surface is not considered in the depth measurements. It is worth noting that in some of the laser scan tracks, a depression with respect to the part surface (rather than a rise) was observed. In these cases, the distance between the highest point of the track and the root was defined as the track depth.

The oxygen/hydrogen (O/H) content of the powders and the fabricated samples was measured using an Instrumental Gas Analyzer (IGA). The equipment used for analyzing O and H were EMGA-920 and EMGA-921, respectively (HORIBA, Ltd., HORIBA Techno Service Co.,Ltd. HORIBA Advanced Technology Center, Japan). The oxygen content in this technique is measured as carbon monoxide and carbon dioxide by a non-dispersive infrared detector. The hydrogen is extracted as Hydrogen gas (H_2), and its concentration in the specimen is determined by a thermal conductivity detector. The reported O/H concentrations for each powder or printed sample represents the average of two distinct measurements. Before the test, specimens were heated to 150 °C for 30 minutes. All samples were then ultrasonically cleaned in acetone and petroleum benzine.

A Java-based materials properties program (JMatPro software) was used to calculate the properties and behaviors of the Al/Al alloys, such as the density of pure Al and AlSi12 alloy as a function of temperature by utilizing the "Aluminum Alloy" database. The derivative of the density with respect to the temperature has been calculated between the melting point and 973 K using data acquired from JMatPro Software. In all of the simulations, the chemical compositions provided in Table 3.1 were defined for the JMatPro software by excluding the elements that exist in trace amounts and elements referred to as "others". For elements with a range of concentration, the average values were used.

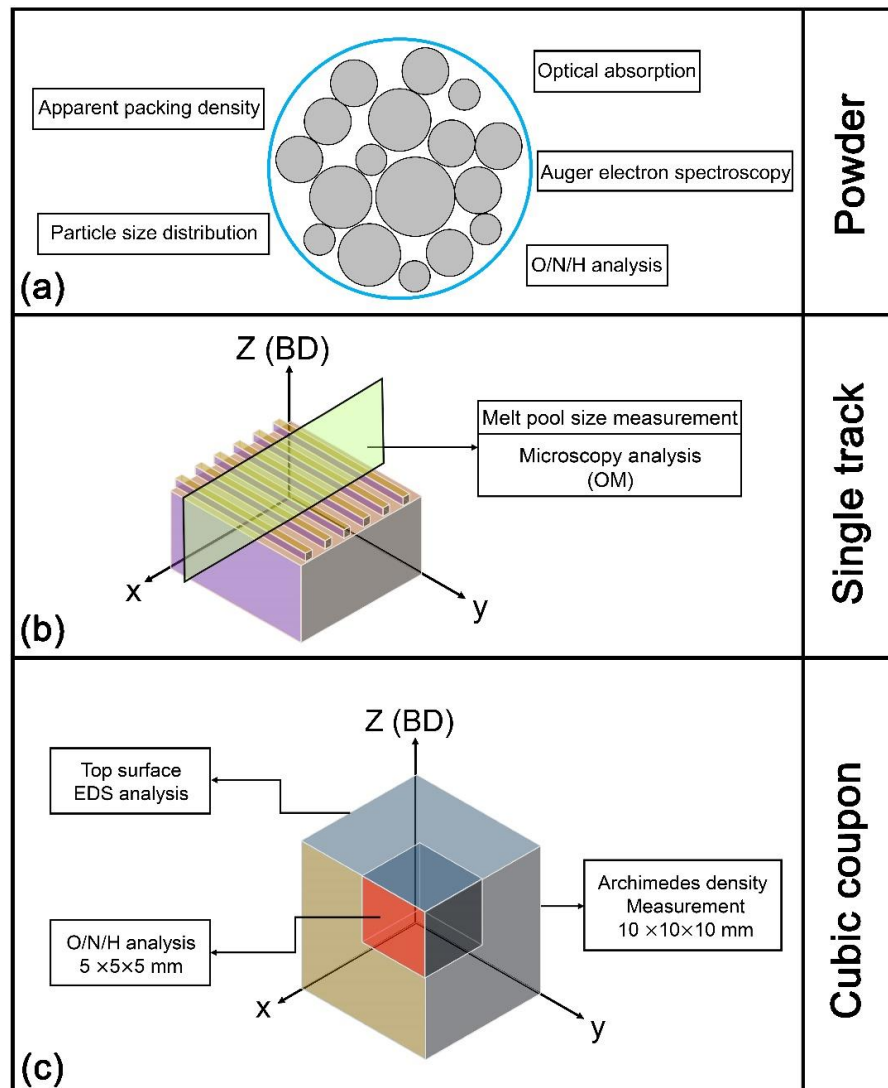


Figure 3.2. The schematic view listing the analysis performed on: (a) powder, (b) single tracks, and (c) cubic coupons.

3.3 Results and Discussion

3.3.1 Processability of Al/Al alloys

The processability of pure Al and Al alloys was studied in a wide range of process parameters through relative density-volumetric energy density ($E_v = P / vht$) plots provided in Figure 3.3. It should be noted that these plots fail to reveal the role of powder

attributes and physical properties in the processability of different materials since the utilized E_v only considers the effect of process parameters. In section 3.3.2, another volumetric energy density equation is used in which not only the process parameters but also the powder attributes (effective powder layer thickness) and laser absorptivity are taken into account.

Figure 3.3(a) shows the relative density versus E_v for pure Al samples. Generally speaking, the densification level first increases with heat input up to the $E_v \sim 50-70 \text{ J/mm}^3$, where the maximum relative density is achieved (99.5%), then decreases slightly up to the $E_v \sim 100 \text{ J/mm}^3$ (98% < relative density < 99.5%), and finally levels off when higher E_v is applied (97% < relative density < 98%). The only exceptions to this general trend are the samples processed by $P = 200 \text{ W}$ at E_v levels higher than 50 J/mm^3 , in which large irregular porosities and delamination decreased the density significantly (Figure 3.3(b, c)). It is worth noting that such delaminations were detected in almost all samples of $P = 200 \text{ W}$ family, regardless of the employed v (dotted oval in Figure 3.3(a)). Samples with relative densities in the range of 97 to 98% featured large/small irregular pores even at extremely high E_v levels (no spherical pores were observed). Samples with relative densities higher than 98.5% are referred to as the highly-dense samples (dashed oval). Almost defect-free samples with relative densities higher than 99% are highlighted as zone (1) in this region. It is self-evident that high P should be exploited in LPBF processing of pure Al to fabricate

almost defect-free parts. Only three pure Al samples with relative densities higher than 99%¹ could be obtained at $P = 370$ W and $v = 1600 - 2000$ mm/s (Figure 3.3(d)).

According to Figure 3.3(e, i), the addition of Si or Si + Mg could significantly change the processability of Al. The relative density of the fabricated AlSi12 and AlSi10Mg samples first shows an ascending trend with increasing E_v up to 50 J/mm³. Then, it reaches a steady-state region in the range of $\sim 50-100$ J/mm³, where a considerable number of highly dense samples (relative density $> 98.5\%$ shown in dashed oval) are achieved. Finally, it follows a sharp decrease by a further increase in the E_v . Despite the pure Al, lower P ($250 - 370$ W) can also lead to the almost defect-free AlSi12 (Figure 3.3(g)) and AlSi10Mg (Figure 3.3(k)) parts (zone (1)). No delamination was observed in samples subjected to the P of 200 W. In the group of samples designated by dotted oval and dash-dotted oval in Figure 3.3(e, i), large irregular (Figure 3.3(f) for AlSi12 and Figure 3.3(j) for AlSi10Mg) and large spherical pores (Figure 3.3(h) for AlSi12, and Figure 3.3(l) for AlSi10Mg) were identified, respectively. While the low E_v causes the former, excessive E_v is the reason behind the latter.

Figure 3.3(m) compares the overall processability of pure Al, AlSi12, and AlSi10Mg samples by depicting the range of E_v in which almost defect-free samples with relative densities higher than 99% were obtained. It is crystal clear that the addition of Si and Mg could noticeably enhance the processing window of Al, the reason behind which is

¹ Based on the 2D image analysis of the non-etched cross-section of the pure Al samples, some of the samples processed at $P = 300$ W also had relative densities higher than 99%.

discussed in detail in the following sections. The Al alloys can benefit from such improved processability in several ways. It is indisputable that complex and various physical phenomena are involved in the LPBF process, and the formation/reshaping of the molten material is a dynamic process [34]. Therefore, the top surface of each consolidated track/layer shows a stochastic nature [35], resulting in the formation of peaks and valleys on the surface (surface roughness). The surface roughness and the powder segregation during the powder spreading cause non-uniformities in the powder layer deposited on each consolidated substrate, making the powder layer thickness and thus the actual heat input location-dependent. When the processing window is narrow (i.e., pure Al), there is a high chance for the formation of isolated defects in random locations due to the minor changes in the actual heat input, even if the optimum set of process parameters is employed. The contrary is the case for AlSi12 and AlSi10Mg alloys with a wide processing window. Besides, the solidification mode and cooling rate are dictated by process parameters during the LPBF processing of a specific material. Being processable in a wide range of E_v (50-100 J/mm³ for AlSi12 and AlSi10Mg alloys) enables fine-tuning of the microstructure or implementation of various process parameters for the printing of different layers (without being worried about the formation of defects) by using a suitable controller to end up with components having functionally graded microstructures [36] and/or heterogeneous grain structures benefiting from multiple strengthening mechanisms [37].

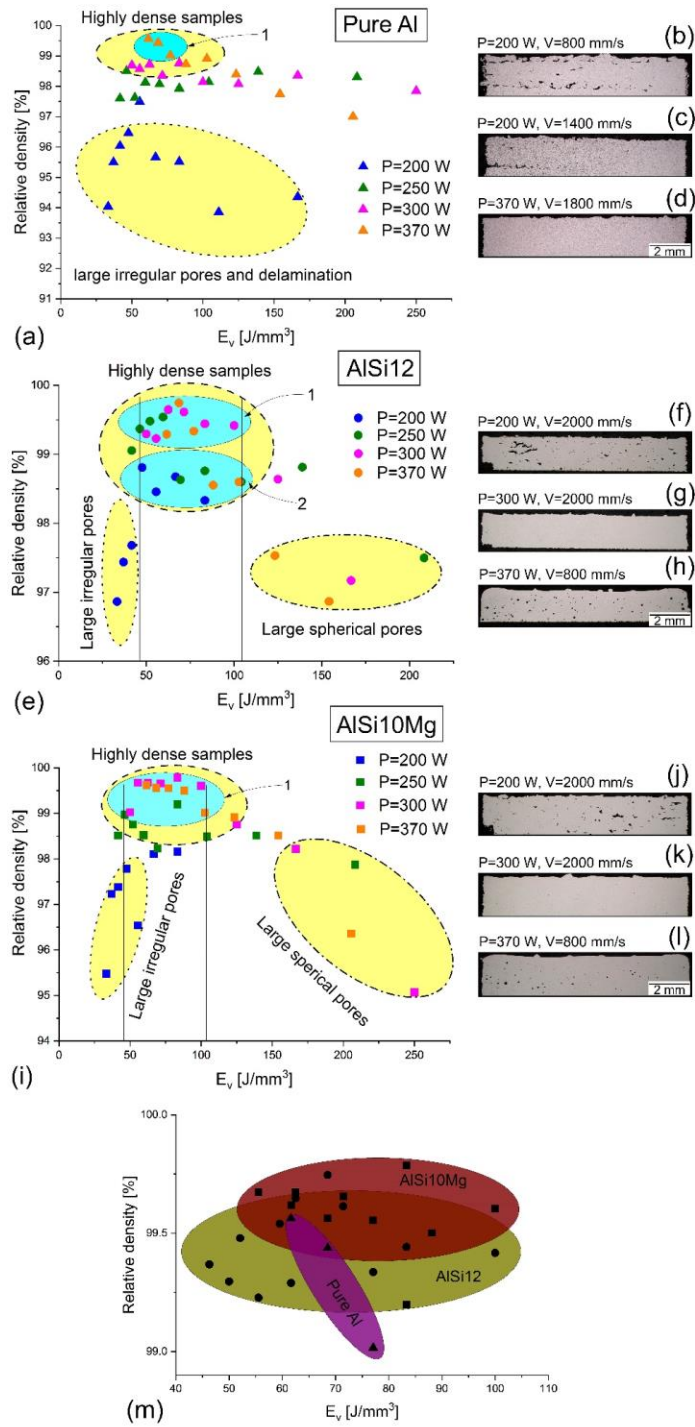


Figure 3.3. Relative density versus E_v of the LPBF-processed: (a) Pure Al, (e) AISi12, and (i) AISi10Mg. The density results are the average of two distinct measurements. The standard deviation from the average values was in the range of 0.04-0.98 for pure Al (a), 0.03-0.48 for AISi12 (e), and

0.03-0.56 for AlSi10Mg (i). The zones designated in (a), (e), and (i) by the ovals with the dotted, dashed, and dash-dotted outlines represent the samples with large irregular pores (and delamination in (a)), highly-dense samples (with a relative density higher than 98.5%), and samples with large spherical pores, respectively. The region named as (1) in (a), (e), and (i) shows the samples having relative densities higher than 99%. The region named as (2) in (e) refers to the samples with relative densities between 98.5 and 99%. The optical micrographs in (b-d) show examples of pure Al samples with large irregular pores, delamination, and almost no defects (zone (1)), respectively. The optical micrographs in (f-h) show examples of AlSi12 samples with large irregular pores, almost no defects, and large spherical pores, respectively. The optical micrographs in (j-i) show examples of AlSi10Mg samples with large irregular pores, almost no defects, and large spherical pores, respectively. The process window for each material leading to relative densities higher than 99% is shown in (m).

The reasons behind the significantly enhanced processability of Al alloys caused by the addition of Si and Si + Mg were assessed from different viewpoints, including (i) powder-laser interactions, (ii) powder bed packing density, (iii) powder and sample oxygen content, and (iv) nature and estimated thickness of the oxide compounds existing on the surface of powder particles. In the following, each factor is thoroughly discussed for pure Al, AlSi12 and AlSi10Mg. By considering these contributing factors simultaneously, the processability and densification level of the fabricated parts are explained in detail in the following sections.

3.3.2 Influence of Powder attributes and laser absorptivity on the processability

Figure 3.4(a) shows the particle size distribution and the SEM micrographs of the pure Al, AlSi12, and AlSi10Mg powders used in this study as the starting material. The SEM micrographs reveal that the morphology of particles is almost identical in all cases (all powders are gas atomized). While most of the powder particles are nearly spherical, semi-spherical, and irregular-shaped particles were also occasionally observed in the powder

systems. According to the particle size distribution analysis results, all powders featured almost the same d_{90} (62.4, 62.3, and 66.5 μm for pure Al, AlSi12, and AlSi10Mg, respectively), though the d_{50} and d_{10} of the pure Al powder ($d_{50} = 34.9 \mu\text{m}$ and $d_{10}=18.3 \mu\text{m}$) were slightly lower than those of the AlSi12 ($d_{50} = 38.8 \mu\text{m}$ and $d_{10}=23.9 \mu\text{m}$) and AlSi10Mg ($d_{50} = 40.0 \mu\text{m}$ and $d_{10}=23.7 \mu\text{m}$) alloys. According to the optical absorption measurement results shown in Figure 3.4(b), regardless of the tested wavelength, the optical absorption of Al alloy powders is significantly higher than that of pure Al. Having almost the same powder morphology, the observed differences in the optical absorption are mainly referable to their chemistry and powder particle size. At the wavelength of 1070 nm, which is the wavelength of the laser used in this study, the optical absorption of pure Al, AlSi12, and AlSi10Mg is 38.6, 58.4, and 56.1%, respectively, meaning that the addition of Si and Si + Mg to the Al significantly enhanced its optical absorption. It is worth noting that although pure Al powder had finer powder particles compared to the Al alloys, which act to enhance the optical absorption of the powder system, the influence of the chemistry on the optical absorption was dominant. This is consistent with the results reported in [33], where the optical absorption of fine ($d_{50} = 9 \mu\text{m}$) and coarse ($d_{50} = 40 \mu\text{m}$) AlSi10Mg powders were found to be almost equal.

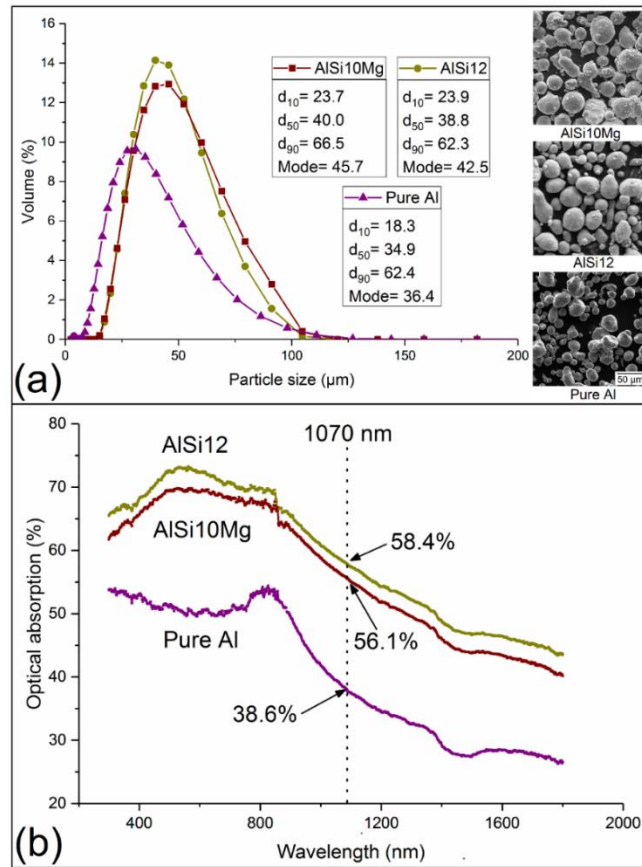


Figure 3.4. (a) Particle size distribution and SEM micrographs, and (b) optical absorption versus wavelength of the pure Al, AlSi12, and AlSi10Mg powders.

The apparent packing density of the powders was measured by means of the Hall flow method. As confirmed in [38], in the size range of the powder used in this study, the apparent packing density is almost equal to the powder bed packing density, which was measured on a single powder layer with the thickness of 100 μm using the computed tomography (CT) technique. Therefore, the powder bed packing density can be reasonably estimated by measuring the apparent density by the Hall flow method. As listed in Table 3.3, both Al alloy powders possessed higher packing densities (1.27 and 1.29 g/cm^3 for AlSi12 and AlSi10Mg, respectively) than that of the pure Al (1.17 g/cm^3). The relative powder packing densities are also provided in Table 3.3. Due to the presence of interstices

in the powder bed, the melting of powder particles and the subsequent consolidation of the molten material during the LPBF process is accompanied by a contraction, creating a gap between the tip of the recoater and the top of the consolidated layer. This gap will be filled during the deposition of the next powder layer, leading to the deviation in the powder layer thickness from its nominal value (30 μm in this study). The increase in the powder layer thickness continues during the printing of several layers until the powder layer thickness approaches a constant value known as the effective powder layer thickness (t_{eff} in μm) [39]:

$$t_{eff} = \frac{t}{\rho} \quad \text{Eq. 1}$$

in which t is the nominal powder layer thickness [μm] and ρ is the relative powder packing density. Using Eq. 1 and the data provided in Table 3.3, t_{eff} was calculated to be 70 and 62 μm for pure Al and Al alloys, respectively. By taking the powder bed packing density and laser absorptivity (Figure 3.4(b)) into consideration, a modified volumetric energy density equation has been proposed as follows [33, 40]:

$$e_v = \frac{AP}{vht_{eff}} = \frac{\rho AP}{vht} = (\rho A)E_v \quad \text{Eq. 2}$$

where A signifies the laser absorptivity of the powder. Implementation of Eq. 2 to calculate the heat input for a specific material would only shift the values obtained by E_v to lower values. However, when comparing the heat input of different materials in a fixed set of process parameters, the E_v would be misleading. According to Eq. 2, the actual heat input in pure Al and Al alloys is $0.17E_v$ and $0.28E_v$, respectively. Under printing

conditions with a fixed set of process parameters, the heat input in pure Al would be \approx 65% lower than that of the AlSi12 and AlSi10Mg alloys. That is why as opposed to the pure Al, which required P levels higher than 300 W to end up with highly-dense parts, lower P (250 W) could lead to the almost defect-free AlSi12 and AlSi10Mg components (Figure 3.3). Therefore, it can be concluded that the addition of Si and Si + Mg to the Al significantly improves the processability by enhancing the laser absorptivity. Although the literature assumes the relatively low laser absorptivity of AlSi12 and AlSi10Mg alloys as one of the main contributing factors behind needing relatively high P for their LPBF processing [18], the optical absorption measurements in this study clearly revealed that their absorption is relatively high and comparable to that of other materials such as H13 tool steel [40], and Ti-6Al-4V [41]. For pure Al, on the other hand, the relatively low laser absorptivity plays a significant role in its inferior consolidation kinetics.

Table 3.3. The apparent packing density of the powders measured by the Hall flowmeter funnel.

Powder	Apparent Packing Density [g/cm ³]	Relative powder packing density
	Hall Funnel	
Pure Al	1.17±0.00	\approx 0.43
AlSi10Mg	1.29±0.00	\approx 0.48
AlSi12	1.27±0.02	\approx 0.48

It should be highlighted here that the absorptivity of not only the powder but also the consolidated material is of utmost importance during the LPBF process [42] since reasonable inter-track and inter-layer overlaps are required in the LPBF-processed parts to ensure high densification levels. Therefore, a portion of the laser beam is in direct contact with the previously consolidated material in the overlap region where not the power, but the bulk is present. Bramson et al. [43] proposed an empirical equation correlating the laser

absorptivity of the bulk material (n_s) to the wavelength of the laser beam (λ) and electrical resistivity of the material (μ):

$$n_s = 0.365\sqrt{\frac{\mu}{\lambda}} - 0.0667\left(\frac{\mu}{\lambda}\right) + 0.006\sqrt{\left(\frac{\mu}{\lambda}\right)^3} \quad \text{Eq. 3}$$

By substituting $\lambda=1070$ nm and μ of 2.85, 4.32, and 4.26 $\mu\Omega\cdot\text{cm}$ into the above equation [44, 45], n_s of 5.8% for pure Al, and 7% for AlSi12, and AlSi10Mg alloys would be obtained. The laser absorptivity of the bulk Al alloys is also considerably higher than pure Al ($\approx 20\%$ higher) but not as significant as the case of powder ($\approx 50\%$ higher). Based on the calculated results, it can be concluded that due to the extremely low bulk laser absorptivity of pure Al and Al alloys, they are noticeably prone to the formation of inter-track and inter-layer defects. Nevertheless, it can be claimed that the formation probability of such defects in pure Al is more pronounced. It should also be underlined that the μ values used in Eq. 11 to calculate the n_s are for conventionally manufactured pure Al/Al alloys. Silbernagel et al. [46] reported that the μ of the LPBF-processed AlSi10Mg samples is in the range of 7.8 to 9.9 $\mu\Omega\cdot\text{cm}$ (orientation dependent) in the as-built condition. Substituting the current values in Eq. 11 yields n_s of 9.4-10.5%, which is considerably greater (up to 50%) than the n_s calculated by using the data on the conventionally manufactured AlSi10Mg alloy.

3.3.3 Influence of the chemical composition on the oxidation tendency and processability

3.3.3.1 Nature of the oxide compounds in the starting powder

As it is well-known, metal powder particles (i.e., pure Al, AlSi12, and AlSi10Mg) are covered by an ultra-thin oxide layer, developed on the surface of the particles during the atomization process or maintaining in an oxygen-containing atmosphere [47]. The nature of these oxide layers can play a crucial role during the LPBF processing of pure Al and Al alloys by influencing the direction of convective flows within the melt pool, thermo-physical properties of the melt, and the evaporation temperature of the oxides. To investigate the surface chemical composition of pure Al, AlSi12, and AlSi10Mg powders, they were analyzed by Auger electron spectroscopy (the acquired spectra and their derivatives are individually available in the “Supplementary Materials”). Figure 3.5 shows the derivative of the acquired data (intensity) as a function of the binding energy along with the reference spectra of Al, Al₂O₃, Si, SiO₂, Mg, and MgO for the sake of comparison. Quantifications were also made on the derivative of the acquired data, the results of which are summarized in Table 3.4. Al, Si, and Mg concentrations are the combination of their metal and oxide components obtained by curve fitting the references for each acquired peak.

Figure 3.5(a) shows the spectrum of the pure Al powder. The shape of the oxygen peak in the acquired data fit well with oxygen from the Al₂O₃ reference spectrum (Figure 3.5(d) and Figure 3.5(j)). The Al peak shape showed characteristics of both the typical Al metal (Figure 3.5(e) and Figure 3.5(l)) and Al₂O₃ (Figure 3.5(d) Figure 3.5(k)) peak shape. This suggests that the thickness of the oxide layer is less than the depth at which Auger electrons

are collected, which is about 6 nm. There is also the possibility that the atomic scale boundary between the oxide and metal is a bit diffuse rather than perfectly sharp, so there may be an oxygen gradient. In both cases, it is impossible to pinpoint the thickness of the oxide layer based on the point spectra. However, it can be claimed that the identified material is not pure Al_2O_3 oxide in the full 0-6 nm depth since the peak shape is a convolution of Al and Al_2O_3 rather than only shaped like the Al peak of Al_2O_3 . Therefore, one shall not expect to observe a spectrum (Figure 3.5(a)) and chemical composition (Table 3.4) that perfectly fits stoichiometric Al_2O_3 since it contains some amount of pure Al (with no oxygen) as well.

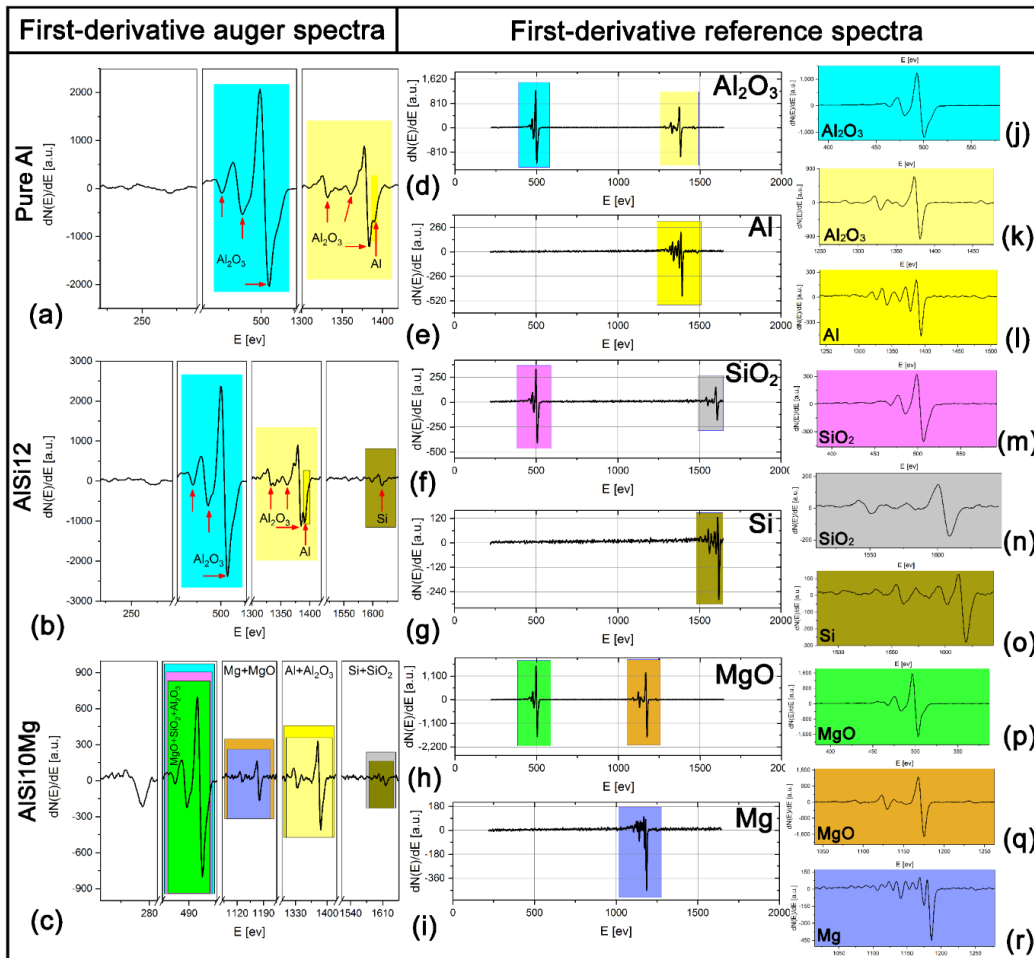


Figure 3.5. The first-derivative Auger spectra for: (a) Pure Al, (b) AlSi12, and (c) AlSi10Mg powders. The reference spectra of Al_2O_3 , Al, SiO_2 , Si, MgO, and Mg, are provided in (d-i), respectively. The higher magnification of the designated colored box in each reference spectrum is shown in (j-r).

Figure 3.5(b) shows the Auger electron spectrum of AlSi12 powder. The particles, in this case, had less Si on the surface than expected. The concentration was very low, so it was difficult to break down Si into metal and SiO_2 (Si^{4+}) peak shape since the differences are subtle. However, the Si reference (Figure 3.5(g) and Figure 3.5(o)) fits the data a little better than Si^{4+} (Figure 3.5(f) and (n)) or a combination of the two, suggesting that the oxide is only/mainly Al_2O_3 , and most of the Si in the data comes from the metal below the

oxide. Similarly, the Al metal fraction of the Al peak was quite high. As a general rule, the thinner the oxide layer, the larger the Al metal contribution to the Al peak, and this applies to Si and Mg as well in other samples. So the sharp Al peak in the spectrum of AlSi12 powder serves as a token of the existence of an oxide layer, thinner than that of the pure Al sample. The oxygen peak fits very well with just the Al_2O_3 reference (Figure 3.5(d) and Figure 3.5(j)) rather than a mix of Al_2O_3 and SiO_2 (Figure 3.5(f) and Figure 3.5(m)). This is a further indication that, most probably, the Si is not significantly in the oxide.

Figure 3.5(c) shows the spectrum of AlSi10Mg powder. Similar to the AlSi12 sample, the Si peak here in AlSi10Mg tends to resemble Si (Figure 3.5(g) and Figure 3.5(o)) more than Si^{4+} (Figure 3.5(f) and (n)), although it is a small peak, so it is hard to be sure through the noise in the data. The Si peak seemed to fit a little better if SiO_2 was also included in the fitting, but it still mostly resembled Si metal. This might indicate some Si oxide in the oxide layer, but some of the metal below is also being collected, which would have metallic Si. The Mg concentration at the surface is much higher than the bulk metal concentrations, and the peak shape fits almost exclusively as MgO (Figure 3.5(h) and (q)) rather than Mg (Figure 3.5(i) and (r)). According to Table 3.4, the concentration of Mg on the surface of the AlSi10Mg powder was 6 at.%, which is ≈ 10 times greater than the bulk concentration of this element. The oxygen peak for these particles fit best as a combination of all three oxide references, namely, Al_2O_3 , SiO_2 , and MgO. Any other combination of these (trying just one, or any two such as $\text{Al}_2\text{O}_3 + \text{MgO}$) did not fit the peak shape as perfectly as using all three.

Table 3.4. Surface chemical composition of the pure Al, AlSi12, and AlSi10Mg powders

Powder sample/Element	O [at.%]	Al [at.%]	Si [at.%]	Mg [at.%]	Nature of oxide layer
Pure Al	57.6	42.6	-	-	Al ₂ O ₃
AlSi12	49.4	48.2	8.4	-	Al ₂ O ₃
AlSi10Mg	48.5	36.6	8.9	6	Al ₂ O ₃ -MgO-SiO ₂

3.3.3.2 Oxygen content of the initial powders and printed parts

Not merely the nature but also the thickness of the oxide layers is a significantly important contributing factor in the processability of Al and Al alloys since it affects the concentration of oxygen in the final printed part. Figure 3.6 shows the oxygen content of the pure Al, AlSi12, and AlSi10Mg starting powders as well the parts printed with these powders using two different sets of process parameters, corresponding to low density ($P = 200$ W) and highly-dense ($P = 300$ W) samples. These results provide an insight into the initial content of oxygen in the powder, as the main source of oxygen, and the oxide evolutions during the LPBF process. Before anything else, the data give strong evidence that the oxygen in the pure Al powder (2260 ppm) is conspicuously higher than that of the AlSi12 and AlSi10Mg powders. The oxygen content in AlSi12 (1299 ppm) and AlSi10Mg (740 ppm) powders was found to be 42.5 and 67.3% lower than that of the pure Al powder, which is consistent with the higher intensity of the metallic constituents detected in the Auger electron spectra of Al alloys compared to the pure Al powder (Figure 3.5). Simultaneous consideration of the powder oxygen content (Figure 3.6) and the Auger electron spectroscopy findings give evidence that the addition of Si and Mg has significantly changed either the nature of the oxide layers or their formation kinetics. While not changing the nature of the oxide layer (Figure 3.5(b) and Table 3.4), Si in AlSi12 remarkably decreased the oxygen content, and, therefore, the thickness of the oxide layer

in this alloy by obstructing the oxidation of Al. Incorporation of a minor percentage of Mg along with Si to the Al (AlSi10Mg) showed a pronounced influence not only on the oxidation tendency but also on the nature of the oxide layers (Figure 3.5(c) and Table 3.4). It is worth noting that the observed differences between the oxygen content of different powder systems are not merely attributable to the chemistry of them but also to their particle size distribution. Referring to Figure 3.4(a), the pure Al powder had finer particles than the Al alloy powders. This is accompanied by a higher surface area to the volume ratio of the particles in the former, resulting in a greater oxygen content.

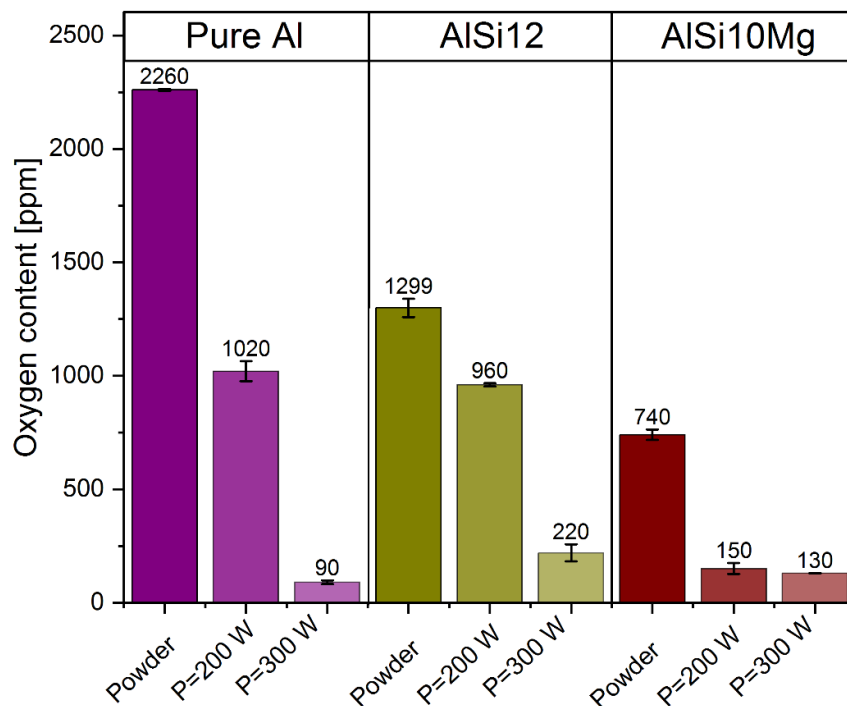


Figure 3.6. The oxygen content (mass ppm) of the starting powders as well as the pure Al, AlSi12, and AlSi10Mg parts fabricated by P=200 W ($v=2000$ mm/s) and P=300 W ($v=1400$ mm/s). The reported O concentrations for each powder or printed sample represent the average of two distinct measurements. Error bars represent the standard deviation from the average values.

By having the oxygen percentage in the powders and knowing the nature of the oxide layers existing on their surface, it is feasible to calculate the average thickness of the oxide layer with reasonable accuracy. Even though the oxide layer thickness calculation is pretty straightforward for pure Al and AlSi12 powders in which the oxide layer is merely Al₂O₃, such a calculation seems to be trickier for AlSi10Mg powder since the combination of Al₂O₃, MgO, and SiO₂ was detected on the powder surface. To render it possible even for the AlSi10Mg case, it was attempted to separate the contribution of oxygen in each oxide based on the deconvolution of the acquired data by curve fitting the references of the pure oxides for the oxygen in the acquired peak. It appeared to have 8.9, 15.9, and 23.7 at.% (from the total of 48.5 at.% shown in Table 3.4) of oxygen from Al₂O₃, MgO, and SiO₂, respectively. By assuming that the oxygen is fully concentrated in the oxide layer on the surface of the powder (the concentration of oxygen in the bulk of powder is assumed to be negligible because the oxygen content of the typical wrought pure Al ingots used to produce the melt for the gas atomization process is around 4 ppm [48]), the thickness of the oxide layers in pure Al (Eq. 4), AlSi12 (Eq. 5), and AlSi10Mg (Eq. 6) powders can be calculated as follows:

$$t_{oxide} = \frac{f_o \rho_{Al} D_{ave} M_{Al_2O_3}}{18 M_o \rho_{Al_2O_3}} \quad \text{Eq. 4}$$

$$t_{oxide} = \frac{f_o \rho_{AlSi12} D_{ave} M_{Al_2O_3}}{18 M_o \rho_{Al_2O_3}} \quad \text{Eq. 5}$$

$$t_{oxide} = \frac{f_o \rho_{AlSi10Mg} D_{ave}}{6 \left[0.18 \left(\frac{3M_o}{M_{Al_2O_3}} \rho_{Al_2O_3} \right) + 0.33 \left(\frac{M_o}{M_{MgO}} \rho_{MgO} \right) + 0.49 \left(\frac{2M_o}{M_{SiO_2}} \rho_{SiO_2} \right) \right]} \quad \text{Eq. 6}$$

In all of the above equations, f_o is the fraction of oxygen detected in each powder (Figure 3.6) and D_{ave} is the average diameter of the powder (the median particle diameter (d_{50}) in Figure 3.4 is used as the average diameter). The M , and ρ represent the molar mass and theoretical density, respectively. Putting some data into the equations, the t_{oxide} in pure Al, AlSi12, and AlSi10Mg is ≈ 19 , 12, and 8.5 nm, respectively, which is in line with the Auger electron spectroscopy findings, where the oxide layers were predicted to be thinner in Al alloys compared to the pure Al case. This shows the significant contribution of alloying elements in reducing the kinetics of oxide layer formation. The calculated t_{oxide} for all of the powders exceeds the depth at which the electrons were collected during the Augers electron spectroscopy analysis (~ 6 nm), suggesting that the oxide layer is not uniform in thickness and/or the boundary at the atomic scale between the oxide and metal is a bit diffuse.

The oxygen content of the printed pure Al, AlSi12, and AlSi10Mg coupons at low and relatively high P are also provided in Figure 3.6. Surprisingly, the oxygen content in the LPBF-processed samples is considerably lower than that of the starting powder, regardless of the employed process parameters and the studied material. Moreover, the oxygen content in samples processed by $P = 300$ W was tremendously lower than that of the $P = 200$ W in pure Al and AlSi12. In AlSi10Mg, the oxygen content of the printed parts was found to be less sensitive to the P level. Kimura et al. [48] have also detected lower oxygen levels in the printed pure Al samples than the starting powder, though the reason behind it has not been discussed. Such a finding leads to a very valuable conclusion that either oxidation does not happen during the LPBF processing of Al and Al alloys or the rate of the oxide diminishment is significantly higher than that of any possible in-situ

oxidation since the oxygen content of the final components is noticeably lower than that of the starting powders. In the following section, a mechanism governing the oxygen release during the LPBF process is proposed. By implementing this mechanism, the results shown in Figure 3.6 are discussed in detail, and the influence of Mg and Si on the processability of Al/Al alloys is elaborated by considering the nature and content of oxide/oxygen.

3.3.3.3 Oxide diminishment mechanism

A mechanism is proposed for the oxide diminishment based on the findings of Cunningham et al. [49] on surface vaporization of the melt pool and Zhao et al. [50] on Marangoni thermocapillary flow directions, which were confirmed through ultrahigh-speed X-ray imaging of the melt pool during the LPBF processing of Ti-6Al-4V alloy and in-situ observation of the laser spot welds (Fe-Cr-Ni alloy) using a high-speed camera, respectively. Based on [49], regardless of the process parameters employed and the corresponding melting mode (conduction or keyhole mode), the evaporation occurs at least on the surface of the melt pool and leaves behind a vapor depression. The latter study proved that the direction of the Marangoni thermocapillary force in the presence of aluminum oxide would not change unless the oxides find enough time to dissolve within the weld pool.

Spallation of the oxide layer- Step 1: During the LPBF process, prior to the melt pool formation, the laser irradiates the powder particles, which can be assumed as pure Al or Al alloy spheres covered by an ultra-thin oxide shell. Olakanmi [32] suggested that the disparity in the coefficient of thermal expansion of the oxide shell (α_{oxide} , $7.4 \times 10^{-6} / K$ for Al_2O_3) and the metal core (α_{core} $27.4 \times 10^{-6} / K$ for pure Al) will generate huge

circumferential stress (σ_c) during the heating stage, which is responsible for the separation and breakdown of the oxide layers:

$$\sigma_c = E \Delta T (\alpha_{core} - \alpha_{oxide}) \quad \text{Eq. 7}$$

in which E signifies Young's modulus of the oxide. Trunov et al. [51] explained the oxide layer's cracking during the heating with a diverse approach to the subject. They proposed that upon heating, the Al_2O_3 layer goes through a series of phase transformations accompanied by volume decrease, promoting the chance of oxide layer fracture. However, both mechanisms fail to address the oxide breakdown during the LPBF process with a non-equilibrium heating nature. The fast heating ($\sim 10^6 \text{ K / s}$) prevents the breakdown of the oxide shell before melting of the metal core [52] on the one hand and the diffusion-controlled phase transformations on the other hand. The fracture of the oxide layer can be explained by considering the pressure build-up within the powder particles as a result of the core melting while the covered oxide layer is still in the solid form [52] (Figure 3.7(a-c)). The solid to liquid phase transformation in pure Al, AlSi12, and AlSi10Mg from solidus to the liquidus temperature is accompanied by a volume change corresponding to 4.9, 3.7, and 3.1 vol.%, respectively. The magnitude of the pressure applied to the oxide shell as a result of this volume strain can be calculated as follows [53]:

$$P_r = B \varepsilon_v \quad \text{Eq. 8}$$

in which P_r , B , and ε_v denote the pressure due to the volume change, bulk modulus, and volume strain, respectively. Assuming the B to be 70 GPa for Al and Al alloys, the P_r exerted to the oxide shell would be 3.7, 2.8, and 2.3 GPa for pure Al, AlSi12, and

AlSi10Mg, respectively. By knowing the P_r , the hoop stress (σ_θ) in the oxide shell is calculated as [54]:

$$\sigma_\theta = \frac{P_r r_{ave}}{2t_{oxide}} \quad \text{Eq. 9}$$

where r_{ave} is the average particle radius. By substituting the calculated t_{oxide} (Eq. 3, Eq. 4, and Eq. 5), and the average particle radius (Figure 3.4), the magnitude of σ_θ would be astronomically high (thousands of GPa) for all powders, meaning that the rapid melting of the metal core is the governing mechanism explaining the fracture and spallation of the oxide layer (Figure 3.7(a-c)). It needs to be noted that the presence of cracks in the oxide shell can significantly reduce the calculated σ_θ by decreasing the chance of liquid pressure build-up within the particle.

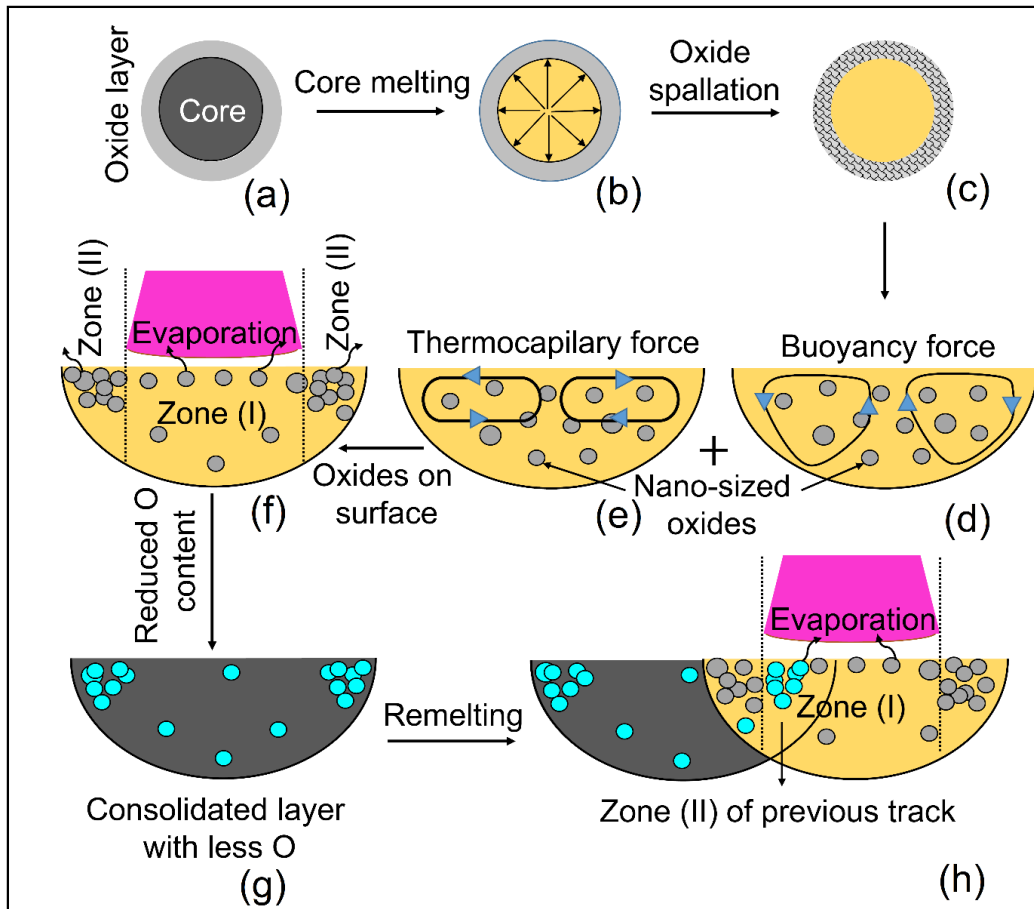


Figure 3.7. The schematic illustration of: (a) Al/Al alloy powder particles having an oxide shell, (b) melting of the core before its separation from the oxide shell caused by the non-equilibrium rapid heating of the powder particles, (c) oxide fracture and spallation through the core melting and pressure build-up mechanism, (d) buoyancy force and (e) Marangoni thermocapillary force in the melt pool causing the nano-sized oxide particles to concentrate on the surface of the melt pool, (f) evaporation of the oxides, especially in zone (I) as a result of their direct interaction with the laser beam, (g) the solidified melt pool and trapped oxides after the laser travels away, and (h) second chance of oxide evaporation during the printing of the subsequent tracks where the oxides in zone (II) of the previous track locate in zone (I) of the new track.

Formation of a melt pool covered by nano-sized oxides- Step 2: As mentioned in the previous section, the laser-powder interaction would create a melt pool from metal powders, which contains solid nano-sized (at least in one dimension) oxides formed due to the severe fracture at the heating stage. The temperature gradient within the melt pool leads

to the formation of surface tension (γ) gradient between the warmer (center of the pool surface) and cooler (edges of the pool) regions. Since the surface tension of the molten Al/Al alloys decreases by increasing the temperature ($d\gamma/dT < 0$), the shear stress induced by the surface tension gradient would result in an outward fluid flow from the center of the surface toward the edges of the melt pool, returning beneath the surface [55] (known as Marangoni thermocapillary fluid flow, Figure 3.7(e)). On the other hand, the temperature gradient also causes density gradients within the melt pool, developing buoyancy forces. Given the fact that the density of molten Al decreases by increasing the temperature ($d\rho/dT < 0$), the heavier Al (cooler region) at the edges moves inward (sink) along the melt pool boundary, and the lighter liquid (warmer region) undergoes an upward movement along the melt pool axis [55] (Figure 3.7(d)). Therefore, it can be concluded that the buoyancy forces facilitate the transfer of solid nano-sized oxides from the bulk of the melt pool toward the surface. Accordingly, the melt pool of Al/Al alloys during the LPBF process is not a bare pure metal/alloy molten phase in which the oxidation can occur, but is a melt pool covered by the solid nano-sized oxides which act as a barrier to the oxidation (Figure 3.7(f)). While it cannot guarantee the lack of melt pool oxidation during the LPBF process, it can definitely reduce the activity and affinity of the melt pool to react with the existing oxygen in the processing chamber. The lower tendency for oxidation plus the short laser-powder interaction time in the order of microseconds significantly reduces the chance of in-situ oxidation.

Evaporation of the nano-sized solid oxide particles- Step 3: Figure 3.8, Figure 3.9, and Figure 3.10 show the width, and depth of the printed single tracks as a function of v at each P for pure Al, AlSi12, and AlSi10Mg, respectively. As it is evident, regardless of the material studied and the process parameter employed, the width of the tracks was found to

be higher than the nominal laser spot diameter (100 μm). Accordingly, it is fair to conclude that the melt pool can be divided into two different zones regarding the laser beam interaction. In zone (I), the melt pools of pure Al and Al alloys with solid nano-sized oxides on their surface directly contact the laser beam. In zone (II), the opposite is the case (Figure 3.7(f)). The solid nano-sized oxides will undergo evaporation in zone (I) due to the direct interaction with a heat source having a high power intensity ($P/A = 2.5\text{-}5 \times 10^{10} \text{ W/m}^2$ in this study). Based on the data available for the oxides of pure Al (Al_2O_3), AlSi12 (Al_2O_3), and AlSi10Mg ($\text{Al}_2\text{O}_3\text{-MgO-SiO}_2$), their melting temperatures are considerably higher than that of the pure Al and Al alloys. Except for the SiO_2 , they all possess a higher boiling temperature as well. Therefore, the evaporation of the oxides in zone (I) might seem impossible at first glance, even after considering their direct interaction with the laser beam. However, the melting-point depression phenomenon caused by the extremely high surface area-to-volume ratio (A/V) of the nanoscale oxide particles can explain the rationale behind their easier evaporation at noticeably lower temperatures during the LPBF process. The melting point of a particle (T_m) can be calculated using the following equation [56]:

$$\frac{T_o - T_m}{T_o} = \frac{A}{\rho_s V \Delta H_m (\gamma_{sv} - \gamma_{lv})} \quad \text{Eq. 10}$$

in which T_o , ρ_s , ΔH_m , γ_{sv} , and γ_{lv} denote the bulk melting temperature, density of the solid material, latent heat of fusion, solid/vapor surface energy, and liquid/vapor surface energy, respectively. In the nano-sized oxides with an extremely high A/V ratio, copious surface atoms with unsaturated bonds (reduced number of cohesive bonds) exist in the particle, reducing the overall thermal energy required to free the atoms from the solid and,

therefore T_m . Joshi et al. [56] studied the T_m of Al_2O_3 films having a thickness in the order of nanoscale and an infinite length (1 μm), which can be the case for the fractured oxide shells during the spallation stage. They reported that the T_m of Al_2O_3 varies in the range of 727 – 2000 °C when the film thickness increases from 1-10 nm ($T_0 = 2072$ °C). The same statement should be valid for the evaporation of nano-sized particles in which their high A/V facilitates their evaporation. Therefore, if P is sufficiently high during the LPBF process, the oxide evaporation can occur in zone (I), decreasing the oxygen concentration in the printed component (Figure 3.6).

The reduction in the oxygen content of the fabricated parts is not merely due to the evaporation of oxides in zone (I) but also zone (II). However, the oxide evaporation takes place on a smaller scale in zone (II) since the maximum temperature experienced by the solid nano-sized oxides is lower than zone (I), in which the oxides are in direct contact with the laser beam (Figure 3.7(f, g)). It should be noted that the nano-sized oxides are accumulated more at the edges of the melt pool surface (zone (II)) than the central region (zone (I)) because of the outward direction of the Marangoni thermocapillary fluid flow (Figure 3.7(d-f)). Thus, conditions enabling the evaporation of oxides in this zone are expected to significantly decrease the overall oxygen of the fabricated part. Although the complete evaporation of the nano-sized oxides in zone (II) is not effectively possible during the printing of an ongoing track, they will undergo evaporation during the printing of the very next track, which has an overlap with it. Simply put, the edges of the previous track (zone (II)) are located in the central region (zone (I)) of the new one, where the oxides effectively evaporate (Figure 3.7(h)). Due to the higher temperature of the melt pool surface, high P provides more favorable conditions for effective evaporation of the oxides.

It should also be borne in mind that during the LPBF process, each consolidated layer might experience repeated remelting, the number of which is dictated by the applied heat input. This provides an opportunity for the evaporation of oxides in the previous layers, which did not find the chance to escape from the melt pool surface. The depth of the laser scan tracks as a function of the v at each P for pure Al, AlSi12, and AlSi10Mg alloys are shown in Figure 3.8, Figure 3.9, and Figure 3.10, respectively. As it is evident, the depth of the melt pool shows an ascending trend with increasing P . At $P = 300$ W, sometimes the depth of the laser scan tracks in AlSi10Mg (the same is valid for pure Al and AlSi12) reached 165 μm . By assuming that the nominal thickness of the consolidated track is 30 μm , such a depth corresponds to five times remelting of any consolidated layer. This factor also plays a major role in reducing the oxygen concentration in the LPBF-processed parts at high P levels.

According to the results provided in Figure 3.6, as well as the abovementioned discussion, it cannot be concluded that the in-situ oxidation of Al/Al alloys does not happen at all during the LPBF process. In other words, the observed decrease in the oxygen content can also be caused by the fact that the level of oxide removal has outweighed any possible in-situ oxidation of the molten Al/Al alloys under the processing condition employed in this study. Nevertheless, it seems that the in-situ oxidation was negligible during the LPBF process of Al/Al alloys based on the oxygen content of the samples printed at the laser power of 300 W and scanning speed of 1400 mm/s. For instance, in the case of pure Al, the oxygen content of the printed sample at such process parameters was 90 ppm, while it was 2260 ppm in the starting powder. Even if it is assumed that all of the oxides in the starting powder (source of oxygen) are evaporated during the LPBF process and the 90 ppm oxygen detected in the printed part is originated from the in-situ oxidation, it can be

concluded that the rate of oxidation was only 4% of the that of the oxide evaporation. It means that the rate of oxidation at high temperatures (high laser power of 300 W) and relatively long interaction time (relatively low scanning speed of 1400 mm/s) is not significant. Then the rate of oxidation at the lower laser power of 200 W and shorter interaction time associated with the faster scan speed of 2000 mm/s should be even less than 4%. The reason behind the detection of higher oxygen content in the samples printed at the laser power of 200 W is not the higher rate of in-situ oxidation but the lower chance of oxide evaporation at lower temperatures and shorter interaction times. This is also valid for the AlSi12 and AlSi10Mg alloys with lower oxidation tendencies than the pure Al.

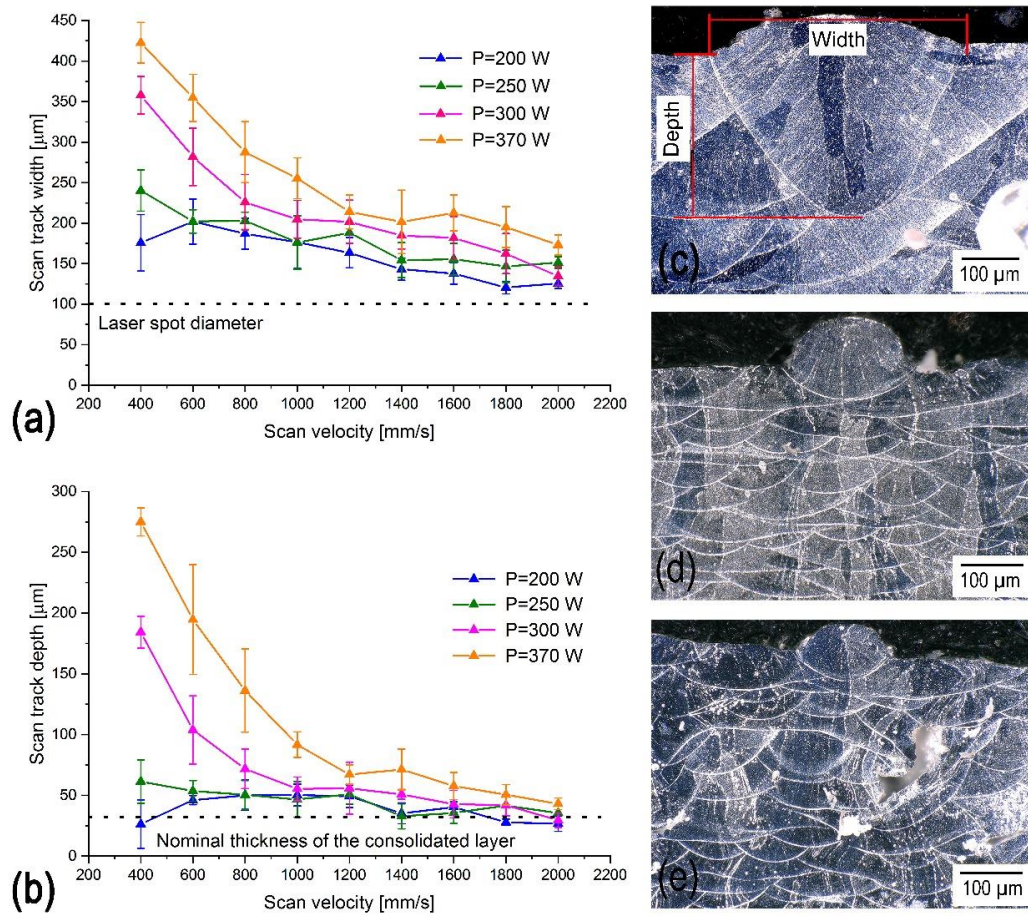


Figure 3.8. The size measurement results of pure Al single tracks: (a) scan track width, and (b) scan track depth as a function of v at different P . The reported values are the average of at least six distinct measurements, and the error bars are the standard deviations from the average values. The cross-sectional view of the tracks processed at high ($P = 370$ W, $v = 400$ mm/s), medium ($P = 370$ W, $v = 1600$ mm/s), and low ($P = 200$ W, $v = 1400$ mm/s) heat inputs are shown in (c-e), respectively.

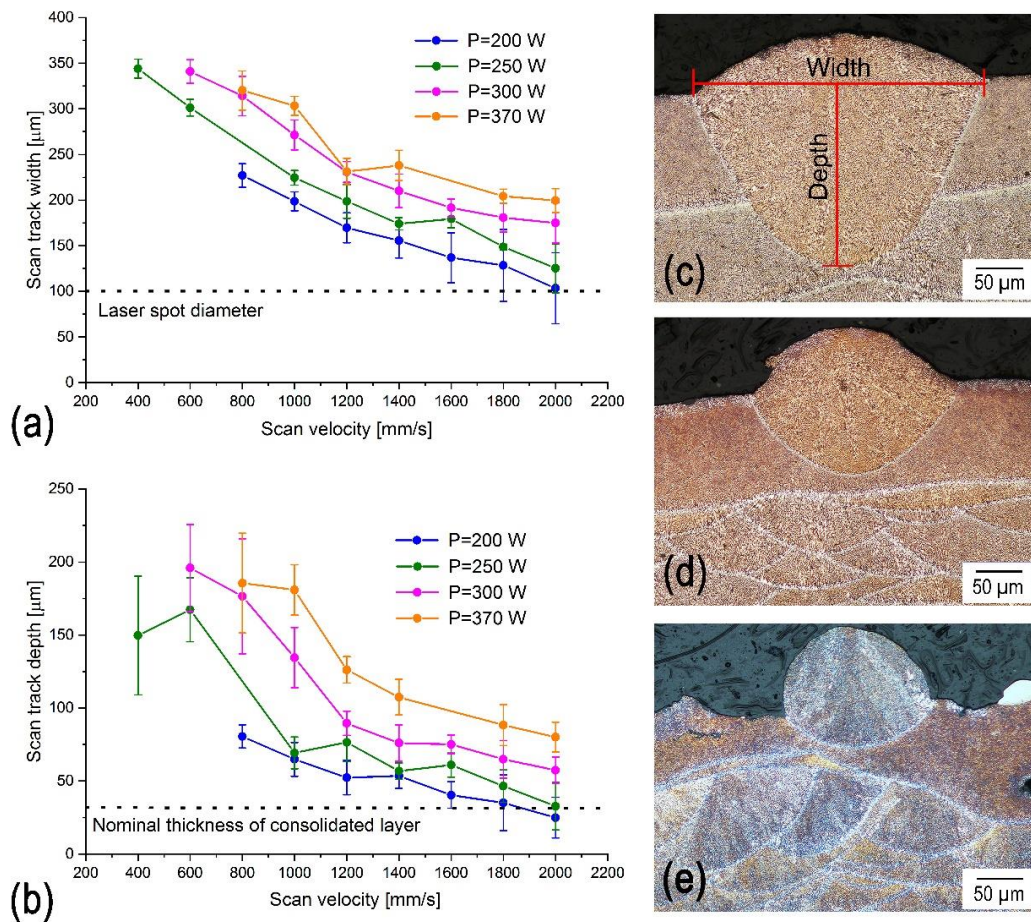


Figure 3.9. The size measurement results of AlSi12 single tracks: (a) scan track width, and (b) scan track depth as a function of v at different P . The reported values are the average of at least six distinct measurements, and the error bars are the standard deviations from the average values. The cross-sectional view of the tracks processed at high ($P=370$ W, $v=800$ mm/s), medium ($P=300$ W, $v=1400$ mm/s), and low ($P=200$ W, $v=1600$ mm/s) heat inputs are shown in (c-e), respectively.

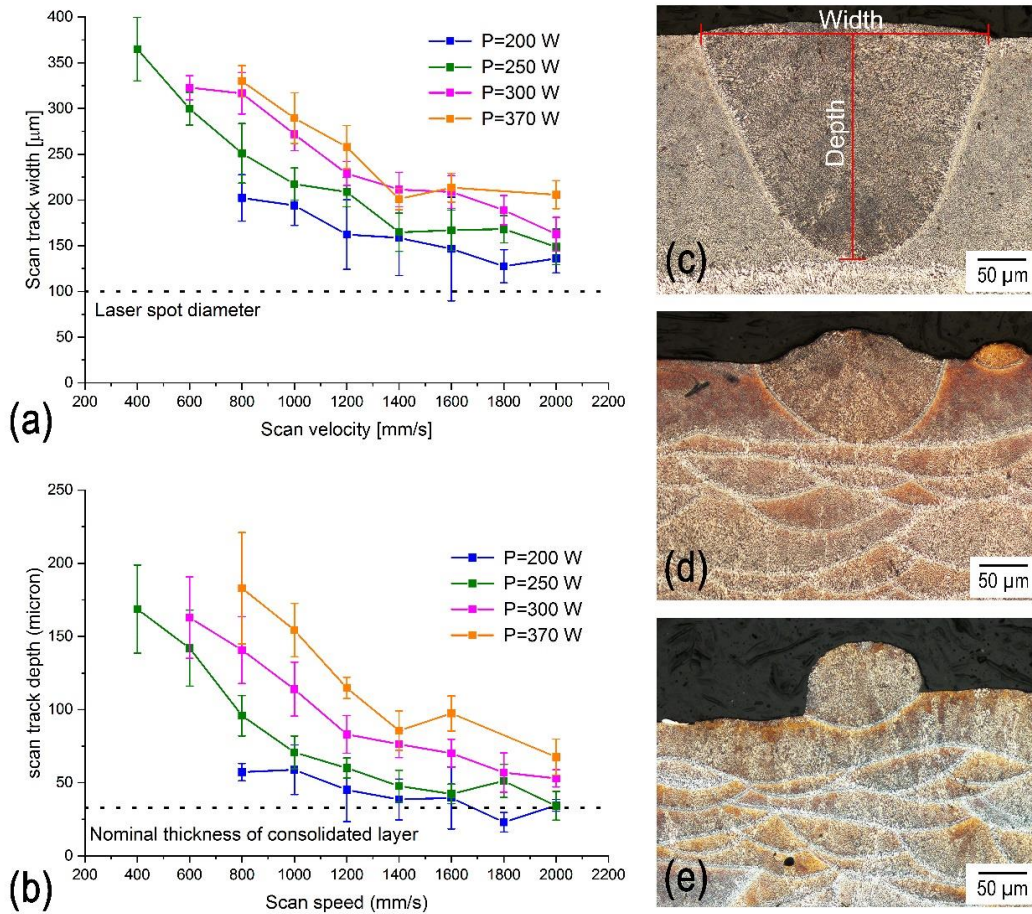


Figure 3.10. The size measurement results of AlSi10Mg single tracks: (a) scan track width, and (b) scan track depth as a function of v at different P . The reported values are the average of at least six distinct measurements, and the error bars are the standard deviations from the average values. The cross-sectional view of the tracks processed at high ($P = 370$ W, $v = 800$ mm/s), medium ($P = 300$ W, $v = 1400$ mm/s), and low ($P = 200$ W, $v = 1800$ mm/s) heat inputs are shown in (c-e), respectively.

3.3.3.4 Verifying the proposed oxide diminishment mechanism through microstructural observations

The proposed mechanism in section 3.3.3.3 was confirmed by the microstructural analysis. Figure 3.11(a-d) shows the top surface SEM micrographs along with the EDS maps showing the oxygen distribution on the top surface of the LPBF-processed pure Al samples

at different P and constant v . As it is evident, the oxygen (of oxides) is mainly concentrated in the inter-track (overlap) regions rather than the center of the laser scan tracks. As explained earlier, this is mainly attributable to the upward and outward fluid flow directions caused by the buoyancy and Marangoni thermocapillary forces, respectively, causing the pile-up of oxides on the surface, especially at the edges of the melt pools. The center of the laser scan tracks and the overlap regions are zone (I) and zone (II), shown in Figure 3.7. At relatively low P of 200 W (Figure 3.11(a)), in addition to zone (II), oxygen was also detected in the zone (I) since the surface temperature of the melt pool was not high enough even for the complete evaporation of oxides in the zone (I), where they are in direct contact with the heat source. However, at P levels exceeding 250 W (Figure 3.11(b-d)), almost no oxide is perceptible in zone (I). In contrast, the amount of oxides in zone (II) is strongly dependent on the employed P . For instance, at P levels of 300 and 370 W, the melt pool surface temperature is considerably high, and the oxides in zone (II) are negligible. It should be noted that the oxides shown in Figure 3.11(a-d) can undergo evaporation during the printing of subsequent layers only for the laser power of 300 W and 370 W, since the depth of laser scan tracks for samples shown in Figure 3.11(a-d) is 35, 36, 50, and 71 μm , respectively. Therefore, not only the population of oxides is significantly low in the as-consolidated layers processed at high P , but also the remaining oxides are given another chance to evaporate.

The same trend as that of the pure Al was also observed for AlSi12 and AlSi10Mg alloys, the only difference being that the oxygen was not mainly concentrated in the edges of the laser scan tracks. The top surface SEM micrographs and oxygen EDS maps of one of the AlSi12 and AlSi10Mg samples processed at $P = 250$ W are shown in Figure 3.11(e, f). The obvious pattern in the pure Al could not be detected in Al alloys, especially for AlSi10Mg.

This can be ascribed to the Marangoni thermocapillary forces in the melt pool of AlSi12 and AlSi10Mg alloys. The driving force of Marangoni thermocapillary flow in the melt pool, which directs the oxides toward the edges is $d\gamma/dT$, reported to be -0.15 and -0.03 $mN \cdot m^{-1} K^{-1}$ for pure Al and AlSi12, respectively [57]. No data is available on AlSi10Mg, but it is fair to assume the same $d\gamma/dT$ as that of the AlSi12 for this alloy [58]. The weaker Marangoni thermocapillary forces in Al alloys are the major reason behind the more uniform distribution of oxides on the top surface of the laser scan tracks. The higher concentration of oxides on the surface of the AlSi12 alloy is consistent with the oxygen content analysis provided in Figure 3.6.

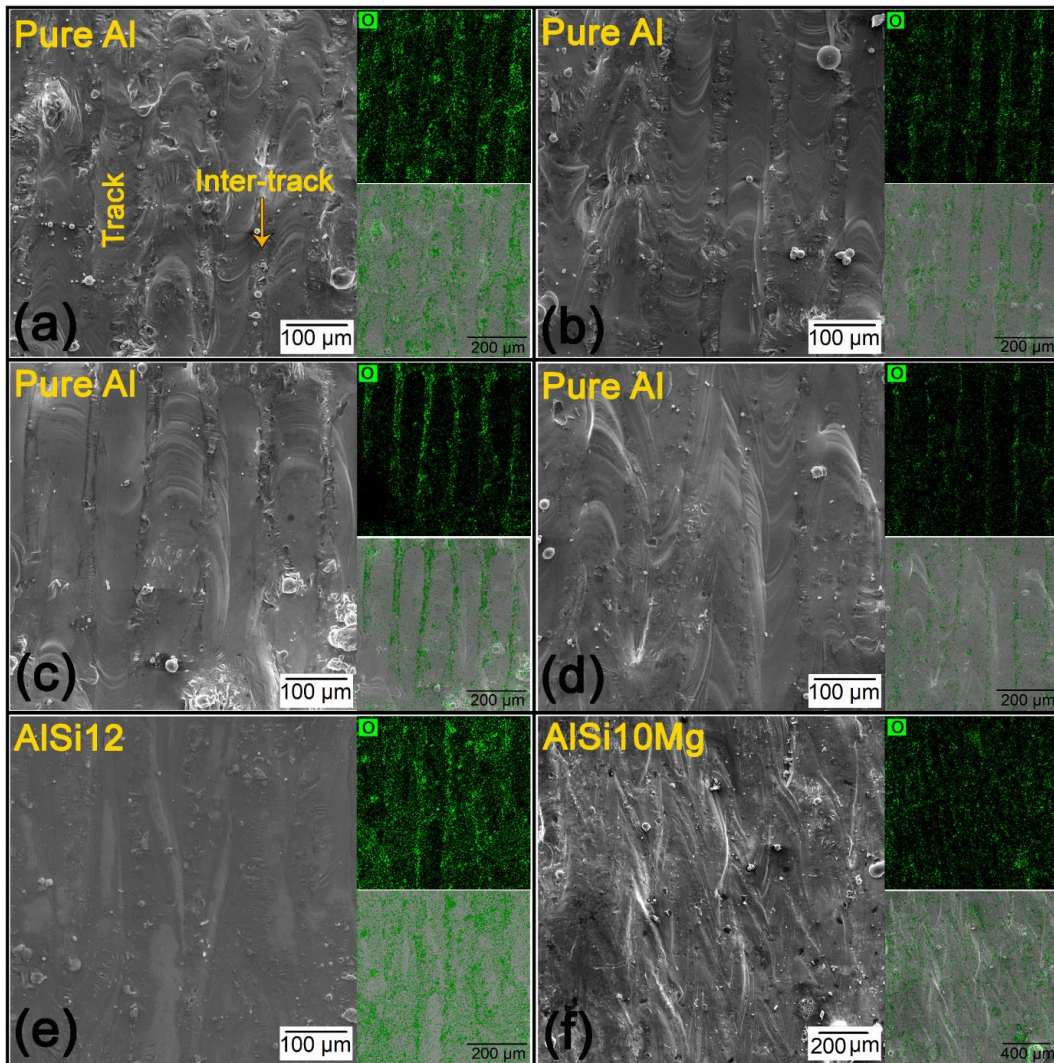


Figure 3.11. Top surface SEM micrographs of pure Al samples processed using $v=1400$ mm/s and P of: (a) 200 W, (b) 250 W, (c) 300 W, and (d) 370 W. (e) and (f) Top surface of AlSi12 and AlSi10Mg samples processed using $v =1400$ mm/s and P of 250 W. There are two insets in each SEM micrograph, the top one is the EDS map showing the oxygen distribution on the top surface, and the bottom one shows the ESD map of oxygen distribution merged with the corresponding SEM micrograph.

3.3.3.5 Rationalization of the lower oxygen content in the printed parts based on the proposed mechanism

The abovementioned discussion can be utilized to justify the oxygen content analysis results provided in Figure 3.6. In the range of the applied P (200 - 370 W), the oxygen content of the LPBF-processed parts was found to be considerably lower than that of the starting powder, proving that not only oxidation did not happen during the LPBF process, but also the employed P levels were enough for the evaporation of nano-sized oxides, especially in the zone (I). According to Eq. 10, higher P can provide higher melt pool temperatures (T) [27]:

$$T = \frac{AP}{\sqrt{2r_0k\pi}^{3/2}} \exp\left(\frac{-r^2}{2r_0^2}\right) \tan^{-1}\left(\sqrt{\frac{2\alpha}{vr_0}}\right) \quad \text{Eq. 11}$$

in which A , k , α , r_0 , and r denote the laser absorptivity, thermal conductivity, thermal diffusivity, beam radius, and radial position in the melt pool, respectively. Higher P can lead to higher temperatures for oxide evaporation in zone (I)/zone (II). Moreover, higher laser powers can enhance the chance of remelting of the previously consolidated layers and, therefore, releasing oxygen. That is why lower oxygen contents were detected in the samples processed by higher P (300 W versus 200 W in Figure 3.6) in both pure Al and Al alloys. For pure Al, 55% and 96% of the oxygen in the starting powder were released at $P = 200$ W and $P = 300$ W, respectively. The corresponding values were 26% and 83% for AlSi12 alloy, intimating that the release of oxygen happened to a less extent in AlSi12 than pure Al. This finding is attributable to the lower magnitude of buoyancy forces in AlSi12 than pure Al ($d\rho/dT = -0.00039$ and -0.00073 g.cm⁻³.K⁻¹ for AlSi12 and pure Al,

respectively²). Hence, a lower fraction of oxides is expected to reach the surface of the melt pool and evaporate due to the upward movement along the melt pool axis. It means that the lower oxygen content in the AlSi12 sample processed by $P = 200$ W is not due to the more oxide evaporation but lower oxygen concentration in the starting AlSi12 powder (Figure 3.6). The influence of the stronger buoyancy forces in the melt pool of pure Al is reflected in the oxygen content results of the samples processed by $P = 300$ W, in which even though its starting powder had higher oxygen content than Al alloys, the fabricated sample had less oxygen content (90 ppm for pure Al versus 220 ppm for AlSi12). For AlSi10Mg alloy, 80% and 82% of the oxygen in the starting powder were released at $P = 200$ W and $P = 300$ W, respectively, meaning that a high fraction of oxides could evaporate at relatively low P levels. This can be explained by considering SiO₂ (Figure 3.5 and Table 3.4) in the AlSi10Mg powder. The bulk melting and boiling temperatures of SiO₂ are significantly lower than those of Al₂O₃ and MgO oxides. These temperatures can be even lower than those of the bulk for nano-sized SiO₂. Therefore, even at lower temperatures (lower P levels), the conditions for SiO₂ evaporation can be satisfied. Since in pure Al and AlSi12 alloys, the SiO₂ oxide is absent, their oxygen reduction percentage at $P = 200$ W was lower than that of AlSi10Mg alloy. However, the increase in the P had the least influence on AlSi10Mg alloy. This is mainly attributed to the presence of MgO oxides in this alloy. The bulk melting and evaporation temperatures of MgO are noticeably higher than Al₂O₃ and SiO₂ oxides, and therefore, they require higher P levels to evaporate. Moreover, according to the Ellingham diagram [59], the Al₂O₃ and SiO₂ oxides

² The $d\rho/dT$ values have been calculated between the melting point and 973 K using data acquired from JMatPro Software.

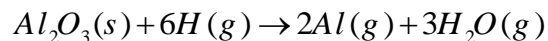
can transform to MgO if enough time is available for their reactions with Mg in the melt pool, further decreasing the chance of oxygen release in light of this scenario.

As a conclusion, although it was expected to have a lower oxygen content in AlSi12 and AlSi10Mg samples due to the lower oxygen content in their starting powder (thinner oxide layers), the opposite was the case. This finding clearly proves that the nature of the oxides, which is dictated by the chemistry of the material, has a crucial impact on the oxygen concentration in final printed parts since it affects their melting/boiling/evaporation temperature during the LPBF process. Nevertheless, the oxygen content of all of the Al/Al alloys processed under $P = 300$ W was noticeably low. The oxygen level of the AlSi10Mg alloy was negligible even at P of 200 W. However, such a P did not lead to almost defect-free parts, meaning that the presence of the oxides is not the factor controlling the densification level of the LPBF-processed AlSi10Mg parts. For pure Al and AlSi12, on the other hand, application of high P seems to be essential to achieve almost oxide-free parts since the level of oxygen is strongly dependent on the P level in these materials. This can also explain why high P levels are required to achieve highly-dense pure Al parts. It is worth noting that the application of relatively high P would also increase the chance of material evaporation and consequently defect formation. Therefore, care must be exercised in selecting the appropriate set of process parameters (e.g., relatively high v in the range of 1600 to 2000 mm/s in this study) to achieve sound oxide-free pure Al parts. These results suggest that reliable, pure Al components with complex geometries meeting the requirements of thermal and electrical applications can be successfully fabricated via the LPBF process. Although not being in the scope of this study, the melt viscosity, thermal conductivity, and melting point are also among the important factors affecting the processability of materials during the LPBF process. Both higher thermal conductivity and

melt viscosity of pure Al compared to Al alloys are believed to adversely affect the processability of pure Al.

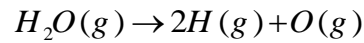
3.3.4 Comments on the inability of decomposition and reduction reactions to decrease the oxygen content

According to the literature in chemistry, two other possible reactions can lead to the release of oxygen upon activation, namely, reduction and decomposition reactions. To prove that the evaporation of the nano-sized oxides on the surface of the melt pool is the only reason behind the decrease in the oxygen content, it should be proved that the reduction and decomposition reactions are impossible during the LPBF process of Al/Al alloys. Dooley et al. reported that the Al_2O_3 could be reduced by hydrogen through the following reaction [60]:



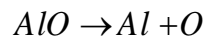
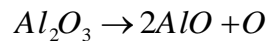
This reduction reaction can proceed spontaneously at temperatures lower than 2100 K [61]. The temperature in a major portion of the melt pool (not the surface) meets this condition during the LPBF process. To investigate the possibility of such a reaction during the LPBF processing of Al/Al alloys, the hydrogen content of the starting powders was measured. The measurement results are shown in Figure 3.12. As it is evident, the concentration of hydrogen detected in the powders is not negligible, especially for pure Al. However, the hydrogen content in the starting powders is significantly lower than the oxygen content (Figure 3.6) and cannot explain the noticeable decrease in the oxygen content of the starting powder after melting and consolidation, especially at high laser powers. Besides, the abovementioned reaction does not happen during the LPBF processing of Al/Al alloys since the hydrogen detected in the powder is not in the form of H (atomic hydrogen) but

moisture (H_2O). Therefore, the reduction of Al_2O_3 with hydrogen can proceed only if the thermal decomposition of H_2O ensues:



Jellinek et al. [62] studied the possibility of such a reaction at high temperatures and concluded that at temperatures as high as 3000 K, only 14% of the H_2O is in the decomposed form. Since this reaction activates effectively at very high temperatures (exceeding 4000 K), H will not be available in the melt pool during the LPBF process to reduce Al_2O_3 and release the oxygen.

The oxygen release can also occur through the partial or complete thermal decomposition of Al_2O_3 based on the following reactions [63]:



The first and second reactions were reported to get activated at temperatures higher than 4000 K and 4400 K [63]. Since the oxides evaporate at significantly lower temperatures than the thermal decomposition temperature of H_2O and Al_2O_3 , it can be concluded that only the evaporation mechanism proposed in section 3.3.3.3 can explain the decreased oxygen content of the LPBF-processed parts.

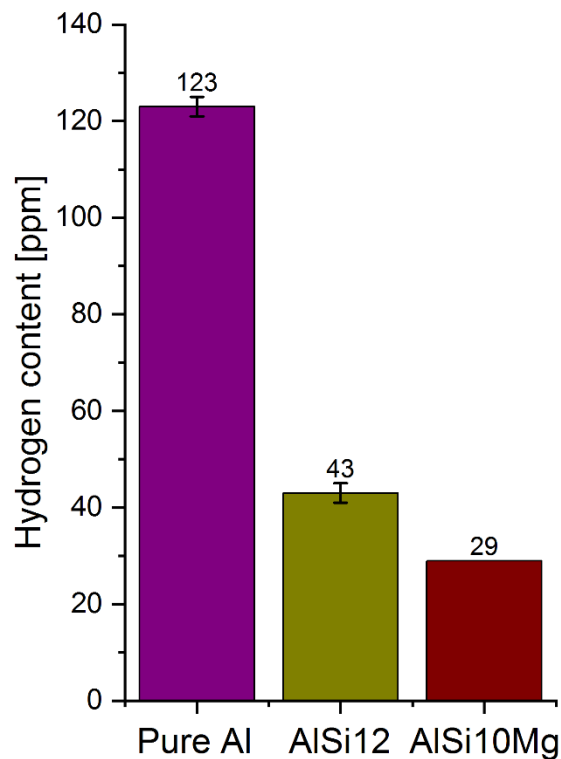


Figure 3.12. The hydrogen content in ppm (by mass) in the pure Al, AlSi12, and AlSi10Mg powders.

3.4 Conclusions

This research study realizes the importance of the laser absorptivity, powder characteristics, powder oxygen content and oxide nature on the processability of Al/Al alloys. The addition of Si and Mg to the Al was found to significantly enhance the laser absorptivity and consolidation kinetics. Moreover, the AlSi12 and AlSi10Mg powders featured a higher packing density than pure Al powder, leading to a slightly lower effective powder layer thickness and consequently lower heat input required for the melting. By obstructing the oxidation of Al, the presence of Si in AlSi12 powder resulted in noticeably lower oxygen content and a thinner oxide layer than pure Al. The addition of a minor amount of Mg along with Si to the Al (AlSi10Mg) could not only significantly reduce the

powder oxygen content but also change its nature. Regardless of the material studied and the process parameters employed, the LPBF-fabricated parts had oxygen contents lower than their starting powders, meaning that either oxidation does not happen during the process or the rate of oxide diminishment (evaporation) outweighs any possible in-situ oxidation. The parts obtained at relatively high laser powers contained lower oxygen content compared to their counterparts processed by lower laser powers. However, the release of oxygen in pure Al and AlSi10Mg showed the highest and lowest sensitivity to the change in the laser power, respectively. While the pure Al powder had the highest oxygen content among all powders, the oxygen level in the pure Al parts fabricated by the optimum process parameters was lower than that of the AlSi12 and AlSi10Mg alloys. This is attributable to the (i) more intense Marangoni thermocapillary fluid flow of pure Al, and (ii) absence of MgO with extremely high melting/evaporation temperature. Therefore, when it comes to the LPBF processing of Al/Al alloys, the nature of the oxides in the starting powder must also be considered to justify the processability. Although pure Al showed a narrower processing window compared to the Al alloys, still sound oxide-free parts could be obtained by careful selection of the process parameters.

Acknowledgement

This paper and the research behind it would not have been possible without the support of HORIBA Advanced Technology Center, Kyoto, Japan where the oxygen/hydrogen (O/H) measurements were performed. We would also like to extend our thanks to Matthieu Chausseau, and Kayvon Savadkouei from HORIBA Scientific, NJ, USA for making these measurements possible. The support of Travis Casagrande from the Canadian Center for Electron Microscopy (CCEM) in carrying out the Auger electron spectroscopy and helping in interpretation of the results is greatly appreciated. The authors would also like to thank

the Elementum 3D company, CO, USA (especially Anthony Manerbino) for manufacturing pure Aluminum test coupons.

References

1. Sélo, R.R., et al., *On the thermal conductivity of AlSi10Mg and lattice structures made by laser powder bed fusion*. Additive Manufacturing, 2020. **34**: p. 101214.
2. Salmi, A., et al., *An integrated design methodology for components produced by laser powder bed fusion (L-PBF) process*. Virtual and Physical Prototyping, 2018. **13**(3): p. 191-202.
3. Fereiduni, E., A. Ghasemi, and M. Elbestawi, *Selective laser melting of aluminum and titanium matrix composites: recent progress and potential applications in the aerospace industry*. Aerospace, 2020. **7**(6): p. 77.
4. Fereiduni, E. and M. Elbestawi, *Process-structure-property relationships in additively manufactured metal matrix composites*, in *Additive Manufacturing of Emerging Materials*. 2019, Springer. p. 111-177.
5. Flores, I., et al., *Implications of lattice structures on economics and productivity of metal powder bed fusion*. Additive Manufacturing, 2020. **31**: p. 100947.
6. Alaña, M., et al., *Understanding elastic anisotropy in diamond based lattice structures produced by laser powder bed fusion: Effect of manufacturing deviations*. Materials & Design, 2020. **195**: p. 108971.
7. Buchbinder, D., et al., *High power selective laser melting (HP SLM) of aluminum parts*. Physics Procedia, 2011. **12**: p. 271-278.
8. Bendsoe, M.P. and O. Sigmund, *Topology optimization: theory, methods, and applications*. 2013: Springer Science & Business Media.
9. Wu, J., X. Quian, and M.Y. Wang, *Advances in generative design*. Comput. Aided Des, 2019. **116**: p. 102733.
10. Jahan, S.A., et al., *Implementation of conformal cooling & topology optimization in 3D printed stainless steel porous structure injection molds*. Procedia Manufacturing, 2016. **5**: p. 901-915.
11. Wang, X., et al., *Topological design and additive manufacturing of porous metals for bone scaffolds and orthopaedic implants: A review*. Biomaterials, 2016. **83**: p. 127-141.

12. Guanghui, S., et al., *An aerospace bracket designed by thermo-elastic topology optimization and manufactured by additive manufacturing*. Chinese Journal of Aeronautics, 2020. **33**(4): p. 1252-1259.
13. Maloney, K.J., et al., *Multifunctional heat exchangers derived from three-dimensional micro-lattice structures*. International Journal of Heat and Mass Transfer, 2012. **55**(9-10): p. 2486-2493.
14. Sabau, A.S., et al., *Design, additive manufacturing, and performance of heat exchanger with a novel flow-path architecture*. Applied Thermal Engineering, 2020. **180**: p. 115775.
15. Dede, E.M., S.N. Joshi, and F. Zhou, *Topology optimization, additive layer manufacturing, and experimental testing of an air-cooled heat sink*. Journal of Mechanical Design, 2015. **137**(11).
16. Louvis, E., P. Fox, and C.J. Sutcliffe, *Selective laser melting of aluminium components*. Journal of Materials Processing Technology, 2011. **211**(2): p. 275-284.
17. Zhang, J., et al., *A review of selective laser melting of aluminum alloys: Processing, microstructure, property and developing trends*. Journal of Materials Science & Technology, 2019. **35**(2): p. 270-284.
18. Aboulkhair, N.T., et al., *Reducing porosity in AlSi10Mg parts processed by selective laser melting*. Additive manufacturing, 2014. **1**: p. 77-86.
19. Fereiduni, E., A. Ghasemi, and M. Elbestawi, *Selective laser melting of hybrid ex-situ/in-situ reinforced titanium matrix composites: Laser/powder interaction, reinforcement formation mechanism, and non-equilibrium microstructural evolutions*. Materials & Design, 2019. **184**: p. 108185.
20. Read, N., et al., *Selective laser melting of AlSi10Mg alloy: Process optimisation and mechanical properties development*. Materials & Design (1980-2015), 2015. **65**: p. 417-424.
21. Yan, Q., B. Song, and Y. Shi, *Comparative study of performance comparison of AlSi10Mg alloy prepared by selective laser melting and casting*. Journal of Materials Science & Technology, 2020. **41**: p. 199-208.
22. Prashanth, K.G., et al., *Microstructure and mechanical properties of Al-12Si produced by selective laser melting: Effect of heat treatment*. Materials Science and Engineering: A, 2014. **590**: p. 153-160.
23. Yang, P., et al., *Microstructure evolution and thermal properties of an additively manufactured, solution treatable AlSi10Mg part*. Journal of Materials Research, 2018. **33**(23): p. 4040-4052.

24. Kimura, T., et al., *Effect of silicon content on densification, mechanical and thermal properties of Al-xSi binary alloys fabricated using selective laser melting*. Materials Science and Engineering: A, 2017. **682**: p. 593-602.
25. Brecher, C., *Advances in production technology*. 2015: Springer Nature.
26. Do, D.K. and P. Li, *The effect of laser energy input on the microstructure, physical and mechanical properties of Ti-6Al-4V alloys by selective laser melting*. Virtual and Physical Prototyping, 2016. **11**(1): p. 41-47.
27. Balbaa, M., et al., *On selective laser melting of Inconel 718: Densification, surface roughness, and residual stresses*. Materials & Design, 2020. **193**: p. 108818.
28. Narvan, M., K.S. Al-Rubaie, and M. Elbestawi, *Process-structure-property relationships of AISI H13 tool steel processed with selective laser melting*. Materials, 2019. **12**(14): p. 2284.
29. Rao, H., et al., *The influence of processing parameters on aluminium alloy A357 manufactured by Selective Laser Melting*. Materials & Design, 2016. **109**: p. 334-346.
30. Tang, M. and P.C. Pistorius, *Oxides, porosity and fatigue performance of AlSi10Mg parts produced by selective laser melting*. International Journal of Fatigue, 2017. **94**: p. 192-201.
31. Askeland, D.R., et al., *The science and engineering of materials*. 2003.
32. Olakanmi, E., *Selective laser sintering/melting (SLS/SLM) of pure Al, Al-Mg, and Al-Si powders: Effect of processing conditions and powder properties*. Journal of Materials Processing Technology, 2013. **213**(8): p. 1387-1405.
33. Balbaa, M., et al., *Role of Powder Particle Size on Laser Powder Bed Fusion Processability of AlSi10Mg Alloy*. Additive Manufacturing, 2020: p. 101630.
34. Khairallah, S.A., et al., *Laser powder-bed fusion additive manufacturing: Physics of complex melt flow and formation mechanisms of pores, spatter, and denudation zones*. Acta Materialia, 2016. **108**: p. 36-45.
35. Körner, C., A. Bauereiß, and E. Attar, *Fundamental consolidation mechanisms during selective beam melting of powders*. Modelling and Simulation in Materials Science and Engineering, 2013. **21**(8): p. 085011.
36. Rezaeifar, H. and M. Elbestawi, *On-line melt pool temperature control in L-PBF additive manufacturing*. The International Journal of Advanced Manufacturing Technology: p. 1-16.
37. Shukla, S., et al., *Hierarchical features infused heterogeneous grain structure for extraordinary strength-ductility synergy*. Materials Research Letters, 2018. **6**(12): p. 676-682.

38. Muñiz-Lerma, J.A., et al., *A comprehensive approach to powder feedstock characterization for powder bed fusion additive manufacturing: A case study on AlSi7Mg*. *Materials*, 2018. **11**(12): p. 2386.
39. Spierings, A.B. and G. Levy. *Comparison of density of stainless steel 316L parts produced with selective laser melting using different powder grades*. in *Proceedings of the Annual International Solid Freeform Fabrication Symposium*. 2009. Austin, TX.
40. Narvan, M., et al., *Laser powder bed fusion of functionally graded bi-materials: Role of VC on functionalizing AISI H13 tool steel*. *Materials & Design*, 2021: p. 109503.
41. Bajaj, P., et al., *Predictive process parameter selection for Selective Laser Melting Manufacturing: Applications to high thermal conductivity alloys*. *Additive Manufacturing*, 2019. **27**: p. 246-258.
42. Childs, T. and C. Hauser, *Raster scan selective laser melting of the surface layer of a tool steel powder bed*. *Proceedings of the Institution of Mechanical Engineers, Part B: Journal of Engineering Manufacture*, 2005. **219**(4): p. 379-384.
43. Bramson, M.A., *Infrared radiation: a handbook for applications, with a collection of reference tables*. 1968.
44. Brandt, R. and G. Neuer, *Electrical resistivity and thermal conductivity of pure aluminum and aluminum alloys up to and above the melting temperature*. *International Journal of Thermophysics*, 2007. **28**(5): p. 1429-1446.
45. Uliasz, P., et al., *The influence of heat treatment parameters on the electrical conductivity of AlSi7Mg and AlSi10Mg aluminum cast alloys*, in *ICAA13 Pittsburgh*. 2012, Springer. p. 129-135.
46. Silbernagel, C., et al., *Electrical resistivity of additively manufactured AlSi10Mg for use in electric motors*. *Additive Manufacturing*, 2018. **21**: p. 395-403.
47. Slotwinski, J.A., et al., *Characterization of metal powders used for additive manufacturing*. *Journal of research of the National Institute of Standards and Technology*, 2014. **119**: p. 460.
48. Kimura, T. and T. Nakamoto, *Thermal and mechanical properties of commercial-purity aluminum fabricated using selective laser melting*. *Materials Transactions*, 2017. **58**(5): p. 799-805.
49. Cunningham, R., et al., *Keyhole threshold and morphology in laser melting revealed by ultrahigh-speed x-ray imaging*. *Science*, 2019. **363**(6429): p. 849-852.
50. Zhao, C., et al., *The effect of oxygen on transitional Marangoni flow in laser spot welding*. *Acta Materialia*, 2010. **58**(19): p. 6345-6357.

51. Trunov, M.A., M. Schoenitz, and E. Dreizin, *Effect of polymorphic phase transformations in alumina layer on ignition of aluminium particles*. Combustion Theory and Modelling, 2006. **10**(4): p. 603-623.
52. Levitas, V.I., et al., *Effect of the alumina shell on the melting temperature depression for aluminum nanoparticles*. The Journal of Physical Chemistry C, 2009. **113**(32): p. 14088-14096.
53. Ferdinand, P., et al., *Mechanics of Materials Mc Graw-Hill*. 2006.
54. Sinclair, G. and J. Helms, *A review of simple formulae for elastic hoop stresses in cylindrical and spherical pressure vessels: What can be used when*. International Journal of Pressure Vessels and Piping, 2015. **128**: p. 1-7.
55. Kou, S., *Welding metallurgy*. New Jersey, USA, 2003: p. 431-446.
56. Joshi, N., et al., *Size effect on melting temperatures of alumina nanocrystals: Molecular dynamics simulations and thermodynamic modeling*. Computational Materials Science, 2018. **145**: p. 140-153.
57. Kobatake, H., et al., *Surface tension of binary Al–Si liquid alloys*. Journal of Materials Science, 2015. **50**(9): p. 3351-3360.
58. Hojjatzadeh, S.M.H., et al., *Pore elimination mechanisms during 3D printing of metals*. Nature communications, 2019. **10**(1): p. 1-8.
59. Gaskell, D.R. and D.E. Laughlin, *Introduction to the Thermodynamics of Materials*. 2017: CRC press.
60. Dooley, D., M. Balooch, and D. Olander, *Chemical reduction of refractory oxides by atomic hydrogen*. 1978, California Univ.
61. Braaten, O., A. Kjekshus, and H. Kvande, *The possible reduction of alumina to aluminum using hydrogen*. Jom, 2000. **52**(2): p. 47-53.
62. Jellinek, H. and H. Kachi, *The catalytic thermal decomposition of water and the production of hydrogen*. International Journal of Hydrogen Energy, 1984. **9**(8): p. 677-688.
63. Rains, R.K. and R.H. Kadlec, *The reduction of Al₂O₃ to aluminum in a plasma*. Metallurgical Transactions, 1970. **1**(6): p. 1501-1506.

4 Chapter 3 Unraveling the low thermal conductivity of the LPBF fabricated pure Al, AlSi12, and AlSi10Mg alloys through substrate preheating

Complete Citation:

Fereiduni E, Ghasemi A, Elbestawi M. Selective laser melting of hybrid ex-situ/in-situ reinforced titanium matrix composites: Laser/powder interaction, reinforcement formation mechanism, and non-equilibrium microstructural evolutions. *Materials & Design*. 2019 Dec 15; 184: 108185.

Authorship contribution statement:

Ali Ghasemi: Writing – original draft, Methodology, Investigation, Conceptualization.

Eskandar Fereiduni: Writing – original draft, Methodology, Investigation, Conceptualization. **Mohamed Balbaa:** Writing – review & editing, Investigation.

Mohamed Elbestawi: Writing – review & editing, Supervision. **Saeid Habibi:** Writing – review & editing, Supervision.

Unraveling the low thermal conductivity of the LPBF fabricated pure Al, AlSi12, and AlSi10Mg alloys through substrate preheating

Abstract

It is essential to employ post-build heat treatment on the laser powder bed fusion (LPBF) fabricated aluminum (Al) and Al alloys due to their thermal conductivity in the as-built condition being inferior to that of the conventionally manufactured counterparts. In this study, substrate preheating (200 °C) was proposed as a solution to achieve high thermal conductivities in the as-built condition. Pure Al, AlSi12, and AlSi10Mg samples were shown to possess up to 15, 25, and 80% higher thermal conductivity values than their non-preheated counterparts reported in the literature. An analytical analysis contingent on calculating electron mean free path in the presence of only intrinsic or a combination of intrinsic and extrinsic scattering phenomena was introduced to justify the thermal behaviors. As per micro X-ray computed tomography, EBSD analysis, and TEM investigations, the extrinsic scattering sites were found to be (i) pores, (ii) grain boundaries, (iii) cell boundaries (Al alloys), (iv) oxides (pure Al), (v) nano-size Si precipitates (AlSi10Mg), (vi) nano-size Mg₂Si phase (AlSi10Mg), (vii) vacancies, (viii) dislocations and (ix) Si supersaturation in α -Al phase (Al alloys). The dominant scattering site(s) was found for each material based on which the difference between the obtained thermal conductivity and its corresponding nominal value or the one reported for the non-preheated condition was unraveled. The implications of the findings in this study are essential not only for Al/Al alloys but also for other metallic materials (i.e., Cu alloys), requiring high thermal conductivity in the as-built condition.

Keywords: Thermal diffusivity and conductivity; Pure aluminum; AlSi12 and AlSi10Mg alloys; Electron mean free path; TEM investigation of nano-constituents.

4.1 Introduction

Additive manufacturing (AM) is a disruptive technology that has revolutionized almost all industries by bringing to the table the possibility of fabricating components that could not be successfully produced before its emergence [1-3]. The laser powder bed fusion (LPBF) process is one of the most up-and-coming AM techniques, which gives designers a free hand to be no longer limited by the manufacturing techniques [4, 5]. In light of this capability, the LPBF process has been utilized in various industries, such as aerospace and automotive, to generate new designs or redesign and manufacture the existing components [6, 7]. For instance, the LPBF process can be adopted to produce highly-efficient electronic battery packs for electric devices or electric vehicles (EVs). Functional battery packs can be fabricated by this technique in which the lattice holding structure or solid casing with channels acts as a heat sink [8, 9] to cool down the batteries through passive cooling. In many of the above industries and applications, aluminum (Al) and Al alloys are prime candidates due to their light weight and high thermal conductivity [10]. Given the fact that the structure-property relationships of materials are dictated by their manufacturing techniques [11], the thermal properties of the LPBF fabricated Al/Al alloy structures have to be preeminently investigated before their reliable implementation.

Referring to studies targeting the simulation/modeling of the melt pool features and temperature field in the LPBF fabricated Al alloy parts, thermal properties of the conventionally manufactured material (not the printed one) have been used as the input data [12-15]. This is while the LPBF process, with an ultrafast cooling rate and non-equilibrium solidification nature, creates microstructures different from conventional processes [16, 17], meaning that the thermal properties are not necessarily identical. While several studies have focused on the mechanical properties of the LPBF-fabricated Al

alloys, only a few research studies focus on their thermal properties [18-23]. Kimura et al. [18] investigated the thermal conductivity of the LPBF fabricated Al-XSi (X=0-20 wt%) and reported that regardless of the concentration of Si, the thermal conductivity was lower than the conventionally manufactured counterpart. For instance, the thermal conductivities of the LPBF fabricated Al-0Si (pure Al), and Al-12Si were ~ 200 and ~ 115 W/mK, respectively [18], while their corresponding values are ~ 237 [24] and ~ 170 W/mK [25] for the wrought condition. According to another study conducted by the same authors on pure Al [19], it was found that annealing heat treatment at 450 °C for 10 min can increase the thermal conductivity from 200 to 240 W/mK. It was claimed that the presence of oxides, residual stresses, and high density of dislocations are the reasons behind the lower thermal conductivity of pure Al in the as-built condition, most of which were mitigated through annealing treatment [19]. In an admirable study, Yang et al. [20] investigated the thermal conductivity of AlSi10Mg alloy within the temperature range of -50 to 500 °C in as-built and annealed (300 °C/2h) conditions. It was shown that the thermal conductivity of the as-built AlSi10Mg at room temperature was almost half of its value after heat treatment (~ 90 vs. 185 W/mK) [20]. This is in good agreement with the thermal conductivity values reported by the EOS GmbH (LPBF machine manufacturer) in as-built and annealed (300 °C/2h) conditions [26]. The thermal conductivity value reported in [20] for the annealed (300 °C/2h) AlSi10Mg was also confirmed by another study [21] and was shown that it is superior to the value reported for the as-cast AlSi10Mg. Yang et al. [20] showed that the lower thermal conductivity of the as-built AlSi10Mg was mainly attributed to the supersaturation of Al matrix from Si, though other factors such as cell size and grain structure of the as-built and heat-treated samples were also considered to justify such disparity. The exolution of the Al matrix from supersaturated Si atoms upon annealing heat

treatment was suggested to be responsible for the improved thermal conductivity. Although Yang et al. [20] calculated the electron and phonon mean free paths for AlSi10Mg alloy, most of their discussion was qualitative and based on data assumptions since no characterization was performed on the level of Si supersaturation or the grain size in their study. Moreover, the effect of some other factors reducing the thermal conductivity of as-built AlSi10Mg alloy such as dislocations, residual stresses, atomic vacancies, and oxides were not considered. Selo et al. [22] investigated the influence of different heat treatment cycles on the thermal conductivity of the LPBF fabricated AlSi10Mg alloy and reached to the same conclusion that the thermal conductivity in the as-built condition is noticeably lower than that of the heat treated samples. It is worth noting that based on the literature [18-20, 22], the thermal conductivity of the LPBF fabricated Al/Al alloys in the build direction is slightly higher than that of the transverse direction.

The aforementioned studies share these two findings that the LPBF fabricated Al/Al alloys show (i) negligible anisotropy of thermal conductivity and (ii) lower thermal conductivity than that of their wrought counterparts in the as-built condition. Although the former eliminates the need for any post-process heat treatments, the latter makes its implementation inevitable. This study proposes an easily attainable solution to obtain high thermal conductivities for the LPBF fabricated pure Al, AlSi12 (Al-Si binary alloy), and AlSi10Mg (Al-Si-Mg ternary alloy) in the as-built condition and eliminate/alleviate the need for time-consuming and cost-prohibitive post-build heat treatments. The microstructural features of the LPBF fabricated pure Al, AlSi12, and AlSi10Mg parts under the proposed processing condition were examined at nano- to micron-scale and compared to their wrought/cast counterparts as well as the LPBF fabricated parts in the literature. Different factors governing the thermal conductivity of the fabricated pure Al/Al alloys

were fundamentally explored and calculated in terms of the electron mean free path. This study fills the knowledge gap in understanding the underlying reasons for the observed thermal behavior of most versatile LPBF fabricated Al/Al alloys for thermal applications and makes their industrial implementation as end-use products more feasible without needing post-build heat treatment.

4.2 Materials and Experimental Procedure

EOS M280 and EOS M290 LPBF machines were utilized to print Al alloys (AlSi12 and AlSi10Mg) and pure Al, respectively, using the optimum set of process parameters reported in a previous study by the same authors [10]. The laser power, hatch spacing, and nominal powder layer thickness were 370 W, 100 μm , and 30 μm for all materials, while the scanning speeds were selected to be 1800, 1800, and 2000 mm/s for pure Al, AlSi12, and AlSi10Mg, respectively. For all samples, the build plate was preheated to 200 °C.

The density (ρ) of samples was measured using the Archimedes method by performing at least five measurements on each sample. The theoretical bulk densities of 2.7 g/cm³ for pure Al and 2.67 g/cm³ for AlSi12 and AlSi10Mg alloys were considered for relative density calculations. A Bruker Skyscan1172 X-ray computed tomography (XCT) system was also utilized to characterize the porosities of the fabricated parts. Samples used for this test were 0.5×0.5×0.5 mm³ in size and were scanned at 90 kV using a 0.5 mm Al filter at a 1.78 μm pixel resolution. Graphical and quantitative post-processing of the XCT images were carried out using the commercial Skyscan1172 software package.

The linear thermal expansion measurements were performed on samples of 4 × 4 × 10 mm³ using a Linseis quenching dilatometer DIL L78 QDT. Samples were mounted in a helium-filled sealed chamber and inductively heated up to 425 °C at 20 °C/min. The peak

temperature was held constant for three minutes; then, the sample was allowed to cool down to room temperature. A linear voltage displacement transducer (LVDT) measured the linear elongation through quartz push rods attached to the sample ends.

The specific heat capacity (C_p) measurements were performed using the sapphire technique (ASTM E1269) using a METTLER Toledo differential scanning calorimetry (DSC)-1 (WMT&R Inc.). STARe software was used for testing and data acquisition. A scanning interval of 1 second was used during testing. The specimen was weighted prior to testing and placed into a 40 μ L Al crucible. The crucible was then inserted into the testing chamber and purged with high purity Ar at a 50 mL/min flow rate. Testing was initiated by cooling the specimen to -20 °C, holding the temperature for 4 min, and then ramping from -20 to 425 °C at a heating rate of 10 °C/min. The samples were discs with a diameter and thickness of 4.57 and 1.52 mm, respectively.

The thermal diffusivity (α) of samples was measured using a Linseis PT1000 LFA-1600°C Laser Flash System (Linseis Messgeraete GmbH, Selb, Germany) with Nd:YAG-Diode-Infrared-Laser and liquid nitrogen cooled InSb-IR detector. The sample temperature was monitored using a thermocouple type C (+/- 0.5 K). Square samples of 10×10 mm² with a thickness of ~3 mm were coated on both sides with a thin graphite layer and placed into the sample holder. The measurements were performed in vacuum from room temperature up to 425 °C. Every 25 °C, three measurements were performed and averaged. Before the measurements, samples were held at the target temperature for 4 min.

Using the above information, the thermal conductivity (K) was calculated at different temperatures as follows [27]:

$$K(T) = \alpha(T) \times \rho(T) \times C_p(T) \quad \text{Eq. (1)}$$

The LPBF-fabricated parts were sectioned along their height, followed by grinding and polishing. AlSi12 and AlSi10Mg samples were etched chemically using Keller's Reagent. For pure Al, a reagent containing 5 mL HNO₃, 5 mL HCl, 5 mL HF, and 95 mL distilled water was used for etching. Microstructural observations were performed using a Nikon LV100 optical microscope as well as a Tescan Vega scanning electron microscope (SEM) operating at an accelerating voltage of 20 kV. To study the texture and grain size of samples, electron backscatter diffraction (EBSD) analysis was performed. For this purpose, an FEI, Versa 3D field-emission SEM (FE-SEM), operating at an accelerating voltage of 20 keV, a tilt angle of 70°, and step size in the range of 0.3–1 μm was utilized. The EBSD data were collected using the TSL OIM 7 software and analyzed using TSL OIM analysis and ATEX software [28]. An FEI Helios Nanolab-650 dual-beam apparatus was utilized to prepare electron-transparent samples for transmission electron microscopy (TEM) studies using the focused ion beam (FIB) lift-out technique. TEM characterizations were conducted using Talos L120C TEM and Talos 200X STEM. The Super-X energy-dispersive X-ray spectroscopy (EDS) system combined with the high current density electron beam in the scanning mode (STEM) was utilized to analyze the oxides and precipitates.

The oxygen content of the fabricated samples was measured using an EMGA-920 Instrumental Gas Analyzer (HORIBA, Ltd., HORIBA Techno Service Co., Ltd. HORIBA Advanced Technology Center, Japan) with a procedure thoroughly explained in [10]. The reported oxygen content for each sample represents an average of four distinct measurements. Wave velocities were measured along longitudinal and transverse directions using an Olympus Epoch 600 equipped with probes with a frequency of 2.25 MHz. The measurement of the distance between the sensor and the back-wall of the

specimen was performed according to the time of flight (ToF) principle. The sound velocity in each direction was calculated by dividing the traveled distance by the ToF value. The reported velocities are the average of four distinct measurements. To eliminate the acoustic impedance mismatch between the air and the solid, honey was used as a couplant between the transducer and the surface of the sample.

4.3 Results

4.3.1 Thermal properties

4.3.1.1 Specific heat capacity (C_p)

The C_p results for the heating cycle are shown in Figure 4.1. According to Figure 4.1(a), the C_p of pure Al increases monotonically over the measured temperature range. The C_p values are almost identical to those reported for its conventionally manufactured counterpart [29]. For AlSi12 (Figure 4.1(b)) and AlSi10Mg (Figure 4.1(c)) alloys, the occurrence of one and two exothermic events for the respective materials caused deviation from the overall increasing trend of C_p in the specific temperature range(s). For AlSi12 alloy, the onset of deviation from the general trend occurred at ~ 175 °C, and the exothermic reaction peaked at 250 °C and terminated at 300 °C, as shown in Figure 4.1(d). In the case of AlSi10Mg, the first and second exothermic reactions peaked at 225 and 300 °C, respectively (Figure 4.1(e) and (f)). The peak in AlSi12 (Figure 4.1(d)) and the first peak in AlSi10Mg (Figure 4.1(e)) correspond to the depletion of the supersaturated α -Al matrix from Si, as confirmed by the microstructural characterization of the AlSi12/AlSi10Mg samples heat-treated at such temperature ranges [30, 31]. The second peak in AlSi10Mg (Figure 4.1(f)) is attributable to the formation of Mg_2Si precipitates [20]. The supersaturation of the α -Al matrix from Mg and/or Si elements in AlSi10Mg and AlSi12

alloys originates from the rapid solidification and fast cooling rates associated with the LPBF process. The results suggest that even 200 °C of preheating could not eliminate the entrapment chance of Si and Mg as the fast-growing solidification front has recaptured some of the rejected Si/Mg during solidification. However, despite the DSC measurement results in the literature for the non-preheated AlSi10Mg alloy [20], there is no difference between the depth of the first and second peaks in AlSi10Mg alloy when 200 °C of preheating is utilized (this study). In other words, even though the supersaturation level of the matrix from Si was believed to be significantly higher than that of the Mg element, their peaks are almost equal, meaning that a considerable amount of the entrapped Si could find the chance to precipitate out as the process proceeded.

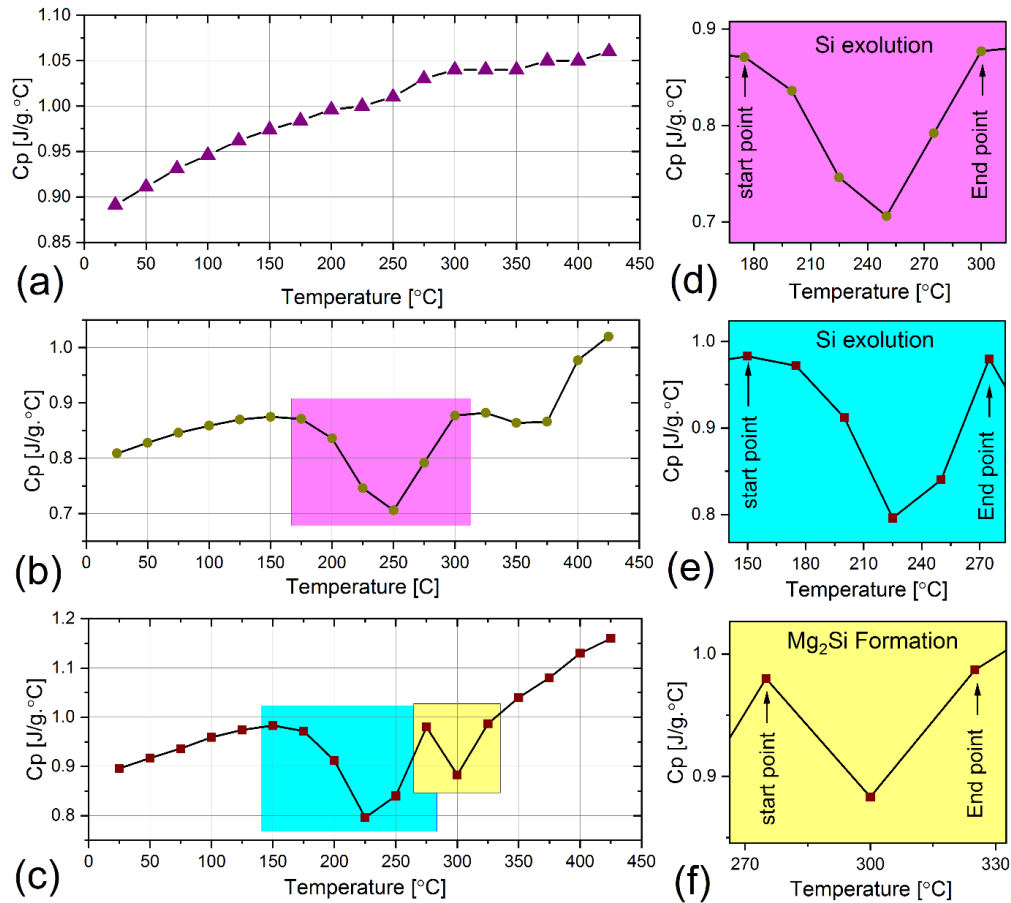


Figure 4.1. Specific heat capacity (C_p) versus temperature for (a) pure Al, (b) AlSi12, and (c) AlSi10Mg. The higher magnification of the designated colored box in (b) and (c) is shown in (d-f).

4.3.1.2 Density and thermal expansion

The relative densities measured by the Archimedes method for pure Al, AlSi12, and AlSi10Mg samples were 99, 99.7, and 99.3%, respectively. In other words, the highest achieved density for the respective materials was 2.673, 2.663, and 2.651 g/cm³. To better understand the size, size distribution, and morphology of the defects in the samples, the XCT test was utilized (Figure 4.2). The XCT results are in agreement with Archimedes density measurements as pure Al shows larger pores with higher volume fraction.

Nevertheless, based on the volume ratio calculations, XCT results suggest that the relative densities of pure Al, AlSi12, and AlSi10Mg samples are 99.87, 99.96, and 99.95%, respectively. Since the Archimedes test was performed on larger samples, its results were used for any calculations hereafter.

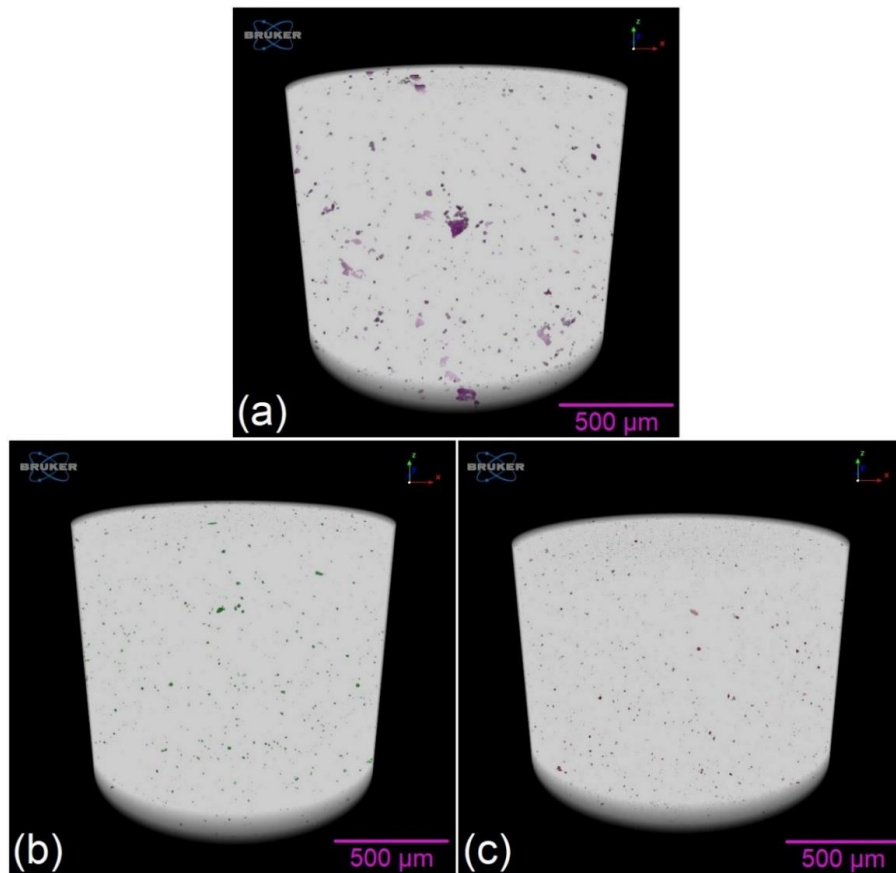


Figure 4.2. XCT image of porosity distribution for (a) pure Al, (b) AlSi12, and (c) AlSi10Mg.

Based on Eq. (1), the density of the printed samples is required not only at ambient (ρ_{RT}) but also at higher temperatures ($\rho(T)$) to calculate the thermal conductivity of Al/Al alloys within the desired temperature range of 25-425 °C. To accurately predict the density of samples at higher temperatures, calorimetry test was utilized. The relative change in the physical dimension ($\Delta L/L_0$, L_0 is the initial sample length) versus temperature in the

heating cycle is shown in Figure 4.3(a-c). The following equation, along with the results shown in Figure 4.3(a-c), were used to calculate the density at any desirable temperature:

$$\rho(T) = \frac{L_0 \rho_{RT}}{L_0 + 3\Delta L} \quad \text{Eq. (2)}$$

The obtained density versus temperature results are shown in Figure 4.3(f). As evident, the density shows a descending trend with increasing temperature. The decrease level is less than 5% of the ρ_{RT} for each material, which is in line with the variation levels reported for their conventionally manufactured counterparts [32]. Nevertheless, a deviation from linearity was observed in AlSi12 and AlSi10Mg alloys at specific temperature ranges, mirroring the trends shown in Figure 4.3(b) and (c). Since this is absent in the conventionally manufactured AlSi12 and AlSi10Mg parts, it can be concluded that the LPBF process has imparted this behavior. According to Figure 4.3(d) and (e), the deviation from linear behavior of the $\Delta L/L_0$ or density starts at 220 and 250 °C and terminates at 385 and 375 °C for AlSi12 and AlSi10Mg, respectively. Although the starting point of deviation (Figure 4.3(d) and (e)) is shifted to higher temperatures compared to the onset of exothermic reactions for AlSi12 and AlSi10Mg (DSC results shown in Figure 4.1(e) and (f)), it is still justifiable that such deviation is mainly due to the depletion of the supersaturated α -Al matrix from Si. The small embedding plots in Figure 4.3(b) and (c) show the $\Delta L/L_0$ versus temperature during the cooling cycle. It is self-evident that the observed anomaly in the heating cycle is absent in this case since the matrix has already been depleted from Si during the heating cycle, proving the validity of the mentioned reason.

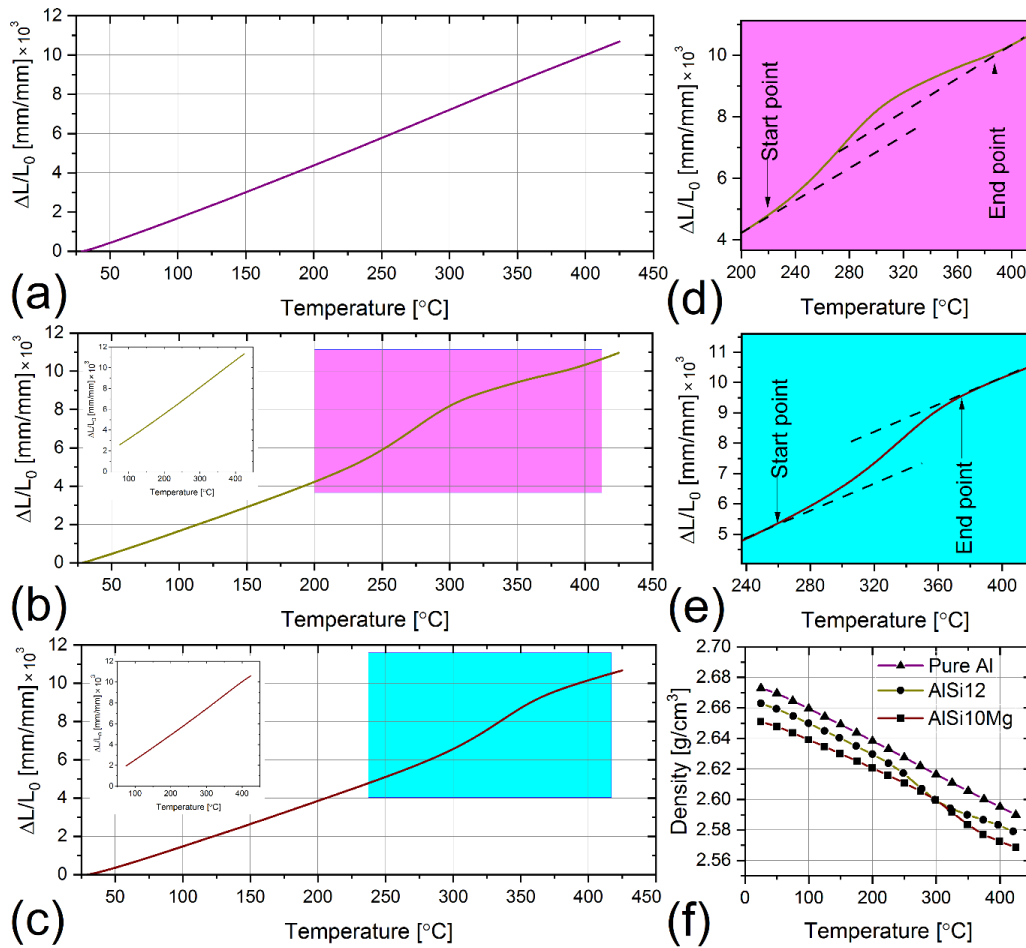


Figure 4.3. The relative change in physical dimension ($\Delta L/L_0$) versus temperature for (a) pure Al, (b) AlSi12, and (c) AlSi10Mg. The inset in (b) and (c) show the $\Delta L/L_0$ versus temperature in the cooling cycle. The higher magnification of the designated colored box in (b) and (c) is shown in (d) and (e), respectively. The variation of density with temperature is shown in (f) for all materials.

4.3.1.3 Thermal diffusivity

The thermal diffusivity results are shown in Figure 4.4. Regardless of the measurement temperature, the thermal diffusivity of pure Al is higher than that of the Al alloys. Based on Figure 4.4(a), the thermal diffusivity of pure Al shows a descending trend versus temperature. An anomaly was observed at 175 °C, in which the thermal diffusivity showed an increase. According to Figure 4.4(b) and (c) for AlSi12 and AlSi10Mg alloys, an almost

constant or slightly decreasing trend with small kinks is perceptible from room temperature up to 175 °C (zone (I)). From 175 °C to 350 °C, the thermal diffusivity showed an ascending trend with increasing temperature (zone (II)). After 350 °C, a decreasing trend was observed (zone (III)). In general, a monotonic decrease in thermal diffusivity was expected for pure Al/Al alloys since thermal agitation caused by the temperature increase enhances the scattering of electrons. However, this trend was only observed in pure Al (excluding 175°C). In Al alloys, the depletion of the supersaturated α -Al matrix from Si (in AlSi12 and AlSi10Mg alloys) and formation of Mg_2Si precipitates (in AlSi10Mg) within the temperature range of 150-350 °C (Figure 4.1) decrease the electron scattering frequency in the matrix and consequently enhance the thermal diffusivity. It should be borne in mind that the perceptible differences between the peak thermal diffusivity in zone (II) and minimum thermal diffusivities in zones (I) and (III) are less than 9% based on Figure 4.4(b) and (c). Therefore, similar to the C_p results (Figure 4.1), it is implied that the supersaturation of α -Al from Si and/or Mg is considerably low.

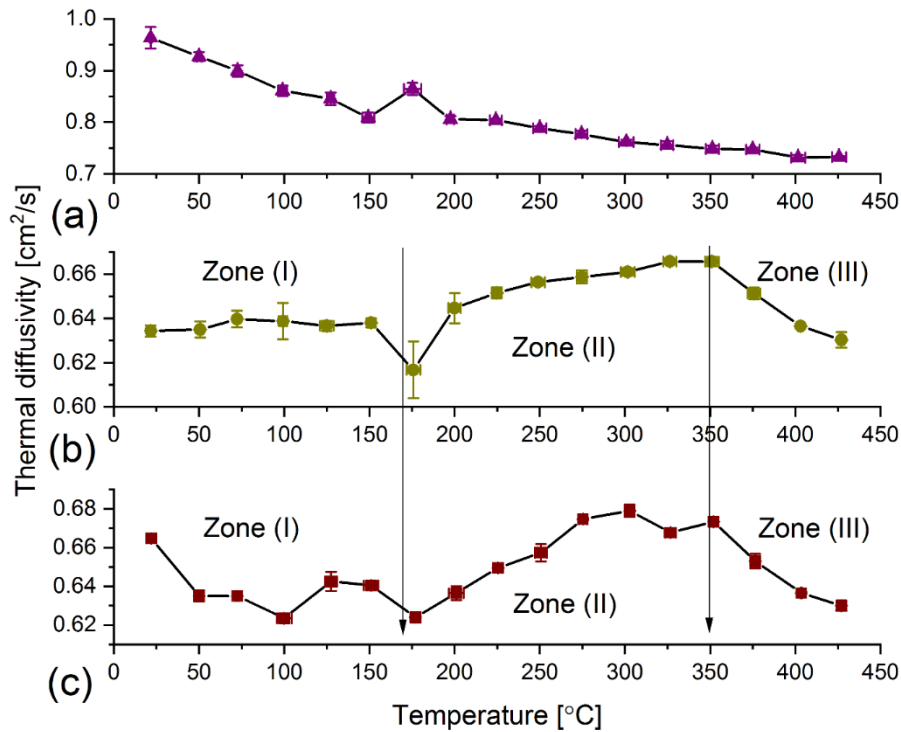


Figure 4.4. Thermal diffusivity versus temperature for (a) pure Al, (b) AlSi12 and (c) AlSi10Mg.

4.3.1.4 Thermal conductivity

By using the C_p and thermal diffusivity results (Figure 4.1 and Figure 4.4) as well as the calculated $\rho(T)$ values, the thermal conductivity ($K(T)$) was calculated using Eq. (1). As shown in Figure 4.5, the thermal conductivity of pure Al slightly decreases from 230 W/mK at room temperature to 200 W/mK at 425 °C. The thermal conductivities of the AlSi10Mg and AlSi12 samples are almost constant up to 150 and 175 °C, respectively. Then, they dip into their lowest values at 225 and 250 °C. The thermal conductivity of AlSi12 gradually recovers after 250 °C and shows an overall ascending trend thereafter. For AlSi10Mg, there is a local minimum at 300 °C after the gradual recovery from the lowest thermal conductivity value. A gradual increase in thermal conductivity of AlSi10Mg was observed after 300 °C, which finally levels off above 350 °C. Referring to

Figure 4.1, it can be understood that the C_p measurement results are reflected in the thermal conductivity trend. The thermal conductivity of AlSi12 and AlSi10Mg at room temperature was ~160 and ~140 W/mK, respectively.

In the previous studies, pure Al and AlSi10Mg having thermal conductivities of 200 [19] and 90 [20] W/mK (at room temperature) in the as-built condition were manufactured. These values were enhanced to 240 and 180 W/mK after heat treatment. However, in this study, the thermal conductivity of the as-built pure Al was almost equal to that of the heat-treated case (~230 W/mK at room temperature). Moreover, the thermal conductivity of the as-built AlSi10Mg in preheated conditions was ~80% higher than that of its non-preheated counterpart. For AlSi12, the preheated sample (this study) showed ~25% higher thermal conductivity than its non-preheated counterpart (115 W/mK) in the as-built state. Therefore, this study has borne out the possibility of 200 °C of preheating to enhance the thermal conductivity of the as-built samples. It must be highlighted that the whole difference observed between the thermal conductivity of the LPBF-fabricated samples in preheated (this study) and non-preheated (literature) conditions is not merely attributable to the preheating. This is because the process parameters, powder attributes, and oxygen content of the printed samples in this study were not identical to those of the previous studies in the literature. By considering the thermal conductivity for the LPBF-fabricated AlSi10Mg in different studies, values of 90 [20], 119 [26], and 130 [22] W/mK (along the building direction) were reported for the non-preheated condition. This clearly shows the role that other variables may have played.

In the case of pure Al, preheating could eliminate the need for post-build heat treatment. For AlSi10Mg and AlSi12, the thermal conductivities of the preheated samples in the as-built condition are equal and greater than those reported for die-cast AlSi10Mg (~160

W/mK) [21] and AlSi12 (120 W/mK) [33], respectively. Nevertheless, the post-build heat treatment cannot be ignored for Al alloys. In other words, it is still possible to further enhance the thermal conductivity of AlSi12 and AlSi10Mg alloys printed in this study by ~20 and ~12% by employing a suitable post-build heat treatment cycle to reach the nominal values of 170 [25] and 185 [20] W/mK reported for their wrought and heat-treated LPBF-fabricated parts, respectively.

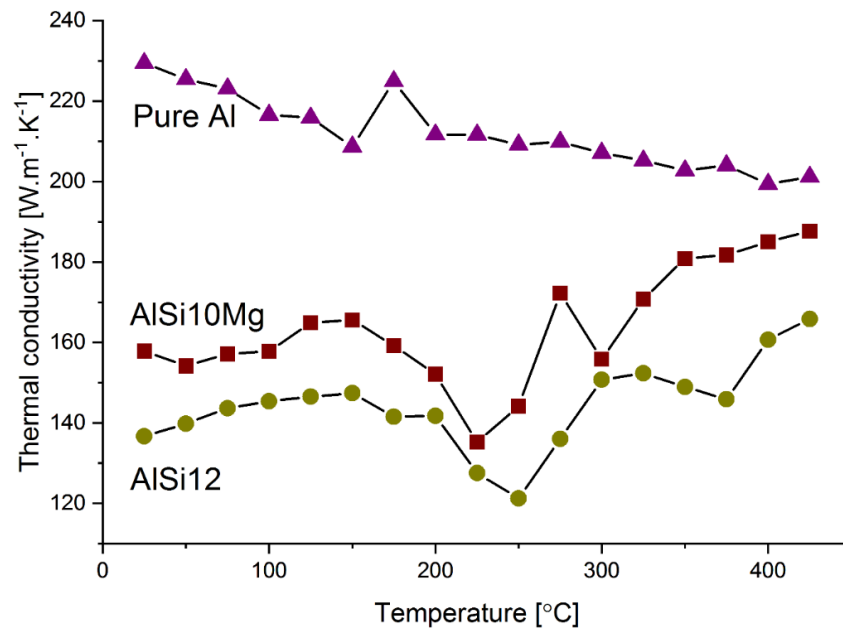


Figure 4.5. Thermal conductivity results versus temperature for pure Al, AlSi12, and AlSi10Mg.

4.3.2 Microstructure

The microstructure of pure Al, AlSi12, and AlSi10Mg parts was studied at three different levels, namely, (i) grain structure, (ii) solidification mode within the grains, and (iii) phases present in the final microstructure. The contribution of each microstructural feature to the electron scattering will be discussed in section 4.4. It should be highlighted that the microstructure of the LPBF fabricated Al/Al alloys is investigated in the as-built condition, not after experiencing the thermal cycle of DSC, dilatometry, or laser flash analysis.

4.3.2.1 Grain structure

The microstructural overview of the printed parts is provided in Figure 4.6(a-c), where almost semi-circular features overlapping each other are perceptible. Judging from their width, which is in the order of the laser beam spot size, they are cross-sections of the laser scan tracks. To have a solid understanding of the grain structure of each material, EBSD analysis was performed, with the results provided as inverse pole figure maps (IPF-Z) in Figure 4.6(d-f). The microstructure of the pure Al sample can be distinguished from the Al alloys by considering its columnar grain structure (Figure 4.6(d)). Both "competitive growth" and "epitaxial growth" phenomena [34] conspired during the layer-wise manufacturing of pure Al samples to result in the formation of columnar grains. Although both phenomena played a role during the LPBF processing of AlSi12 and AlSi10Mg alloys, such grain structure is absent in the IPF-Z maps shown in Figure 4.6(e, f). This is attributable to the segregation of alloying elements (e.g., Si, Mg, and Fe) during the solidification, leading to a constitutionally undercooled liquid region near the solidification front where the level of undercooling exceeds the critical undercooling required for the nucleation of new crystals. The nucleation of new equiaxed grains impedes further growth of columnar grains and results in a columnar to equiaxed transition of the grain structure at the top of the melt pools (Figure 4.6(e,f)). It is of note that the nucleation of new grains rather than the growth of the previous ones can also become feasible at the melt pool boundaries due to the high thermal gradient at the early stages of the solidification. The dominance of the extremely large columnar grains in the microstructure of the LPBF-processed pure Al as well as the simultaneous presence of equiaxed and columnar grains in the microstructure of AlSi10Mg and AlSi12 alloys have also been reported in the literature [35-37].

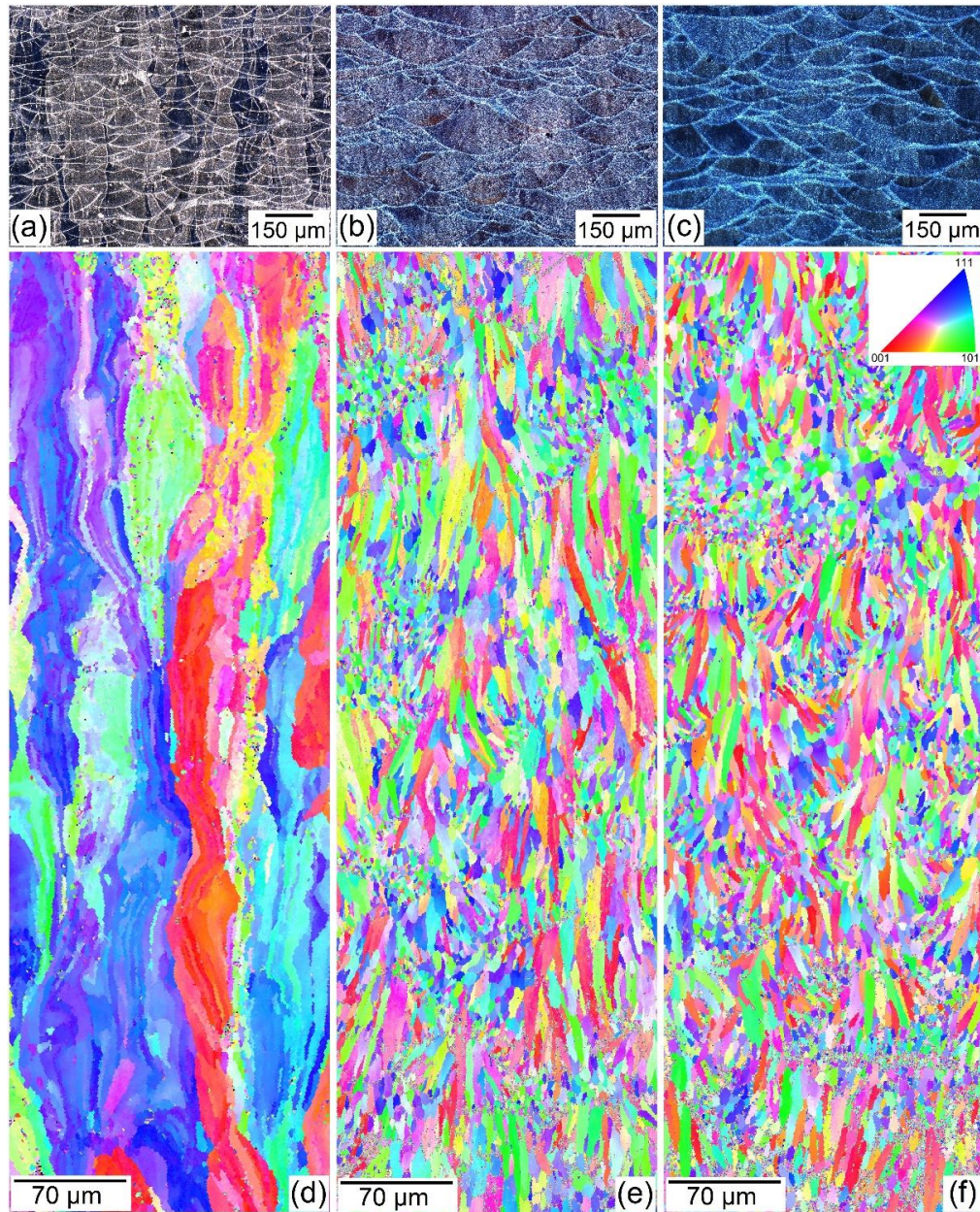


Figure 4.6. Optical micrographs of cross-sections parallel to the building direction for (a) pure Al, (b) AlSi12, and (c) AlSi10Mg. The EBSD IPF-Z maps for the respective materials are shown in (d), (e), and (f).

4.3.2.2 *Microstructure within grains*

SEM micrographs in Figure 4.7 show the details of the microstructure for pure Al/Al alloys. The microstructural observations for pure Al confirm the absence of cellular/dendritic features, giving evidence of planar solidification mode (Figure 4.7(a) and (b)). Referring to Figure 4.7(a), no difference was found between the microstructures of the track borders and interiors. No sign of cellular/dendritic solidification mode was detected even at higher magnifications (Figure 4.7(b)). The microstructural details of AlSi12 and AlSi10Mg shown in Figure 7(c, d) and (f, g) reveal that an ultrafine, textured, divorced eutectic cellular microstructure has been developed due to the rapid solidification. This means that adding Si and/or Mg to Al has led to the instability of the solidification front and deviation in the solidification mode from planar (in pure Al) to cellular. The reason behind such a deviation can be scrutinized by knowing the solidification parameters such as thermal gradient (G) and growth rate (R) of the solidification front during the LPBF process. The G/R ratio determines the mode of solidification [34]. Based on the solidification front instability criterion, the planar mode is only possible when the G/R ratio is greater than a critical value defined as follows for a binary system [38]:

$$\left(\frac{G}{R}\right)_{Critical} = \frac{\Delta T}{D_L} \quad \text{Eq. (3)}$$

in which ΔT and D_L are the solidification range and solute diffusivity in the liquid material, respectively. Although both Al alloys feature a narrow solidification range (especially AlSi12), the relatively slow diffusivity of Si/Mg causes the $(G/R)_{critical}$ to be higher than the (G/R) values achieved during the LPBF process. To find the ΔT for AlSi12 and AlSi10Mg alloys, Scheil-Gulliver solidification modeling (SGSM) was utilized (Figure 4.7(e,h)). According to Figure 4.7(e,h), $\Delta T = 40$ K and 6 K for AlSi10Mg and AlSi12 alloys,

respectively. Qin et al. [39] implemented a first principal molecular dynamic simulation to predict the self-diffusivity of Si in binary Al-Si molten alloys at high levels of overheating (at $T=1823$ K corresponding to 970 K overheating for AlSi12 and AlSi10Mg alloys), which is the case for the LPBF process. Based on their results, the D_L of Si in molten Al-10wt.%Si (assumed to be the same as AlSi10Mg) and Al-12wt.%Si binary alloys is 9×10^{-9} and 8.7×10^{-9} m²/sec, respectively. Therefore, the $(G/R)_{critical}$ would be 4.4×10^9 and 6.9×10^8 K.s.m⁻² for AlSi10Mg and AlSi12, respectively. These $(G/R)_{critical}$ values are higher than the (G/R) values for the LPBF-processed AlSi10Mg (in the range of 2.18×10^9 to 8.4×10^8 K.s.m⁻²) [15] and AlSi12 ($\sim 10^6$ K.s.m⁻², as derived from the cooling rate simulation) [40] alloys. Thus, planar solidification mode conditions cannot be satisfied, and cellular microstructure is developed. It is worth noting that the cellular structure of the AlSi12 and AlSi10Mg scan track borders are different from their interior (Figure 4.7(c) and (f)) owing to the formation of the partially melted zone and heat affected zone as a result of the thermal cycle of the subsequent track(s) on the previous one(s).

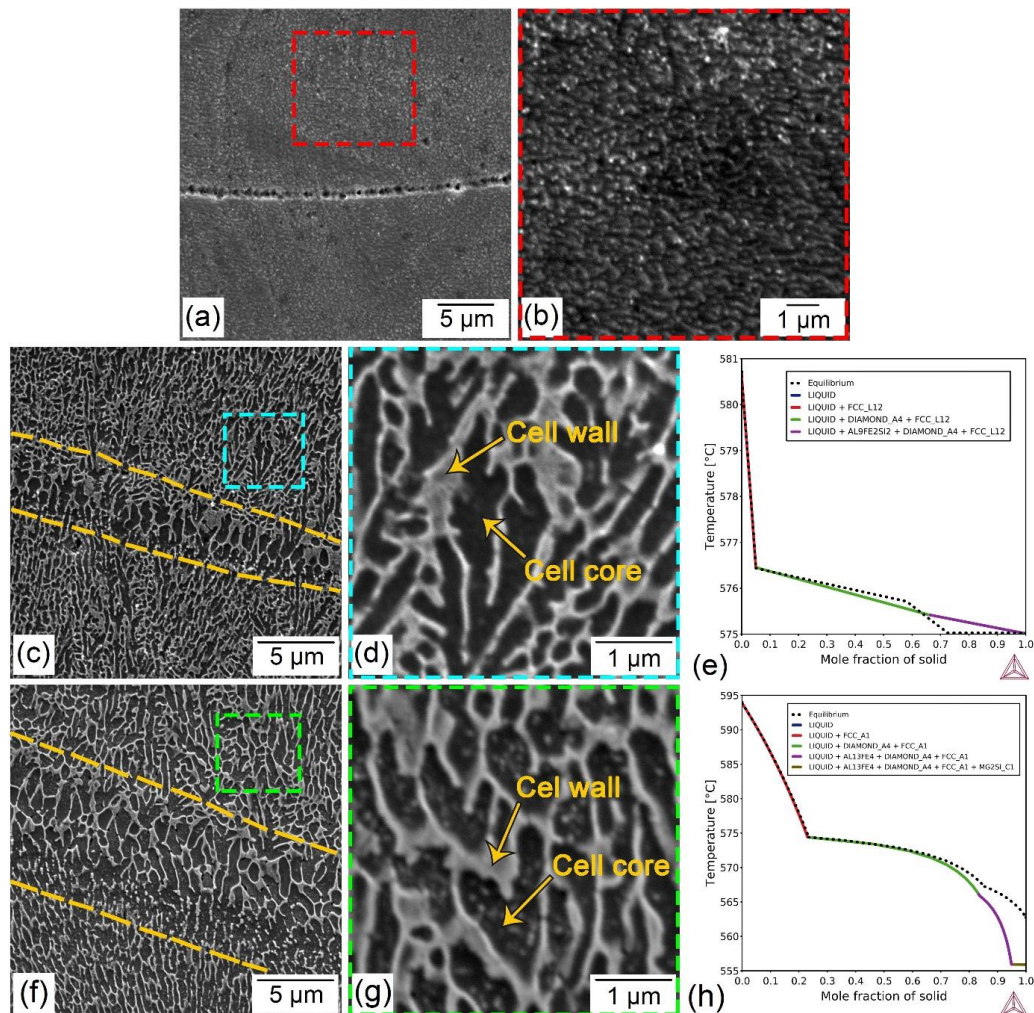


Figure 4.7. SEM micrographs of (a,b) pure Al, (c,d) AlSi12, and (f,g) AlSi10Mg. The images provided in (b), (d), and (g) are the higher magnifications of regions designated by the dashed box in (a), (c), and (f), respectively. The Scheil Gulliver solidification modeling (SGSM) for AlSi12 and AlSi10Mg are shown in (e) and (h), respectively.

4.3.2.3 Identification of micro- and nano-constituents

For in-depth investigation of the existing micro- and nano-constituents, samples were subjected to TEM imaging and EDS elemental analysis, as shown in Figure 4.8, Figure 4.9, and Figure 4.10. The bright-field image in Figure 4.8(a) shows the overview of the pure Al TEM sample encompassing a few grains, with arrows indicating the grain boundaries. There are also some features in the vicinity of the grain boundary that are distinguishable

from α -Al and are shown with higher magnification in Figure 4.8(b). As it is evident, these are dislocations with random size and orientation pinned by ultra-fine precipitates. The bright-field images in Figure 4.8(c) and (d) show these precipitates at higher magnifications. The high-angle annular dark-field scanning transmission electron microscopy (HAADF-STEM) image in Figure 4.8(e) and the EDS elemental mapping results in Figure 4.8(f, g) revealed that these almost spherical nano-size precipitates are aluminum oxide (i.e., Al_2O_3). Based on the size measurement performed by ImageJ software (Figure 4.8(h)), the mean size of oxides is 28.9 nm, and none of them exceeds 70 nm. Figure 8(i, j) shows the EBSD grain boundary map and its corresponding geometrically necessary dislocation (GND) map. A maximum disorientation angle of 5° and Burger's vector of 2.86 \AA were assumed to generate the GND map, in which the average GND density was $4.6 \times 10^{13} \text{ m}^{-2}$.

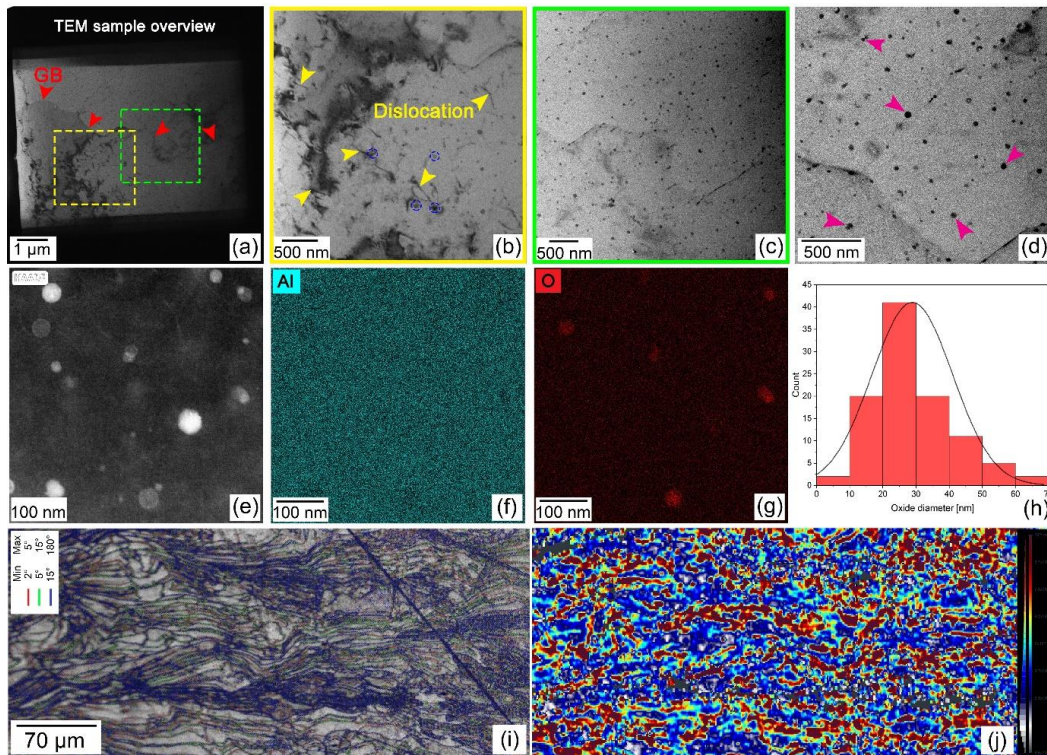


Figure 4.8. Pure Al samples: Bright-field TEM images showing (a) the TEM sample overview, (b) dislocations, and (c,d) oxides. The HAADF STEM image and EDS elemental mapping results for Al and O are shown in (e-g), respectively. (h) The size distribution of nano-size oxides observed in (c,d). (i,j) The EBSD grain boundary map and its corresponding geometrically necessary dislocation (GND) map.

The bright-field image in Figure 4.9(a) shows the overview of the AlSi12 TEM sample with a cellular structure, as also confirmed by SEM micrographs shown in Figure 4.7(c,d). It can be inferred from the high magnification bright-field images shown in Figure 4.9(b-d) that (i) the cell regions are almost free from precipitates, (ii) the inter-cellular region contains a high volume fraction of discrete nano-size precipitates, and (iii) dislocations are mainly located near the cell walls. It should be noted that a few nano-size precipitates were observed within cells (Figure 4.9(e)). However, they were absent in most of the cells (Figure 4.9(a-c)). Regarding dislocations, imaging at different tilt angles (not shown here) proved that the cell regions are almost free from dislocations. According to the EDS

elemental map analysis results (Figure 4.9(f-i)) taken from the region shown in Figure 4.9(e), it can be understood that the inter-cellular region mainly consists of discrete nano-size Si precipitates having α -Al in between. Moreover, some Fe-rich precipitates and a few oxides were also detected in the inter-cellular region. The cell region is α -Al (Figure 4.9(f)) which has 2.4 at% Si based on the point EDS analysis result shown in Figure 4.9(j,k). The EBSD grain boundary map and its corresponding geometrically necessary dislocation (GND) map are provided in Figure 4.9(l, m). With the same disorientation factor and Burger's vector size as those for pure Al, the average GND density was $1.3 \times 10^{14} \text{ m}^{-2}$.

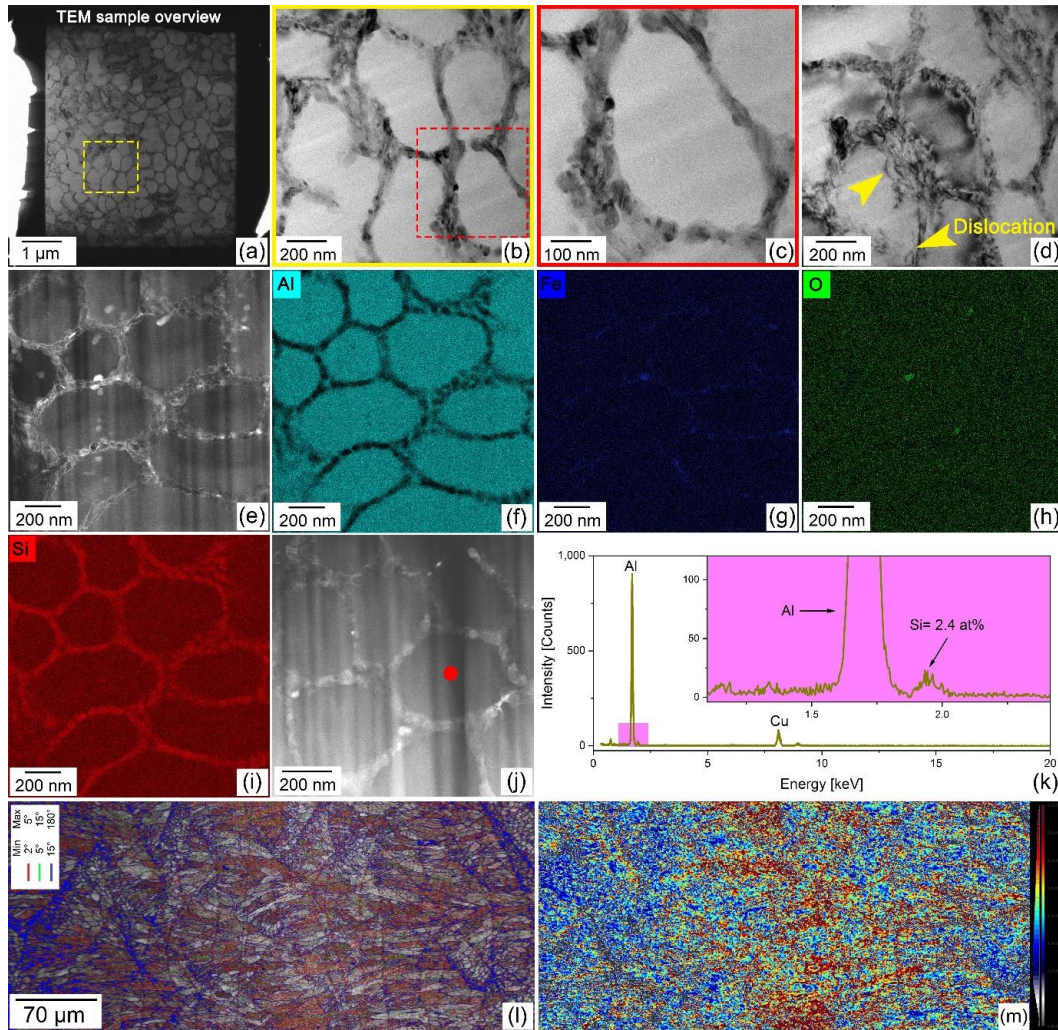
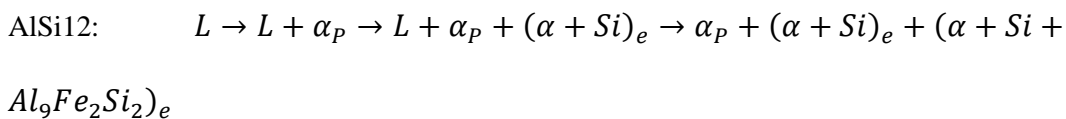


Figure 4.9. AlSi12 sample: Bright-field TEM images showing (a) TEM sample overview, (b,c) cells and cell boundaries, and (d) dislocations. The EDS elemental map analysis performed on HAADF image (e) showing the distribution of (f) Al, (g) Fe, (h) O, and (i) Si elements. (j,k) The point EDS analysis location and spectrum. (l,m) The EBSD grain boundary map and its corresponding geometrically necessary dislocation (GND) map.

To grasp a better idea about the identified phases and the reason behind such a solidification path, the SGSM results were considered. According to the SGSM results shown in Figure 4.7(e), the solidification path of AlSi12 (Al-12wt%Si-0.25wt%Fe) should be as follows:



The solidification in AlSi12 starts with the formation of the primary α -Al phase (α_p) at ~ 581 °C. The formation of α_p as the primary solidification product in which the solubility of Si and Fe elements are negligible (equilibrium partition coefficient of 0.12 and 0.008, respectively) is accompanied by the enrichment of the remaining liquid phase from these elements, encouraging the Al-Si pseudo-binary eutectic reaction in the intercellular region from 576.3 to 575.3 °C. Thus, the cell walls are mainly composed of the binary eutectic $(\alpha + Si)_e$, consistent with the EDS elemental map analysis results in Figure 4.9(f,i). Finally, the Fe concentration in the inter-cellular region reaches a critical value that triggers the Al-Si-Fe ternary eutectic reaction, resulting in the formation of $(\alpha + Si + Al_9Fe_2Si_2)_e$ phases. Therefore, the Fe-rich phase shown in Figure 4.9(g) is most probably $Al_9Si_2Fe_2$. It should be noted that some oxides were also rarely observed in the inter-cellular region, the nature of which could not be confidently identified by the EDS analysis.

The bright-field image in Figure 4.10(a) shows the overview of the AlSi10Mg TEM sample. A cellular structure, as observed in SEM micrographs (Figure 4.7(f,g)), is discernable in this image. The high magnification bright-field images shown in Figure 4.10(b-d) give evidence that (i) the cell regions contain two different nano-size phases with equiaxed and needle-type morphologies, (ii) the inter-cellular region contains a high volume fraction of discrete nano-size precipitates, and (iii) dislocations are more concentrated near the cell walls, though some could also be observed in the cell regions. The HAADF-STEM image in Figure 4.10(e) shows where the EDS elemental map analysis was performed to get a general idea about the present phases. Based on Figure 4.10(f-j), the inter-cellular region is mainly composed of Si precipitates with Fe-rich, Mg-rich, and oxide phases randomly dispersed among them. By excluding the nano-size phases, cell cores are α -Al with a minor amount of Mg and 1.9 at% Si, as determined by the point EDS

analysis results shown in Figure 4.10(k,i). The EDS elemental map analysis was also performed at high magnifications within a cell to characterize the observed nano-size precipitates. As shown in Figure 4.10(m-p), the equiaxed and needle-type phases are Si and Mg₂Si precipitates, respectively, as also reported elsewhere [41]. This means that the applied preheating could successfully reduce the supersaturation level of the α -Al matrix and provide favorable conditions for the alloying elements to precipitate out. According to the size measurement performed by ImageJ, the mean diameter and length of Si and Mg₂Si phases within the cells are 24.5 and 119 nm, respectively. The maximum characteristic size of the respective phases was 50 and 252 nm. With the same approach for pure Al and AlSi12 alloy, the average GND density was $6.5 \times 10^{13} \text{ m}^{-2}$.

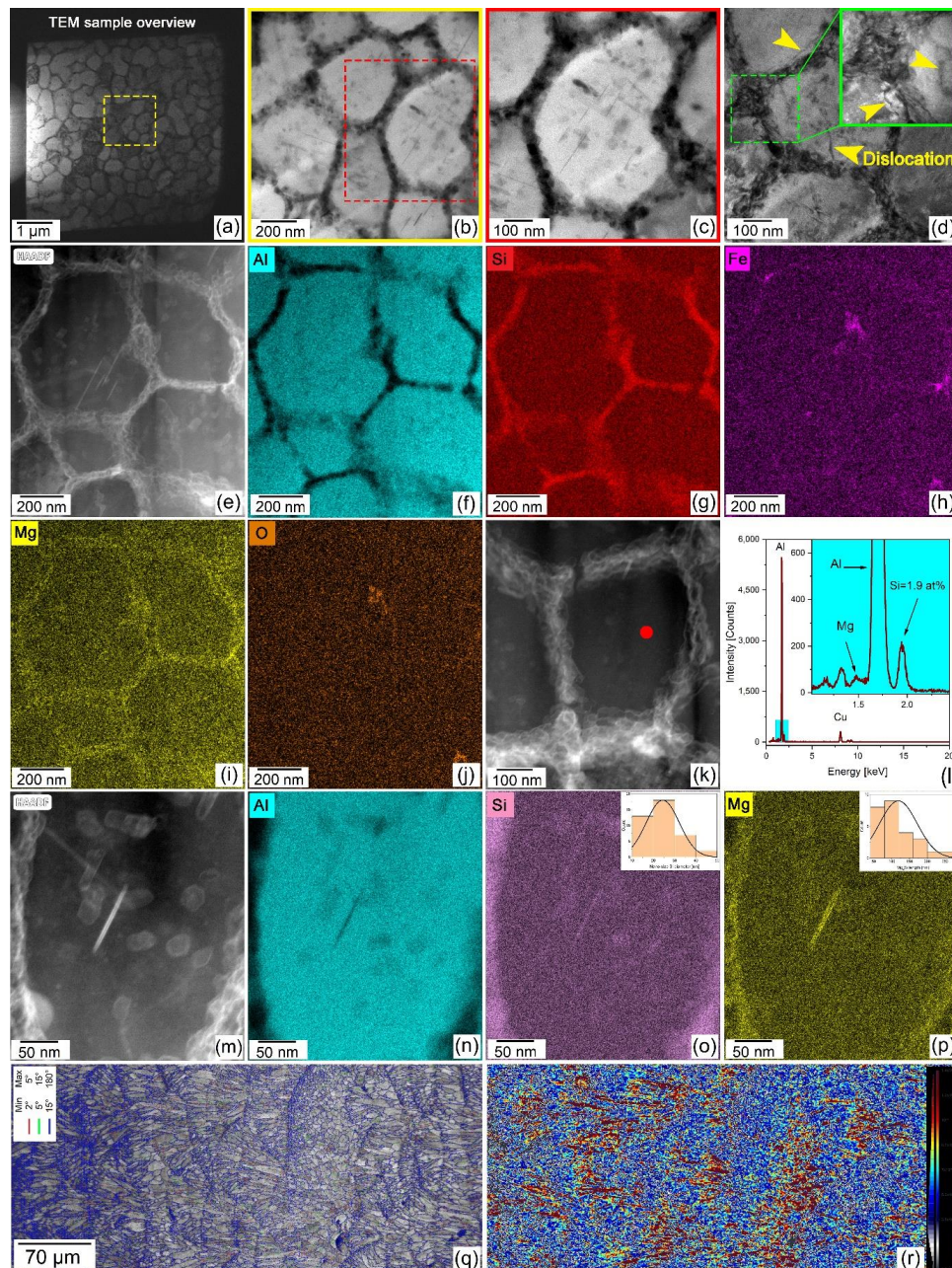
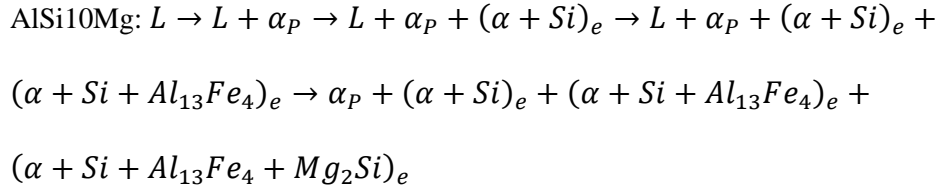


Figure 4.10. AlSi10Mg sample: Bright-field TEM images showing (a) TEM sample overview, (b,c) cell walls and phases within cells and (d) dislocations. The EDS elemental map analysis performed on the HAADF image in (e) showing the distribution of (f) Al, (g) Si, (h) Fe, (i) Mg, and (j) O elements. (k,l) The point EDS analysis location and spectrum. The EDS elemental map analysis performed on the HAADF image in (m) showing the distribution of (n) Al, (o) Si, and (p) Mg elements in the phases observed within cells. (q,r) The EBSD grain boundary map and its corresponding geometrically necessary dislocation (GND) map.

The SGMS result shown in Figure 4.7(h) suggests the following solidification sequence for AlSi10Mg alloy (Al-10wt%Si-0.35wt%Mg-0.25wt%Fe):



The first and second stages of solidification in AlSi10Mg are the same as those explained for AlSi12, with the only difference being the temperature ranges within which these reactions happen (~594-574 °C for α_P formation and ~574-566 °C for pseudo-binary reaction). In the third stage, the accumulated Fe, which had not participated in any reactions, leads to a pseudo ternary eutectic reaction (Al-Si-Fe), with solidification products being $(\alpha + Si + Al_{13}Fe_4)_e$. Therefore, the Fe-rich solidification product shown in Figure 4.10(h) should be $Al_{13}Fe_4$ based on the SGMS results. However, the Fe-rich phases were reported to be Al_3FeSi and $Al_8FeMg_3Si_6$ intermetallics based on the equilibrium Al-10Si-0.33Mg-0.55Fe (wt%) equilibrium isopleth calculated by FactSage [42]. Because of this discrepancy between the SGSM results and FactSage equilibrium calculations, one cannot be confident about the nature of the observed Fe-rich phase. Although the SGSM results can better resemble the solidification condition during the LPBF process, this phase is referred to as Al-Si-Fe intermetallic hereafter. The solidification of AlSi10Mg terminates by a quaternary reaction in which $(\alpha + Si + Al_{13}Fe_4 + Mg_2Si)_e$ solidification products are formed. If accepting that the Fe-rich phase in Figure 4.10(h) is $Al_{13}Fe_4$, then the (Mg,Si)-rich phase observed in the inter-cellular region in Figure 4.10(i) is Mg_2Si . But, if it is $Al_8FeMg_3Si_6$ intermetallic (containing Mg element), the fourth stage of solidification has not even happened during the LPBF process. In other words, the fast-growing solidification front has captured Mg and mitigated the

enrichment of the remaining liquid phase from this element, eliminating the chance of Al-Si-Mg-Fe quaternary eutectic reaction. Therefore, the Si and Mg_2Si nano-size precipitates observed within the cells (Figure 4.10(c)) should not be mistaken for the binary and quaternary reaction products since these phases are not located in the inter-cellular region. These phases were formed through solid-state reactions during the cooling stage or printing of the subsequent layers.

TEM images can provide valuable information about the nature and size of oxides in pure Al and Al alloys, as shown in Figure 4.8(c-h), Figure 4.9(h), and Figure 4.10(j). However, to have a general idea about the total oxygen content in the printed parts, the measurements have to be performed at the part-scale level. Figure 4.11 shows the oxygen content of the pure Al, AlSi12, and AlSi10Mg samples. These oxygen contents are remarkably lower than those of the starting powders (2260, 1299, and 740 for pure Al, AlSi12, and AlSi10Mg, respectively). The reason behind this observation is thoroughly explained in a study conducted by the same authors [10]. In short, it was found that the rate of diminishment of nano-size oxides is extremely higher than the oxidation rate due to the extremely short laser/melt interaction time, the low oxygen content of the chamber, and surface evaporation of the melt pool covered by nano-size oxides.

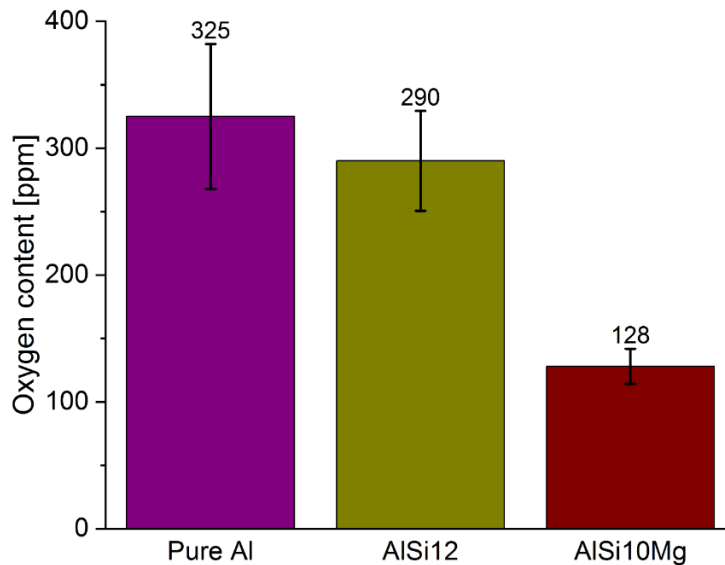


Figure 4.11. The oxygen content of pure Al, AlSi12, and AlSi10Mg samples.

4.4 Discussion

4.4.1 Electron mean free path at room temperature

Heat can be transferred either by electrons or lattice vibrations (phonons as heat carriers). In metallic materials, the main mechanism governing the heat transfer is the movement of valance electrons with high energy from the warmer regions to the cooler ones [11]. During their journey, electrons face obstacles known as scattering sites. The scattering phenomena can be divided into two categories of intrinsic and extrinsic events [43]. While intrinsic scattering events such as thermally-induced vibration of atoms (phonon scattering) are mainly material-dependent [44], the extrinsic ones are highly sensitive to the processing condition. Referring to the microstructural features shown in Figure 4.8, Figure 4.9, and Figure 4.10, along with the XCT results (Figure 4.2), the extrinsic scattering sites in the LPBF-fabricated Pure Al, AlSi12, and AlSi10Mg alloys are (i) Si element in the supersaturated α -Al matrix in Al alloys, (ii) non-equilibrium vacancies and dislocations,

(iii) nano-size Si and Mg₂Si precipitates in the cell regions of AlSi10Mg, (iv) copious cell boundaries due to the formation of an ultrafine, textured, divorced eutectic cellular microstructure in Al alloys, (v) oxides in pure Al, (vi) grain boundaries, and (vii) porosities. The mean free path is the average distance between two consecutive scattering sites. The electron mean free path (l_e) can be calculated as follows [44]:

$$l_e = V_F \tau \quad \text{Eq. (4)}$$

where V_F and τ are the velocity of electrons above the Fermi level and the average time between two subsequent electronic collisions, respectively. The V_F in Eq. (4) can be calculated by:

$$V_F = \sqrt{\frac{2E_f}{m_e}} \quad \text{Eq. (5)}$$

in which E_f and m_e are the Fermi energy and mass of electrons, respectively. τ in Eq. (4) can be calculated as follows [44]:

$$\tau = \frac{m_e}{\rho n e^2} \quad \text{Eq. (6)}$$

in which ρ , n , and e are the electrical resistivity, number of atoms per volume, and electron charge, respectively. ρ in Eq. (6) can be accurately estimated by the Wiedemann-Franz law as [45]:

$$\rho = \frac{T}{3K} \left(\frac{\pi k}{e} \right)^2 \quad \text{Eq. (7)}$$

in which T is the absolute temperature, K is thermal conductivity, and k is the Boltzmann constant. By using Eq. (4)-(7) and the input data provided in Table 4.1, l_e can be calculated.

Depending on the input data, either the intrinsic or combination of intrinsic and extrinsic scattering events can be taken into account. For instance, upon using the theoretical data available in the literature for highly pure and defect-free pure Al with equilibrium microstructure and large grains, the l_e value would only represent the intrinsic scattering (phonon scattering) during the heat transfer. However, for the LPBF-fabricated parts, the obtained l_e is the aftermath of both intrinsic and extrinsic scattering phenomena. Since the literature has proven that the contribution of phonons as heat carriers (not as scattering sites) is negligible in pure Al [46], it is not considered in the calculations provided in Table 4.1 for Al/Al alloys.

Table 4.1. Parameters used to calculate the electron mean free paths for the LPBF-fabricated pure Al, AlSi12, and AlSi10Mg and theoretical mean free paths for pure Al.

Parameters/electron mean free path	LPBF-fabricated			Theoretical-Pure Al
	Pure Al	AlSi12	AlSi10Mg	
Boltzmann constant [m ² .Kg/s ² .K]	1.3806×10 ⁻²³			
electron charge [c]	1.602×10 ⁻¹⁹			
electron mass [kg]	9.11×10 ⁻³¹			
Al lattice parameter [Å]	4.048 [47]			
Atomic density [atom/m ³]	^a 6.031×10 ²⁸			
Free electron density [e/m ³]	^a 1.809×10 ²⁹			
Fermi level energy at 295 K [J]	^a 3.477×10 ⁻¹⁹ [48]			
Electron velocity at Fermi level [m/s]	*873691			
electrical resistivity [Ω.m]	^b 3.166×10 ⁻⁸	^b 5.315×10 ⁻⁸	^b 4.608×10 ⁻⁸	2.71×10 ⁻⁸ [49]
Time between subsequent collisions [s]	1.859×10 ⁻¹⁴	1.107×10 ⁻¹⁴	1.277×10 ⁻¹⁴	2.180×10 ⁻¹⁴
Electron mean free path [nm]	16.2	9.7	11.1	^c 19

^a Due to the lack of data on AlSi12 and AlSi10Mg alloys, values for pure Al were also used for Al alloys.

^b The electrical resistivity for the LPBF-fabricated parts was calculated using Eq. (7).

^c The estimated electron mean free path for pure Al is very close to the values reported in the literature, i.e., 18.9 nm [50] and 22.7 nm [48].

Some important inferences can be drawn from the mean free path calculation results in Table 4.1. First, the l_e of the LPBF-fabricated pure Al (16.2 nm) is considerably greater than those of AlSi10Mg (11.1 nm) and AlSi12 (9.7 nm). The l_e values are consistent with the results shown in Figure 4.4 and Figure 4.5, in which materials with smaller l_e values showed lower thermal diffusivity and conductivity. The absence of foreign atoms in pure Al is the main reason behind its higher l_e and thermal diffusivity/conductivity compared to the Al alloys. Second, based on the theoretical calculations for pure Al, in which the scattering events are only dictated by intrinsic phenomena, the l_e value is in the nanometer length scale. On this account, it can be inferred that extrinsic scattering phenomena at such length scales or smaller could have a major influence on the obtained overall mean free path in the LPBF-fabricated parts. Finally, the theoretical l_e value for pure Al was ~15% lower than the one calculated for the LPBF-fabricated pure Al, meaning that the extrinsic scattering phenomena are not extremely strong in this case.

4.4.2 Contribution of extrinsic scattering phenomena at room temperature

As a general rule, the inverse mean free paths of electrons (l_e in Table 4.1) for different scattering events are additive [51]. In light of this scenario and consideration of the micro-/nano-constituents shown in Figure 4.8-Figure 4.10, the following general equation can be written for the LPBF-fabricated pure Al, AlSi12, and AlSi10Mg:

$$\left(\frac{1}{l_e}\right)_{LPBF} = \left(\frac{1}{l_e}\right)_{theoretical}^{Al} + \frac{1}{l_{pore}} + \frac{1}{l_{gb}} + \frac{1}{l_{cb}} + \frac{1}{l_{oxide}} + \frac{1}{l_{Si}} + \frac{1}{l_{Mg_2Si}} + \frac{1}{l_{vac}} + \frac{1}{l_{dis}} + \frac{1}{l_{SS}^{Si}} \quad \text{Eq. (8)}$$

in which l_{pore} , l_{gb} , l_{cb} , l_{oxide} , l_{Si} , l_{Mg_2Si} , l_{vac} , l_{dis} , and l_{SS}^{Si} denote the mean free path of electrons when scattering sites are porosities, grain boundaries, cell boundaries in Al alloys,

Al₂O₃ oxides in pure Al, nano-size Si precipitates within the cells of AlSi10Mg, nano-size Mg₂Si phase within the cells of AlSi10Mg, atomic vacancies, dislocations, and Si atoms supersaturated in the α -Al matrix of Al alloys, respectively. It is worth noting that the contribution of oxides and ternary/quaternary phases in Al alloys on the scattering of electrons is embedded in the l_{cb} since these precipitates are located at the cell boundaries (Figure 4.9(g,h) and Figure 4.10(h,j)). The data required to calculate the l_i for each scattering phenomenon are shown in Figure 4.12 and listed in Table 2. l_{gb} and l_{cb} were determined by performing grain (Figure 4.12(d-f)) and cell size (Figure 4.12(g,h)) measurements on IPF-Z EBSD maps (Figure 4.6) and TEM images (Figure 4.9 and Figure 4.10), respectively. For l_{oxide} , l_{Si} and l_{Mg_2Si} , the mean free path was defined as the mean chord length in the matrix phase (α -Al), determined from TEM images (e.g., Figure 4.8-Figure 4.10) taken from random locations. l_{pore} was defined as the mean chord length in the solid phase derived from the XCT data (Figure 4.12(a-c)). For l_{vac} , one of the approaches is to use the $n_v = n_0 \exp\left(\frac{-Q_v}{RT}\right)$ equation [52] to calculate the density of vacancies (n_v) at the desired temperature (T) by knowing the atomic density (n), the energy required to produce one mole of vacancies (Q_v), and the gas constant (R , 8.314 J.mol⁻¹.K⁻¹). However, the output of this equation is the density of vacancies at equilibrium conditions, which is not valid for materials subjected to non-equilibrium solidification and cooling. Based on this equation, n_v is significantly large at high temperatures. In non-equilibrium conditions, when the material is quenched to room temperature, most of these vacancies will remain. Near the melting point of the Al/Al alloys, the n_v/n_0 ratio was reported to be 1/1000 [11]. For l_{vac} calculations, it was assumed that the same ratio is valid for the LPBF-fabricated Al/Al alloys at room temperature due to the high cooling rates

associated with the manufacturing process. The magnitude of l_{vac} was estimated using the following equation [44]:

$$l_{vac} = \frac{1}{n_v \sigma_v} \quad \text{Eq. (9)}$$

in which n_v is the number of vacancies per unit volume and σ_v is the cross-section for the scattering of the electrons by vacancies (Table 4.2). The magnitude of n_v was determined by calculating the volume occupied by 1000 Al atoms (250 Al unit cells). For σ_v , the value reported by Khotkevich et al. [53] for a bulk specimen of polycrystalline Al was used to predict the l_{vac} of the LPBF-fabricated parts (Table 4.2).

With the same approach as that of vacancies, the contribution of dislocations to the electron scattering (l_{dis}) was calculated using the following equation [44]:

$$l_{dis} = \frac{1}{n_d \sigma_d} \quad \text{Eq. (10)}$$

where n_d is the dislocation density or total length of dislocations per unit volume and σ_d is the scattering cross-section of the electrons per unit length of dislocations. Referring to GND density measurement results provided in section 4.3.2.3, the magnitude of n_d for the LPBF-fabricated pure Al, AlSi12 and AlSi10Mg was found to be 4.6×10^{13} , 1.3×10^{14} , and $6.5 \times 10^{13} \text{ m}^{-2}$, respectively. Fiks [54] used the following formula to estimate σ_d :

$$\sigma_d = \frac{ne^2(\Delta\rho_d^*)}{mV_F} \quad \text{Eq. (11)}$$

in which $\Delta\rho_d^*$ signifies the resistivity per unit dislocation density [$\Omega \cdot \text{m}^3$]. The rest of the parameters have the same definition as before and are tabulated in Table 4.1. Raeisinia et al. [55] experimentally measured the magnitude of $\Delta\rho_d^*$ for Al at room temperature, the

result of which is shown in Table 4.2. By knowing all the parameters in above equation, σ_d and consequently the l_{dis} was calculated for the LPBF-fabricated pure Al, AlSi12, and AlSi10Mg, respectively (Table 4.2). Finally, l_{SS}^{Si} for AlSi12 and AlSi10Mg alloys was estimated as follows [44]:

$$l_{SS}^{Si} = \frac{1}{n_{SS}\sigma_{SS}} \quad \text{Eq. (12)}$$

in which n_{SS} is the number of solid solution Si atoms in the matrix per unit volume and the σ_{SS} is the cross-section for the scattering of the electrons by solid solution atoms. Referring to the point EDS analysis results shown in Figure 4.9(k) and Figure 4.10(l), 2.4 and 1.9 at% of Si exists in the α -Al matrix of the LPBF-fabricated AlSi12 and AlSi10Mg alloys, respectively. It means that among 100 atoms occupying 25 FCC unit cells (4 atoms per unit cell), 2.4 and 1.9 atoms are Si and the rest of them are Al in the respective materials, based on which n_{SS} was calculated. Couch et al. [56] measured the electron scattering cross section of non-magnetic impurities in Al foils. They reported σ_{SS} values in the range of $0.25\text{-}5 \times 10^{-20} \text{ m}^2$ for Au, Zn, Mg, Cu and Ag as solid solution impurities. Due to the lack of data on Si, the average value of $3 \times 10^{-20} \text{ m}^2$ was used for σ_{SS} calculation. By knowing the n_{SS} and σ_{SS} , the l_{SS}^{Si} was calculated for the LPBF-fabricated AlSi12 and AlSi10Mg, respectively (Table 4.2). The $(l_e)^{LPBF}$ values in Table 4.2 obtained from Eq. (8) are in great agreement with the ones directly calculated from Eq. (4)-Eq. (7) using the experimental data on thermal conductivity of the LPBF-fabricated Al/Al alloys, proving the accuracy of this method in predicting the electron mean free path.

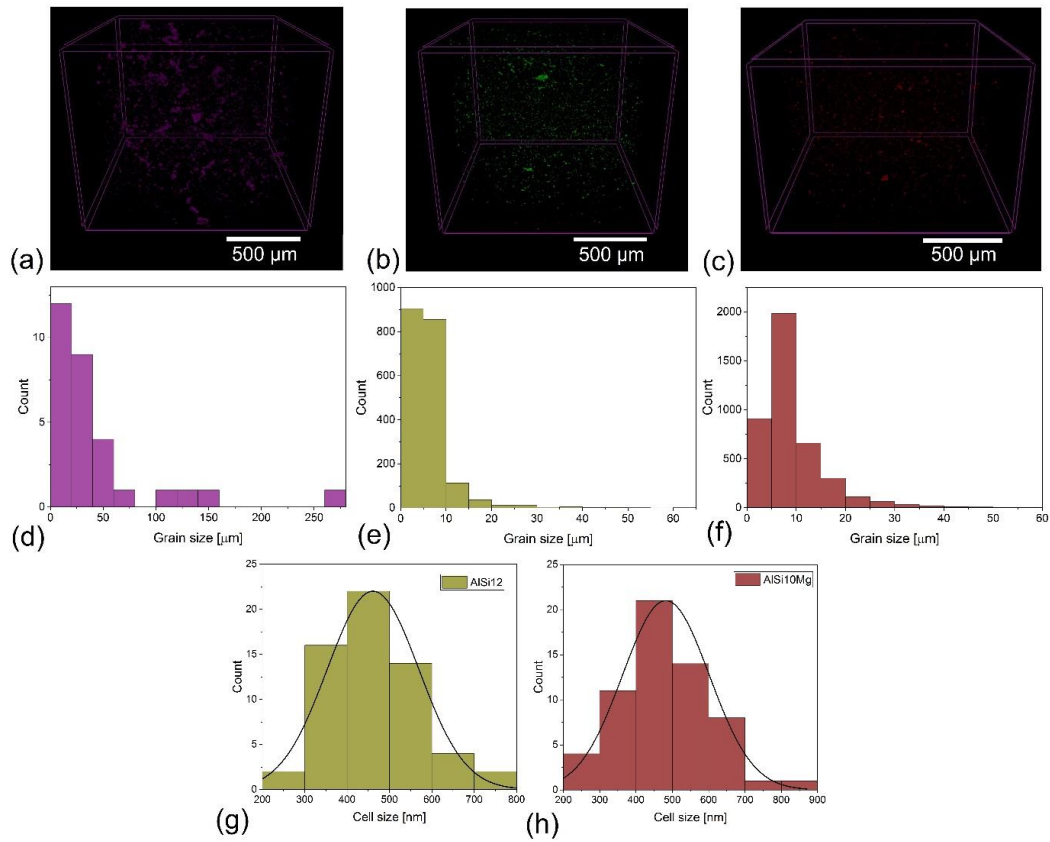


Figure 4.12. XCT results used to measure the mean chord length for (a) pure Al, (b) AlSi12, and (c) AlSi10Mg. The range of grain size and/or cell size for (d) pure Al (e,g) AlSi12 and (f,h) AlSi10Mg.

Table 4.2. Parameters used to calculate the electron mean free path in the presence of each extrinsic scattering site.

Parameters/mean free path of each extrinsic factor	Pure Al	AlSi12	AlSi10Mg
Density of vacancies, n_v [$1/m^3$]		6.03×10^{25}	
Scattering cross-section of electrons-vacancy, σ_v [m^2]		3.2×10^{-20}	
GND dislocation density [$1/m^2$]	4.6×10^{13}	1.3×10^{14}	6.5×10^{13}
Electrical resistivity per dislocation density, $\Delta\rho_d^*$ [$\Omega.m^3$]		2×10^{-24}	
Scattering cross-section of electrons-dislocation, σ_d [m]		1.17×10^{-8}	
Si concentration in α -Al matrix [at%]		2.4	1.9
Density of solid solution Si atoms in α -Al matrix, n_{ss} [$1/m^3$]	NA	1.477×10^{27}	1.146×10^{27}

Scattering cross-section of electrons-solid solution			
Si, σ_{SS} [m^2]	3×10^{-20}		
l_{pore} [μm]	190	283	193
l_{gb} [μm]	44.8 ± 55.6	6.5 ± 4.45	9.2 ± 6.33
l_{cb} [nm]	NA	461 ± 108.1	482 ± 119.4
l_{oxide} [nm]	245 ± 205.2		NA
l_{Si} [nm]		NA	139.8 ± 104.9
l_{Mg_2Si} [nm]	NA		449.2 ± 392.3
l_{vac} [nm]		518	
l_{dis} [nm]	1858	657	1315
l_{SS}^{Si} [nm]	NA	22.5	29.1
$(l_e)^{LPBF}$ [nm]	16.90	9.74	9.89

The contribution of each scattering phenomenon (intrinsic and extrinsic) to the overall mean free path of conducting electrons is obtained from the data listed in Table 4.2 (contribution = $\frac{1/l_i}{(1/l_e)^{LPBF}}$) and is shown in Figure 4.13. Valuable information can be obtained from the results listed in Table 4.2 and provided in Figure 4.13. Before anything else, it should be noted that pores and grains are the weakest extrinsic scattering sites in all materials because their length scale is in the order of μm , while the intrinsic scattering phenomena are happening on the nanometer length scale (their contribution is not shown in Figure 4.13). For pure Al, the rest of the extrinsic scattering sites are more or less affecting the thermal conductivity, and their contribution is not insignificant. With that being noted, the nano-size Al_2O_3 observed in TEM images (Figure 4.8) with the lowest mean chord length in the matrix is the most important contributing factor (6.9%). This is the main reason behind the difference observed between the thermal conductivity of the LPBF-fabricated pure Al part (~ 231 W/mK) and its nominal value (237 W/mK [24]). Vacancies and dislocations are the next two important extrinsic scattering sites with contributions of 3.2 and 1%, respectively.

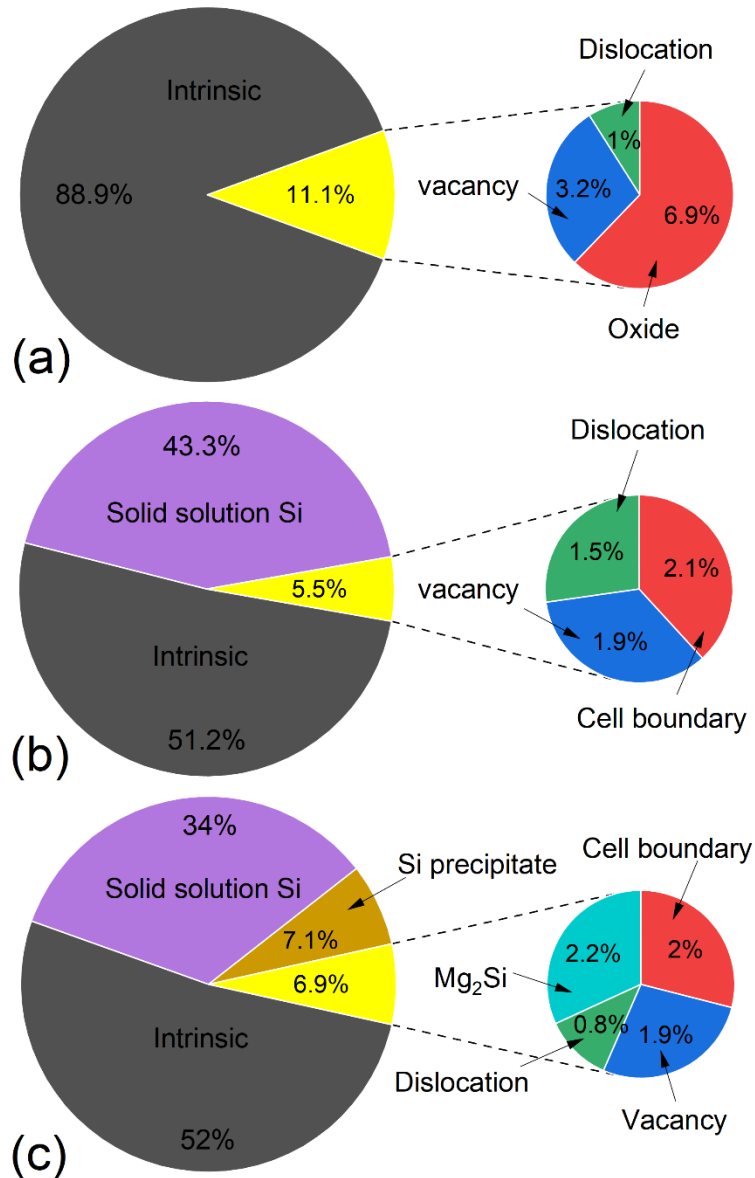


Figure 4.13. Contribution of intrinsic and different extrinsic scattering phenomena for the LPBF-fabricated: (a) Pure Al, (b) AlSi12, and (c) AlSi10Mg. Since being negligible, the contributions of pore and grain boundary are not shown for all materials.

For Al alloys, the supersaturation of Si in the α -Al matrix is by far the most important extrinsic scattering site with a contribution of 43.3% (AlSi12) and 34% (AlSi10Mg), comparable to that of the intrinsic scattering by phonons. This is the main reason behind

the difference observed between the obtained thermal conductivity for AlSi12 (~140 W/mK) and AlSi10Mg (~160 W/mK) alloy and their nominal values (170 and 185 W/mK for the respective materials). Among the other factors playing a minor role in the lower thermal conductivity of the AlSi10Mg part, the nano-size Si precipitates within the cells have the highest impact (7.1%). Yet the l_{Si} is one order of magnitude greater than l_{SS}^{Si} and cannot compete with the solid solution Si atoms in terms of scattering strength. In other words, given that there is a mixture between Al and Si elements in an atomic scale in the supersaturated α -Al matrix, these Si atoms are the most detrimental extrinsic scattering sites. This agrees with the findings of a study conducted by Cauwenbergh et al. [57], which showed that the electrical resistivity of AlSi10Mg was directly proportional to the Si supersaturation level. The overall contribution of dislocations, vacancies, cell boundaries, and Mg₂Si (only in AlSi10Mg) to the scattering of electrons was found to be 5.5% and 6.9% for AlSi12 and AlSi10Mg, respectively. Therefore, it is fair to conclude that they did not play a significant role in decreasing the $(l_e)^{LPBF}$ of LPBF-fabricated Al alloys. Yang et al. [20] suggested that the contribution of cell boundaries in electron scattering cannot be ignored as copious cell boundaries exist within the microstructure of the LPBF fabricated AlSi10Mg alloy. However, the l_{cb} measurements revealed that this value is one order of magnitude greater than the l_e value for Al/Al alloys (Table 4.1) and therefore, its contribution is negligible (Table 4.2 and Figure 4.13) compared to those of the solid solution Si and nano-size Si precipitates.

Results shown in Table 4.2 and Figure 4.13 also provide valuable insights into the main reasons behind the higher thermal conductivity of as-built Al/Al alloys in this study (preheated) than the non-preheated counterparts reported in the literature. Previously, Kimura et al. [19] reported thermal conductivity of ~200 W/mK for the as-built pure Al

(non-preheated) with an oxygen content of 1240 ppm. According to the oxygen content measurements provided in Figure 4.11, the optimum pure Al part in this study has 325 ppm oxygen. Therefore, the considerably lower oxygen content of the optimized pure Al part in this study, along with the lower density of dislocations obtained by preheating, justifies the higher thermal conductivity (31 W/mK). While acknowledging that the contribution of dislocations in the non-preheated condition might be higher, it is still logical to conclude that the reported improvement in thermal conductivity of the post-build heat-treated pure Al samples (from 200 to 240 W/mK) in [19] is not merely due to the elimination of dislocations or formation of larger grains, as stated by the authors. The coalescence of the high population of existing nano-size oxides (higher than the oxides of the pure Al sample printed in this study) and a significant increase in their mean chord length in the matrix is another missing factor that can explain such an improvement. As the l_{oxide} in pure Al is tremendously lower than l_{gb} and considerably lower than l_{dis} (Table 4.2), it can be inferred that, in fact, the coalescence of nano-sized oxides is the main cause behind the enhanced thermal conductivity after the heat treatment.

The lower thermal conductivity of AlSi12 and AlSi10Mg alloys in previous studies compared to this study (Figure 4.5) must be mainly caused by the higher Si concentration in the supersaturated α -Al matrix in the non-preheated condition. As explained earlier, the Si element is rejected into the remaining liquid phase during the solidification since its partition coefficient is less than unity. However, before the Si finds the chance of redistribution in the liquid phase, it can be captured by the solidification front due to the extremely high cooling rate and rapid solidification in the LPBF process. The literature has reported that the level of Si in α -Al can reach ~6.8at% [16] and 4at% [30] in non-preheated AlSi12 and AlSi01Mg, respectively. The l_{SS}^{Si} at such Si concentrations in the α -Al matrix

is 8.1 nm for AlSi12 and 13.8 nm for AlSi10Mg (Eq. (12)), which are significantly lower than the values listed in Table 4.2 for parts fabricated in this study. This justifies the low thermal conductivity of 90 W/mK for AlSi10Mg and 110 W/mK for AlSi12 in the non-preheated condition reported in [20] and [18], respectively. The application of 200 °C of preheating could successfully reduce the chance of Si entrapment since the Si content of the α -Al matrix was measured to be 2.4 and 1.9 at% for AlSi12 (Figure 4.9(k)) and AlSi10Mg (Figure 4.10(l)), respectively. The nano-size Si particles within the cell regions of the AlSi10Mg (Figure 4.10) give evidence that the depletion of the supersaturated α -Al matrix from Si has occurred under preheating condition. The formation of such Si precipitates increases the mean free path of electrons by ~5 times (Table 4.2). Referring to Figure 4.9, it is surprising that these nano-size Si precipitates are absent in AlSi12. Li et al. [16] reported that Si precipitates would not form in the cell cores even after post-build heat treatment, meaning that the Si exolution happens in inter-cellular regions. Therefore, one should not wonder why the difference between the Si content of the α -Al matrix in parts printed under non-preheated and preheated conditions does not show itself in the form of nano-size Si precipitates in AlSi12, as opposed to the AlSi10Mg alloy.

Finally, as pointed out in section 4.3.1.4, even in the non-preheated condition, thermal conductivities ranging from 90 to 130 were reported for the LPBF-fabricated AlSi10Mg alloy [20, 22, 26]. According to the above discussion, different process parameters used in these studies (especially laser power and scanning speed) may have resulted in different solidification rates and, therefore, the chance of capturing the rejected Si during solidification. In other words, different supersaturation levels of Si in samples printed with different process parameters are probably the main reason behind the relatively wide range of thermal conductivities reported in the as-built condition when no preheating was applied.

Due to insufficient data on thermal conductivity of the LPBF-fabricated pure Al [18, 19] and AlSi12 [18], no comment can be added to the role that different process parameters can play in these materials.

4.4.3 Role of temperature in scattering phenomena and thermal properties

Referring to the DSC measurement results shown in Figure 4.1, exothermic event(s) were observed for AlSi12 and AlSi10Mg alloys, which were related to the Si precipitation and/or Mg₂Si formation (only for AlSi10Mg). The onset of deviation from the general trend and occurrence of exothermic reactions is a temperature at which the corresponding thermally activated diffusion processes become active. In other words, a critical temperature can be defined above which the vibrations of the lattice reach its maximum cut-off frequency, where vigorous lattice vibrations can remarkably enhance the diffusion [20]. This temperature is referred to as Debye temperature (θ_D) that reads as follows [44]:

$$\theta_D = \frac{hv}{2\pi k} (6\pi^2 n)^{\frac{1}{3}} \quad \text{Eq. (13)}$$

in which h , v , k , and n denote the Plank's constant, sound velocity in the medium (average acoustic velocity), Boltzmann constant, and the number of atoms per unit volume, respectively. The sound velocity (v) in Eq. (13) can be determined by measuring the longitudinal (v_L) and transverse (v_T) sound velocity components based on the following equation [58]:

$$v = \left[\frac{1}{3} \left(\frac{1}{v_L^3} + \frac{2}{v_T^3} \right) \right]^{-\frac{1}{3}} \quad \text{Eq. (14)}$$

By using Eq. (13), Eq. (14), and the input data provided in Table 4.3, θ_D can be calculated.

Table 4.3. Parameters used to calculate the Debye temperature for the LPBF-fabricated pure Al, AlSi12, and AlSi10Mg

Parameters/ Debye temperature (θ_D)	LPBF-fabricated		
	Pure Al	AlSi12	AlSi10Mg
Planck's constant [$\text{m}^2/\text{kg.S}$]	6.626×10^{-34}		
Longitudinal sound velocity [m/s]	6412	6603	6645
Transverse sound velocity [m/s]	3160	3315	3322
Average acoustic velocity [m/s]	3548	3718	3727
*Debye temperature [$^{\circ}\text{C}$]	141	161	162

*The Boltzmann constant (k) and the number of atoms per unit volume (n) used to calculate the Debye temperature are provided in Table 4.1.

As shown in Figure 4.1, the onset of deviation from the general trend of C_p occurred at 175 $^{\circ}\text{C}$ (AlSi12) and 150 $^{\circ}\text{C}$ (AlSi10Mg), which is in great agreement with the calculated θ_D provided in Table 4.3. The samples in this study were built on a substrate preheated to 200 $^{\circ}\text{C}$. Since this temperature is above the θ_D of both Al alloys, and the samples are kept at this temperature for a relatively long time during the build, the diffusion-controlled depletion of the supersaturated α -Al matrix from Si is activated. It is worth noting that the microstructure of the as-consolidated AlSi12 and AlSi10Mg alloys progressively evolves from the non-equilibrium state toward equilibrium due to the thermal effects of the next layers on the previous ones during the printing process. Therefore, a region can be defined below the fusion line where the temperature is lower than the solidus point (575 $^{\circ}\text{C}$ for AlSi12 and 555 $^{\circ}\text{C}$ for AlSi10Mg) of the alloy but exceeds the Debye temperature (θ_D) or preheat temperature, where Si diffusion becomes active. Moreover, the application of 200 $^{\circ}\text{C}$ preheating ($\sim 1/2$ liquidus temperature) significantly reduces the cooling rate and, consequently, the chance of Si entrapment. These factors explain the point EDS findings provided in Figure 4.9(k) and Figure 4.10(l) about the reduced level of matrix supersaturation from Si in the preheated samples in this study compared to the previously reported values (non-preheated). These factors can also explain the formation of Si nano-

size precipitates within the cells of the LPBF-fabricated AlSi10Mg alloy under preheating conditions (Figure 4.7(g) and Figure 4.10).

According to Figure 4.3, the LPBF-fabricated Al alloys showed a deviation from the linear expansion at specific temperature ranges during the heating cycle. The absence of the observed deviations in the cooling cycle gave evidence that the depletion of the supersaturated matrix from Si was the main governing reason. However, the start temperature of this anomaly in the linear expansion was around the temperature at which Si exsolution exothermic reaction peaked (Figure 4.1), not θ_D (the onset of deviation). This means that the deviation from the linear expansion behavior started as the matrix was effectively depleted from Si. The depletion of the supersaturated α -Al lattice from smaller Si atoms (radius=110 pm) is accompanied by an increase in the lattice parameter [20, 59] which manifests itself in the form of a relatively sharp increase in physical dimensions at the microscopic level. It is worth noting that the exsolution of Mg from α -Al in AlSi10Mg reduces the lattice parameter of the matrix since Mg atoms (radius=160 pm) are larger than the atoms of the parent Al lattice (radius=143 pm). Nonetheless, the aftermath of α -Al matrix depletion from Si and Mg in AlSi10Mg has shown itself in the form of an increase in the dimensions because the Si concentration of the matrix is remarkably higher than Mg.

According to the thermal conductivity results shown in Figure 4.5, it can be understood that thermal conductivity remains almost unchanged from room temperature up to θ_D . This is because the microstructural features and electron-phonon scattering contribution do not change significantly over this temperature range. Therefore, to embrace the discussion of temperature on thermal conductivity, calculations of the electron mean free path (l_e) and time between subsequent collisions (τ) only at temperatures higher than θ_D was exercised.

According to a research study conducted by Palenskis et al. [60], the dependency of l_e and τ on the temperature (above θ_D) can be formulated for metals as follows:

$$l_e(T) = 1.39(D(T_0))^{2/3}\left(\frac{T_0}{T}\right) \quad \text{Eq. (15)}$$

$$\tau(T) = 0.64(D(T_0))^{1/3}\left(\frac{T_0}{T}\right) \quad \text{Eq. (16)}$$

here $l_e(T)$ is in nm, $\tau(T)$ is in units 10^{-14} s, T is any temperature above θ_D , and $D(T_0)$ is the diffusion coefficient of electrons in cm^2/s at $T_0=295$ K that can be calculated as follows [60]:

$$D(T_0) = \frac{1}{3}l_e V_F \quad \text{Eq. (17)}$$

It should be noted that only the theoretical data for pure Al (Table 4.1) can be substituted in these equations, not the ones calculated for LPBF-fabricated Al/Al alloy. Referring to Eq. (15) and Eq. (16), it can be inferred that both $l_e(T)$ and $\tau(T)$ show a descending trend with increasing temperature due to the enhanced vibration and agitation of atoms. Therefore, theoretically speaking, it is expected to observe a continuous decrease in thermal conductivity with increasing temperature. Nevertheless, according to Figure 4.5, such behavior was observed only for the LPBF-fabricated pure Al. To understand why not valid for Al alloys, it should be borne in mind that Eq. (15) is predicting the mean free path of electrons (as carriers of heat) when phonons are the only scattering sites. In other words, these equations predict the intrinsic scattering behavior with increasing temperature, assuming that no extrinsic scattering event happens during the heat transfer. This may be an acceptable assumption for the LPBF-fabricated pure Al with weak extrinsic scattering sites, but not for Al alloys. Based on Table 4.1 and Table 4.2, the electron mean free paths

for the strongest extrinsic scattering sites in the LPBF-fabricated pure Al are 125.8 nm (oxides) and 147.2 nm (dislocations), which are one order of magnitude greater than the electron mean free path for phonon scattering (19 nm). The obtained thermal conductivity also attests to the negligible contribution of extrinsic scattering phenomena for the LPBF-fabricated pure Al (231 W/mK), which is almost equal to its nominal value (where extrinsic scattering is absent-237 W/mK). That is why the continuous decrease in thermal conductivity of this material is in line with the decrease in $l_e(T)$ and $\tau(T)$ with temperature. However, as explained in section 4.4.2, the extrinsic scattering events in the LPBF-fabricated AlSi12 and AlSi10Mg alloys can be up to one order of magnitude stronger than intrinsic ones. For instance, according to Table 4.2, l_{SS}^{Si} is 2 and 3.2 nm in AlSi12 and AlSi10Mg, respectively. Therefore, the influence of temperature not only on the electron-phonon scattering (intrinsic) but also on the microstructural evolutions of the LPBF-fabricated Al alloys must be considered to explain the $K(T)$ behavior observed in Figure 4.5. From θ_D -250, thermal conductivity of AlSi12 reduces with temperature (Figure 4.5) due to the decreased C_p (Figure 4.1(b)), $l_e(T)$ and $\tau(T)$. Despite the descending trend of $l_e(T)$ and $\tau(T)$, thermal conductivity increases above 250 °C, owing to the fact that the supersaturated solid solution α -Al matrix is depleted from Si element, which significantly increases the total mean free path of electrons. Generally speaking, the rate of increase in thermal conductivity reduces with temperatures since the electron-phonon scattering intensifies as the temperature goes up. The same discussion is valid for AlSi10Mg, with the only difference being that there is a decreasing trend in thermal conductivity in the range of 270-300 °C. This is because of the Mg_2Si formation, which reduces the C_p and leads to a slight decrease in thermal conductivity at this temperature range.

4.5 Conclusion

This study strived to quantitatively understand the underlying reasons for the low thermal conductivity of the LPBF-fabricated pure Al, AlSi12, and AlSi10Mg reported in the literature and propose an attainable solution to achieve high thermal conductivity conductivities in the as-built condition. By applying 200 °C of preheating, thermal conductivities of 230, 140, and 160 W/mK were obtained for pure Al, AlSi12, and AlSi10Mg, respectively, which are up to 15, 25, and 80% higher than the values reported for their non-preheated counterparts. While for pure Al, the application of preheating could successfully eliminate the need for post-build heat treatment, it might be necessary for Al alloys since thermal conductivity-temperature results suggested that the AlSi12 and AlSi10Mg alloys have the potential to reach thermal conductivities as high as 166 and 188 W/mK. Nevertheless, the achieved thermal conductivities for Al alloys in as-built condition was greater than those reported for their die-cast counterparts. The electron mean free paths of the LPBF-fabricated Al/Al alloys were calculated and compared to the theoretical value for pure Al. The total mean free path of electrons in the LPBF-fabricated pure Al and Al alloys was the aftermath of intrinsic and extrinsic scattering events, as opposed to the theoretical mean free path of electrons in pure Al in which the extrinsic phenomena are absent. The extrinsic scattering phenomena were porosities, grain boundaries, cell walls (in Al alloys), Al₂O₃ oxides (in pure Al), nano-size Si and Mg₂Si precipitates within the cell regions (in AlSi10Mg), vacancies, dislocations, and supersaturation of Si in α -Al (in Al alloys). The contribution of each scattering site on the total mean free path of electrons was calculated, based on which it was unraveled that the total mean free path was heavily weighted by extrinsic scattering processes with smaller mean free paths at nanometer or angstrom length scales. The dominant contributing factors explaining the difference

between the determined thermal conductivities (for preheated samples) and their nominal values were proved to be oxides for pure Al, and Si atoms in the supersaturated α -Al for AlSi12 and AlSi10Mg alloys.

Acknowledgment

This study and the science behind it would not have been possible without the support of Linseis Messgeraete GmbH, Selb, Germany, especially Erika Hahn, where thermal diffusivity measurements were performed. We would also like to extend our thanks to Kayvon Savadkouei from HORIBA Scientific, NJ, USA, for measuring the oxygen content of the samples. Special thanks should also go to Ibrahim Aydin in Welding Technology and NDT Center as well as Cemil Hakan Gur in the Department of Metallurgical and Materials Engineering, both at Middle East Technical University, Ankara, Turkey, for sound velocity measurements. We are also grateful to Westmoreland-Mechanical Testing & Research (WMT&R) Inc., Canadian Center for Electron Microscopy (CCEM) at McMaster University, and the Center for Advanced Nuclear Systems (CANS) at McMaster University for carrying out the DSC measurements, TEM investigations, and EBSD analysis, respectively. Finally, the authors would like to thank the anonymous reviewers for their helpful and constructive comments that significantly contributed to improving the paper.

1. Bandyopadhyay, A. and K.D. Traxel, *Invited review article: Metal-additive manufacturing—Modeling strategies for application-optimized designs*. Additive manufacturing, 2018. **22**: p. 758-774.
2. Fereiduni, E., A. Ghasemi, and M. Elbestawi, *Selective laser melting of aluminum and titanium matrix composites: recent progress and potential applications in the aerospace industry*. Aerospace, 2020. **7**(6): p. 77.
3. Narvan, M., et al., *Laser powder bed fusion of functionally graded bi-materials: Role of VC on functionalizing AISI H13 tool steel*. Materials & Design, 2021. **201**: p. 109503.
4. Salmi, A., et al., *An integrated design methodology for components produced by laser powder bed fusion (L-PBF) process*. Virtual and Physical Prototyping, 2018. **13**(3): p. 191-202.
5. Fereiduni, E., A. Ghasemi, and M. Elbestawi, *Unique opportunities for microstructure engineering via trace B₄C addition to Ti-6Al-4V through laser powder bed fusion process: As-built and heat-treated scenarios*. Additive Manufacturing, 2022. **50**: p. 102557.
6. Reddy K, S.N., et al. *Application of topology optimization and design for additive manufacturing guidelines on an automotive component*. in *International design engineering technical conferences and computers and information in engineering conference*. 2016. American Society of Mechanical Engineers.
7. Monaheng, L., et al. *Topology optimisation of an aircraft nose-wheel fork for production in Ti6Al4V by the Aeroswift high-speed laser powder bed fusion machine*. in *MATEC Web of Conferences*. 2020. EDP Sciences.
8. Jafari, D. and W.W. Wits, *The utilization of selective laser melting technology on heat transfer devices for thermal energy conversion applications: A review*. Renewable and Sustainable Energy Reviews, 2018. **91**: p. 420-442.
9. Balbaa, M., et al., *Role of Powder Particle Size on Laser Powder Bed Fusion Processability of AlSi10Mg Alloy*. Additive Manufacturing, 2020: p. 101630.
10. Ghasemi, A., et al., *Influence of alloying elements on laser powder bed fusion processability of aluminum: A new insight into the oxidation tendency*. Additive Manufacturing, 2021. **46**: p. 102145.
11. Askeland, D.R., et al., *The science and engineering of materials*. 2003.
12. Li, Y. and D. Gu, *Parametric analysis of thermal behavior during selective laser melting additive manufacturing of aluminum alloy powder*. Materials & design, 2014. **63**: p. 856-867.

13. Samantaray, M., D.N. Thatoi, and S. Sahoo, *Modeling and optimization of process parameters for laser powder bed fusion of AlSi10Mg alloy*. Lasers in Manufacturing and Materials Processing, 2019. **6**(4): p. 356-373.
14. Azizi, H., et al., *Characterizing the microstructural effect of build direction during solidification of laser-powder bed fusion of Al-Si alloys in the dilute limit: a phase-field study*. Acta Materialia, 2021. **214**: p. 116983.
15. Hu, H., X. Ding, and L. Wang, *Numerical analysis of heat transfer during multi-layer selective laser melting of AlSi10Mg*. Optik, 2016. **127**(20): p. 8883-8891.
16. Li, X., et al., *A selective laser melting and solution heat treatment refined Al-12Si alloy with a controllable ultrafine eutectic microstructure and 25% tensile ductility*. Acta Materialia, 2015. **95**: p. 74-82.
17. Yan, Q., B. Song, and Y. Shi, *Comparative study of performance comparison of AlSi10Mg alloy prepared by selective laser melting and casting*. Journal of Materials Science & Technology, 2020. **41**: p. 199-208.
18. Kimura, T., et al., *Effect of silicon content on densification, mechanical and thermal properties of Al-xSi binary alloys fabricated using selective laser melting*. Materials Science and Engineering: A, 2017. **682**: p. 593-602.
19. Kimura, T. and T. Nakamoto, *Thermal and mechanical properties of commercial-purity aluminum fabricated using selective laser melting*. Materials Transactions, 2017. **58**(5): p. 799-805.
20. Yang, P., et al., *Microstructure evolution and thermal properties of an additively manufactured, solution treatable AlSi10Mg part*. Journal of Materials Research, 2018. **33**(23): p. 4040-4052.
21. Strumza, E., O. Yeheskel, and S. Hayun, *The effect of texture on the anisotropy of thermophysical properties of additively manufactured AlSi10Mg*. Additive Manufacturing, 2019. **29**: p. 100762.
22. Sélo, R.R., et al., *On the thermal conductivity of AlSi10Mg and lattice structures made by laser powder bed fusion*. Additive Manufacturing, 2020. **34**: p. 101214.
23. Butler, C., et al., *Effects of processing parameters and heat treatment on thermal conductivity of additively manufactured AlSi10Mg by selective laser melting*. Materials Characterization, 2021. **173**: p. 110945.
24. Touloukian, Y., et al., *Thermophysical properties of matter-the TPRC data series. Volume 1. Thermal conductivity-metallic elements and alloys.(Reannouncement). Data book*. 1970, Purdue Univ., Lafayette, IN (United States). Thermophysical and Electronic
25. Angadi, B., et al., *Studies on the thermal properties of hypereutectic Al-Si alloys by using transient method*. Journal of Mechanical Engineering, 2014. **2**(1): p. 536-544.

26. (05.2014), M.D.S.E.A.A.M., 49, EOS GmbH - Electro Optical Systems (2014), pp. 1-5.
27. Gaskell, D., *An introduction to transport phenomena in materials engineering*. 2012: Momentum Press.
28. Beausir, B. and J. Funderberger, *Analysis Tools for Electron and X-ray diffraction*. ATEX-software, www. atex-software. eu, Université de Lorraine-Metz, 2017.
29. Dragulin, D. and M. R  ther, *Specific heat capacity of alu-minium and aluminium alloys*. Heat. Process., 2018. **3**: p. 81-85.
30. Marola, S., et al., *A comparison of Selective Laser Melting with bulk rapid solidification of AlSi10Mg alloy*. Journal of Alloys and Compounds, 2018. **742**: p. 271-279.
31. Birol, Y., *Microstructural evolution during annealing of a rapidly solidified Al–12Si alloy*. Journal of Alloys and Compounds, 2007. **439**(1-2): p. 81-86.
32. Hidnert, P. and H. Krider, *Thermal expansion of aluminum and some aluminum alloys*. Journal of research of the national bureau of standards, 1952. **48**(3): p. 209-220.
33. Nagaumi, H., et al., *A NOVEL HIGH THERMAL CONDUCTIVITY AL-SI CASTING ALLOY AND APPLICATION*.
34. Kou, S., *Welding metallurgy*. New Jersey, USA, 2003: p. 431-446.
35. Liu, X., et al., *Microstructure of selective laser melted AlSi10Mg alloy*. Materials & Design, 2019. **168**: p. 107677.
36. Hadadzadeh, A., et al., *Columnar to equiaxed transition during direct metal laser sintering of AlSi10Mg alloy: effect of building direction*. Additive Manufacturing, 2018. **23**: p. 121-131.
37. Hadadzadeh, A., et al., *Role of hierarchical microstructure of additively manufactured AlSi10Mg on dynamic loading behavior*. Additive Manufacturing, 2019. **28**: p. 1-13.
38. Kurz, W. and D.J. Fisher, *Fundamentals of solidification*. 1984.
39. Qin, J., et al., *The self-diffusion coefficients of liquid binary M-Si (M= Al, Fe, Mg and Au) alloy systems by first principles molecular dynamics simulation*. AIP Advances, 2019. **9**(3): p. 035328.
40. Ma, Y., et al., *On the study of tailorable interface structure in a diamond/Al12Si composite processed by selective laser melting*. Materialia, 2019. **5**: p. 100242.
41. Hadadzadeh, A., B.S. Amirkhiz, and M. Mohammadi, *Contribution of Mg2Si precipitates to the strength of direct metal laser sintered AlSi10Mg*. Materials Science and Engineering: A, 2019. **739**: p. 295-300.

42. Hadadzadeh, A., et al., *Deformation mechanism during dynamic loading of an additively manufactured AlSi10Mg_200C*. Materials Science and Engineering: A, 2018. **722**: p. 263-268.
43. McGaughey, A.J., et al., *Phonon properties and thermal conductivity from first principles, lattice dynamics, and the Boltzmann transport equation*. Journal of Applied Physics, 2019. **125**(1): p. 011101.
44. Kittel, C. and P. McEuen, *Kittel's Introduction to Solid State Physics*. 2018: John Wiley & Sons.
45. Mahan, G. and M. Bartkowiak, *Wiedemann–Franz law at boundaries*. Applied physics letters, 1999. **74**(7): p. 953-954.
46. Jain, A. and A.J. McGaughey, *Thermal transport by phonons and electrons in aluminum, silver, and gold from first principles*. Physical Review B, 2016. **93**(8): p. 081206.
47. Buerger, M., *A handbook of lattice spacings and structures of metals and alloys*. Zeitschrift für Kristallographie, 1961. **115**(3-4): p. 319-320.
48. Palenskis, V., *Drift mobility, diffusion coefficient of randomly moving charge carriers in metals and other materials with degenerated electron gas*. 2013.
49. Brandt, R. and G. Neuer, *Electrical resistivity and thermal conductivity of pure aluminum and aluminum alloys up to and above the melting temperature*. International Journal of Thermophysics, 2007. **28**(5): p. 1429-1446.
50. Gall, D., *Electron mean free path in elemental metals*. Journal of Applied Physics, 2016. **119**(8): p. 085101.
51. Kanter, H., *Slow-electron mean free paths in aluminum, silver, and gold*. Physical Review B, 1970. **1**(2): p. 522.
52. Smart, L.E. and E.A. Moore, *Solid state chemistry: an introduction*. 2012: CRC press.
53. Khotkevich, V., V. Morgun, and G. Zaitsev, *The influence of vacancies on the transversal magnetoresistance of thin aluminium films at 4.21° K*. physica status solidi (a), 1973. **16**(1): p. 43-48.
54. Fiks, V., *Interaction of conduction electrons with single dislocations in metals*. Phys. Solid State, 1959. **1**: p. 14.
55. Raesinia, B. and W.J. Poole. *Electrical resistivity measurements: a sensitive tool for studying aluminium alloys*. in *Materials science forum*. 2006. Trans Tech Publ.
56. Couch, N., J. Sambles, and A. Stesmans, *Measurements of the spin scattering cross sections of low levels of non-magnetic impurities in aluminium foils*. Journal of Physics F: Metal Physics, 1984. **14**(8): p. 1967.

57. Van Cauwenbergh, P., et al., *Unravelling the multi-scale structure–property relationship of laser powder bed fusion processed and heat-treated AlSi10Mg*. Scientific reports, 2021. **11**(1): p. 1-15.
58. Tao, X., et al., *Phase stability and physical properties of Ta₅Si₃ compounds from first-principles calculations*. Physical Review B, 2009. **80**(10): p. 104103.
59. Fite, J., et al., *Evolution of the microstructure and mechanical properties of additively manufactured AlSi10Mg during room temperature holds and low temperature aging*. Additive Manufacturing, 2020. **36**: p. 101429.
60. Palenskis, V. and E. Žitkevičius, *Phonon mediated electron-electron scattering in metals*. World journal of condensed matter physics, 2018. **8**(3): p. 115-129.

5 Chapter 4 On the preparation and characterization of AlSi12-graphene powder for powder bed fusion additive manufacturing applications

Authorship contribution statement:

Ali Ghasemi: Conceptualization, Methodology, Investigation, Writing - original draft, Writing – review & editing. **Eskandar Fereiduni:** Conceptualization, Methodology, Investigation, Writing – review & editing. **Mohamed Elbestawi:** Supervision, Writing – review & editing. **Jasmin Kathrin Saewe:** Investigation, Writing – review & editing. **Niklas Hartke:** Investigation, Writing – review & editing. **Fran Adar:** Investigation, Writing – review & editing. **Kayvon Savadkouei:** Investigation, Writing – review & editing. **Yoshinori Fukushima:** Investigation, Writing – review & editing. **Saeid Habibi:** Supervision, Writing – review & editing.

On the preparation and characterization of AlSi12-graphene powder for powder bed fusion additive manufacturing applications

Abstract

This study investigates the possibility of using dry mechanical mixing techniques to prepare ideal composite powders for L-PBF applications. For this purpose, two AlSi12-reinforced composite powders with 0.5 and 1wt% graphene were prepared by ball milling and regular mixing processes. The powder attributes (size, size distribution and shape), behaviors (absorptivity, packing density, and flowability), relative humidity, and O/C/H content of the composite powders were quantitatively assessed after mixing and compared to those of monolithic AlSi12. The attachment of the graphene particles and their evolutions during each mixing technique were qualitatively investigated. The quality of the graphene powder before and after mixing was studied by Raman spectroscopy, and the nature of the carbonaceous constituent in the composite powders was identified based on the Raman peak positions, shapes and relative intensities. The results of this study prove that only through ball milling ideal composite powders for the L-PBF applications can be achieved.

Keywords: Laser powder bed fusion; Graphene; Aluminum matrix composite; Ball milling and regular mixing; Raman spectroscopy; Powder flowability.

5.1 Introduction

With the ever-growing interest in lightweight materials with superior mechanical, thermal and electrical properties, aluminum (Al) matrix composites (AMCs) are being considered as novel engineering materials, meeting a part of the growing industrial demands [1]. Given the desired intrinsic properties of AMCs, they have been deemed as superseded candidates for the automotive and aerospace industries to fill the present technological gaps. In recent years, the emergence of cost-effective production techniques for carbonaceous materials such as graphene has opened a new window toward their implementation as favorable reinforcements [2]. The incorporation of the graphene into the Al matrix should not only lead to increased mechanical properties, which could be achieved by adding other families of reinforcements, but also may have the potential to (i) increase thermal and electrical conductivity, (ii) increase damping capacity, and (iii) decrease the wear rate and friction coefficient at the same time, improvements which are unique to carbonaceous over other reinforcements [3, 4].

Since the AMC components used in the abovementioned industries are complex in geometry, their manufacturing through conventional processes is rather challenging. To address this concern, additive manufacturing (AM) is the best choice for the near-net-shape fabrication of complex components [5, 6]. Among various AM techniques, only directed energy deposition (DED) and powder bed fusion (PBF) processes can be used to manufacture metallic and AMC components. Despite the DED processes, pre-processing powders prior to the printing is an inseparable part of AMC production when employing PBF processes [1]. This originates from the absence of different nozzles for feeding composite constituents in the PBF processes, requiring a composite powder feedstock as the starting material [7]. Referring to the literature, it is usually liquid-assisted mixing

techniques that have been taken advantage of to prepare graphene, graphene oxide, or carbon nanotube reinforced composite powders for PBF purposes [8-17]. Despite the advantages that the liquid-assisted mixing techniques are claimed to offer, namely, minimum damage to the graphene sheets [18], preserving the spherical shape of metallic powder particles [9], and production of homogeneous composite powders [19], they suffer from one or multiple of the following drawbacks, (i) time-consuming- as the final mixture usually needs to be filtered, rinsed with alcohol and dried at low temperatures for relatively long times (up to 24 h) [13], (ii) low yield of composite powder production and difficult to be scaled up [1], and (iii) high chance of picking up contamination upon improper rinsing and drying of the mixture.

Some studies utilized fast and easy-to-use dry mixing techniques such as ball milling to overcome the above problems [20-35]. In all the mentioned studies, solid graphene powder, usually in the form of graphene agglomerates (graphite particles), was used as the starting powder and subjected to low- to high-energy ball milling process with [25, 28, 31] or without [21, 26, 27] the application of processing control agent (lubricant) with the hope being that the impacts experienced by the graphene bundles (graphite) due to their collisions with balls and jar wall would lead to the formation of graphene nanoplatelets attached to the metallic particles. Nevertheless, none of them has acknowledged the possibility of transforming the starting material to other forms of carbon, such as disordered carbon or nanographite. This originates from the absence of a powerful carbon characterization technique [23, 24, 31, 34], namely Raman spectroscopy, or inconclusive interpretation of its results [10, 27, 29, 32]. Moreover, to the best of the author's knowledge, there is no study in which the attributes and behaviors of the AlSi12-graphene composite powders produced by dry mechanical mixing techniques have been

systematically characterized from the PBF perspective. This is while the quality of the final printed parts is directly influenced by the attributes/behaviors of the starting powder [36].

Therefore, this study strives to answer two questions: (1) upon using dry graphene powder (usually in the form of graphite) as the starting reinforcement, is the output of dry mechanical mixing methods a composite powder with graphene nanoplatelets or it transforms to other types of carbon? And (2) regardless of the type of carbonaceous material in the fabricated mixed powder, is it suitable for PBF applications? To answer these questions, a carbonaceous powder purchased as graphene and a metallic powder (AlSi12 alloy) were mixed through ball milling and regular mixing (absence of balls), with the latter causing less damage to the starting powders. Raman spectroscopy was performed on the initial carbonaceous powder and the composite powders to comment on their quality and crystallinity before and after mixing (answer to the first question). The produced composite powders were also compared in terms of packing density, flowability, moisture content, level of oxygen/carbon/hydrogen (O/C/H), and quality/nature of the carbonaceous material after mixing (answer to the second question). For comparison purposes, a thorough characterization was also performed on monolithic AlSi12 powder.

5.2 Experimental procedure

To prepare the composite powder feedstock, the regular mixing and the ball-milling processes were utilized. In the regular mixing, the host (AlSi12 alloy-Al-11.46Si-0.13Fe (wt%) provided by VALIMET Inc.) and guest (graphene nanoplatelets- nominal purity and thickness of 99.5+% and 2-8 nm provided by US Research Nanomaterials Inc.) powders were mixed in the absence of the balls, while 10 mm stainless steel balls were added to the system in the ball-milling process. The composite powder systems contained 0.5 and 1

wt.% guest, and the powders were mixed without using a protective gas. The mixing process was performed using a high-performance planetary Pulverisette 6 machine in a range of rotational speeds (200-300) rpm and mixing times (1-8) h. During ball milling and regular mixing, every 30 min of mixing was followed by a 15, and 10 min pause, respectively, to avoid overheating of the powder during the mixing process. In the case of ball milling, the ball-to-powder ratio between 1:3 to 1:10 were selected. The optimum ball milled, and regularly mixed composite powders were chosen based on the morphological observations of the composite systems (homogeneous dispersion of guest particles). The sets of mixing parameters to achieve optimum condition for each composite powder are shown in Table 5.1. All the powder characterizations explained hereafter were performed on the optimum composite powders.

Table 5.1. sets of mixing parameters for optimum condition for regularly mixed and ball milled powders.

Sample	Total mixing time (h)	Rotational speed (rpm)	Ball-to-powder ratio
0.5 wt%Gr-AlSi12 (B1.5*)	1.5	200	6.5:1
0.5 wt%Gr-AlSi12 (R4*)	4	300	No ball
1 wt%Gr-AlSi12 (B2*)	2	200	8:1
1 wt%Gr-AlSi12 (R6*)	6	300	No ball

*Regularly mixed and ball-milled composite powders are designated by R and B, respectively, and the number in the front represents the total mixing time. Gr refers to graphite/graphene nanoplatelets.

The morphological observation of the composite and monolithic powders was performed by Tescan Vega scanning electron microscope (SEM) equipped with energy-dispersive X-ray spectroscopy (EDS) analysis. The dispersion state of the guest particles was analyzed qualitatively using EDS elemental mapping. For average particle size, size distribution, and sphericity measurements, dynamic particle size measurements were performed by a Camsizer X2 instrument in accordance with ISO 13322-2. The apparent packing density

of the powders was measured as per DIN EN ISO3923 standard using a Carney funnel with the reported values being the average of three distinct measurements. For flowability measurements, Revolution Powder Analyzer instrument, consisting of a rotating drum covered on both sides with transparent glass was used. A camera existed in one side of the drum during the powder flowability measurements to capture pictures from the cross section of the rotating drum with a backlight on the other side. The process ran for 150 avalanches from which the avalanche power and angle profiles were determined. Optical absorption of the powders was analyzed by means of diffuse reflectance spectroscopy (DRS) in the wavelength range of 900–1200 nm using an integrating sphere equipped with Tungsten lamp as light source. The reported values are the average of three distinct measurements. Relative humidity of powder materials was determined using AND MS-70 instrument (heating from room temperature up to 100 °C in 10 minutes) with three repetitions to ensure consistency in the obtained results. The oxygen/hydrogen (O/C/H) content of the powders was measured using an Instrumental Gas Analyzer (IGA). The equipment used for analyzing O, C and H were EMGA-820, EMIA-Pro, and EMGA-921, respectively. For O and C measurements, no sample preparations were done prior to the test. The details of the test procedure and sample preparations for H measurements can be found in [37]. The reported results are the average of six distinct measurements. A HORIBA XploRA confocal Raman microscope was used to investigate the quality of starting carbonaceous powder and guest particles after mixing. Raman mapping was performed to study the distribution and type of carbonaceous material in each powder sample. The acquisition of Raman spectra was carried out at ambient conditions by utilizing a diode laser with a wavelength of 532 nm at 1% power.

5.3 Results and Discussion

5.3.1 Powder attributes

In this section, the attributes of the produced composite powders, namely, size, size distribution, shape and morphology are qualitatively and quantitatively investigated and compared to those of the monolithic AlSi12 powder.

5.3.1.1 Microscopical observations

SEM micrographs of the AlSi12 (reference) and composite powders shown in Figure 5.1 provide important **qualitative** information about the evolutions of the **host** (not guest) particles during the mixing. First, owing to the absence of balls during the regular mixing, the host particles have almost preserved their starting shape in R4 and R6 samples (Figure 5.1(a-c)). Second, host particles were subjected to the plastic deformation during the ball milling process evidenced by a high population of the moderately deformed (relatively spherical) and severely deformed (flake-shaped) particles in B1.5 and B2 samples (Figure 5.1(d,e)). The level of deformation is more pronounced in the B2 sample, originating from the higher ball-to-powder ratio and mixing time in B2 than B1.5 sample. Third, although no crumbling of the host particles has happened during the ball milling process at the applied mixing times, some of the flake-shaped particles have fractured (it is only shown for B2 in Figure 5.1(f)) and subsequently cold-welded to the larger host particles, as shown in Figure 5.1(g,h). Finally, only a few cold-welded host particles were perceptible in the B1.5 and B2 powders, meaningfully below what has been expected for such high ball-to-powder ratios. A logical explanation for this observation is the presence of guest particles among or on the surface of the host ones, acting as obstacles to the cold welding of host particles. To prove this hypothesis, monolithic AlSi12 powder was subjected to ball milling with a ball-to-powder ratio of 5:1 for 1 h. As can be seen in Figure 5.1(i,j), severe cold-welding (agglomeration) of AlSi12 particles has happened in the absence of guest particles,

with agglomerates sometimes exceeding 0.4 mm in size. Therefore, although some fragments-particle cold welding was observed in the B1.5 and B2 samples, almost no particle-particle cold welding was perceptible owing to the presence of guest particles.

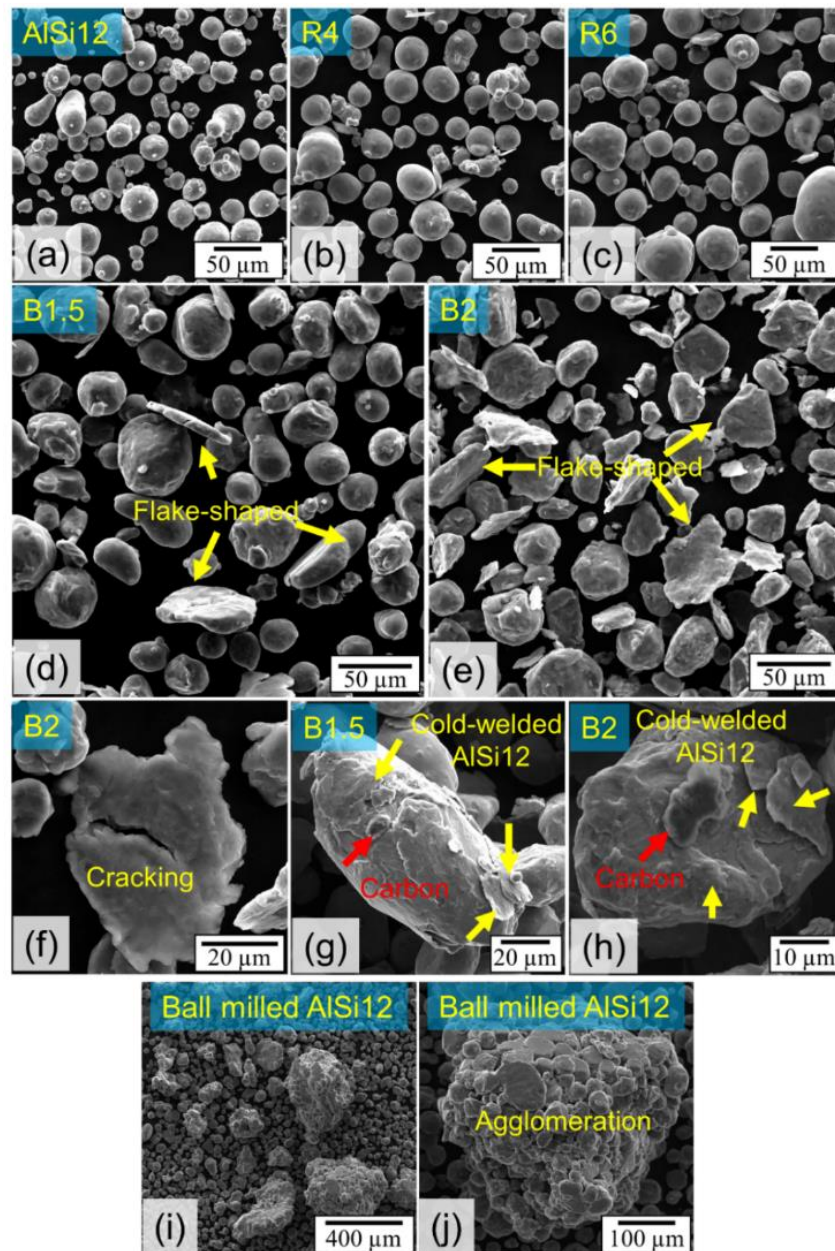


Figure 5.1. SEM micrographs of different powders (a) AlSi12, (b) R4, (c) R6, (d,g) B1.5, (e,f,h) B2, and (i,j) ball milled unreinforced AlSi12.

SEM micrographs and the EDS mapping results of the composite powders shown in Figure 5.2 and Figure 5.3 provide important **qualitative** information about the evolutions of the **guest** (not host) particles during the mixing. For comparison purposes, the starting carbonaceous powder is also shown in Figure 5.2(a). The starting powder mainly consists of fine particles with thicknesses generally within the range of sub-micron to a few microns. In addition to these fine particles, coarse particles with lateral dimensions exceeding 500 μm and relatively high thicknesses were also detected in this powder. Both fine and coarse powders resemble graphite more than graphene, meaning that the dry graphene particles have agglomerated during the storage due to the existence of strong Van der Waals forces among them. A general overview of the guest particles after regular mixing is shown in Figure 5.2(b-e) for R4 and R6 samples. The guest particles are distributed in a relatively homogeneous way among the host particles. However, some of the starting coarse carbonaceous particles still exist in these powder systems (Figure 5.2(c,e)). It signifies that the impacts experienced by these coarse particles due to their collisions with host particles and jar wall during the regular mixing process (even at a prolonged mixing time of 6 h) were not strong enough to fracture them and produce fine and relatively thin platelets. Higher magnification micrographs and their corresponding EDS carbon maps shown in Figure 5.2(f,g) prove that the added guest particles are generally not attached to the host ones due to the insufficient impact energy of the regular mixing process in the absence of balls. Having said that, carbon was also detected on the surface of the host powder particles. According to powder close-ups and their corresponding EDS carbon maps shown in Figure 5.2(h-k), it can be understood that two groups of host particles exist in R4 and R6 samples. The first group is negligibly coated by carbon as only tiny dots on the surface of host particles are detected as carbon (Figure

5.2(h,j)). The second group possesses much more carbon at specific regions, which can be seen as dark gray color on the host particles in Figure 5.2(i,k). It must be noticed that the detected carbon on the host particles is not the starting carbonaceous particles attached to the host surfaces. They are basically carbon layers removed from the guest particles and transferred to the host ones as the host and guest particles rubbed against each other during the regular mixing process.

Figure 5.3(a,d,g,j) shows the overview of the guest particles after ball milling for B1.5 and B2 samples. Unlike the regularly mixed powders, no coarse carbonaceous particle (Figure 5.2(a)) from the starting powder remained, and the guest particles were finer in the ball milled samples. Higher magnification SEM micrograph and EDS analysis results in Figure 5.3(b,c,e,f) for B1.5 and in Figure 5.3(h,i,k,l) for B2 confirm that almost all guest particles are attached to the host ones, and their size is smaller than those of the regularly mixed composite powders. It means that the ball milling process enables more effective deagglomeration or fragmentation of the starting guest particles and their full attachment to host powder particles at the expense of moderate to severe deformation of the host particles. It is worth noting that not only attachment but also embedment of the guest particles was captured through microscopical observations (Figure 5.3(c,f)). The embedment mechanism involves the attachment of guest particles to host ones, followed by the cold welding of the fractured flake-shaped pieces of host particles to them. Finally, similar to regularly mixed powders, carbon was also detected all over the surface of all host particles, not just where the guest particles were attached, since guest and host particles have rubbed against each other during the mixing.

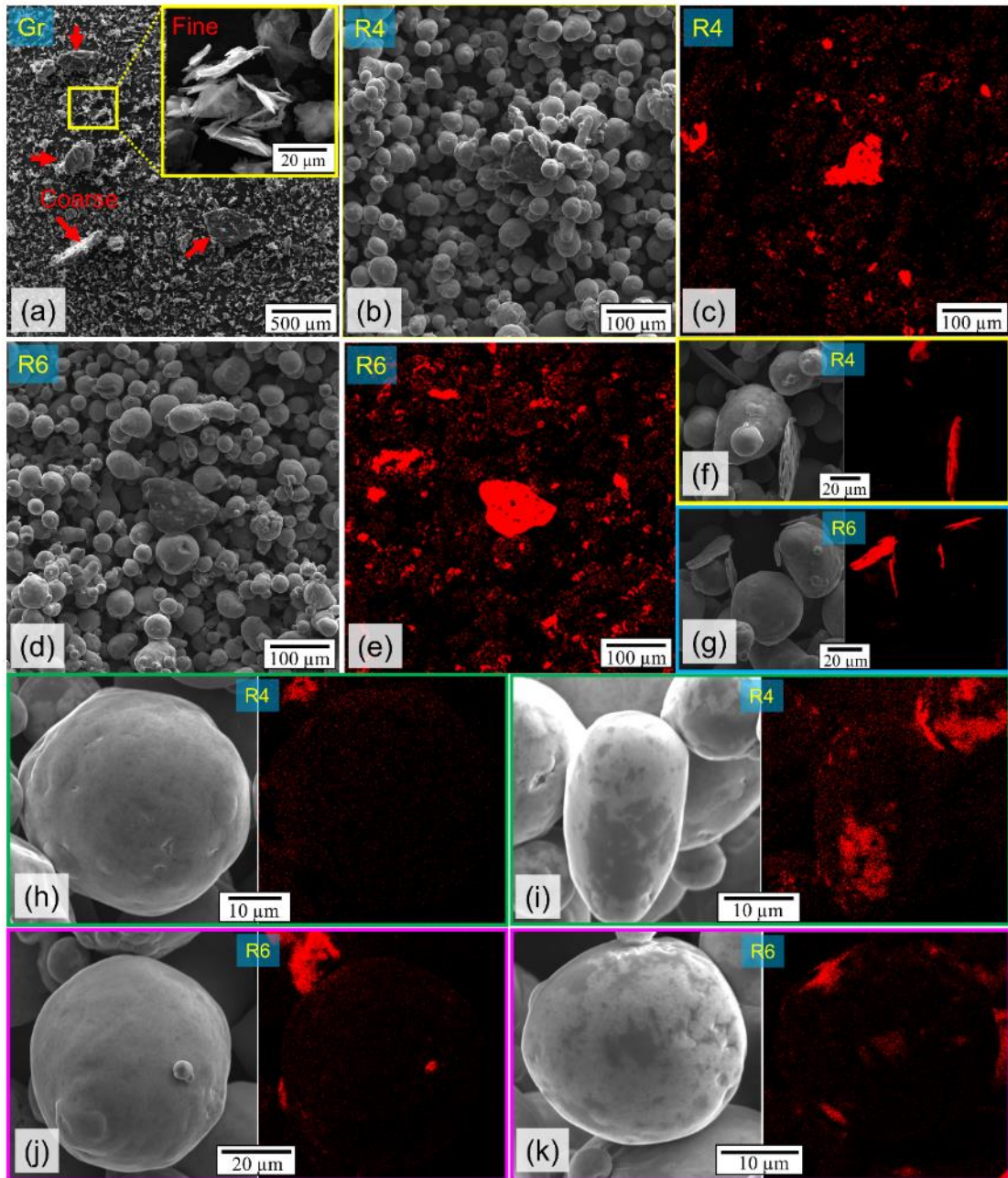


Figure 5.2. (a) SEM micrograph of carbonaceous powder with an inset showing the fine particles at higher magnification, and (b-k) SEM micrographs and their corresponding EDS mapping results showing the C distribution for the designated powders.

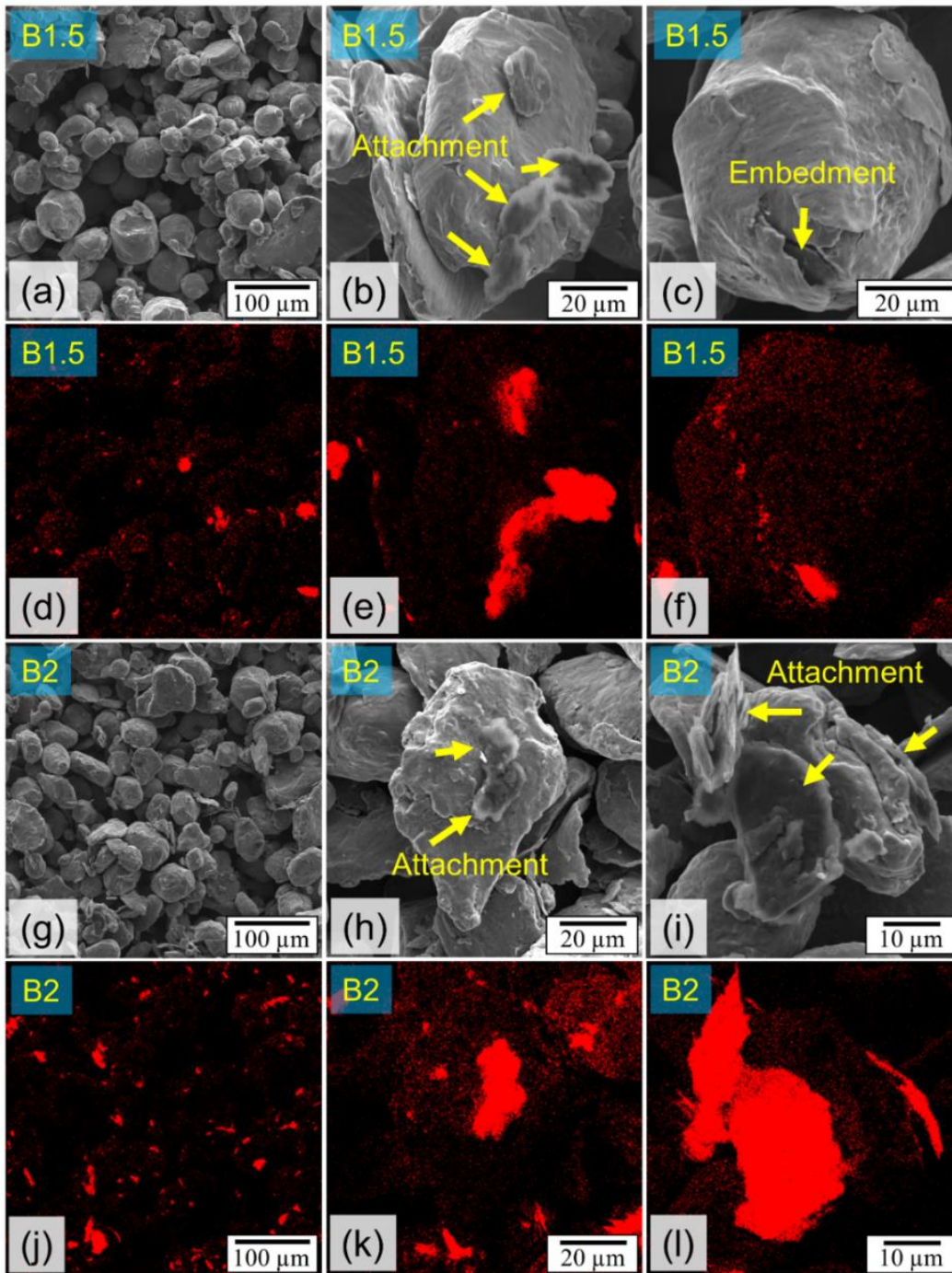


Figure 5.3. SEM micrographs and their corresponding EDS mapping results showing the C distribution for (a-f) B1.5 and (g-l) B2 powders.

According to the above results, the regularly mixed powders benefit from almost spherical host particles, a shape which is known for its excellent flowability and high packing density for L-PBF application [1]. On the other hand, the ball milled composite powders benefit from the attachment/embedment of guest particles to the host ones. This alleviates the chance of segregation of the guest powder particles during handling or deposition on the substrate during the L-PBF process, leading to AMC components with a more uniform distribution of reinforcing particles [38].

5.3.1.2 *Size and size distribution*

To gain a **quantitative** understanding of the influence of the mixing process on the **size characteristics** of the starting particles, size measurements were performed on the AlSi12 and composite powders. Figure 5.4(a-e) shows the cumulative distribution and relative frequency versus the area mean diameter of the particles in each powder sample. In each case, D_{10} , D_{50} , and D_{90} are specified, representing particle diameters larger than 10, 50 and 90 vol% of all particles. It should be borne in mind that the size distribution curves (volume-based not number-based particle size distribution) of composite powders shown in Figure 5.4(b-e) provide quantitative information mainly about **host** particles, not guest ones, since the size of the latter is below the detection limit. The followings can be extracted from particle size measurements: (i) size distribution curves and D_{10} , D_{50} , and D_{90} of the R4 and R6 samples are almost identical to that of the AlSi12 powder due to the absence of balls, confirming the findings of SEM observations (Figure 5.1(a-c)), (ii) B1.5 sample possesses almost the same D_{10} , and D_{50} as those of the reference powder, but higher D_{90} (13.2% increase) mainly because of the deformation of the host particles during the ball milling process (Figure 5.1(d)), and (iii) B2 sample showed similar D_{10} to that of the AlSi12 powder, but 10 and 32% increase in D_{50} and D_{90} , proving more deformation of host

particles in this powder than B1.5 as also attested by SEM micrographs in Figure 5.1(e). It is worth noting that in all composite powder samples, particles larger than 120 μm were also detected, which are not shown in particle size distributions in Figure 5.4(b-e). These particles account for 0.5, 1, 1.2 and 2.7 vol% of total particles in R4, R6, B1.5 and B2 samples, respectively. It is believed that such unusually large particles are either coarse carbonaceous particles (in R4/R6, see Figure 5.2(b-e)) or cold-welded/flake-shaped host particles (in B1.5/B2, see Figure 5.1(d-h)). To better understand the changes in the particle size distribution, not just based on comparing D_{10} , D_{50} , and D_{90} of different powders, the distribution width of AlSi12 and composite powders were mathematically formulated using uniformity index (UI) and span as follows [39, 40]:

$$UI = \frac{D_5}{D_{90}} * 100 \quad \text{Eq. (1)}$$

$$Span = \frac{D_{90} - D_{10}}{D_{50}} * 100 \quad \text{Eq. (2)}$$

The calculated UI and span values are shown in Figure 5.4(f). Moving from AlSi12 to regularly mixed and ball milled powders, a monotonic decrease and increase were observed for UI and span, respectively. The UI and span values for R4 and R6 are only slightly lower (~8%) and higher (~7%) than those of AlSi12. This is while UI decreases by ~17 and ~30%, and span increases by ~19 and ~42% for B1.5 and B2 samples, respectively. The noticeable change in the distribution width of the ball milled powders originates from larger particles in these powders compared to the reference one since their D_5 and D_{10} are almost identical. The problem of large particles that disturb the distribution width can be easily solved by sieving the ball milled powders before the L-PBF process. Removal of the large powder particles is also essential from other perspectives, such as surface roughness and

densification level of the printed parts, since these particles do not sit on the substrate and sweep the particles ahead of them during powder spreading.

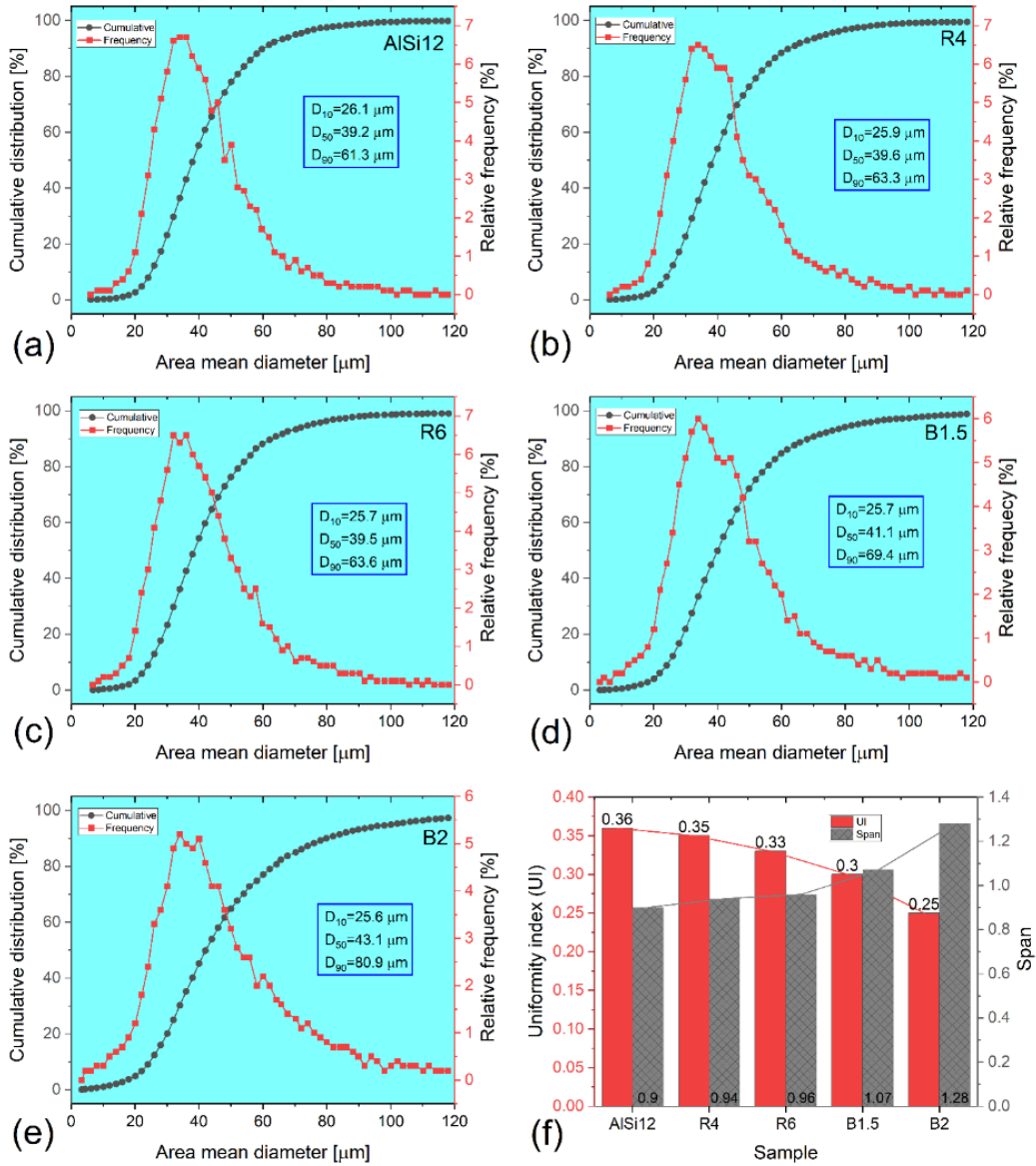


Figure 5.4. (a-e) Cumulative and relative frequency distributions of the designated powders, and (f) UI and span values for different powders.

5.3.1.3 Shape characteristics

To gain a **quantitative** understanding of the influence of the mixing process on the **shape/morphological characteristics** of the **host** particles, three parameters, namely, sphericity (SPHT), symmetry (Symm), and breadth-to-length ratio (b/l), were calculated using the measured projection images of the powder particles as follows [40, 41]:

$$SPHT = \frac{4\pi A}{P^2} \quad \text{Eq. (3)}$$

$$Symm = \frac{1}{2} [1 + \min\left(\frac{r_1}{r_2}\right)] \quad \text{Eq. (4)}$$

$$\frac{b}{l} = \frac{X_{c,min}}{X_{Fe,max}} \quad \text{Eq. (5)}$$

SPHT uses a measured perimeter of a particle projection (P) and a measured area covered by a particle projection (A) to judge how close the shape of the detected particle is to a perfect sphere (SPHT=1). In the Symm parameter, r_1 and r_2 are distances from the center of the projection area of the particle to borders in the measuring direction. The term $\min(r_1/r_2)$ shows that the values for Symm are calculated from the smallest r_1/r_2 ratio. The b/l parameter, calculated from the minimum chord length ($X_{c,min}$) and maximum Feret diameter ($X_{Fe,max}$), refers to the particle aspect ratio and hints at the overall macro shape of the particles. The results of SPHT, Symm, and b/l calculations, as well as a schematic illustration of each parameter, are shown in Figure 5.5. For the AlSi12 powder, the SPHT, Symm, and b/l lie generally within the range of (0.8-0.95), (0.85-0.95), and (0.7-0.9), respectively, with the mean values for the respective parameters shown in Figure 5.5(a,f,k). The percentage of particles having SPHT and Symm values equal to or greater than 0.9 (e.g., $[1-Q(SPHT=0.9)]$), as well as mean b/l values, are also shown in Figure 5.5(a,f,k). From the SPHT, Symm, and b/l values, starting AlSi12 powder was not perfectly but nearly spherical. All shape parameters for R4 and R6 samples were almost identical to those of

the AlSi12, meaning that the regular mixing had no influence on the shape of the host particles (Figure 5.5(b,c,g,h,l,m)). The B1.5 sample possessed the same mean SPHT value as that of the AlSi12 powder; however, a lower percentage of particles had a minimum SPHT of 0.9 due to the plastic deformation of the host particles during ball milling (Figure 5.5(d)). A moderate decrease in the mean b/l value was observed, proving the presence of disk-shaped particles in this ball milled composite powder (Figure 5.5(n)). Regarding the Symm parameter, B1.5 was almost identical to the AlSi12 powder (Figure 5.5(i)). The deviation of the SPHT, Symm and b/l values for the B2 sample from those of AlSi12 powder was more conspicuous as longer milling time and higher ball-to-powder ratio were used in this sample (Figure 5.5(e,j,o)). The findings for B1.5 and B2 samples are in line with the SEM observations in Figure 5.1, where the B2 sample was shown to have more deformed and disk-shaped particles. It is worth noting that even in the B2 sample, the morphological changes based on the defined parameters are not that significant (e.g., less than 15% decrease in b/l value and the population of particles with SPHT and Symm equal/greater than 0.9).

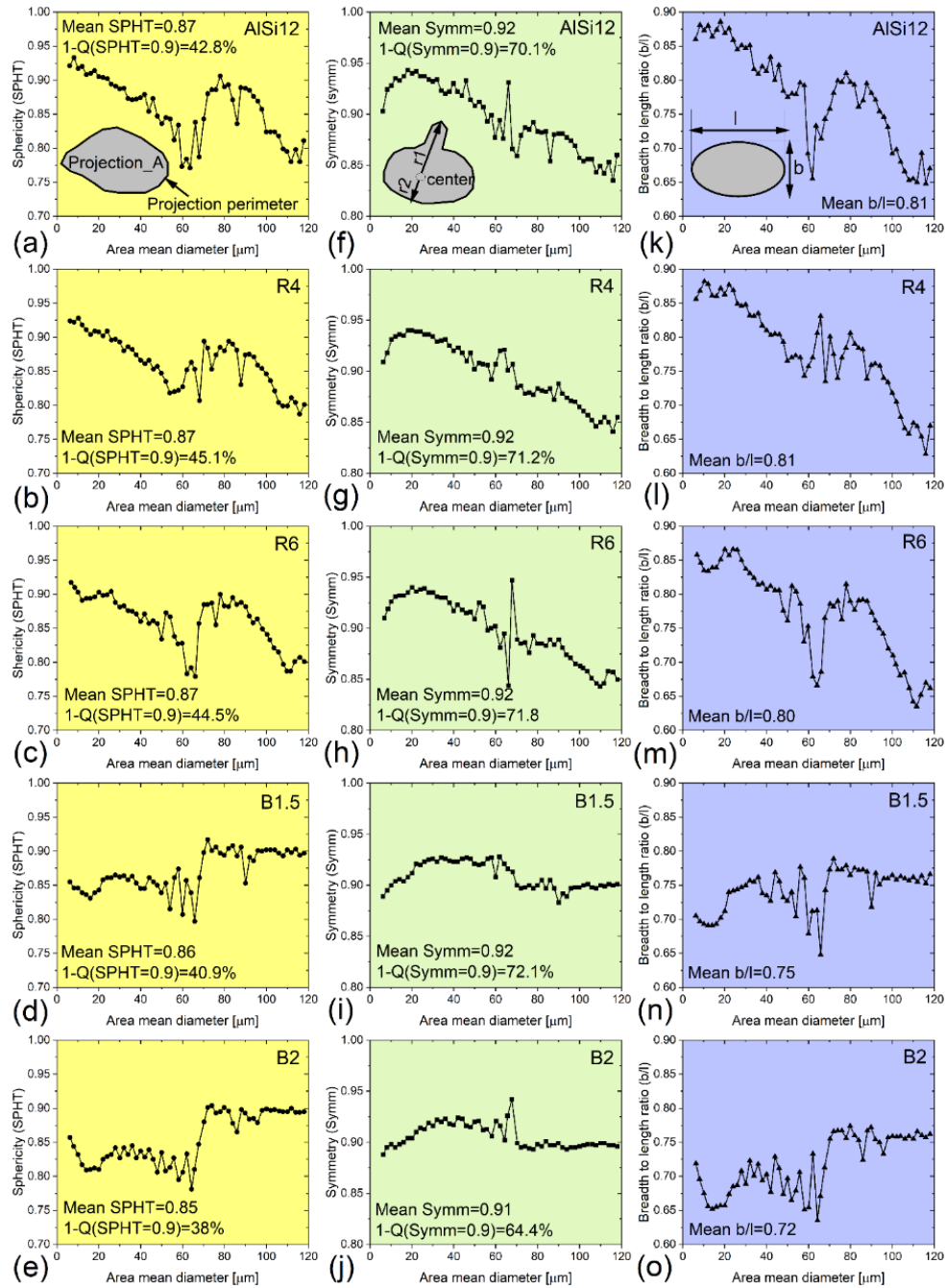


Figure 5.5. (a-e) SPHT, (f-j) symmetry, and (k-o) b/l versus area mean diameter for the designated powders.

5.3.2 Powder behaviors

In this section, the behaviors of the composite powders, namely, absorptivity, packing density, and flowability are investigated and compared to those of the monolithic AlSi12 powder. Since the powder behaviors are directly influenced by the powder attributes, their correlation is also discussed.

5.3.2.1 Absorptivity

Figure 5.6 shows the absorption percentage of different powders in the wavelength range of 900-1200 nm. Since a laser beam with a wavelength of 1070 nm is usually used in commercial L-PBF machines, the average absorption percentage of each powder at this wavelength is shown in Figure 5.6(f). According to Figure 5.6(f), the starting carbonaceous powder possesses a significantly higher absorption than AlSi12 (~30% higher). All composite powders showed an increase in absorption in the range of 5.5 to 12% compared to AlSi12 powder at the wavelength of 1070 nm due to the following reasons: (i) a fraction of the host powder is replaced by a higher absorptive constituent (guest) [5], and (ii) increase in the number of light ray-particle interactions because of the surface roughening effects of decorating second constituent as reported in [42]. While the nature of the guest powder dictates the former, the latter is influenced by the location of the guest relative to the host particles. R4 and B1.5 samples with 0.5 wt% guest showed almost identical absorptions. However, the absorptivity of R6 and B2 samples, both having 1 wt% guest, were slightly different. Besides, while the R6 sample with more percentage of guest constituent showed higher absorptivity than R4, the contrary was the case for the ball milled ones, as a slight decrease in absorptivity of B2 was observed compared to B1.5 (6%). A rational explanation for the lower absorptivity of B2 than the B1.5 could be the presence of coarser **host** particles in the B2 than the B1.5 sample, reducing the overall

surface-to-volume ratio of the powder system and resulting in lower absorptivity [36] (Figure 5.4). The difference between the absorption of B2 and R6 samples is mainly attributable to a higher chance of **guest** particle embedment into the host ones in the B2 sample due to the remarkably higher impact energy exerted by the stainless steel balls during the ball milling process (Figure 5.3(c,f)). The guest particles within the host do not participate in light ray-powder interactions, leading to the reduced absorptivity in the B2 sample. In addition, the presence of finer host powder particles in R6 (Figure 4) and lower waste of guest constituent during the regular mixing process (see section 5.3.3) are other reasons justifying the higher absorptivity of R6 than B2 sample.

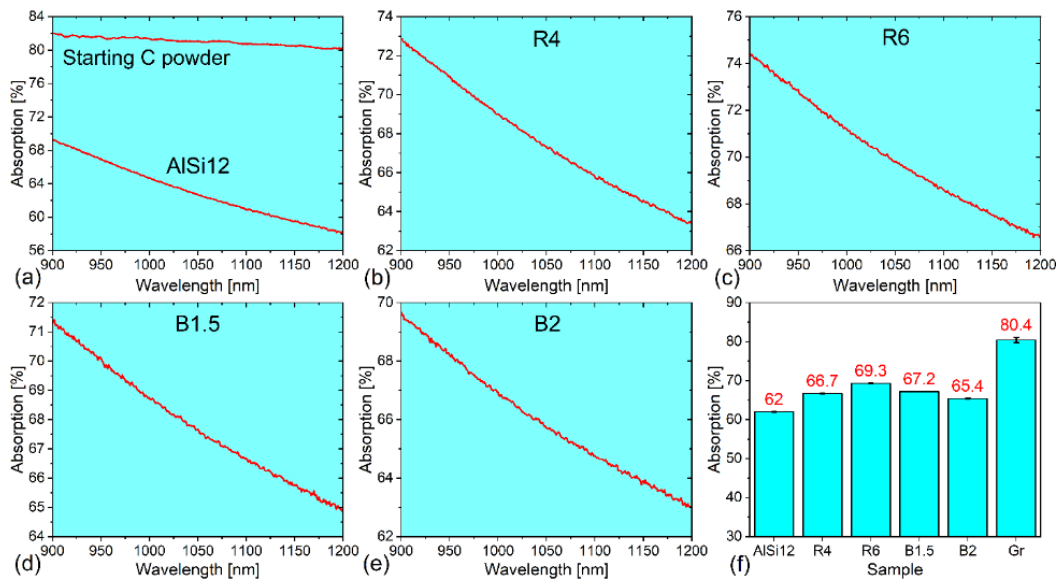


Figure 5.6. (a-e) Absorptivity versus wavelength for the designated powders and (f) average absorptivity values at the wavelength of 1070 nm.

5.3.2.2 Packing density

The apparent packing densities of the reference and composite powders are summarized in Table 5.2. Regardless of the amount of guest particles added or the mixing process used, the composite powders showed lower apparent density than the AISi12 powder. The

highest apparent density among composite samples corresponds to the B1.5, with a relative density of ~49%, very close to that of the monolithic AlSi12 powder. The slight decrease in the apparent packing density of this sample compared to the AlSi12 powder traces back to the presence of more deformed host powder particles generated during the mixing process [7] (compare [1-Q(SPHT=0.9)] and b/l two powders in Figure 5.5). Comparing B1.5 with regularly mixed powders, a number of factors must be taken into consideration to justify the findings. The B1.5 sample has a lower volume percentage of **host** particles with a minimum SPHT of 0.9 and a lower mean b/l value than R4/R6 (Figure 5.5), both negatively affecting the apparent packing density. However, B1.5 has a higher percentage of coarse **host** particles (compare D_{90} of B1.5 and R4/R6 samples in Figure 5.4), leading to the reduced overall area to the volume fraction of the particles, and, therefore, lower interparticle friction and cohesive forces. Also, the **guest** particles decorating the surface of the host ones in the B1.5 sample (Figure 5.3) have self-lubricating properties [43], helping the host particles to flow easier relative to each other and arrange more efficiently. This is while the non-attached **guest** particles in R4 and R6 samples (Figure 5.2) act as obstacles for the host particles and introduce new sources of inter-particle friction to the powder system. It seems like in the B1.5 sample, the increase in packing density due to the coarsening of host particles and full guest-to-host attachment has not only compensated for the decrease in packing density because of the morphological changes but also provided an overall better condition for the arrangement of particles (compared to R4/R6). The B2 sample showed almost the same apparent density as those of the R4 and R6 samples. It seems like the contribution of factors decreasing the apparent density, such as deviation from spherical shape due to severe deformation and the presence of a higher fraction of disk-shaped particles (Figure 5.1), was higher in this powder system.

Table 5.2. Apparent packing density, its standard deviation and relative density for different powders

Powder sample	Apparent density [g/cm ³]	Standard deviation [g/cm ³]	*Relative density [%]
AlSi12	1.43	0.0021	53.4
R4	1.18	0.0076	44.0
R6	1.23	0.0067	45.9
B1.5	1.31	0.0049	48.9
B2	1.19	0.0123	44.4

*For relative density calculations, the true density of 2.68 g/cm³ was used as the reference density.

5.3.2.3 Flowability

Revolution Powder Analyzer was utilized to investigate the influence of the mixing process on the flowability of the composite powders (see the videos in supplementary materials). Three important flow parameters of avalanche angle, avalanche energy and fractal dimension were measured for reference and composite powders. The avalanche angle is the angle of a linear regression of the free powder surface, measured with respect to a horizontal line [44], as shown in Figure 5.7(a,c,e). It indicates the average angle required to start and continue the flow of the powder. By plotting the avalanche angle versus occurrences (avalanche number), the graphs shown in Figure 5.8(a-e) can be achieved, which help to determine the average avalanche angle required to start and maintain the flow of powder as well as its standard deviation (SD). The lower these values, the easier and more consistent the powder flow. The energy level of powder in the rotating drum was also measured during the test. The sudden change in the energy level of powder indicates the occurrence of an avalanche. By subtracting the energy level of the powder before and after an avalanche, the avalanche energy for that avalanche can be obtained. Figure 5.8(f-j) shows the avalanche energy versus number along with the mean avalanche energy and its SD. Low mean avalanche energy and SD are features of powders with better flowability. For B1.5 and B2 samples (Supplementary videos 2 and 3), the mean avalanche angle has

only increased by 7.6 and 18.3% with SD values 2.5 and 1.3 times greater than those of the AlSi12 powder (Supplementary video 1), respectively. On the other hand, the R4 and R6 samples (Supplementary videos 4 and 5) showed remarkably higher mean avalanche angles, 51.6 and 91.1% higher than that of the AlSi12 powder, respectively. The avalanche angle SD for the respective powders was 7.4 and 13.5 times greater than that of the AlSi12 powder. The regularly mixed powders were also inferior to AlSi12, and ball milled composite powders in terms of mean avalanche energy and SD. The B1.5, B2, R4 and R6 samples showed 6.9, 32.8, 394.8, and 422.4% increases in the mean avalanche energy, respectively, and the SD values for the regularly mixed powders were one order of magnitude greater than those of the AlSi12 and ball milled composite powders. Based on the avalanche angle and energy results, it is fair to conclude that the ball milled powders are undisputed winners of the flowability competition. This can also be understood visually from the supplementary videos 1-5, where B1.5 and B2 samples show a flow behavior very close to the AlSi12 powder.

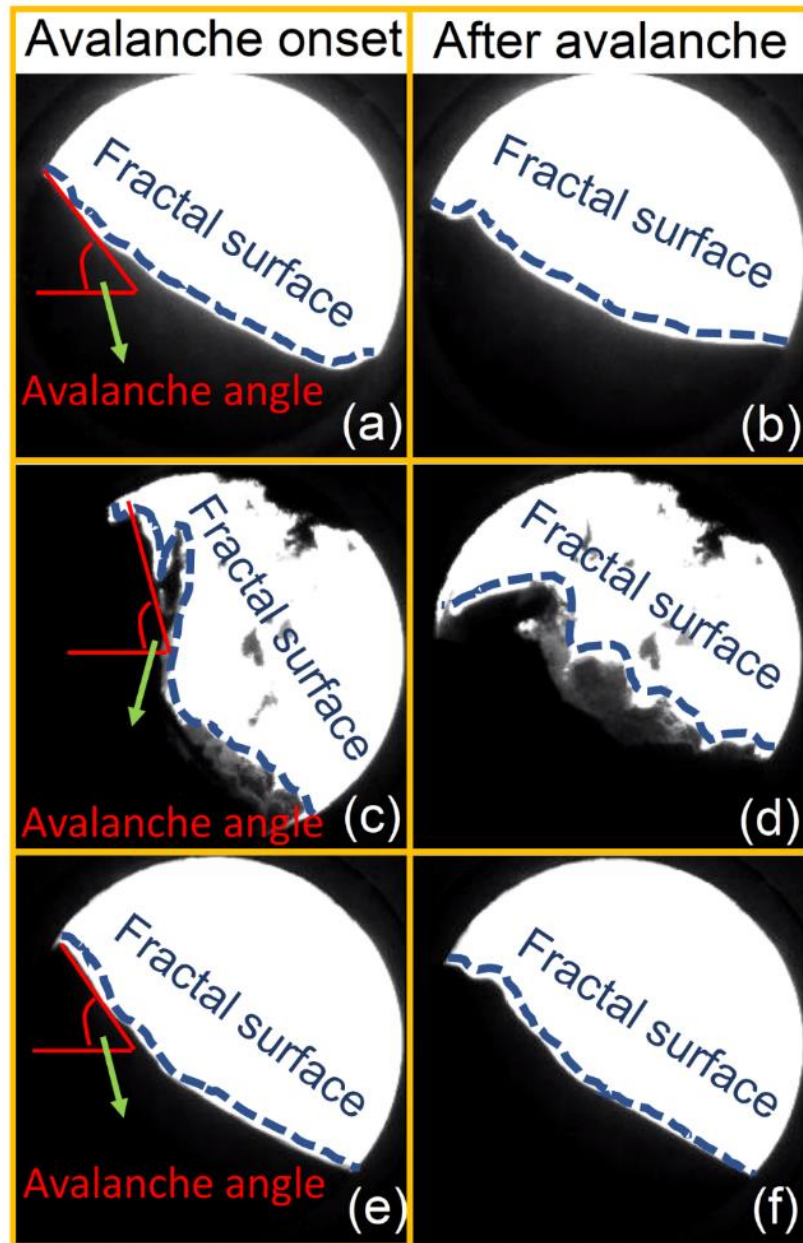


Figure 5.7. Images captured from the powder in the rotating drum at the onset and after an avalanche for (a,b) AlSi12, (c,d) R4 and (e,f) B1.5 powders showing the avalanche angle and/or fractal surface.

Generally speaking, the flowability of powders is dictated by the inter-particle cohesive forces as well as adhesive forces. The fractal dimension is a flowability parameter which can be measured from the fractal surface of the powder and is basically an indirect

measurement of inter-particle cohesive forces [44]. The fractal surface here refers to the real length between two points on the powder surface (Figure 5.7), and a fractal dimension is a ratio (dimensionless) providing a statistical index of complexity comparing how the magnitude of the fractal surface changes with the scale at which it is measured [45]. The existence of a very smooth and even fractal surface (fractal dimension in the range of 1.5-2 [46]) during rotation implies weak inter-particle cohesive forces, letting particles rearrange efficiently during rotation like the ones observed for AlSi12 and B1.5 powders in Figure 5.7(a,b,e,f). However, powders with rough, uneven, or jagged fractal surfaces (large fractal dimensions) are caused by strong inter-particle cohesive forces that do not allow the particles to move efficiently relative to each other to form a smooth surface during drum rotation (R4 powder in Figure 5.7(c,d)). The fractal dimension measurement was made every 0.1 sec to understand how the powder is rearranged during the drum rotation, not just after each avalanche. By plotting the surface fractal dimensions versus test time in Figure 5.8(k-o), the average fractal dimension and its SD was determined for all powders. As it is evident, B1.5 and B2 samples showed fractal dimensions only up to 18% higher than that of the AlSi12 powder, though the SD values increased up to 5 times. On the other hand, the R4 and R6 samples showed noticeably higher fractal dimensions, up to 273.2% higher than that of the reference powder. The same trend was observed for the SD values. This very evidence proves the existence of significantly stronger inter-particle forces in the R4 and R6 samples than the B1.5 and B2 ones. That is why the drum had to rotate to higher angles to force the former powders to avalanche. The L-PBF process is one of the manufacturing techniques which requires the deposition of a very thin layer of powder. The powder bed must be uniform, even, and smooth to ensure the quality of the printed part is not location dependent. Therefore, powders with surface fractals closer to

that of the AlSi12 powder, e.g., B1.5 and B2, lead to parts with more uniform and better qualities.

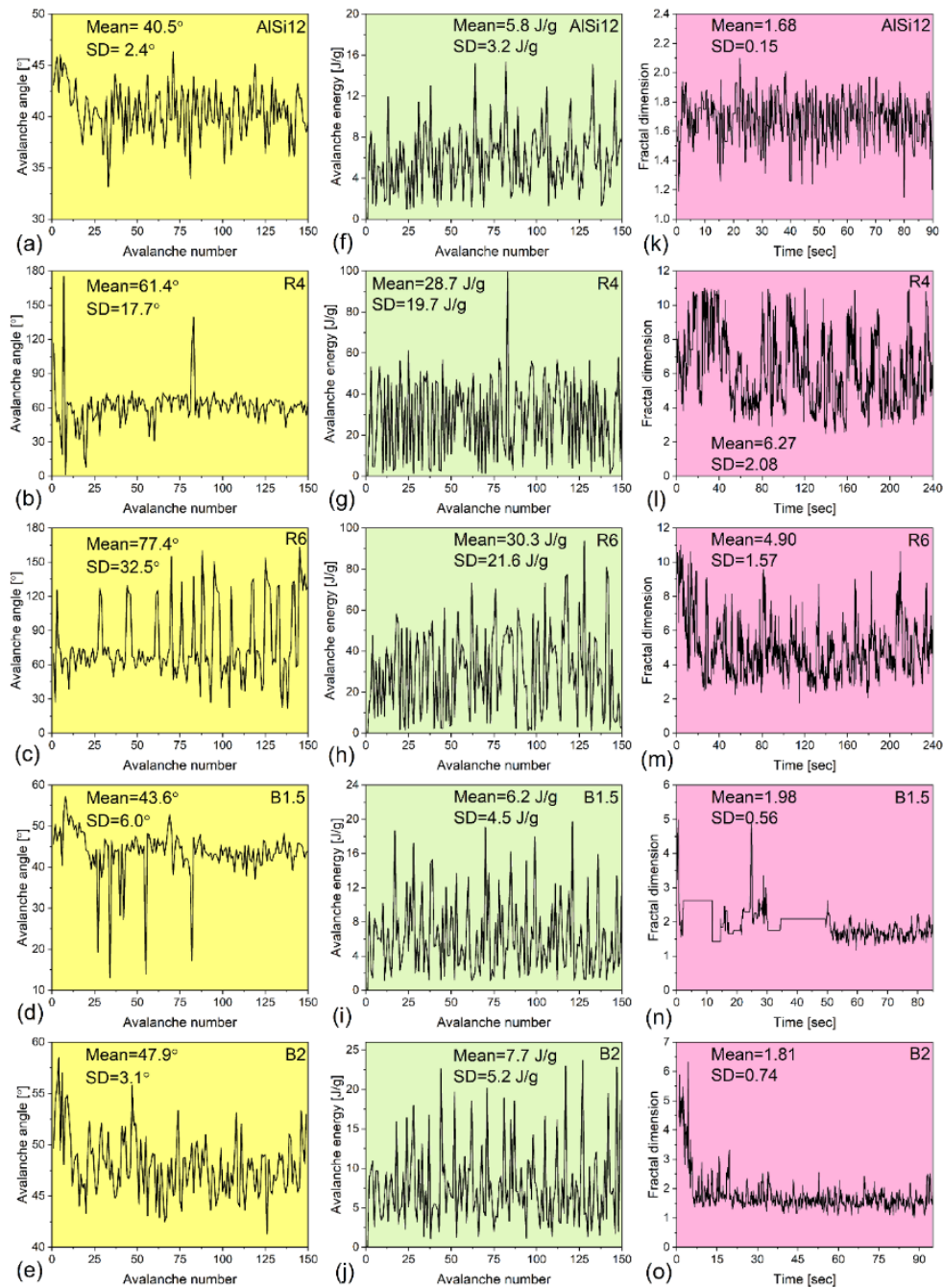


Figure 5.8. (a-e) Avalanche angle, (e-j) avalanche energy, and (k-o) fractal dimension for the designated powders.

But why the regularly mixed powders are showing significantly lower flowability and higher inter-particle cohesive forces than ball milled ones? Since R4 and R6 powder samples possess more **host** particles with attributes closer to those of the AlSi12 powder, it can be inferred that the above findings have nothing to do with the **host** but the **guest** particles. To answer the above question, a simplified calculation of Van der Waals forces (one of the inter-particle cohesive forces) was exercised in the absence and presence of the guest particles. In the presence of guest particles, two scenarios, (i) interaction of a guest-decorated host particle with a non-decorated host particle and (ii) interaction of two guest-decorated host particles, were taken into account. When having only host powder particles (Figure 5.9(a)), the van der Waals attraction force between two adjacent particles can be calculated as follows [47]:

$$P_{Non-decorated} \cong \frac{A_{hh}}{12} \frac{D}{2} \frac{1}{h_0^2} \quad \text{Eq. (6)}$$

in which A_{hh} is the Hamaker constant for the interacting host particles, D_h denotes the diameter of the host particles, and h_0 signifies the atomic-scale separation between particles.

In cases where a g_1 -decorated h_1 particle interacts with a non-decorated h_2 particle (Figure 5.9(b)), the amount of force required to separate the g_1 - h_1 assembly from h_2 particle can be estimated by the following equation [48]:

$$P_{Decorated/Non-decorated} \cong \frac{A_{hg}}{12} \frac{dD}{d+D} \frac{1}{h_0^2} \quad \text{Eq. (7)}$$

in which A_{hg} is the Hamaker constant for the interaction between host (h_2) and guest (g_1) particles, and d denotes the diameter of the guest particle. It should be noted that the above equation has another term for the interaction between the h_1 and h_2 particles, but because it is orders of magnitude smaller than the first term, it can be neglected. Since d is much

smaller than D in the composite powder systems with nano to submicron scale guest powder particles in this study, Eq. (7) can be simplified as [48]:

$$P_{Decorated/Non-decorated} \cong \frac{A_{hg}}{12} d \frac{1}{h_0^2} \quad \text{Eq. (8)}$$

Therefore, the force required to detach the decorated/non-decorated particles compared to that for the fully non-decorated host particles is given by the following ratio:

$$\frac{P_{Decorated/Non-decorated}}{P_{Non-decorated}} = 2 \frac{A_{hg} d}{A_{hh} D} \quad \text{Eq. (9)}$$

When two guest-decorated host particles have their guest particles in contact with each other (Figure 5.9(c)), the force needed to break down this contact can be estimated by [48]:

$$P_{Decorated} \cong \frac{A_{gg} d}{12} \frac{1}{2 h_0^2} \quad \text{Eq. (10)}$$

where A_{gg} is the Hamaker constant for the interaction between g_1 and g_2 guest particles.

This equation also has three other terms considering the interaction between (h_1, g_2) , (h_2, g_1) , and (h_1, h_2) particles, but they are neglected since they are several orders of magnitude smaller than the provided term. Dividing Eq. (10) by Eq. (6) yields the detachment force in the fully decorated case compared to the fully non-decorated one as:

$$\frac{P_{Decorated}}{P_{Non-decorated}} = \frac{A_{gg} d}{A_{hh} D} \quad \text{Eq. (11)}$$

Referring to Eqs. (9) and (11), decoration of host particles by guest particles with a thickness in the range of submicron to a few microns definitely reduces the cohesive force compared to that of fully non-decorated host powder particles. Given that the decoration of host particles by guest ones happened only in the case of the ball milled samples (Figure 5.3), their lower inter-particle cohesivity (fractal dimension-Figure 5.8(k-o)) and higher flowability (avalanche angle and energy-Figure 5.8(a-j)) than regularly mixed powders are justifiable.

Table 5.3 summarizes the Hamaker constants and van der Waals attraction force ratios in Eq. (9) and Eq. (11) as a function of d . As can be seen, the amount of the decrease in Van der Waals forces is proportional to the guest diameter for a fixed host diameter. It is not possible to find the size distribution of the guest particles in the B1.5 and B2 samples. Still, it can be said that a range of guest particle thickness (not length) from submicron to a few microns was detected based on SEM and EDS observations and measurements (Figure 5.2 and Figure 5.3). In any case, the $\frac{P_{Decorated/Non-decorated}}{P_{Non-decorated}}$ and $\frac{P_{Decorated}}{P_{Non-decorated}}$ ratios would be considerably smaller than unity, meaning that presence of the guest particles attached to the surface of the host ones is the key factor determining the flowability of the composite powders. The existence of non-attached guest particles in R4 and R6 samples not only does not change the host-host inter-particle Van der Waals forces but also adds new sources of cohesion, namely, host-guest and guest-guest, leading to a significant reduction in composite powder flowabilities. It is worth mentioning that C was also detected on the surface of most of the host particles in R4 and R6 samples (on all B1.5/B2 particles); however, as explained before, these are just the carbon layers separated from the guest particles and transferred to the surface of host ones as they were rubbing against each other during mixing, and the surface of the particles partially covered by C have remained pretty smooth (Figure 5.2). Therefore, they cannot act as fine surface roughening agents to distance the host particles during flow and reduce the inter-particle forces. In other words, it is not existence of carbon on the surface but attachment of guest particles that should be taken into consideration to understand the flow behavior.

Table 5.3. Hamaker constants and van der Waals attraction force ratios for B1.5 and B2 powder samples.

Sample	A_{hh} [J]	A_{hg} [J]	A_{gg} [J]	D_{50} [μm]	$\frac{P_{Decorated/Non-decorated}}{P_{Non-decorated}}$	$\frac{P_{Decorated}}{P_{Non-decorated}}$
B1.5	3.3×10^{-19}	2.9×10^{-19}	2.6×10^{-19}	41.1	$0.0428d$	$0.0192d$
B2	¹⁹ [49]	¹⁹ [50]	¹⁹ [51]	43.1	$0.0408d$	$0.0183d$

Based on the above discussion, the ball milled powders should have also shown flowabilities superior to that of the AlSi12 powder. This is while the fractal dimension and avalanche angle/energy results proved a lower inter-particle cohesivity and better flowability for AlSi12 powder, respectively. To resolve this contradiction, it must be highlighted that the Van der Waals force is not the only inter-particle force that affects the flowability of powders. The liquid bridging of the moisture in powder systems upon existence causes another source of forces known as adhesive forces. Liquid bridges are formed at the contact zones of the particles, and because of the surface tension of the water, the particles are attracted to one another [52]. To investigate the role that moisture may have played in flowability, the relative humidity of the AlSi12 and composite powders was measured. According to Figure 5.9(d), the difference between the relative humidity of the ball milled and regularly mixed powders is subtle, and therefore, humidity has nothing to do with the differences observed between the flowability of B1.5/B2 and R4/R6 samples. However, comparing the moisture content of B1.5/B2 to that of the AlSi12 powder, a ~62% increase in relative humidity was observed. This factor, along with the intensified interlocking of the host powder particles due to their deformation and cold-welding in ball milled powders [7] are believed to be the main reasons behind the lower flowability of B1.5/B2 than AlSi12 powder.

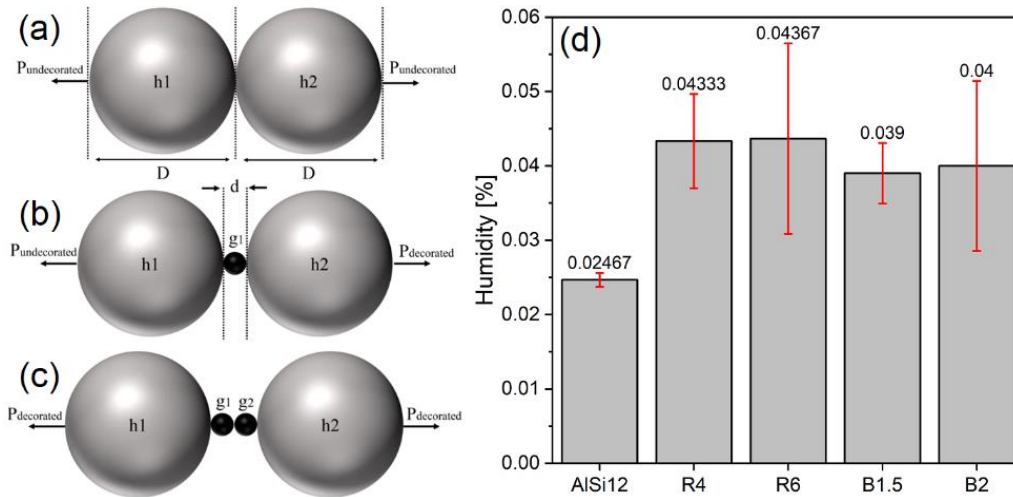


Figure 5.9. Schematic illustration of (a) two non-decorated host particles, (b) a guest-decorated particle with an undecorated one, and (c) two guest-decorated host particles and (d) relative humidity of different powders.

5.3.3 O/C/H content of the powders

The nominal content of guest added to the R4/B1.5 and R6/B2 powders was 0.5 and 1 wt%, respectively. The results of C content measurements (in wt%) for different powders are shown in Figure 5.10(a). The C content of the AlSi12 powder and the purity of the C guest powder used in this study are also provided in this graph. For R4 and B1.5 powders, the detected C content was almost identical to the nominal value. However, 0.14 and 0.19 wt% loss of C was observed for the R6 and B2 samples, respectively. Apparently, at higher guest percentages, the chance of the attachment of the guest particles to the jar wall (in both regular mixing and ball milling) and stainless steel balls (just in ball milling) has increased, leading to a meaningful reduction in the percentage of the guest constituent in the prepared composite powders. Therefore, it is recommended to perform a pilot test prior to production of the main composite powder batch to understand how much extra guest constituent must be added in the beginning to compensate for the losses that may happen during the mixing process. In section 5.3.2.1, the absorptivity of B2 powder was found to

be slightly lower than R6. One of the reasons that can describe such a difference can be attributed to the slightly lower percentage of guest powder in the former sample.

Figure 5.10(b) shows the oxygen content (in ppm) of AlSi12 and composite powders. The oxygen content of the starting carbonaceous constituent (in wt%) is also provided on the graph. For AlSi12, the detected oxygen is mainly because of the nano-size oxide layers on the surface of the particles [37]. For R4, R6, B1.5 and B2 samples with 0.5 or 1 wt% guest, the oxygen content was found to be 178, 246, 867, and 1438 ppm higher than that of the AlSi12 powder, respectively. Considering the oxygen content of the guest constituent (1.5 wt% or 15000 ppm) and using the mixture rule, an oxygen content of 795 and 867 ppm was expected for R4/B1.5 and R6/B2 samples, respectively. While the oxygen content of the regularly mixed powders is relatively closer to these estimated values, the oxygen content of the ball milled ones is significantly far from them. This study conducted powder mixing under no protective gas to make it closer to the real conditions of mass composite powder production for industrial applications. What basically has happened during the mixing process is that, especially for ball milling, the repeated collisions with jar and/or balls experienced by the host particles have resulted in the breakdown of the oxide layers covering these particles. On this account, the fresh AlSi12 was exposed to the air, causing the formation of new oxide layers and an increase in the total oxygen content of the powder. The higher the impact energy during the mixing, the higher the chance of host particle deformation, oxide layer breakdown and formation of new oxide layers. This is evidenced by the higher oxygen content of the B1.5/B2 than R4/R6 samples, as well as the higher oxygen of B2 than B1.5 due to the higher ball-to-powder ration, longer mixing time, and probably higher temperature of the powder system in the former case. It is worth noting that a part of the detected oxygen in all powder systems is attributed to moisture (Figure

5.9(d)). According to these results, protective gas is recommended, especially when ball milling is utilized. However, the oxygen content of the powders should not be considered as a criterion for selection of the mixing process as the oxides were proved to remarkably diminish through oxide spallation and evaporation in the case of pure Al, AlSi12 and AlSi10Mg alloys during the L-PBF process [37].

Figure 5.10(c) shows the hydrogen content of the AlSi12 and composite powders, respectively. As can be seen, R4, R6, B1.5 and B2 samples possess 32.2, 81.8, 85.8, and 155.8 ppm higher hydrogen than AlSi12 powder, respectively. The increase in the hydrogen content originates from the pickup of moisture from the environment during the mixing process and storing of powders, as well as the impurities of the guest constituent. Generally speaking, the amount of hydrogen in all powder systems is relatively insignificant, and most of it is expected to diminish during the L-PBF process.

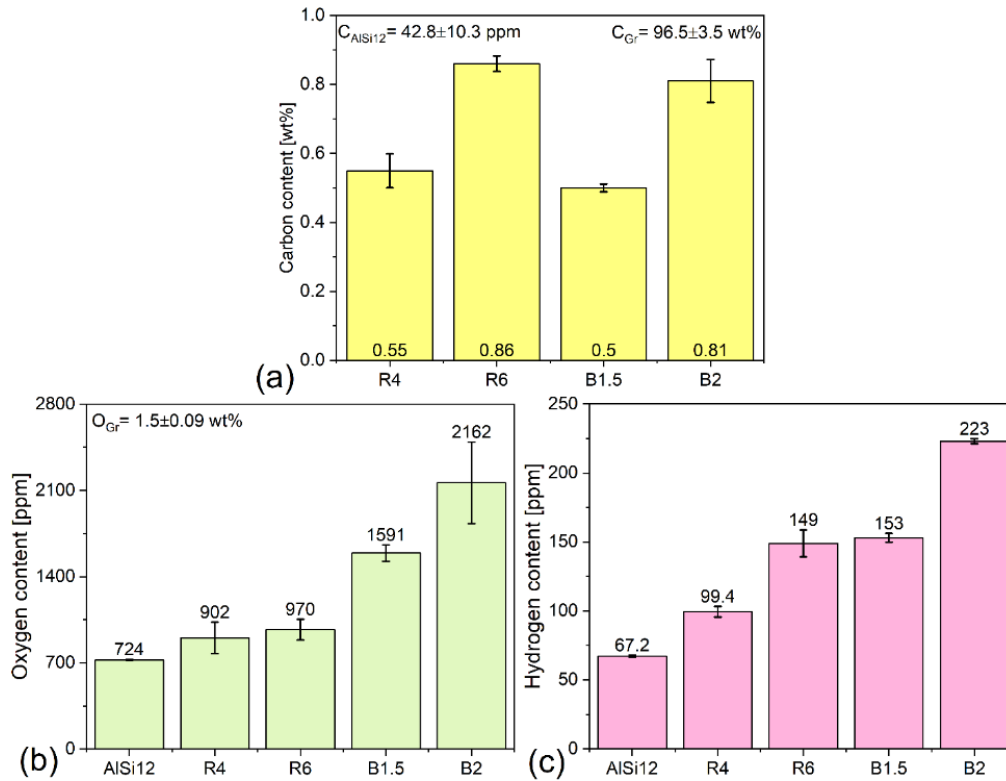


Figure 5.10. (a) Carbon, (b) oxygen and (c) hydrogen content of different powders.

5.3.4 Carbon quality and type: Raman spectroscopy

Figure 5.12, Figure 5.13, and Figure 5.14 show the Raman spectroscopy results for starting carbonaceous powder, ball milled and regularly mixed composite powders, respectively. The reference Raman spectra of graphite, monolayer graphene, nanographite, damaged graphene, and crystalline Si are shown in Figure 5.11 as guides for the interpretation of the results. Before delving into the discussion, three characteristic peaks, namely, D, G and 2D should be defined (Figure 5.11). These peaks are perceptible in all forms of carbon shown in Figure 5.11; therefore the **position**, **shape**, and **intensity ratios** of the peaks should be considered as the criteria to judge the type of carbon [53], not the mere presence of these peaks. The G peak is the so-called “graphite mode” and originates from in-plane vibration/bond-stretching of pairs of sp^2 carbon atoms (carbon atoms with three bonds)

both in rings and chains [54]. The D band is due to the breathing of sp^2 atoms in rings due to the presence of disorder in sp^2 hybridized carbon systems and is representative of defects in the carbonaceous materials [55]. The 2D peak is the second most prominent peak perceptible in the graphite, historically named as G band; however, this is referred to as 2D band since it has been proved to be second order overtone of the D band [53]. This peak provides helpful information about the stacking order and number of graphene layers for a few-layer graphene samples (up to 5 layers) [56]. The reference Raman spectrum shown in Figure 5.11 (a,d,e) shows a G band at $\sim 1580\text{ cm}^{-1}$ for graphite (**peak position factor**), while the D peak ($\sim 1350\text{ cm}^{-1}$) is almost absent due to insignificant amount of defects in the graphite sample. The 2D band in graphite consists of two components (**peak shape factor**), namely, $2D_1$ and $2D_2$, locating at 2685 and 2722 cm^{-1} , with intensities $1/4$ and $1/2$ of the G peak [53] (**relative intensity factor**), respectively. The reference Raman spectrum of monolayer graphene is shown in Figure 5.11 (b,f,g) with a G peak at $\sim 1580\text{ cm}^{-1}$. The typical identification criterion for monolayer graphene is that the 2D band is more intense than the G band (**relative intensity factor**) and as opposed to graphite, 2D is a single sharp peak (**peak shape factor**) [56]. Moreover, compared to graphite, the 2D position downshifts to a lower Raman shift of $\sim 2672\text{ cm}^{-1}$ (redshifts to longer wavelengths) in monolayer graphene (**peak position factor**). In some studies, 2D peaks with intensities up to 4 times greater than that of G peak were reported for monolayer graphene [53]. It is worth noting that increasing the number of graphene layers from 1 to 5 yields to a Raman spectrum almost identical to that of the bulk graphite [56]. Figure 5.11 (j,k) shows the Raman spectrum of nanographite and damaged graphene with D, G and 2D positions at ~ 1350 , 1582 , and 2700 cm^{-1} , respectively. Although the **band positions** are almost identical to that of the defect-free bulk graphite (Figure 5.11 (a,d,e)), (i) the D peak

intensifies due to the presence of structural defects such as grain boundaries in nanographite (I_D/I_G increases-**relative intensity factor**), (ii) D' peak appears at $\sim 1620\text{ cm}^{-1}$, and (iii) peak broadening occurs due to the increased structural disorder (**peak shape factor**) [53]. In some studies, it has been reported that the increased structural disorder disturbs the doublet structure of the D and 2D bands as well [53]. For highly disorder nanographite, the broadening of G and D' is such that only one peak can be observed, named as the G peak, and its position upshifts from 1580 cm^{-1} to 1600 cm^{-1} (blueshifts to shorter Raman wavelengths) [57]. Moreover, the I_D/I_G ratio exceeds unity in such cases [58]. The $2D'$ band is also perceptible for carbonaceous materials, which is the second order of the intra-valley D' peak [53]. Finally, the $D+D'$ and $D+G$ peaks shown in damaged graphene and nanographite, respectively, are located at a position identical to sum of the D and D' or D and G Raman shifts for the respective materials.

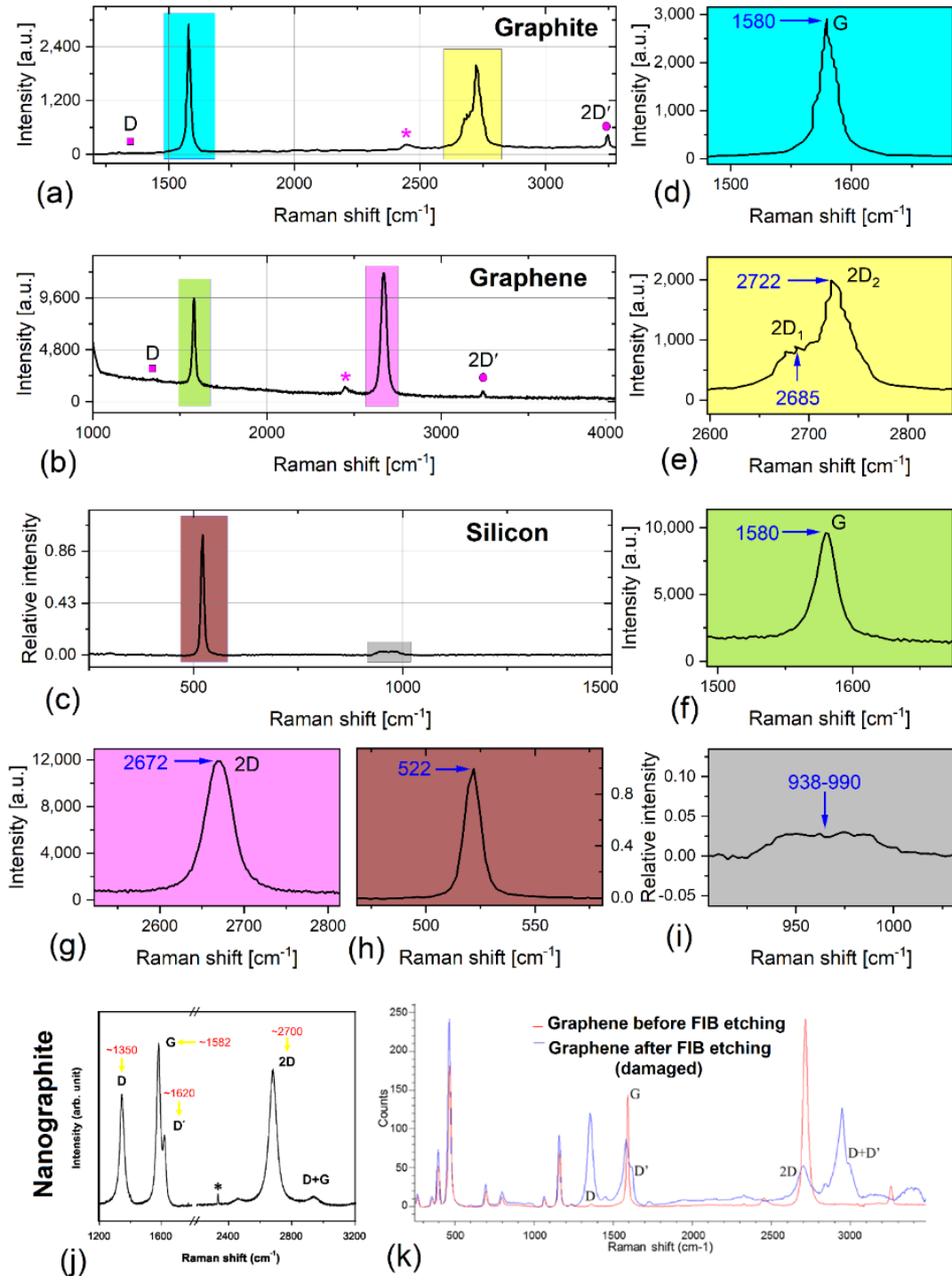


Figure 5.11. Reference Raman spectra for (a,d,e) graphite [59], (b,f,g) graphene [60], (c,h,i) crystalline silicon [61], (j) nanographite [62], and (k) damaged graphene [63].

Using the lessons drawn from the close examination of the graphite, monolayer graphene, damaged graphene, and nanographite, the true nature of the starting carbonaceous powder and the guest particles after mixing can be explored. Figure 5.12 shows the three particles subjected to the Raman mapping and their representative Raman spectra. As can be seen, the acquired spectra resemble the reference Raman spectrum of bulk graphite (Figure 5.11 (a,d,e)) in terms of peak shapes and relative intensities. However, slight to moderate changes in the peak position compared to bulk graphite can be observed, especially for D and $2D_1$ bands. The deviations from the nominal peak positions of bulk graphite are believed to be due to oxygen (1.5 wt%) and other possible impurities in the starting carbonaceous powder. Referring to Figure 5.12, the D peak shows low intensity for flakes 1 and 2, though high intensity for flake 3. This implies that carbon particles with different amounts of structural disorder exist in the starting powder. Given that the Raman spectrum of multi-layer graphene (more than 5 layers) is the same as that of the bulk graphite, it is almost impossible to identify whether the starting carbonaceous powder is graphite or graphene nanoplatelets [56] (up to 150 layers is still called graphene [54]) unambiguously from the Raman results. However, based on the SEM micrographs (Figure 5.2(a)) and Raman results, it can be claimed that the starting carbon powder is a combination of graphite (coarse particles and fine particles) and graphene nanoplatelets (ultra fine particles), with features leaning toward graphite more than graphene. As mentioned earlier, the starting carbon powder was purchased as the graphene nanoplatelets with a thickness range of 2-8 nm (up to 24 graphene layers). Nevertheless, the dry multi-layer graphene powders tend to form agglomerates with features closer to graphite than graphene during storage due to the strong Van der Waals forces existing among them.

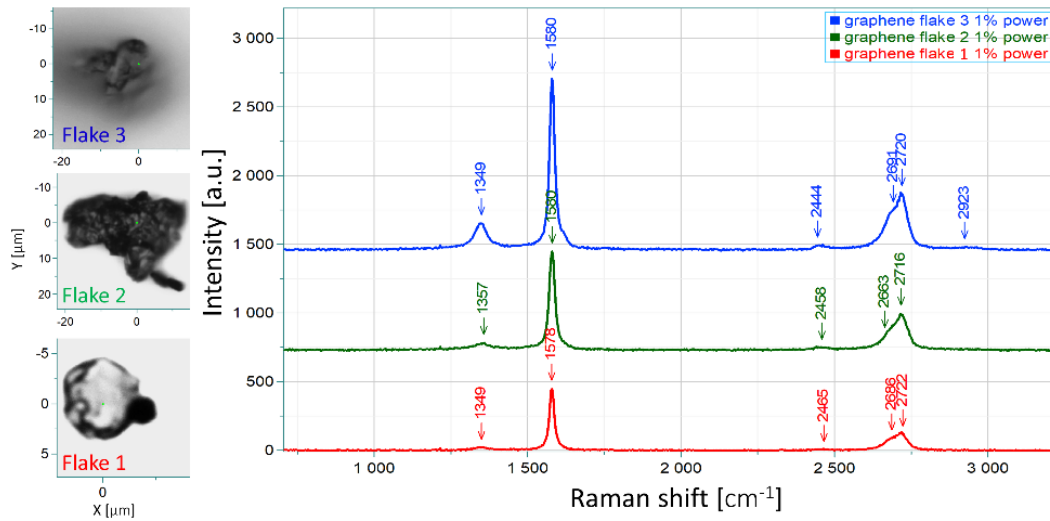


Figure 5.12. (a) Raman mapping results for three starting C particles, (b) Range of G, D and 2D positions detected for a C particle.

The Raman mapping results for the B1.5 and B2 samples are shown in Figure 5.13. Figure 5.13(a) shows two different types of detected carbon plus the sample Raman spectrum of each carbon type. The red color is attributed to the carbon layers transferred from guest particles to the surface of host ones due to the rubbing of the guest/host particles against each other during the ball milling process (Figure 5.3). The blue color represents the guest particles attached to the host ones. By comparing the red spectrum shown in Figure 5.13(a) with the Raman spectra in Figure 5.11, it can be inferred that the carbon layers on the surface of host particles in the B2 sample are more like nanographite since the I_D/I_G ratio is greater than unity, and peaks are broad. Due to the high level of structural disorder, G and D' peaks have merged into one peak. Apart from the peak shapes and relative intensities, the peak positions are also close to the ones reported for nanographite, as the G peak's position is at 1600 cm⁻¹. Regarding the position of D peak, a downshift from 1350 to 1342 cm⁻¹ can be observed most probably due to the compressive stresses induced on the guest particles during the ball milling process. The two less intense and broad peaks at 2692 and 2933 cm⁻¹ have Raman shifts close enough to the nominal values shown in Figure 5.11(j)

for 2D, and D+G bands of nanographite and almost identical to values reported in [64] for nanographite. It should be noted that due to the absence of D+ D' peak in the red color spectrum, the detected carbon layer on the surface of host particles cannot be considered as damaged graphene.

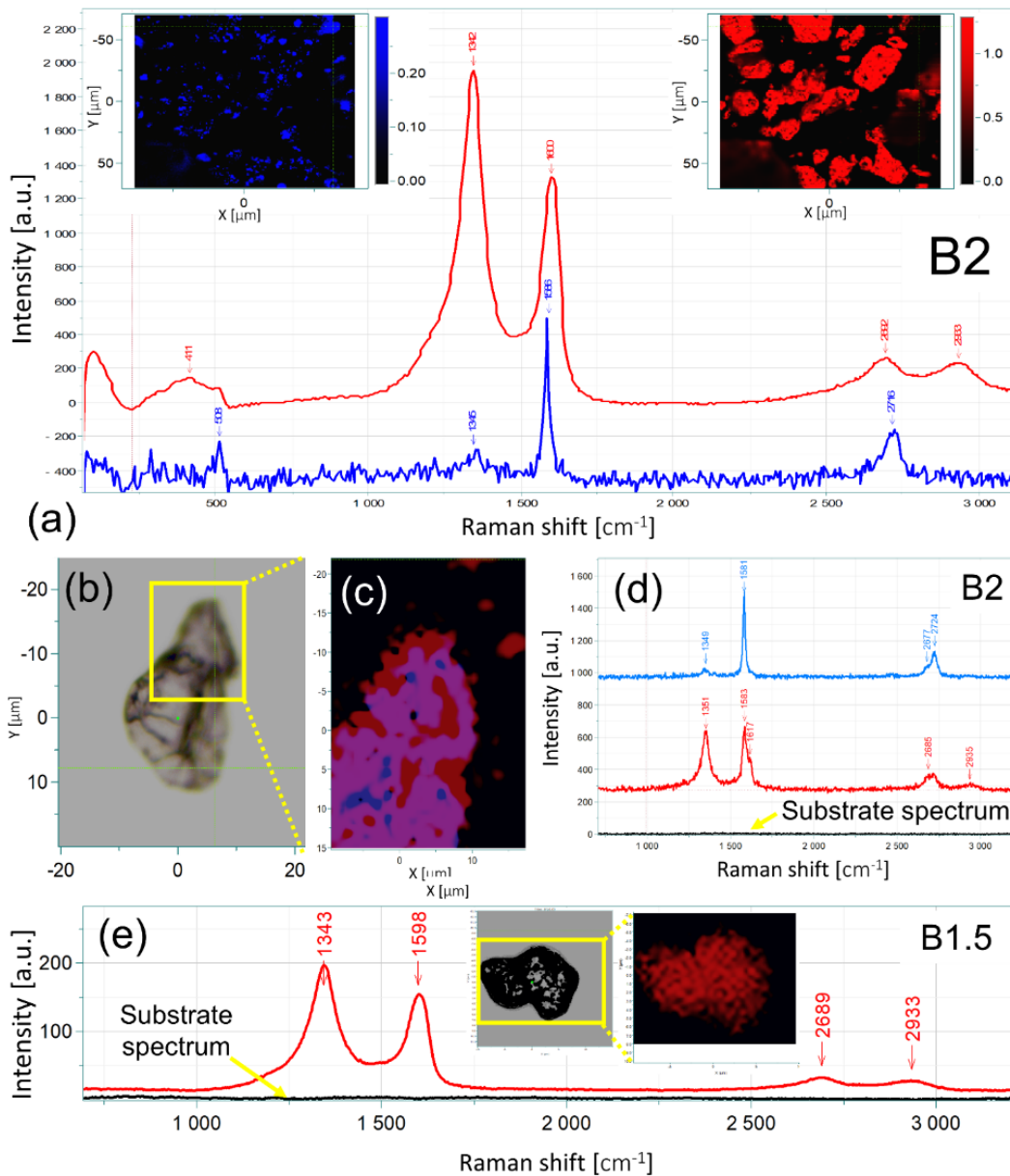


Figure 5.13. Raman mapping results for (a-g) B2 and (h) B1.5 samples. In the blue spectrum in (a) only the 2D₂ peak is labeled.

By comparing the blue color spectrum (for attached guest particles) in Figure 5.13(a) to the spectra in Figure 5.11(a,d,e,k), it can be inferred that the guest particles are more like graphite than any other form of carbon. As explained before, the bulk graphite and graphene nanoplatelets (more than 5 layers) have the same Raman spectrum, meaning that among the graphitic guest particles, graphene nanoplatelets may also exist but their presence cannot be proved unambiguously with Raman spectroscopy [56]. The low intensity of the D band suggests insignificant structural defects in the studied guest particles. The upshift in the G band and downshifts in the D band can be attributed to the compressive stresses and strains induced to the guest particles by the mixing process [54]. The red and blue spectra in Figure 5.13(a) show two peaks (i) a broad peak at 411 and (ii) a relatively sharp peak at 508 cm^{-1} , respectively. The Raman spectrum of the crystalline Si is shown in Figure 5.11(c,h,i), from which a peak at 522 cm^{-1} can be observed. It is believed that the mentioned two peaks are attributed to the Si precipitates in AlSi12 host powder particles. The slight to significant downshifts in the peak position from the nominal value can be due to the presence of nanosized and amorphous Si precipitates in the host particles [65]. For further examinations, Raman mapping was conducted on a single particle in the B2 sample, the results of which are shown in Figure 5.13(b-d). The blue, and red regions in the Raman map shown in Figure 5.13(c) represent two distinct types of carbon with Raman spectra shown in Figure 5.13(d). The purple color in Figure 5.13(c) has features of both types of the detected carbon. With the same logic as before, the position, shape, and intensity of the peaks for the blue color spectrum are almost identical to that of the bulk graphite/graphene nanoplatelets (Figure 5.11(a,d,e)). The red color spectrum resembles nanographite (Figure 5.11(j)) since the I_D/I_G approaches unity, D' peak appears at 1617 cm^{-1} (close to the nominal value of 1620 cm^{-1}) and D+G peak exists at 2935 cm^{-1} in the detected

spectrum. The increased structural disorder has disturbed the doublet structure of the D and 2D bands as the latter was observed at 2685 cm^{-1} instead of 2702 cm^{-1} [53]. Almost the same finding were achieved for the particles of B1.5 sample decorated by guest powder particles (not shown here); By managing to find a non-decorated particle in B1.5 sample (Figure 5.13(h)) and performing Raman mapping, it was proved that the carbon layers are more like nanographite than anything else with G and D' peaks merged into one peak with a Raman shift close to the nominal value of $\sim 1600\text{ cm}^{-1}$ (1598 cm^{-1}) and the fact that the I_D/I_G higher than unity. The same as before, due to the absence of D+ D' peak, the carbon layer on the host particles cannot be considered as damaged graphene.

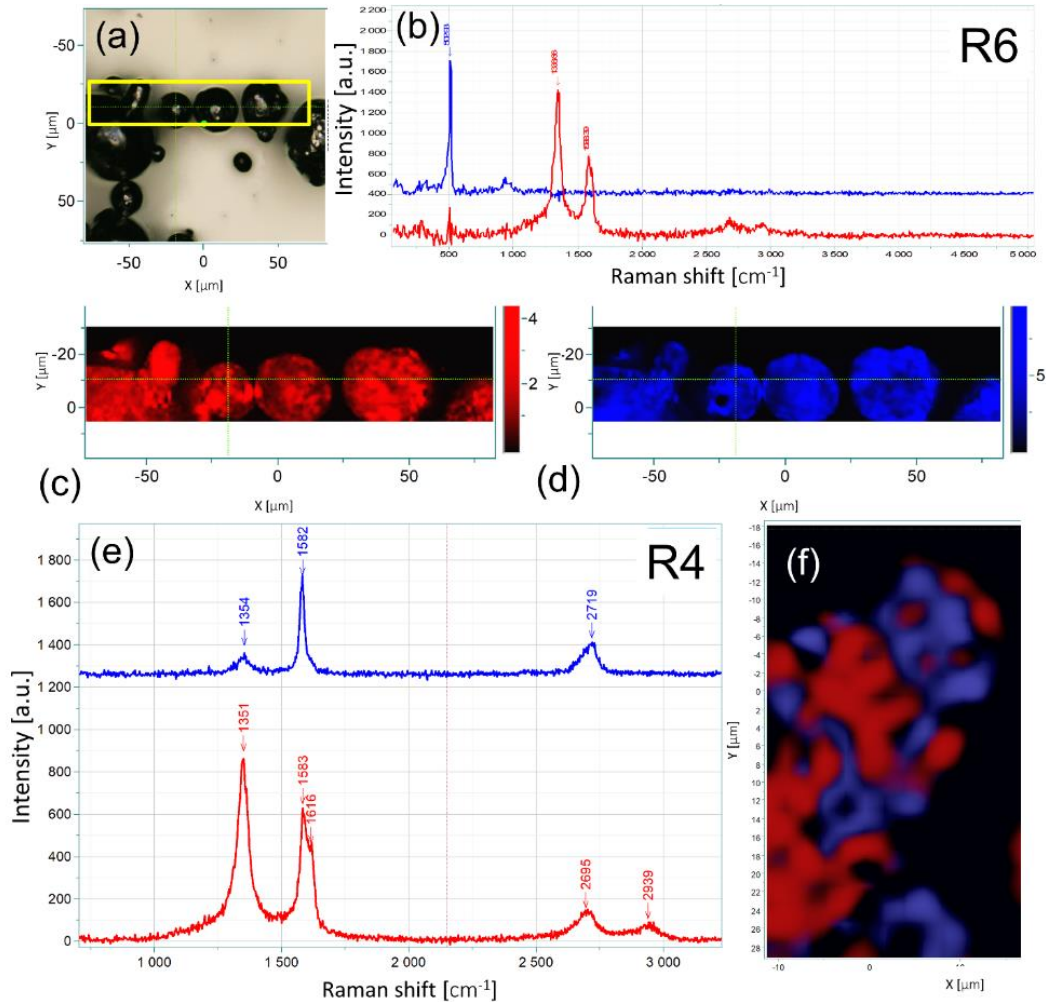


Figure 5.14. Raman mapping results for R6 and R4 samples.

The Raman results for regularly mixed powders are shown in Figure 5.14. Figure 5.14(a-d) shows the Raman mapping results of a few host particles in the R6 sample with carbon layers on their surface, similar to those shown in Figure 5.2(h-k). No guest particles existed among the host particles in the selected region of interest. Two bands are perceptible in the blue color spectrum at ~ 503 and 942 cm^{-1} , signifying that the blue color map (Figure 5.14(d)) is attributed to Si (Figure 5.11). The downshift from 522 cm^{-1} in the reference Raman spectrum to 503 cm^{-1} in the host particles of the R6 sample is due to the presence of nanosized Si precipitates in AlSi12 particles [65]. The red color spectrum also shows a

peak at $\sim 505 \text{ cm}^{-1}$ which is attributable to Si. Other than that, five peaks were detected at ~ 1340 (D), ~ 1588 (G), ~ 1609 (D'), ~ 2685 (2D), and ~ 2935 (D+G), proving that the detected carbon layers on the surface of host particles are nanographite with high intrinsic structural defects (Figure 5.11(j)). The slight deviations from the reference peak positions could be attributed to the compressive stresses and strains induced on the powder particles by the regular mixing process [54]. For the R4 sample, a host particle with some guest ones on and around it was selected for Raman mapping, the results of which are shown in Figure 5.14(e,f). The guest particles with blue color map and spectrum resemble bulk graphite and graphene nanoplatelets (more than 5 layers [56]), judging from the peak positions, and shapes. The low I_D/I_G ratio proves that the graphite/graphene nanoplatelet has a relatively low disorder, though it is damaged. The red color map and spectrum have the features of the nanographite with peak shape, intensity, and positions almost identical to the ones detected in the R6 sample.

The Raman results on the ball-milled, and regularly mixed powders can be summarized as follows, (i) the carbon layers transferred from guest particles to the surface of host ones as they rub against each other during mixing are nanographite in both systems and (ii) the attached guest particles in ball milled powders and free guest particles in regularly mixed powders are bulk graphite/graphene nanoplatelets with relatively low structural damage. This brings the study to the conclusion that not only the ball milled powders show superior flowability to the regularly mixed ones, essential for L-PBF purposes, but also ball milling is capable of producing carbonaceous-reinforced composite powders without significantly damaging the guest particles. A quantitative investigation of the level of structural damage to the starting carbonaceous powder cannot be made with enough confidence from the above results, as Raman measurements have been carried out on a few random areas.

However, it makes perfect sense to surmise that the level of disorder should be higher in the ball-milled powders than the regularly mixed ones due to the presence of balls in the former. Finally, the guest constituent of the dry mechanically mixed composite powders was found to be more like graphite rather than monolayer or multi-layer graphene. This is in fact a blessing in disguise because upon existence of monolayer or few layer graphene particles in the composite powders, they would easily react with molten AlSi12 during the L-PBF process and turn into aluminum carbide [16]. This is while even if reaction between submicron/a few micron graphite particles (of the composite powders prepared in this study) with molten AlSi12 happens, a part of the guest particles remain intact due to the short interaction time of the L-PBF process (hopefully nanosized), leading to graphene nanoplatelets reinforced nanocomposites.

5.4 Conclusions

This study strived to answer two questions: (1) upon using dry graphene powder (usually in the form of graphite) as the starting reinforcement, is the output of dry mechanical mixing methods a composite powder with graphene nanoplatelets reinforcement or it turns into another form of carbon? And (2) regardless of the type of carbonaceous material in the fabricated mixed powder, is the produced composite powder suitable for the PBF applications? For this purpose, two composite powders, namely, AlSi12-0.5 wt%Gr (B1.5 or R4) and AlSi12-1 wt%Gr (B2 or R6) were prepared through ball milling (B1.5/B2) and regular mixing (R4/R6) processes. To answer the second question, the powder attributes (size, distribution, and shape), behaviors (absorptivity, packing density, and flowability), relative humidity, and O/C/H content of the powders were examined. Although the regularly mixed composite powders possessed relatively spherical host (AlSi12) particles with attributes closer to that of the starting AlSi12 powder, they failed to meet acceptable

flowability required for L-PBF applications due to the existence of non-attached guest particles. It was shown that the full decoration of host particles by the guest ones in the ball milled composite powders is the main reason behind their flow behavior close to that of the monolithic AlSi12. Regarding other behaviors, such as absorptivity and packing density, the ball milled powders were superior to or almost the same as the regularly mixed powders. From the relative humidity, particle size, and O/C/H measurements it was suggested to (i) dry ball-milled powders for a limited time in a furnace after mixing, (ii) sieve ball-milled powders, and (iii) perform ball milling in a protective atmosphere to achieve composite powders with better qualities. To answer the first question, Raman spectroscopy was carried out on the starting carbonaceous powder, ball milled and regularly mixed composite powders. By acknowledging the higher chance of structural damage of the guest particles in the case of ball milling, it was shown that both composite powders possess graphite/graphene nanoplatelet guest particles with low disorder and nanographite layers on the surface of all host particles (formed through host/guest rubbing against each other during mixing). Considering everything, this study suggests ball milling technique for the preparation of the graphite/graphene nanoplatelet-reinforced AlSi12 composite powders for the L-PBF purposes.

Acknowledgement

The authors would like to thank Dr J. E. Greedan and Evan Smith from the Department of Chemistry at McMaster University for providing us with the ball milling facility.

References

1. Fereiduni, E., A. Ghasemi, and M. Elbestawi, *Selective laser melting of aluminum and titanium matrix composites: recent progress and potential applications in the aerospace industry*. Aerospace, 2020. **7**(6): p. 77.
2. Zhang, F., et al., *Recent Advances on Graphene: Synthesis, Properties, and Applications*. Composites Part A: Applied Science and Manufacturing, 2022: p. 107051.
3. Tjong, S.C., *Recent progress in the development and properties of novel metal matrix nanocomposites reinforced with carbon nanotubes and graphene nanosheets*. Materials Science and Engineering: R: Reports, 2013. **74**(10): p. 281-350.
4. Saboori, A., et al., *An overview of metal matrix nanocomposites reinforced with graphene nanoplatelets; mechanical, electrical and thermophysical properties*. Metals, 2018. **8**(6): p. 423.
5. Narvan, M., et al., *Laser powder bed fusion of functionally graded bi-materials: Role of VC on functionalizing AISI H13 tool steel*. Materials & Design, 2021. **201**: p. 109503.
6. Fereiduni, E., A. Ghasemi, and M. Elbestawi, *Microstructural characterization and mechanical properties of nano-scale/sub-micron TiB-reinforced titanium matrix composites fabricated by laser powder bed fusion*. Journal of Alloys and Compounds, 2022. **896**: p. 163054.
7. Fereiduni, E., A. Ghasemi, and M. Elbestawi, *Characterization of composite powder feedstock from powder bed fusion additive manufacturing perspective*. Materials, 2019. **12**(22): p. 3673.
8. Zhao, X., et al., *Selective laser melting of carbon/AlSi10Mg composites: Microstructure, mechanical and electrical properties*. Journal of Alloys and Compounds, 2016. **665**: p. 271-281.
9. Wang, Y., et al., *Investigation of porosity and mechanical properties of graphene nanoplatelets-reinforced AlSi10 Mg by selective laser melting*. Journal of Micro and Nano-Manufacturing, 2018. **6**(1).
10. Zhang, S., et al., *Graphene/ZrO₂/aluminum alloy composite with enhanced strength and ductility fabricated by laser powder bed fusion*. Journal of Alloys and Compounds, 2022. **910**: p. 164941.
11. Zhang, S., et al., *Wear properties of graphene/zirconia biphasic nano-reinforced aluminium matrix composites prepared by SLM*. Materials Today Communications, 2022. **30**: p. 103009.

12. Li, P., et al., *Mechanically strong, stiff, and yet ductile AlSi7Mg/graphene composites by laser metal deposition additive manufacturing*. Materials Science and Engineering: A, 2021. **823**: p. 141749.
13. Ardila-Rodríguez, L., et al., *Surface modification of aluminum alloys with carbon nanotubes by laser surface melting*. Surface and Coatings Technology, 2019. **377**: p. 124930.
14. Du, Z., et al., *Aluminium-carbon nanotubes composites produced from friction stir processing and selective laser melting: Komposite aus Aluminium und Kohlenstoffnanoröhren durch Reib-Rühr-Schweißen und selektives Laserschmelzen*. Materialwissenschaft und Werkstofftechnik, 2016. **47**(5-6): p. 539-548.
15. Jiang, L., et al., *Preparation and mechanical properties of CNTs-AlSi10Mg composite fabricated via selective laser melting*. Materials Science and Engineering: A, 2018. **734**: p. 171-177.
16. Zhou, W., et al., *In situ formation of uniformly dispersed Al₄C₃ nanorods during additive manufacturing of graphene oxide/Al mixed powders*. Carbon, 2019. **141**: p. 67-75.
17. Dong, M., et al., *Microstructure and mechanical property of graphene oxide/AlSi10Mg composites fabricated by laser additive manufacturing*. Materials Characterization, 2020. **170**: p. 110678.
18. Liu, L.-Y., et al., *Anisotropic and elastoplastic characteristics of 3D printed graphene/aluminum composites by coupled experimental and numerical analysis*. Mechanics of Advanced Materials and Structures, 2021: p. 1-12.
19. Lüddecke, A., et al., *Powder properties and flowability measurements of tailored nanocomposites for powder bed fusion applications*. Materials & Design, 2021. **202**: p. 109536.
20. Wang, L.-z., T. Chen, and S. Wang, *Microstructural characteristics and mechanical properties of carbon nanotube reinforced AlSi10Mg composites fabricated by selective laser melting*. Optik, 2017. **143**: p. 173-179.
21. Hu, Z., et al., *3D printing graphene-aluminum nanocomposites*. Journal of Alloys and Compounds, 2018. **746**: p. 269-276.
22. Liu, X., et al., *CNT-reinforced AlSi10Mg composite by selective laser melting: microstructural and mechanical properties*. Materials Science and Technology, 2019. **35**(9): p. 1038-1045.
23. Zhao, Z., et al., *AlSi10Mg alloy nanocomposites reinforced with aluminum-coated graphene: Selective laser melting, interfacial microstructure and property analysis*. Journal of Alloys and Compounds, 2019. **792**: p. 203-214.

24. Bai, P., et al., *Microstructure and tribological behavior of graphene/Al composites produced by selective laser melting*. Materials Research Express, 2019. **6**(10): p. 1065c1.
25. Aboulkhair, N.T., et al., *Evolution of carbon nanotubes and their metallurgical reactions in Al-based composites in response to laser irradiation during selective laser melting*. Materials Science and Engineering: A, 2019. **765**: p. 138307.
26. Gu, D., et al., *Laser additive manufacturing of carbon nanotubes (CNTs) reinforced aluminum matrix nanocomposites: Processing optimization, microstructure evolution and mechanical properties*. Additive Manufacturing, 2019. **29**: p. 100801.
27. Tiwari, J.K., et al., *Investigation of porosity, microstructure and mechanical properties of additively manufactured graphene reinforced AlSi10Mg composite*. Additive Manufacturing, 2020. **33**: p. 101095.
28. Lee, E.R., et al., *Manufacturing aluminum/multiwalled carbon nanotube composites via laser powder bed fusion*. Materials, 2020. **13**(18): p. 3927.
29. Tiwari, J.K., et al., *Novel approach for micrographical investigation of graphene in additively manufactured graphene/AlSi10Mg composite*. Materials Letters, 2021. **284**: p. 128923.
30. Yu, T., et al., *Microstructure and wear characterization of carbon nanotubes (CNTs) reinforced aluminum matrix nanocomposites manufactured using selective laser melting*. Wear, 2021. **476**: p. 203581.
31. Wu, L., et al., *Wear resistance of graphene nano-platelets (GNPs) reinforced AlSi10Mg matrix composite prepared by SLM*. Applied Surface Science, 2020. **503**: p. 144156.
32. Tiwari, J.K., et al., *Effect of graphene addition on thermal behavior of 3D printed graphene/AlSi10Mg composite*. Journal of Alloys and Compounds, 2022. **890**: p. 161725.
33. Xi, L., et al., *In-situ synthesis of aluminum matrix nanocomposites by selective laser melting of carbon nanotubes modified Al-Mg-Sc-Zr alloys*. Journal of Alloys and Compounds, 2022. **891**: p. 162047.
34. Qiu, J., C. Chen, and M. Zhang, *Effects of graphene on the mechanical properties of AlSi10Mg melted by SLM*. Materials Science and Technology, 2022: p. 1-11.
35. Yoo, S., et al., *Aluminum matrix composites reinforced with multi-walled carbon nanotubes and C60 manufactured by laser powder bed fusion*. Journal of Materials Science, 2022: p. 1-16.
36. Balbaa, M., et al., *Role of powder particle size on laser powder bed fusion processability of AlSi10mg alloy*. Additive Manufacturing, 2021. **37**: p. 101630.

37. Ghasemi, A., et al., *Influence of alloying elements on laser powder bed fusion processability of aluminum: A new insight into the oxidation tendency*. Additive Manufacturing, 2021. **46**: p. 102145.
38. Fereiduni, E., A. Ghasemi, and M. Elbestawi, *Selective laser melting of hybrid ex-situ/in-situ reinforced titanium matrix composites: Laser/powder interaction, reinforcement formation mechanism, and non-equilibrium microstructural evolutions*. Materials & Design, 2019. **184**: p. 108185.
39. Bitra, V.S., et al., *Direct mechanical energy measures of hammer mill comminution of switchgrass, wheat straw, and corn stover and analysis of their particle size distributions*. Powder Technology, 2009. **193**(1): p. 32-45.
40. *Operating instructions/Manual particle size analysis system CAMSIZER*. Retsch Technology GmbH, Rheinische StraBe 43, 42781 Haan, Germany
41. Mitterlehner, M., et al., *Comparative Evaluation of Characterization Methods for Powders Used in Additive Manufacturing*. Journal of Materials Engineering and Performance, 2021. **30**(9): p. 7019-7034.
42. Gu, D., et al., *Laser absorption behavior of randomly packed powder-bed during selective laser melting of SiC and TiB₂ reinforced Al matrix composites*. Optics & Laser Technology, 2019. **119**: p. 105600.
43. Tan, H., et al., *Tribological properties of Al-20Si-5Fe-2Ni-Graphite solid-lubricating composites*. Tribology International, 2018. **121**: p. 214-222.
44. Spierings, A.B., et al., *Powder flowability characterisation methodology for powder-bed-based metal additive manufacturing*. Progress in Additive Manufacturing, 2016. **1**(1): p. 9-20.
45. Allen, M., G.J. Brown, and N.J. Miles, *Measurement of boundary fractal dimensions: review of current techniques*. Powder Technology, 1995. **84**(1): p. 1-14.
46. Spurek, M.A., et al., *Influence of the particle size distribution of monomodal 316L powder on its flowability and processability in powder bed fusion*. Progress in Additive Manufacturing, 2022. **7**(4): p. 533-542.
47. Massimilla, L. and G. Donsi, *Cohesive forces in fluidization of fine particles*. Int. Congr. Chem. Eng., Chem. Equip. Des. Autom.,[Proc.], 5th, 1975.
48. Yang, J., et al., *Dry particle coating for improving the flowability of cohesive powders*. Powder technology, 2005. **158**(1-3): p. 21-33.
49. Tolias, P., *Non-retarded room temperature Hamaker constants between elemental metals*. Surface Science, 2020. **700**: p. 121652.

50. Lüddecke, A., et al., *Powder properties and flowability measurements of tailored nanocomposites for powder bed fusion applications*. *Materials & Design*, 2021. **202**: p. 109536.
51. Tolias, P., *Lifshitz calculations of Hamaker constants for fusion relevant materials*. *Fusion Engineering and Design*, 2018. **133**: p. 110-116.
52. Schulze, D., *Powders and bulk solids*. Behaviour, characterization, storage and flow. Springer, 2008. **22**.
53. Ferrari, A.C., *Raman spectroscopy of graphene and graphite: Disorder, electron-phonon coupling, doping and nonadiabatic effects*. *Solid state communications*, 2007. **143**(1-2): p. 47-57.
54. Ni, Z., et al., *Raman spectroscopy and imaging of graphene*. *Nano Research*, 2008. **1**: p. 273-291.
55. Dresselhaus Mildred, S., et al., *Perspectives on carbon nanotubes and graphene Raman spectroscopy*. *Nano letters*. **10**: p. 751-758.
56. Ferrari, A.C., et al., *Raman spectrum of graphene and graphene layers*. *Physical review letters*, 2006. **97**(18): p. 187401.
57. Diaf, H., et al., *Revisiting thin film of glassy carbon*. *Physical Review Materials*, 2020. **4**(6): p. 066002.
58. Childres, I., et al., *Raman spectroscopy of graphene and related materials*. *New developments in photon and materials research*, 2013. **1**: p. 1-20.
59. <https://ramanlife.com/library/graphite/>.
60. <https://ramanlife.com/library/graphene-raman/>.
61. <https://ramanlife.com/library/silicon-raman/>.
62. Pimenta, M., et al., *Studying disorder in graphite-based systems by Raman spectroscopy*. *Physical chemistry chemical physics*, 2007. **9**(11): p. 1276-1290.
63. Saadani, A., et al. *FIB-Induced damage in graphene electrodes for piezoelectric resonators*. in *2018 Symposium on Design, Test, Integration & Packaging of MEMS and MOEMS (DTIP)*. 2018. IEEE.
64. Fishlock, S., et al., *Mechanical characterisation of nanocrystalline graphite using micromechanical structures*. *Microelectronic Engineering*, 2016. **159**: p. 184-189.
65. Meier, C., et al., *Raman properties of silicon nanoparticles*. *Physica E: Low-dimensional Systems and Nanostructures*, 2006. **32**(1-2): p. 155-158.

6 Chapter 5 Influence of the graphene incorporation on nanostructure and thermal properties of the laser powder bed fusion processed AlSi12 matrix composites

Authorship contribution statement:

Ali Ghasemi: Conceptualization, Methodology, Investigation, Writing - original draft, Writing – review & editing. **Eskandar Fereiduni:** Conceptualization, Methodology, Investigation, Writing – review & editing. **Mohamed Elbestawi:** Supervision, Writing – review & editing. **Kayvon Savadkouei:** Investigation, Writing – review & editing. **Fran Adar:** Investigation, Writing – review & editing. **Jasmin Kathrin Saewe:** Investigation, Writing – review & editing. **Niklas Hartke:** Investigation, Writing – review & editing. **Saeid Habibi:** Supervision, Writing – review & editing.

Influence of the graphene incorporation on nanostructure and thermal properties of the laser powder bed fusion processed AlSi12 matrix composites

Abstract

The successful fabrication and implementation of graphene-reinforced aluminum (Al) matrix composites (AMCs) have been obstructed by the undesirable graphene-Al reactions during their casting or inability of complex part manufacturing through powder metallurgy technique. The emergence of the laser powder bed fusion (L-PBF) process with extremely short melt duration and almost no limitations in terms of the manufacturing of intricate features has renewed the interests for fabrication of graphene-reinforced AMCs. In this study, the influence of graphene incorporation into AlSi12 on L-PBF processability and defect formation is studied. The specific heat capacity, coefficient of thermal expansion, thermal diffusivity and thermal conductivity of composites were compared to those of the monolithic AlSi12 alloy. Microstructure-thermal properties relationship was studied through transmission electron microscopy (TEM), high-resolution TEM (HRTEM), electron backscatter diffraction (EBSD), electron dispersive spectroscopy (EDS) and Raman spectroscopy. This study provides valuable knowledge about (i) the chance of survival of graphene, (ii) possibility of graphene changing into other forms of carbon, and (iii) graphene-Al reactions during the L-PBF process.

Keywords: Laser powder bed fusion; Aluminum matrix composites; Graphene; Thermal conductivity; Raman spectroscopy.

6.1 Introduction

In recent years, carbonaceous nanomaterials such as graphene and carbon nanotubes have garnered great interest as a new class of materials owing to their exceptional elastic modulus, tensile strength, and thermal conductivity in specific directions [1]. According to a study conducted by Lee et al. [2], graphene possesses elastic modulus and tensile strength of 1.02 TPa and 130 GPa, respectively, measured through nanoindentation in an atomic force microscope. Regarding thermal properties, an extremely high room temperature thermal conductivity in the range of 4840-5300 W/m.K was reported by Balandin et al. [3] for monolayer graphene prepared by mechanical cleavage. The same statement is valid for carbon nanotubes as elastic moduli (measured from bending of a pinned multi-wall carbon nanotube inside an atomic force microscope), and room temperature thermal conductivities as high as 1.28 TPa and 3500 W/m.K were reported for this nanomaterial by Lieber's group [4] and Pop et al. [5], respectively. In light of their extraordinary mechanical and thermal properties, incorporating these carbonaceous nanomaterials as a second constituent into a matrix to end up with a composite material with properties superior to those of the monolithic material has become a topic of interest in many fields. The first application of the mentioned carbonaceous reinforcements was in polymer matrixes to produce conductive polymers [1]. The successful results of the polymer matrix composites increased the incentives to add these carbonaceous nanomaterials to metal matrixes.

The incorporation of the graphene and carbon nanotubes into metal matrixes, especially pure aluminum (Al) and Al alloys, was exercised through various manufacturing routes with the hope being to fabricate high-performance aluminum matrix composites (AMCs) with higher strength, thermal/electrical conductivity, and damping capability than the monolithic Al/Al alloy [6]. However, soon enough, researchers realized that it is almost

impossible to fabricate graphene or carbon nanotube-reinforced AMCs through conventional liquid metallurgy processes such as stir casting due to the following challenges:

- **Insufficient wetting:** The molten Al cannot wet the surface of the carbonaceous reinforcement because of the significant difference in their surface tensions [7]. For instance, the wetting angle of the molten Al on the surface of graphite was reported to be 140° [8], meaning that the carbonaceous reinforcements are virtually super Al-phobic. The lack of reinforcement wetting results in the formation of porosities and cracks at the matrix/reinforcement interface leading to composites with reinforcing particles not participating in the load bearing under mechanical loading during service [9].
- **Formation of aluminum carbide:** molten Al and carbonaceous particles easily react during casting and form Al_4C_3 due to the significantly low free energy of formation of carbide in this system [10]. Formation of Al_4C_3 carbides is a double-edged sword. From one hand it is favorable since it reduces the wetting angle between molten Al and carbonaceous reinforcements and ensures the formation of a metallurgical interfacial bonding. On the other hand, it is unfavorable because such a reaction sacrifices the structural integrity of the graphene and carbon nanotube nanomaterials [11]. During melting stirring, the stirring is continued for a few minutes before the slurry is cast, leading to the complete transformation of carbonaceous nanomaterials to Al_4C_3 , detrimental for mechanical and thermal properties.

- **Agglomeration or surface suspension of carbonaceous nanomaterials:**

Carbonaceous nanomaterials with large surface area to volume ratio and strong Van der Waals force among them tend to agglomerate into clusters to reduce their surface energy [12]. Moreover, due to the difference between their densities, graphene and carbon nanotubes tend to suspend on the surface of the molten Al [1]. Rigorous stirring for several minutes is required to deagglomerate carbonaceous nanoparticles and homogeneously disperse them in the molten Al; even if it can be done successfully, there will be more than enough time for a complete Al/carbonaceous nanomaterial reaction to form Al_4C_3 .

Ever since the challenges of the liquid metallurgy techniques were understood, literature has mainly focused on the fabrication of graphene/carbon nanotube reinforced AMC through powder metallurgy technique to avoid melting of the Al/Al alloys and resolve the above issues. Despite the successful results obtained in some studies [13-16], powder metallurgy is unable to produce intricate and complex shapes [17]. Moreover, it can be cost-prohibitive as a unique tool and die setups are required for each part geometry [18]. Also, powder metallurgy can be time-consuming for composites since it requires several manufacturing stages, such as powder mixing, sintering, forging/extrusion, and some post-processing steps to achieve final products [18].

The emergence of the laser powder bed fusion (L-PBF) process as one of the most promising additive manufacturing techniques can be considered as a game changer to the above scenario. In this technique, powder serves as the starting material and with the aid of a laser beam, components can be manufactured in a layer-by-layer manner [19, 20]. The L-PBF process benefits from almost no limitations in manufacturing of parts with complex geometries due to the absence of tools, molds, dies or other auxiliaries [21, 22] that are

required for powder metallurgy techniques. In addition, short design-to-product cycle [23] and the ability of near-net-shape [24] fabrication of intricate features in the L-PBF process precludes the need for many post processing steps as opposed to the powder metallurgy. The L-PBF process is a liquid metallurgy method but unlike the conventional techniques (e.g., stir casting) it benefits from a short melt duration in the order of micro- to milliseconds (few minutes for stir casting) and micron size melt pools [25] (part scale melt for stir casting [26]). For graphene/carbon nanotube reinforced AMCs, this hypothesis was proposed that the short melt duration may partially or completely suppress the reaction (formation of Al_4C_3) between molten Al/Al alloy and solid carbonaceous nanoparticles during the L-PBF process. In addition, due to the micron-size melt pools and layer-wise nature of the L-PBF process, it was hoped to obtain relatively uniform graphene/carbon nanotube reinforced AMCs without being concerned about surface suspension of the reinforcing nanoparticles in the part scale [27]. In light of the forgoing, the L-PBF process was proposed as an alternative for powder metallurgy and conventional liquid metallurgy techniques to overcome their limitations and provide an opportunity to meet a part of demand for graphene/carbon nanotube reinforced AMCs with complex geometries especially in aerospace and automotive industries [9].

Research studies on the L-PBF processing of graphene or carbon nanotube-reinforced AMCs started from 2016. Zhao et al. [28] added CNTs to AlSi10Mg alloy. They surmised their complete evaporation or decomposition followed by supersaturation during the L-PBF process only because they could not observe CNTs or Al_4C_3 through scanning electron microscopy (SEM) observations. This is while transmission electron microscopy (TEM) is essential to investigate the existence of the mentioned nanophases. Later in 2017, Wang et al. [29] investigated the same composite system and confirmed Zhao and his co-worker's

findings through TEM observations. From 2018 to the present, different research studies proved the wrong statements made by the mentioned studies, and in almost all of them, it was shown or claimed that either Gr/CNT nanomaterials partially survive (rest transforms to Al_4C_3) [11, 30-40] or completely survive [27, 41-46] during the L-PBF process, though a few studies suggest complete transformation to Al_4C_3 [47, 48]. The differences between the mentioned studies are the type of Al/Al alloy used as the matrix, the type of carbonaceous nanomaterial (graphene, single-wall CNT, or multi-wall CNT), the weight fraction of the reinforcement, composite powder preparation method, process parameters used for the L-PBF processing, and the investigated properties of the fabricated AMCs. Even though the provided evidence for the formation of Al_4C_3 is convincing in all studies (e.g., X-ray diffraction and TEM) [11, 30-40, 47, 48], in many cases, no firm evidence of graphene/CNT survival can be found. For instance, Yu et al. [45] and Gu et al. [34] used optical and/or SEM micrographs to prove the existence of CNTs in the L-PBF fabricated parts! When TEM imaging is used, the absence of carbon mapping with TEM electron dispersive spectroscopy (EDS) analysis tool, misinterpretations from EDS analysis results, or absence of the selected area electron diffraction pattern of the phase introduced as graphene/CNT makes the conclusions inconclusive [37, 38, 41, 42]. For instance, Liu et al. [42] used the TEM EDS map of carbon and identified the carbon-rich phases as CNTs, though they could have also been carbide. Even when high-resolution TEM (HRTEM) imaging was used, either the atomic planes of the phase from which the existence of graphene/CNTs was concluded cannot be clearly distinguished, or no fast Fourier transform (FFT) patterns are shown to judge whether the detected nanoparticle was graphene/CNT [11, 30, 31, 33, 35, 36]. Moreover, except in a few studies [43, 44], no comment can be found in the mentioned studies on how frequent the detected

graphene/CNT particles were in the printed parts. In some studies, detecting the characteristic G peak in the Raman spectra of the printed parts was used to prove the existence of graphene/CNT [11, 27, 33, 34, 40, 43, 44]. However, this peak proves the presence of carbon, not necessarily in the form of graphene/CNT but maybe other carbon allotropes such as glassy or disordered carbon. To rule out other possibilities, at least the exact Raman shift values of D, G, and 2D bands and their relative intensities must have been precisely considered before and after printing and compared to the reference spectra of various carbon allotropes.

Based on the above literature survey, this study aims at criticizing the existing literature and answering the following three questions by considering graphene-AlSi12 system as a composite model, (i) does graphene completely transform to Al_4C_3 during the L-PBF process or the short melt duration hinders complete reaction? (ii) upon detection of carbon in the printed part, is it the starting graphene used or other forms of carbon? And (iii) considering the evolutions of graphene during the L-PBF process, can this reinforcement improve thermal properties of AlSi12 alloy? The answers to these questions suggest that exaggerations have been made in the literature on the capability of graphene nanoparticles in improving thermal properties.

6.2 Materials and experimental procedure

In this study, AlSi12 powder with a nominal chemical composition of Al-11.46Si-0.13Fe (wt%) provided by VALIMET Inc., and graphene nanoplatelets with nominal purity and thickness of 99.5+% and 2-8 nm provided by US Research Nanomaterials Inc., were used as matrix and reinforcing agent, respectively. Two groups of composite powders, AlSi12-0.25 wt%Gr, and AlSi12-0.5 wt%Gr, were produced using ball milling process with ball-

to-powder ratios of 5:1 and 6.5:1, respectively. While different mixing times of 1 h and 1.5 h were used to produce the respective composite powders, the rest of the parameters, such as rotational speed (200 rpm), pause time to avoid overheating (15 minutes after every 30 minutes of mixing), and mixing atmosphere (air) were identical. These optimum mixing parameters were selected based on preliminary trials and microscopy examinations made by authors to ensure complete attachment of Gr particles (guest) to AlSi12 ones (host) along with the minimum possible deformation of the host particles; attributes which were proved to be essential for acceptable flowability and packing density of the composite powders for the L-PBF application based in a previous research study conducted by the same authors [an under review paper]. The attributes and behaviors of the produced composite powders were studied and compared to the monolithic AlSi12 powder (reference powder). For particle size, size distribution, and shape analysis of powders, dynamic particle measurements were conducted by Camsizer X2 instrument as per ISO 13322-2 standard. Revolution Powder Analyzer (rotating drum) test was utilized to investigate the flowability of powders by measuring a series of parameters such as avalanche angle, avalanche energy, and fractal dimension. The rotation speed of the drum was set to 0.3 rpm, and the test was continued for 150 avalanches. The static and dynamic apparent packing density of powders were examined using the Carney funnel (as per ASTM B417-11 standard) and Revolution Powder Analyzer, respectively. The reported static apparent packing density results are the average of three distinct measurements. The relative humidity of powders was determined using AND MS-70 instrument with three repetitions to ensure consistency in the obtained results. The Optical absorption of the powders was analyzed employing diffuse reflectance spectroscopy (DRS) in the wavelength range of

900–1200 nm. The reported absorptivity values are the average of three distinct measurements.

The AlSi12 (unreinforced) and composite powders were subsequently loaded into an EOS-M280 machine with a maximum laser power of 400 W and laser wavelength of 1070 nm to print two sets of 10×10×7 mm³ cuboids (one being a replica of another). For AlSi12, the optimum process parameters were used from a previous study conducted by the authors [20]. A wide range of process parameters was used for the composites, tabulated in Table 1. The details of the process parameters used to print samples can be found in the supplementary material (Table S1). All cuboid coupons were printed on an Al alloy build plate (no preheat) under the protection of a highly pure argon gas atmosphere (oxygen content below 0.1%) with a scanning strategy of stripe hatching pattern, alternating 67° between subsequent layers. One set of the printed cuboids was sectioned along the building direction, ground, and polished according to the standard metallographic procedure. The density of samples was measured using the Archimedes method. Samples having the highest relative densities were selected as optimum samples, and their corresponding sets of process parameters were used to print thermal diffusivity specimens with dimensions shown in Figure 6.1. For thermal diffusivity (α) measurements along (BD) and perpendicular (PD) to the building direction, the LFA-1600 °C Laser Flash System was used. The thermal diffusivity samples shown in Figure 6.1 were coated on both sides with a thin graphite layer prior to the test. The measurements were performed in the vacuum from room temperature up to 450 °C. Every 25 °C, samples were held at the target temperature for 4 min; then, three measurements were performed and averaged. To calculate the thermal conductivity of the samples using Eq. (1), the specific heat capacity (C_p) and density (ρ) of the samples at each temperature were required [49]:

$$K(T) = \alpha(T) \times C_p(T) \times \rho(T) \quad \text{Eq. (1)}$$

The C_p measurements were performed using the sapphire technique using a METTLER Toledo differential scanning calorimetry (DSC) (Westmoreland Mechanical Testing & Research Inc., PA, USA) in the temperature range of 25-450 °C as per ASTM E1269 standard. The samples were disc-shaped with a diameter and thickness of 5 and 2 mm, respectively. The volume change and therefore, change in the density of samples versus temperature were measured on samples of $4 \times 4 \times 10 \text{ mm}^3$ using a Linseis quenching dilatometer DIL L78 QDT from 25-450 °C at a heating rate of 20 °C/min.

For microstructure-property relationship studies, (i) scanning electron microscopy (SEM-Tescan Vega) equipped with electron dispersive X-ray spectroscopy (EDS), (ii) electron backscatter diffraction (EBSD-FEI, Versa 3D field-emission SEM) analysis, (iii) transmission electron microscopy (TEM-Talos L120C and Talos 200X) equipped with EDS and electron energy loss spectroscopy (EELS), and (iv) high-resolution TEM (HRTEM- TITAN LB) were utilized. The EBSD data were collected at an accelerating voltage of 20 keV and a tilt angle of 70° using the TSL OIM 7 software and analyzed using TSL OIM analysis software. An FEI Helios Nanolab-650 dual-beam apparatus was utilized to prepare TEM samples using the focused ion beam (FIB) lift-out technique. The oxygen, carbon, and hydrogen (O/C/H) content of the powders and some of the printed samples (second set) were measured using EMGA-820, EMIA-Pro, and EMGA-921, respectively. The O and C measurements were performed on as-built samples without any sample preparations. For H measurements, the sample preparation and test procedure details can be found in [20]. The reported results are the average of at least four distinct measurements. A HORIBA XploRA confocal Raman microscope was used to investigate the quality of

carbonaceous constituent in the printed parts. The acquisition of Raman spectra was carried out at ambient conditions by utilizing a diode laser with a wavelength of 532 nm.

Table 6.1. Range of process parameters used to print AlSi12-0.25Gr and AlSi12-0.5Gr samples.

Laser power [W]	Scanning speed [mm/s]	Hatch spacing [μm]	Nominal powder layer thickness (platform displacement) [μm]
200-370	600-3000	70-190	30

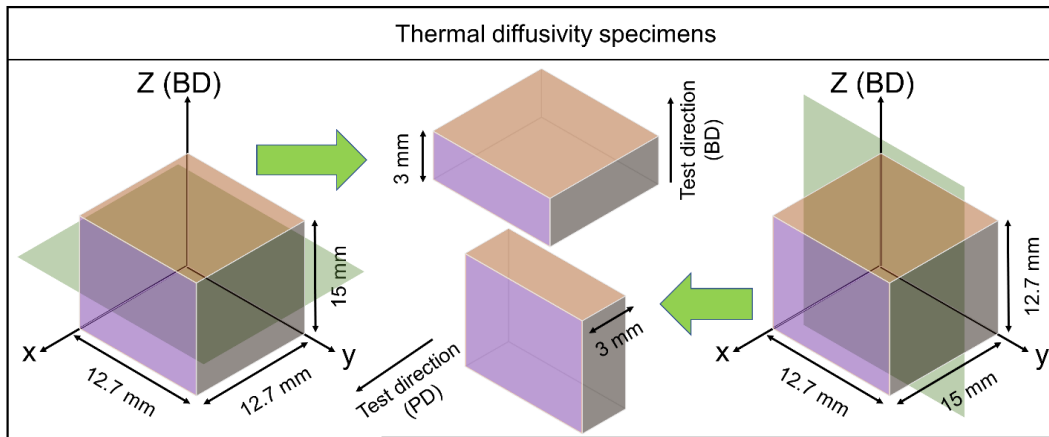


Figure 6.1. Schematic of the printed samples for thermal diffusivity measurement along and perpendicular to the building direction.

6.3 Results and Discussion

In this study, ball milling was used to prepare AlSi12-0.25Gr and AlSi12-0.5Gr composite powders. The size and shape attributes of the composite powders as well as their packing density and flowability behaviors were qualitatively assessed and compared to AlSi12 reference powder (supplementary materials). It was found that the attributes and behaviors of the composite powders are almost identical to those of the unreinforced powder (Figure S1), signifying that the mixing parameters were appropriately selected, and the composite powders are ideal for the L-PBF application. The reason behind using dry ball milling instead of wet mixing techniques was mainly to avoid composite powders with ultra-thin graphene nanoplatelets as they can easily react with molten AlSi12 and transform to Al

carbide during fabrication of the AMC components. For instance, Zhou et al. reported complete transformation of graphene oxide (GO) to Al carbide and oxide during laser-PBF (L-PBF) upon having ultra-thin GO nanosheets composed of only 3 to 5 monolayers in the composite powder [47]. The idea was to prepare a composite powder in a cost-and-time effective manner with relatively thick graphene nanoplatelets (more like graphite than graphene) so that even upon reaction of solid guest particles with molten Al alloy during the L-PBF process, a part of the starting reinforcements (hopefully nanosized) remains intact in the printed part as graphene. Figure 6.2 shows the SEM micrographs of AlSi12, graphene, AlSi12-0.25Gr and AlSi12-0.5Gr powders plus the EDS maps of carbon for composite powders. Guest particles with thicknesses up to a few microns were detected attached to/embedded into the host particles. This mitigates the chance of guest particle separation during handling or powder deposition during the L-PBF process and leads to AMCs with a uniform dispersion of reinforcements. Other than the attached guest particle, carbon layers were detected on the surface of all host particles. It is basically the carbon layers removed from the guest particles and transferred to the host ones as the host and guest particles rubbed against each other during the mixing process (Figure 6.2(h,m)).

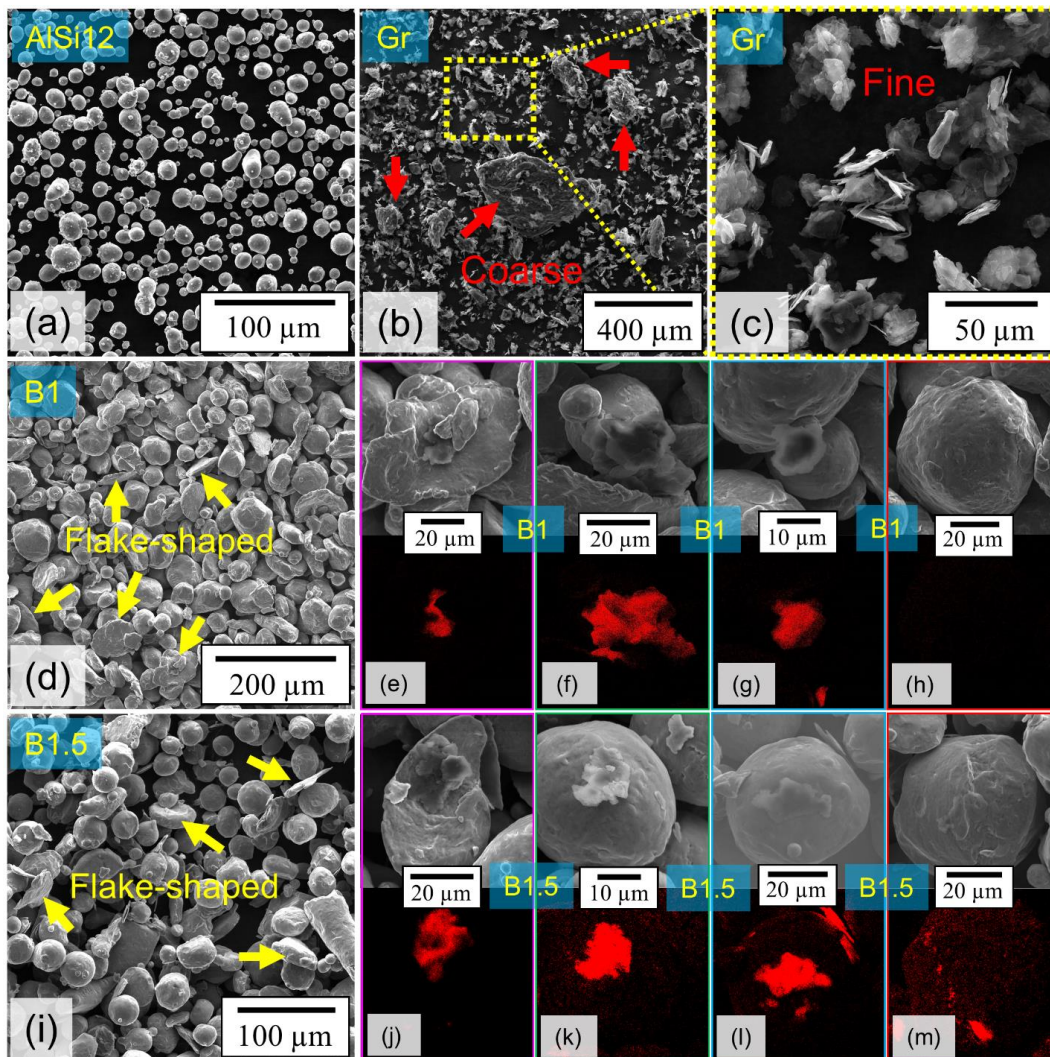


Figure 6.2. (a) SEM micrograph of AlSi12 powder, (b,c) SEM micrographs of carbonaceous powder, and (d-m) SEM micrographs and their corresponding EDS mapping results showing the C distribution for the designated powders.

6.3.1 Processability of AlSi12-Gr composites

To minimize the influence of defects on the thermal properties of the fabricated composite parts, the process parameters were optimized prior to their characterization. For AlSi12, a sample printed under laser power, scanning speed and hatch spacing of 300 W, 1800 mm/s and 100 μm was selected as the optimum sample (relative density of 99.8%) based on a previous study [20]. Figure 6.3(a,b) shows the relative density versus laser power and

scanning speed of the AlSi12-0.25Gr and AlSi12-0.5Gr samples at five different hatch spacing. Samples having relative densities higher than 99% (highly dense samples) are designated by yellow ovals. Optical micrographs of representative samples printed at low, medium, and high volumetric energy densities are also shown in Figure 6.3(c-h). Valuable information can be obtained from the relative density-process parameter results and optical micrographs. First, the processability of AlSi12-0.25Gr is superior to that of the AlSi12-0.5Gr as eleven samples possessed relative densities higher than 99% in the former versus one sample in the latter system. The processability of AlSi12-0.25Gr itself is inferior to that of the monolithic AlSi12 [20], signifying that the possibility of manufacturing almost defect free parts decreases by increasing the carbonaceous reinforcement content. Second, compared to the unreinforced AlSi12 (thoroughly investigated in [20]), dense AlSi12-0.25Gr and AlSi12-0.5Gr parts could be manufactured at lower laser powers and higher scanning speeds. According to the powder absorptivity measurement results shown in Figure 6.4(a), this is attributable to the higher absorptivity of composite powders compared to the monolithic AlSi12 powder, which increases the melt efficiency. The increase in the laser absorptivity from 59% for AlSi12 to 67.7% and 67.2% for AlSi12-0.25Gr and AlSi12-0.5Gr originates from the incorporation of a second constituent (guest powder) with higher absorptivity (80.4%) compared to AlSi12 alloy. It is worth mentioning that the increase in laser absorptivity due to the presence of guest particles in the composite systems made the densification level very sensitive to the change in process parameters especially for AlSi12-0.5Gr case in which a dense part could be printed only at a specific set of process parameters. In other words, slight deviation from the process parameters leading to highly dense composites could significantly reduce the relative density. For instance, the range of volumetric energy densities resulting in highly dense parts changed from 45-100

J/mm^3 in AlSi12 [20] to $40-70 J/mm^3$ in AlSi12-0.25Gr, proving a narrower processing window for the composites.

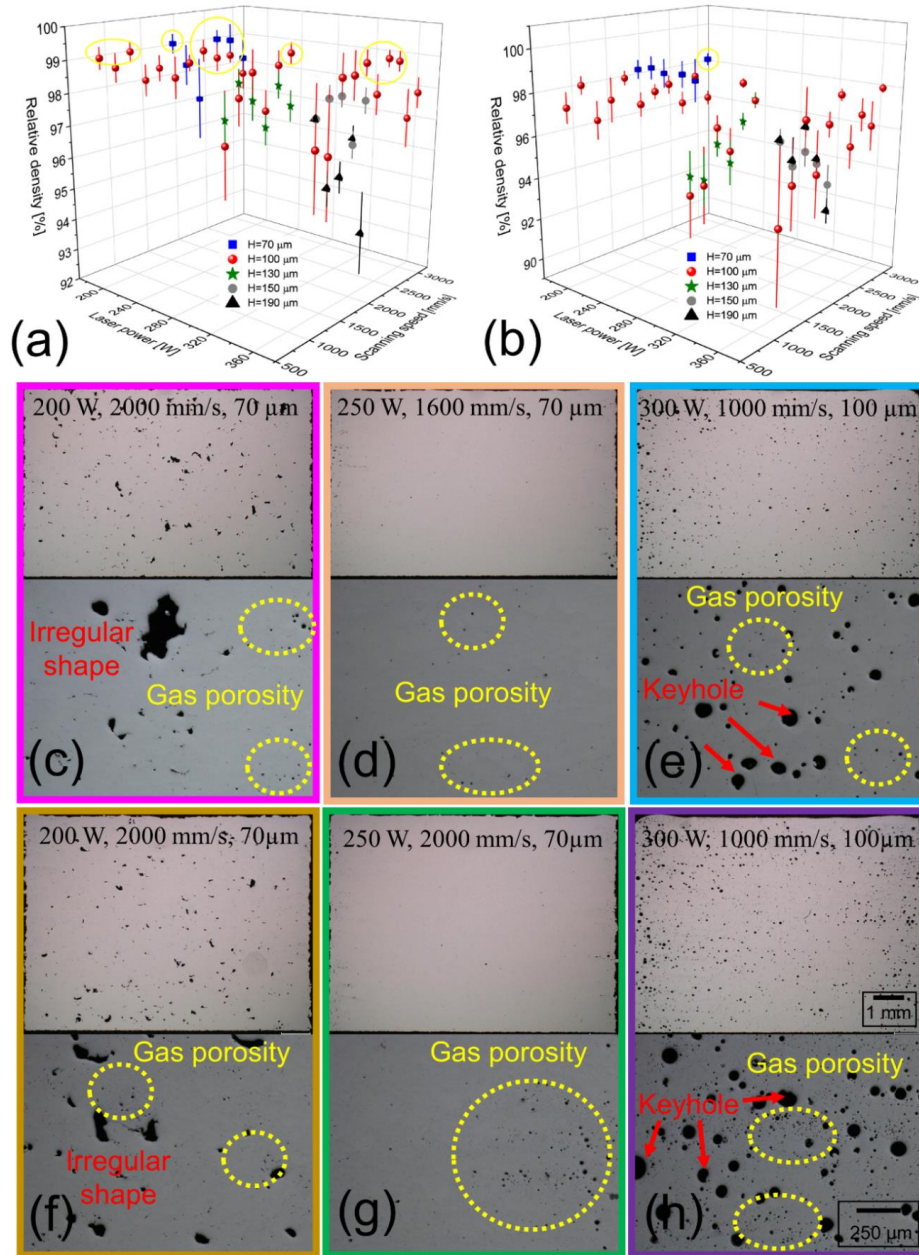
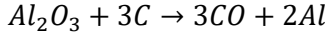


Figure 6.3. Relative density versus laser power and scanning speed for (a) AlSi12-0.25Gr and (b) AlSi12-0.5Gr samples printed at different hatch spacing. Optical micrographs of (c-e) AlSi12-0.25Gr and (f-h) AlSi12-0.5Gr samples at different level of energy densities (low, medium, and high) with sets of process parameters shown on the images.

As can be seen in Figure 6.3(c-h), three types of defects were observed in the printed composites, (i) large irregular discontinuities appeared in parts printed at very low volumetric energy densities due to incomplete penetration of laser scan tracks to the previously consolidated tracks or insufficient time for the flow of the molten material during the printing [50], (ii) coarse spherical porosities, also known as keyhole porosities, which formed at high volumetric energy densities owing to the evaporation of a portion of the melt pool and its entrapment in the melt [51], and (iii) fine spherical porosities observed in all samples even highly dense ones, named as gas porosities. Such gas porosities were absent or less frequent in the L-PBF fabricated monolithic AlSi12 samples [20]. To find the origins of gas porosities observed in the composite parts, the relative humidity of powders along with the oxygen, carbon, and nitrogen content of the powders and some of the printed parts were measured, the results of which are shown in Figure 6.4(b-e). Based on the relative humidity measurements it was found that the moisture content of the composite powders was 56% higher than that of the AlSi12 powder (Figure 6.4(b)). The increase in the moisture content which has happened during the mixing process can be one of the origins of the observed gas porosities in the printed composite parts, especially since the high cooling rates associated with the L-PBF process enhance the chance of vapor entrapment. Another major source of gas porosities is believed to be carbon monoxide (CO). According to the carbon measurements, the printed AlSi12-0.25Gr and AlSi12-0.5Gr parts under a wide range of energy densities possessed up to 25 and 28% lower carbon than their starting powders, respectively (Figure 6.4(d)). This implies that carbon has transformed into a gaseous product during the L-PBF process, a part of which escaped from the melt pool, and the rest formed the gas porosities. The oxygen content measurements (Figure 6.4(c)) also support this hypothesis as a significant reduction in the

oxygen content has happened during the printing process. The discussion on the nature of gas porosities in the composite parts should be paused here first to justify the trends observed in the oxygen content of the powders and the parts made out of them. For the unreinforced AlSi12, a significant reduction of 72.5% (from 724 ppm in powder to 202 ppm in the printed part) in the absence of carbonaceous particles is perceptible (Figure 6.4(c)). In a previous study conducted by the authors [21], it was proved that the oxide diminishment of the monolithic AlSi12 happens through (i) spallation of the nanosized oxide layer on the AlSi12 particles during the rapid heating cycle of the L-PBF process, followed by (ii) the accumulation of the nanosized oxide particles (formed during the spallation stage) on the surface of the melt pool due to the upward buoyancy forces at the center of the melt pools and outward Marangoni flow at the surface of the melt pools, and finally (iii) the evaporation of nanosized oxides due to their direct interaction with the high-intensity laser beam. The AlSi12-0.25Gr and AlSi12-0.5Gr powders possessed considerably higher oxygen content than the monolithic AlSi12 powder (Figure 6.4(c)). This is because, in this study, ball milling has been performed without a protective atmosphere (to make it closer to industrial conditions). What has happened during the ball milling process is that the collisions experienced by the AlSi12 particles resulted in the breakdown of their oxide layers, exposure of the fresh metallic material to the air, and more oxidation. Despite the higher oxygen content of the starting powder in the composites, the printed parts still contained relatively low oxygen content, even lower than that of the AlSi12 in some cases. Of course, the explained mechanism is responsible for diminishing a portion of the oxides in the composite systems. Still, other reasons must have led to such sharp oxygen reductions of (up to) 90 and 83% for AlSi12-0.25Gr and AlSi12-0.5Gr, respectively. One rational explanation for the simultaneous decrease of the oxygen and

carbon contents in the composites after printing can be the reduction of the Al_2O_3 by carbon through the following reaction during the process [52]:



Referring to the Ellingham diagram, the favorable condition for the above reaction is provided at temperatures higher than ~ 2000 °C. Therefore, this reaction can be activated in a region in the melt pool, presumably close to the surface where melt evaporation takes place ($T > 2470$ °C for pure Al). Returning to the discussion of gas porosity, the gaseous product of the above reaction (CO gas) can be one of the other origins for the observed fine spherical porosities. According to Figure 6.3(c-h), more gas porosities can be detected in samples printed at higher volumetric energy densities owing to the increased temperature of the melt pool and activation of the mentioned reaction in a larger portion of the melt pool. The generated CO at the deeper regions of the melt pool has a higher chance of entrapment, justifying the results. One of the reasons that highly dense composite parts could be manufactured at relatively low laser powers and high scanning speeds is the lower temperature of the melt pool at such conditions (based on Eq. (2)), reducing the region where this reaction can be activated and increasing the chance of CO escape from the melt pool [53]:

$$T = \frac{AP}{\sqrt{2}r_0K\pi^2} \exp\left(\frac{-r^2}{2r_0^2}\right) \tan^{-1}\left(\sqrt{\frac{2\alpha}{vr_0}}\right) \quad \text{Eq. (2)}$$

in which A, P, K, r_0 , r, α , and v denote the laser absorptivity, laser power, thermal conductivity, beam radius, radial position in the melt pool, thermal diffusivity, and scanning speed, respectively. It is worth noting that reducing the volumetric energy density can be a double-edged sword as it also leads to narrower laser scan tracks due to lower energy delivered to the powder and a lower chance of flow/reshaping of the melt. That is

why highly dense composite samples were achieved at low hatch spacing of 70 and 100 μm for AlSi12-0.25Gr and 70 μm for AlSi12-0.5Gr. This is while highly dense AlSi12 samples were reported to be successfully printed with a hatch spacing as high as 190 μm [19]. Therefore, the trick to obtaining highly dense AlSi12-0.25Gr and AlSi12-0.5Gr parts is to reduce the P/v and hatch spacing to ensure low temperatures of the melt pool (less chance of CO generation) while having sufficient overlap between narrow tracks. Samples printed at 250 W (P), 1800 mm/s (v), and 70 μm (hatch spacing) for AlSi12-0.25Gr and 250 W, 2000 mm/s, and 70 μm for AlSi12-0.5Gr possessed the highest combination of density and building rate, used for the following investigations. The relative densities of the optimum samples were 99.5 and 99.2% for AlSi12-0.25Gr and AlSi12-0.5Gr, respectively.

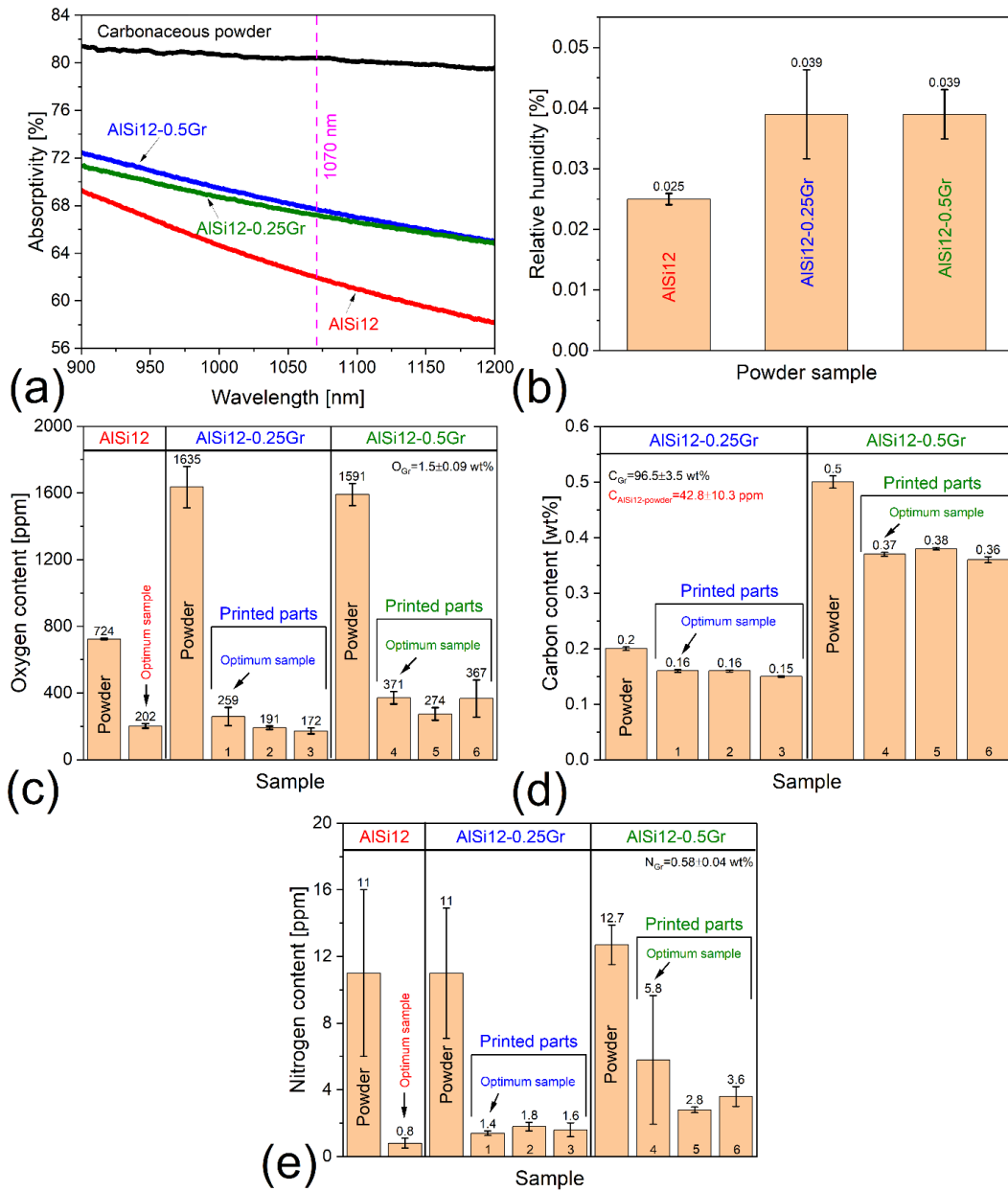


Figure 6.4. (a) Laser absorptivity versus wavelength of powders, (b) relative humidity of powders, (c) oxygen content, (d) carbon content, and (e) nitrogen content of the starting powders and printed parts. Sample 1,4 (optimum AISi12-0.25Gr and AISi12-0.5Gr), Sample 2,5 (300 W, 1200 mm/s, 100 μ m, 30 μ m), sample 3,6 (370 W, 2200 mm/s, 100 μ m, and 30 μ m). The absorptivity, relative humidity, oxygen and carbon content of the AISi12 and AISi12-0.5Gr powders were previously reported in [an under review paper].

6.3.2 Microstructure

Before delving into the discussion of the microstructural evolutions during the L-PBF processing of AlSi12-0.25Gr and AlSi12-0.5Gr composites, first, the microstructure of the unreinforced AlSi12 needs to be studied. Figure 6.5 shows the TEM and EDS elemental analysis results of the L-PBF fabricated AlSi12 alloy. The bright field (BF) image in Figure 6.5(a) shows the overview of the AlSi12 microstructure with an ultrafine, textured, divorced eutectic cellular microstructure developed due to the rapid solidification nature of the L-PBF process. Higher magnification BF images in Figure 6.5(b,c) revealed that the intercellular regions consist of discrete nanosized precipitates, and most of the dislocations are adjacent to these regions. The high-angle annular dark-field scanning transmission electron microscopy (HAADF-STEM) image and its corresponding EDS elemental mapping results shown in Figure 6.5(d,e) revealed that the nanosized phases at the intercellular regions are Si precipitates and the cell cores are α -Al phase. Other than the two phases, a Fe-rich phase was also detected at the inter-cellular regions, as shown in Figure 6.5(e). According to the Scheil-Gulliver solidification modeling (SGSM) of AlSi12 alloy [21], this should be the $\text{Al}_9\text{Fe}_2\text{Si}_2$ phase. According to the SGSM results, the solidification of AlSi12 alloy starts with the formation of α -Al, followed by the enrichment of the remaining liquid phase from Si/Fe and formation of Al-Si binary eutectic reaction products $(\alpha+\text{Si})_e$, and finally, further enrichment of the terminal liquid from Fe and formation of Al-Si-Fe ternary reaction products $(\alpha+\text{Si}+\text{Al}_9\text{Fe}_2\text{Si}_2)_e$. From the point EDS analysis of the cell cores (and the α -Al at intercellular regions), it was understood that the α -Al is supersaturated from Si as 3.51 at%Si was detected in this phase. This is while the equilibrium solubility of Si in α -Al is close to zero based on the Al-Si binary phase diagram. The high cooling rates of the L-PBF process result in a fast-growing solidification front

that captures some of the segregated Si atoms during solidification and creates an α -Al matrix supersaturated from Si atoms. According to a previous work conducted by the authors [21], the level of Si solute entrapment was 2.4 at% for L-PBF fabricated AlSi12 samples under 200 °C of substrate preheating. This study shows that level of solute entrapment is even more remarkable when no substrate preheating is applied as that significantly increases the cooling rate. Interestingly, it was found that a portion of the nanosized Si phase (adjacent to the cell cores) at the inter-cellular region is also supersaturated by Al (Figure 6.5(f-h)) due to the high cooling rates (the equilibrium solubility of Si from Al is also close to zero). In the following, the influence of Gr addition on the solidification mode and the level of α -Al supersaturation from Si is investigated for AlSi12-0.25Gr and AlSi12-0.5Gr composites. In addition, these questions are answered, (i) does carbonaceous guest constituent survive in the L-PBF fabricated composites? (ii) Upon survival of the carbonaceous constituent, has it transformed into other forms of carbon? (iii) Upon reaction between carbonaceous guest and molten AlSi12, what are the reaction product and mechanism? After answering the above questions, the grain structures of the composites are discussed and compared to that of the monolithic AlSi12 alloy.

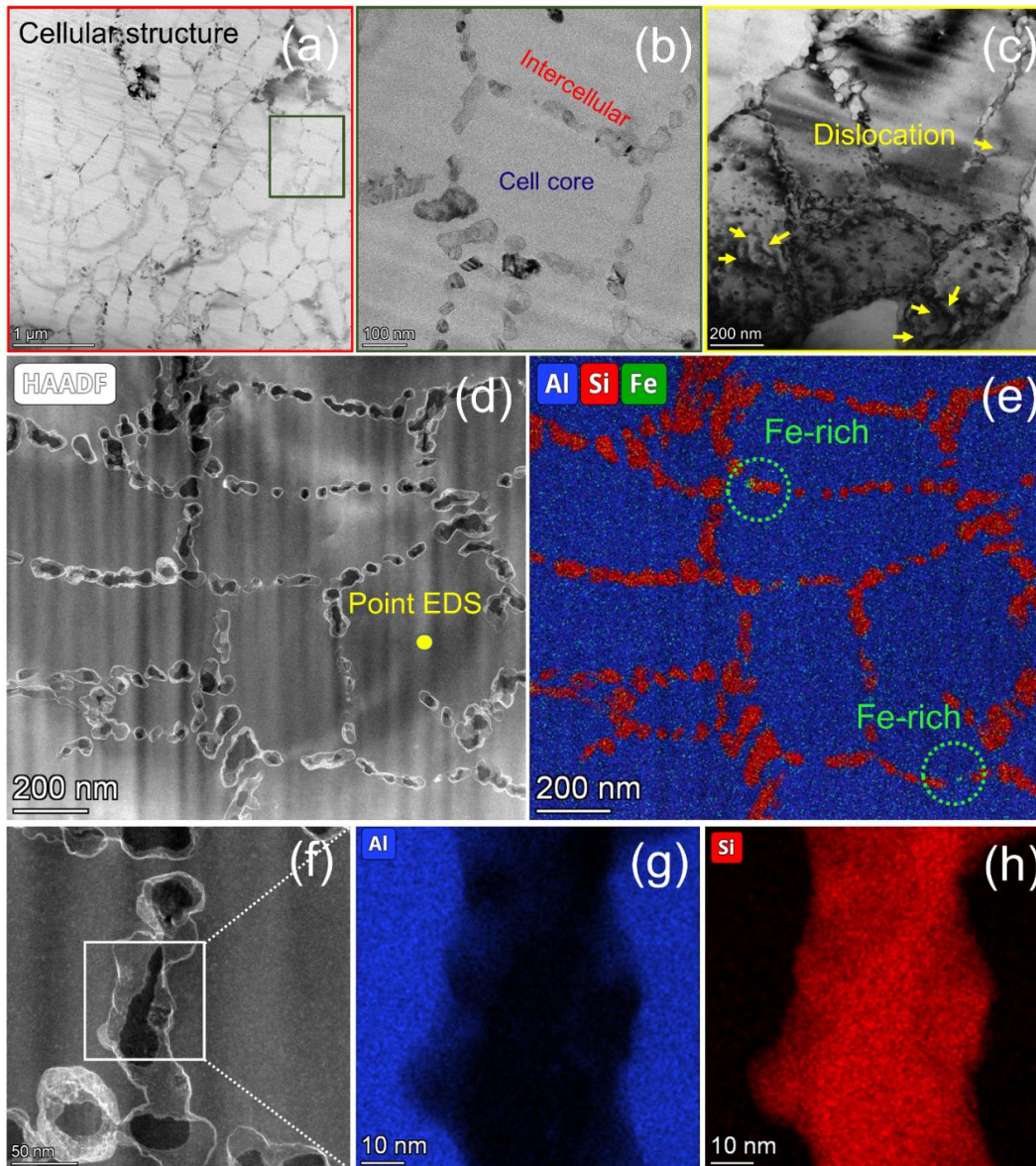


Figure 6.5. AlSi12 sample: BF TEM images (a) overview, (b) cell and cell boundaries, and (c) dislocations. HAADF-STEM images and their corresponding EDS maps for cell structure (d,e) and Si particles at intercellular region (f-h).

6.3.2.1 Investigation of the survival of Gr

For microstructural investigations of the L-PBF fabricated AlSi12-0.25Gr and AlSi12-0.5Gr composites, first uniform TEM samples with a thickness of ~ 100 nm were prepared; but for some reasons explained in the following, these samples were turned into wedge-

shaped samples by FIB. Figure 6.6 shows the overview of the prepared TEM sample, and the EELS thickness measurement results from the thin (<40 nm) and thick (~60-100 nm) sections. Figure 6.7 shows the EDS analysis results performed on the thick section of the TEM specimens. According to the HAADF image and its corresponding EDS elemental mapping results for AlSi12-0.25Gr (Figure 6.7(a,b)) and AlSi12-0.5Gr (Figure 6.7(c,d)), supersaturated α -Al (3.28 at%Si and 3.8 at%Si based on point EDS analysis for AlSi12-0.25Gr and AlSi12-0.5Gr) and nanosized Si precipitates/ $\text{Al}_9\text{Fe}_2\text{Si}_2$ were detected in the cellular and intercellular regions, respectively (the same as AlSi12-Figure 6.5(d,e)). In addition, C-rich phases were also detected in the intercellular regions. These phases can be carbides, graphene nanoplatelets, other allotropes of carbon or a combination of all. However, it is hard to distinguish the C-containing precipitates from the surrounding in the intercellular region since a lot of nanosized precipitates having overlap with each other are perceptible there. In other words, one of the judging criteria for the nature of the C-containing phases can be their morphology, which is not quite discernable in the coexistence of other nanosized phases in the intercellular regions. The idea behind thinning of a part of the TEM sample (making a wedge-shaped TEM sample) was to make the overlapping of these phases as minimum as possible through removing a part of the sample.

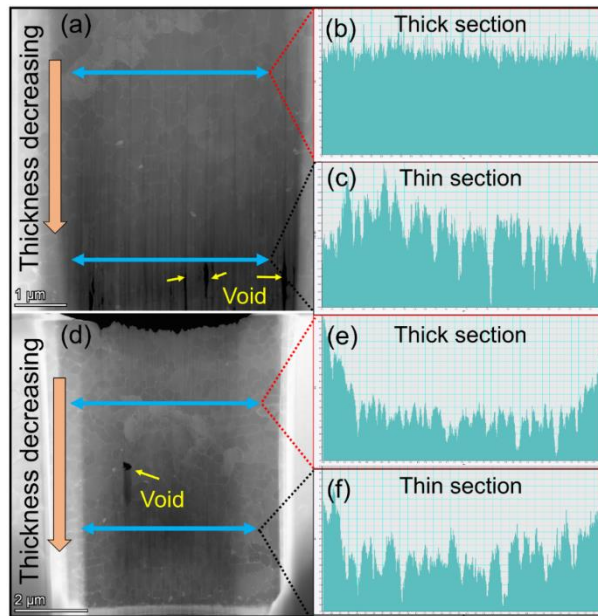


Figure 6.6. Overview of the wedge-shaped TEM images and their thickness profiles in the thick and thin sections obtained by EELS for (a-c) AlSi12-0.25Gr and (d-f) AlSi12-0.5Gr.

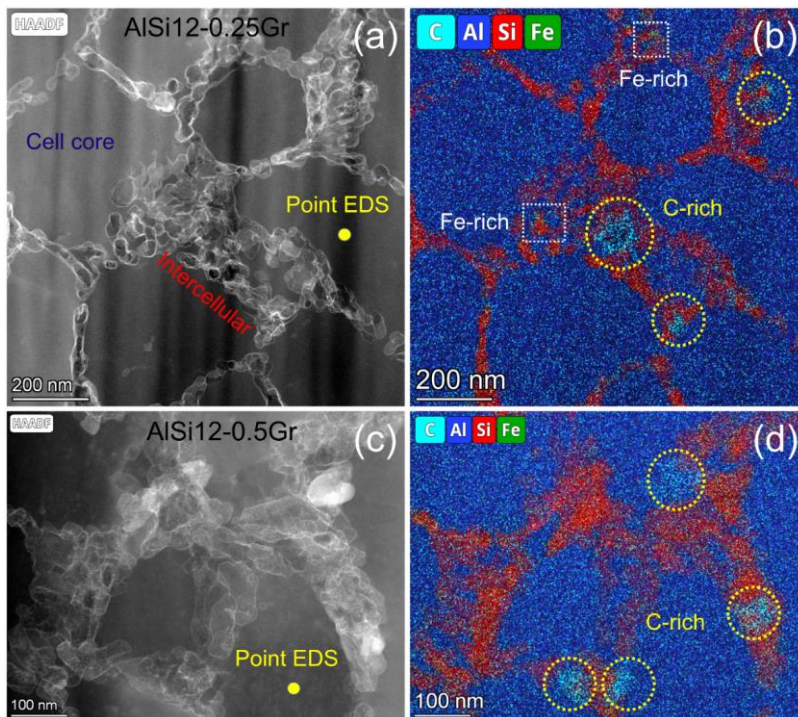


Figure 6.7. Thick section: HAADF-STEM images and their corresponding EDS maps for cell structure of (a,b) AlSi12-0.25Gr and (c,d) AlSi12-0.5Gr.

Figure 6.8(a-d) shows the HAADF-STEM and EDS analysis results of the thin section of AlSi12-0.25Gr and AlSi12-0.5Gr TEM samples. According to the HAADF images shown in Figure 6.8(a,c) for AlSi12-0.25Gr and AlSi12-0.5Gr samples, an irregularly shaped nano-constituent, which is sort of transparent, is perceptible. According to the EDS maps of the respective images, these nano-constituents must be nano-sized carbonaceous particles that survived during the thermal cycle of the L-PBF process. To confirm that whether the detected carbonaceous nano-constituents were Gr, HRTEM was utilized (only the results of AlSi12-0.5Gr are shown here). Figure 6.8(e) shows the HRTEM image of the exact location shown in Figure 6.8(c), the only difference being that it is rotated. Figure 6.8(f,g) shows the high magnification HRTEM image and FFT pattern of the location where a carbonaceous nano-constituent was detected in Figure 6.8(c). For Gr, no characteristic patterns could be identified, even though some of the brighter cloud dots appear to be located at the same distances from the center, two of which are designated by yellow circles. This ring-like spot distribution probably is the contribution of the combination of the orderly and randomly overlapping Gr clusters or layers. It seems like due to the laser shock and the molten AlSi12/solid Gr reactions during the LPBF process, the structural integrity of the starting Gr constituent has been disturbed, though it has not entirely turned into amorphous carbon as some brighter dots are still visible. Figure 6.8(h,i) shows the inverse FFT of the yellow circles in Figure 6.8(g) and the intensity-distance profile of the arrow in Figure 6.8(h), suggesting an interatomic distance of ~ 0.3 nm for the detected carbonaceous nano-constituent. This is close enough to the nominal value of 0.334 nm interplane spacing of graphene layers in graphite, meaning that the detected phases are damaged Gr nanoplatelets.

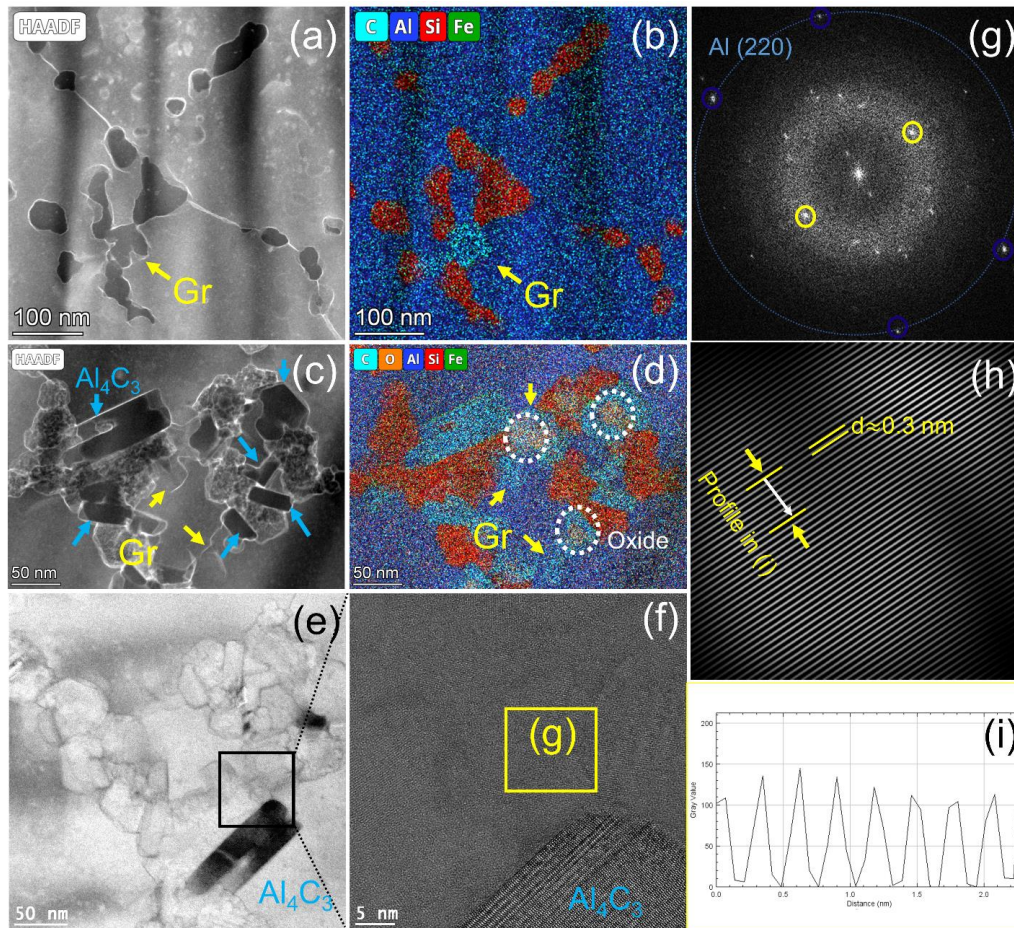


Figure 6.8. Thin section: HAADF-STEM images and their corresponding EDS maps for (a,b) AlSi12-0.25Gr and (c,d) AlSi12-0.5Gr. (e,f) HRTEM images of the carbonaceous nano-constituent phase detected in (c), (g) FFT pattern of the designated area in (f), and (h,i) inverse FFT of the yellow circles in (g) and the intensity-distance profile of the arrow in (h).

It is worth noting that, some oxides were also detected in the L-PBF fabricated composites (only shown for AlSi12-0.5Gr), originating from the oxide layers existing on the surface of host particles in the composite powders or oxygen of the guest constituent (Figure 6.4(c)). Given that the oxides are adjacent to the detected carbonaceous nano-constituent, their origination from the latter is more plausible. Finally, most of the C-containing phases based on several EDS analysis on different locations were found to be Al_4C_3 (Figure 6.8(c)), which is explained in section 6.3.2.2.

The optimum composite samples were subjected to Raman spectroscopy to confirm the survival of non-reacted carbonaceous nano-constituent inferred from the TEM results. Figure 6.9(a-c) shows the Raman mapping results for the L-PBF fabricated AlSi12-0.25Gr optimum sample performed on the material inside one of the fine spherical pores. As can be seen, two types of carbonaceous constituents with the characteristics D (defect) and G (graphite) peaks were detected, meaning that unreacted carbon nano-constituents exist in the L-PBF fabricated AlSi12-0.25Gr sample. The I_D/I_G ratio, indicating the level of defects and structural integrity of the carbonaceous material, was significantly higher than that of the starting Gr and the guest constituents in the ball-milled powders [an under review paper]. It means that the survived carbonaceous nano-constituents have a high degree of structural disorders. For carbon type 2, the I_D/I_G ratio is greater than unity, meaning that the survived carbon is more amorphous than crystalline. This is while the level of crystallinity of carbon type 1 is higher as the I_D/I_G ratio is lower than unity. Silicon was also detected besides carbon; however, the peaks were downshifted compared to the reference silicon Raman spectrum. This happens due to the presence of nanosized silicon particles (Figure 6.5 and Figure 6.7), as reported elsewhere [54]. Figure 6.9(d-i) shows the Raman mapping results for two different areas of the L-PBF fabricated AlSi12-0.5Gr optimum sample. According to Figure 6.9(d-f), silicon and highly disordered carbon (I_D/I_G ratio > 1) were detected in the AlSi12-0.5Gr sample. Further investigations on this sample revealed that the highly crystalline Gr still exists (Figure 6.9(g-i)). It is fair to conclude from the TEM and Raman mapping results that carbonaceous guest particles have survived in the printed parts, meaning that the idea of incorporating relatively thick Gr particles through ball milling to end up with nanosized Gr-reinforced AlSi12 composite parts has

worked. Nevertheless, most survived Gr particles have lost their structural integrity and crystallinity.

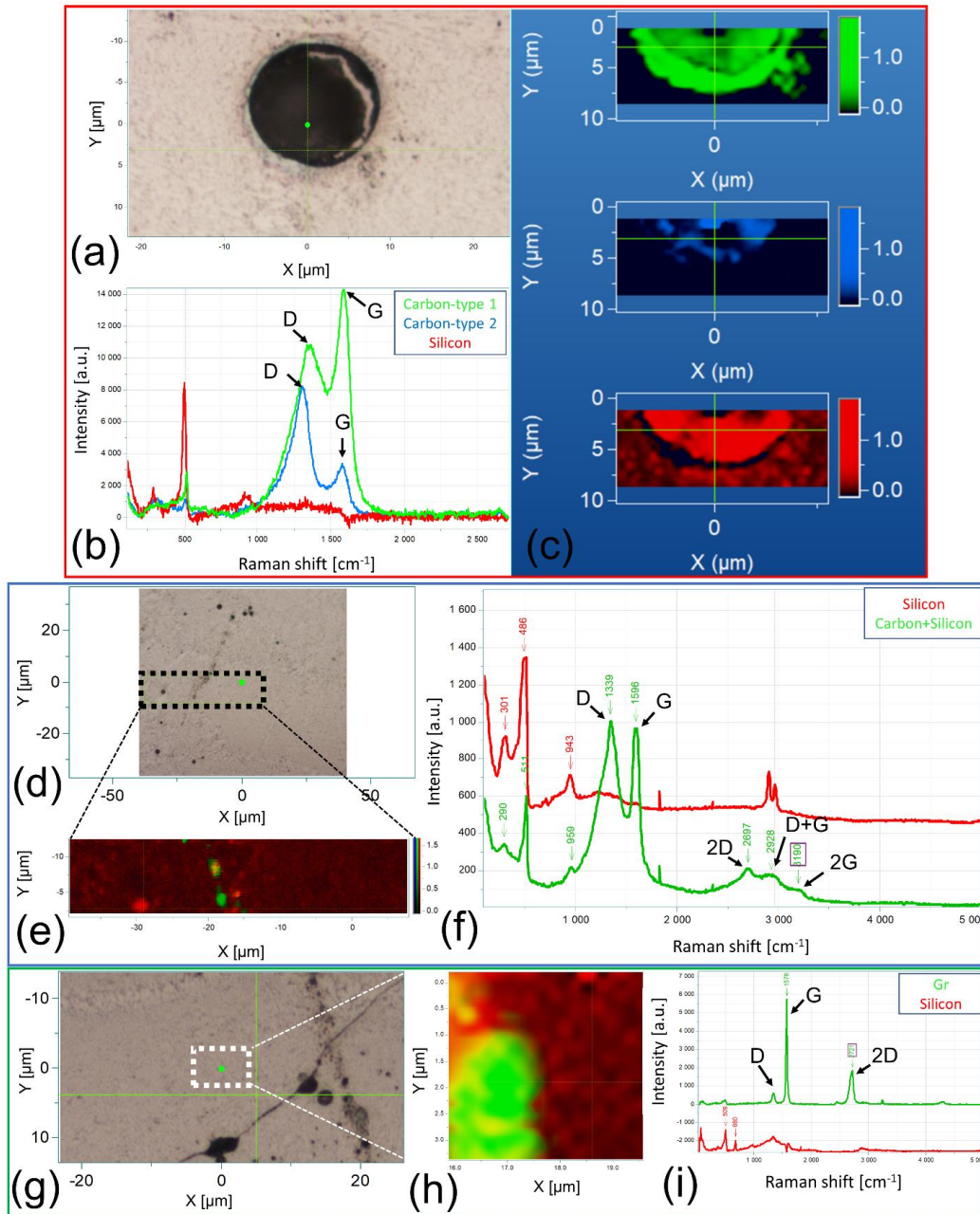


Figure 6.9. Raman mapping results for (a-c) AlSi12-0.25Gr and (d-i) AlSi12-0.5Gr samples.

6.3.2.2 Transformation of Gr to Al_4C_3

As mentioned earlier, most of the incorporated Gr have transformed to Al_4C_3 during the L-PBF process (Figure 6.8(c)). This was evidenced by the fact that most of the detected C-containing phases in the intercellular regions possess acicular morphology. This is the typical morphology of the Al_4C_3 phase reported in other studies in the L-PBF fabricated Al alloy-Gr or Al alloy-CNT composites [33, 36]. Another token for being Al_4C_3 is that both carbon and aluminum (not just carbon) were detected in the acicular phases (see Figure 6.10(a-e) for AlSi12-0.25Gr and Figure 6.10(h-k) for AlSi12-0.5Gr samples). Since based on the Al-C binary phase diagram (Figure 6.11(a)) only one type of carbide compound is possible to form in this system, it has to be Al_4C_3 . The fact that the acicular phases are Al_4C_3 was also confirmed by the HRTEM imaging and the extracted FFT patterns from this phase, shown in Figure 6.10(f,g) for AlSi12-0.25Gr and Figure 6.10(l,m) for AlSi12-0.5Gr samples. The in-situ formation of Al_4C_3 during the L-PBF process is the main reason behind the damaged integrity of starting Gr constituent (Figure 6.9).

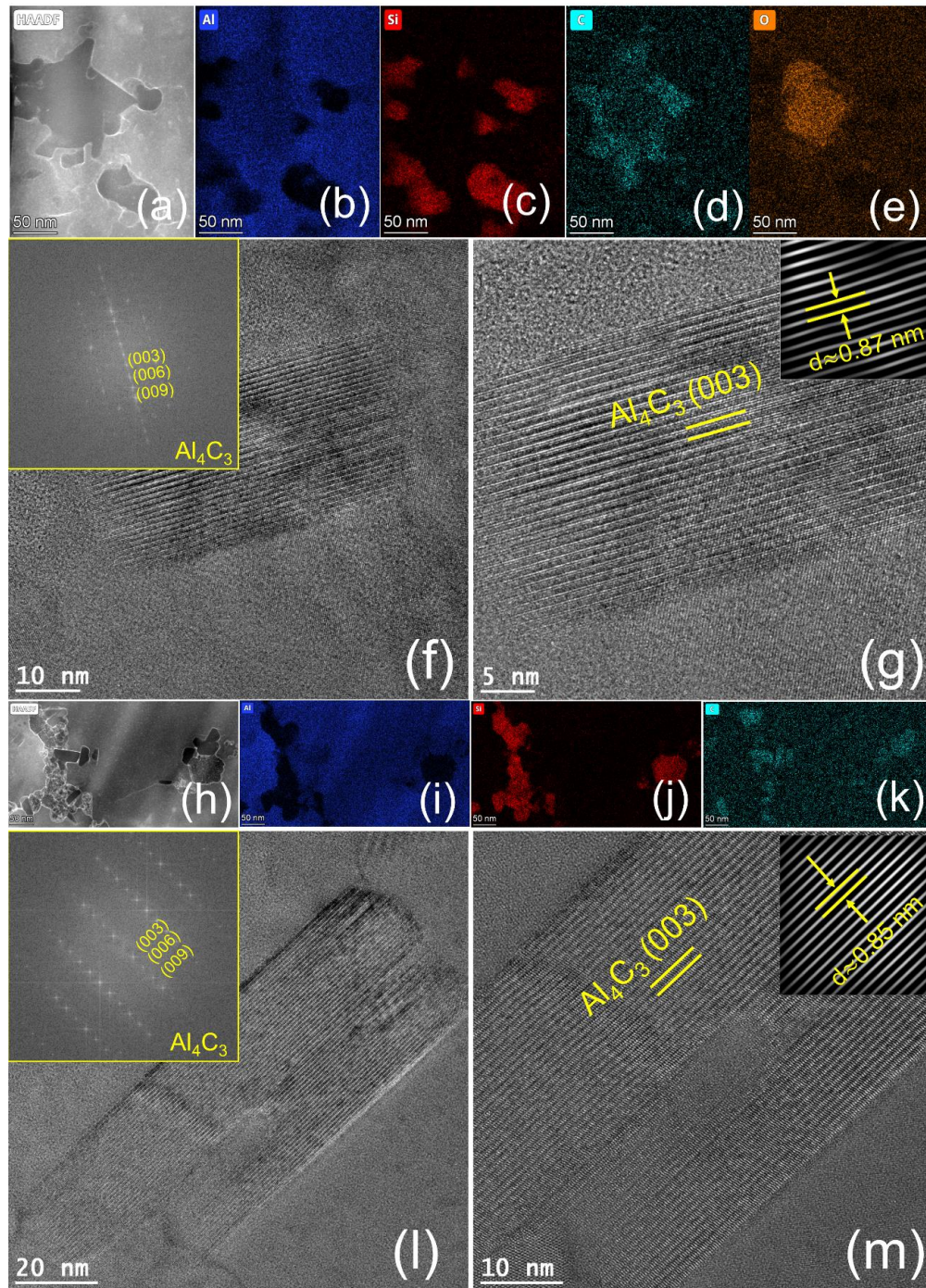
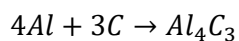


Figure 6.10. Thin section: HAADF-STEM images and their corresponding EDS maps for (a-e) AlSi12-0.25Gr and (h-k) AlSi12-0.5Gr samples. (f,g) HRTEM images of Al₄C₃ at two different magnifications and their corresponding FFT patterns and inverse FFT for (f,g) AlSi12-0.25Gr and (l,m) AlSi12-0.5Gr samples.

To comprehend the reason behind the formation of Al_4C_3 during the L-PBF processing of AlSi12-0.25Gr and AlSi12-0.5Gr, the coexisting phases at any given temperature at equilibrium conditions need to be identified. Although the conditions associated with the L-PBF process are far from equilibrium, the equilibrium phase diagrams can be used as a guide to understanding the microstructural evolutions. To briefly explain the concept based on a simple system, the Al-C binary phase diagram (Figure 6.11(a)) was calculated using Thermo-Calc Software. Any temperature above 660 °C and below 2474 °C (between melting and boiling temperatures of pure Al) resembles the temperature of the melt pool during the L-PBF processing of the Al-C system. At such a temperature range, the carbon particles will remain solid since they experience a temperature below their melting point. At T^* temperature in the range of 660-2156 °C, molten pure Al and solid C particles with chemical compositions represented by point 1 (C=0) and point 2 (C=100%), respectively, are not at equilibrium conditions. To establish an equilibrium condition between the liquid and solid phases, their chemical compositions must shift to points 3 (liquidus line) and 4 (solidus line). According to Figure 6.11(a), the region between solidus and liquidus lines is where molten Al is at equilibrium with solid Al_4C_3 . It means that upon the presence of solid C particles in molten Al, because the solid/liquid interface is not at equilibrium conditions, the following reaction happens spontaneously and results in the formation of the Al_4C_3 phase (solid), at least at the solid/liquid interface, to provide equilibrium conditions:



According to Figure 6.11(a), in the range of 2156-2474 °C, graphite (C) and molten Al can coexist at equilibrium upon dissolution of a significant amount of carbon in the liquid phase, meaning that the formation of Al_4C_3 is unfavorable at such a temperature range. The

pseudo-binary phase diagram of AlSi12-C is shown in Figure 6.11(b); on the ordinate is plotted the temperature, while the abscissa gives the mass percentage of the C element. The chemical composition of the left-hand side endmember was fixed at (Al-11.46Si-0.13Fe in wt%), and it was assumed that Al is a dependent variable. Unlike the Al-C binary system, molten AlSi12 is at equilibrium with different solid phases in the range of melting to boiling temperatures (~585-2370 °C). Four zones were defined on the AlSi12-C phase diagram (Figure 6.11(b)). Figure 6.11(c-f) shows different zones and the solid phase in equilibrium with molten AlSi12 at each of them. In zone I (2109-2517 °C), the C-rich molten AlSi12 is in equilibrium with solid Gr, meaning that no reaction occurs between the two constituents except for the dissolution of Gr. Therefore, only the dissolution of Gr may happen in a portion of the melt pool that is presumably close to the surface where the laser beam is concentrated. Even if a slight dissolution of Gr happens at zone I due to the short interaction time of the L-PBF process (50-55 μ s in this study for AlSi12-0.25Gr and AlSi12-0.5Gr composites), it transforms into Al₄C₃ during the cooling stage since the solubility of Al from C is negligible at low temperatures. In zone II (1354-2109 °C), molten AlSi12 is in equilibrium with Al₄C₃ at low concentrations of C, which is the case for AlSi12-0.25Gr and AlSi12-0.5Gr composites. In this temperature range (bulk of the melt pool), Gr transforms into Al₄C₃, and molten AlSi12 is enriched with C to reach equilibrium conditions at the solid/liquid interface. Owing to the significantly low free energy of the formation of carbide in the Al-C system ($\Delta G \left[\frac{kJ}{mol} \right] = -266520 + 96.2T[K]$) [55], such reaction can occur even in the short interactions times and melt durations of the L-PBF process. Zones III (880-1354 °C) and IV (585-880 °C) represent the bottom of the melt pool in which molten AlSi12 is in equilibrium with Al₈C₇Si and Al₄C₄Si compounds, respectively. However, such low temperature reaction products predicted by the

solid phase formed in the melt pool, it was expected to be seen in the cellular rather than intercellular regions. To resolve the contradiction, the critical velocity of the solidification front must be calculated. To clarify, depending on the velocity of the solid/liquid front during the solidification stage, the reinforcing particles get either pushed by the solidification front to the intercellular/inter-dendritic regions or captured by cells/dendrites (reinforcement engulfment). On this account, a critical velocity (V_{cr}) can be defined above which the engulfment mechanism is activated [57]:

$$V_{cr} = \frac{\Delta\sigma_o d_o}{6(n-1)\eta r} \left(2 - \frac{k_p}{k_l}\right) \quad \text{Eq. (3)}$$

in which d_o is the interatomic distance of the matrix alloy, $n = 2$ to 7 , η is the melt viscosity, r is the radius of solid reinforcement, which is assumed to be spherical, and k_p and k_l denote thermal conductivities of reinforcement and liquid, respectively. $\Delta\sigma_o = \sigma_{ps} - (\sigma_{pl} + \sigma_{sl})$, in which σ_{ps} , σ_{pl} and σ_{sl} are reinforcement-interface, reinforcement-liquid, and interface-liquid surface energies, respectively. Using the data tabulated in Table 6.2 for AlSi12 melt and Al_4C_3 particles (reinforcement), V_{cr} was found to be 4666 mm/s. The velocity of the solidification front ($V_{S/L}$) in the L-PBF fabricated AlSi12-0.25Gr and AlSi12-0.5Gr samples can be calculated as follows [58]:

$$V_{S/L} = V \cos(\theta) \quad \text{Eq. (4)}$$

in which V denotes the scanning velocity used to print optimum AlSi12-0.25Gr (1800 mm/s) and AlSi12-0.5Gr (2000 mm/s) samples and θ signifies the angle between the scanning direction and the normal to the melt pool boundary ($0 < \theta < 90^\circ$). Regardless of the θ value, the $V_{S/L}$ would always be smaller than V , and V itself is smaller than V_{cr} , justifying the movement of Al_4C_3 reinforcements with the solidification front and their accumulation in the intercellular regions.

Table 6.2. Parameters used to calculate the critical velocity of the solidification front.

Parameters	* σ_{SL}	* σ_{PL}	σ_{PS}	$\Delta\sigma_0$	n	d_0	** η	r	** K_P	** K_L
Magnitude	0.0388	0.545	4.25	3.67	7	3×10^{-10}	5.17×10^{-4}	21×10^{-8}	36.9	107.9
Unit	N/m				-	m	Pa.s	m	W/m.K	

* σ_{SL} and σ_{PL} were calculated at $T=1500$ °C using the “Interfacial Energy” module of the Thermo-Calc Software. The selected temperature was the average of melting and boiling points of the melt and was assumed to be average melt pool temperature.

** η , K_P and K_L were calculated at $T=1500$ °C using JMatPro Software.

6.3.2.3 Influence of Al_4C_3 formation on the grain structure

Figure 6.12 shows the IPF-Z EBSD maps of the AlSi12, AlSi12-0.25Gr and AlSi12-0.5Gr optimum samples along and perpendicular to the building direction. According to the IPF-Z EBSD maps of AlSi12 sample along the building direction (Figure 6.12(a-c)), it can be understood that the dominant type of grains in the L-PBF fabricated AlSi12 is columnar, though fine equiaxed grain were also formed at the boundaries and on top of the melt pools. The formation of columnar grains is attributed to the epitaxial and competitive growth of grains during the L-PBF process [21], while the equiaxed grains were formed through nucleation of new grains at the bottom (due to high thermal gradients and undercoolings [59]) and top (due to the formation of a constitutionally undercooled liquid region ahead of the solidification front because of solute segregation [60]) of the melt pools. Figure 6.12(d-f) shows the IPF-Z EBSD map of AlSi12 perpendicular to the building direction, where cross section of the columnar and equiaxed grain in Figure 6.12(a-c) can be seen. According to the IPF-Z EBSD maps shown in Figure 6.12(a-c), incorporation of Gr into AlSi12 could not change the dominance of the columnar grains. In fact, some of the columnar grains grew longer than those observed in AlSi12 sample (equiaxed grains can still be seen). Therefore, it can be concluded that the detected carbonaceous and Al_4C_3 phases could not act as inoculant for α -Al matrix during the L-PBF processing of the composites since the grains became neither equiaxed nor refined. According to Table 6.3,

the addition of Gr had no influence on the average equivalent circle grain size of AlSi12-0.25Gr sample and had slight influence on AlSi12-0.5Gr. However, based on the measurements performed on the IPF-Z EBSD maps perpendicular to the building direction it was found out that the diameter of the cross-section of columnar (and equiaxed) grains has reduced meaningfully as a result of Gr addition. According to Table 6.3, the average grain size of the cross-section of columnar grains was found to be ~9 and ~20% lower than that of the monolithic AlSi12. The formation of Al_4C_3 phase and its movement toward the cell boundaries and grain boundaries is believed to be the cause of diameter reduction of the columnar grains. The presence of Al_4C_3 at the boundaries can act as a barrier for lateral growth of grains, making them narrower. Finally, The percentage of high angle grain boundaries (HAGBs $>15^\circ$), low angle grain boundaries ($5^\circ < \text{LAGBs} < 15^\circ$) and sub-grain boundaries ($< 2^\circ$) has changed significantly as a result of Gr addition to AlSi12. For unreinforced AlSi12 sample, most of the grain boundaries were found to be high angle, and the percentage of sub-grain boundaries was negligible. However, the percentage of sub-grain boundaries were found to be remarkably higher than that of the AlSi12 sample in both composites, meaning that the cells inside the grains are not perfectly aligned and are slightly tilted relative to each other. Maybe, and it is pure speculation, the presence of Al_4C_3 and carbonaceous phases are responsible for such disturbance in the alignment of cells and increase in the percentage of sub-grain boundaries.

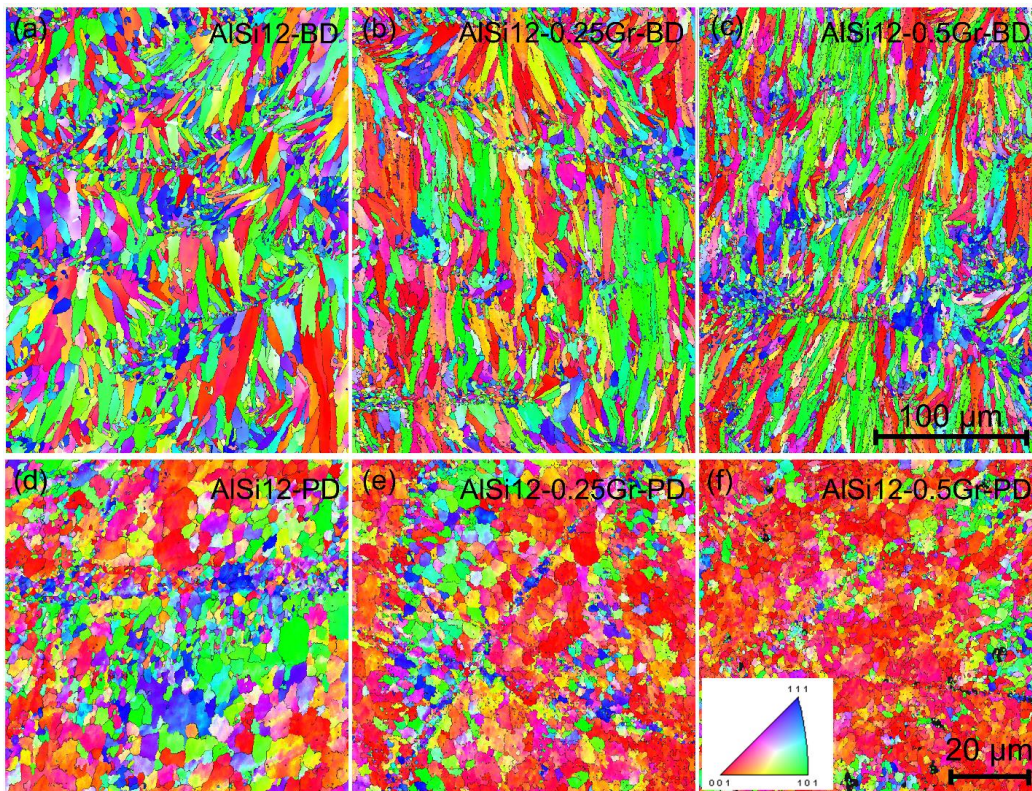


Figure 6.12. IPF-Z EBSD maps for the designated samples (a-c) along the building direction, and (d-f) perpendicular to the building direction.

Table 6.3. Average grain size and percentage of different angle grain boundaries for different materials.

Sample	Average grain size-BD [μm]	Average grain size-PD [μm]	HAGBs-BD [%]	LAGBs-BD [%]	Sub-grain boundaries-BD [%]
AlSi12	10.8	4.7	89.8	8.98	1.24
AlSi12-0.25Gr	10.8	4.3	51.6	9.50	38.9
AlSi12-0.5Gr	9.7	3.8	67.0	13.1	19.9

6.3.3 Microstructure-thermal/electrical properties relationship

6.3.3.1 Specific heat capacity

Figure 6.13 shows the C_p versus temperature for monolithic AlSi12, AlSi12-0.25Gr, and AlSi12-0.5Gr optimum samples in the range of 25-450 °C. An exothermic event was observed for each material, the indication of which is the deviation from the C_p trend and

reduction of the C_p value. The onset and end temperatures of the exothermic reaction in each case are shown in Figure 6.13(b,d,f). As can be seen, the reaction starts at 150-175 °C and ends at 250-300 °C for the tested materials. Such an exothermic reaction is related to the depletion of the supersaturated α -Al matrix from Si atoms [61]. To clarify, the high cooling rates of the L-PBF process result in a fast-growing solidification front that captures some of the segregated Si atoms during solidification and creates an α -Al matrix supersaturated from Si atoms. This was confirmed by point EDS measurements results, where 3.51, 3.28, and 3.8 at% Si were detected in α -Al of AlSi12, AlSi12-0.25Gr, and AlSi12-0.5Gr samples, respectively, significantly higher than its equilibrium value (close to zero based on Al-Si binary phase diagram). What happened during the heating cycle of the C_p measurement is that after a specific temperature, known as Debye temperature, the vibrations of the α -Al lattice reached its maximum cut-off frequency, where vigorous lattice vibrations could remarkably enhance the diffusion of Si. According to a previous study conducted by the authors [21], the Debye temperature was found to be 161 °C for the L-PBF fabricated AlSi12, which is perfectly in agreement with the start temperature of the mentioned exothermic events of all materials. This proves that the above exothermic events appeared because of the Si exsolution. Since the start temperature of the exothermic reaction for AlSi12-0.25Gr and AlSi12-0.5Gr composites is relatively the same as that of the monolithic AlSi12, it can be concluded that incorporation of Gr into AlSi12 had negligible influence on the Debye temperature. As it is perceptible, the exothermic reactions in all cases peaked at a temperature in the range of 200-225 °C. This is basically a temperature where most of the supersaturated Si atoms have already left the α -Al lattice, and thereafter an increase in C_p starts to occur.

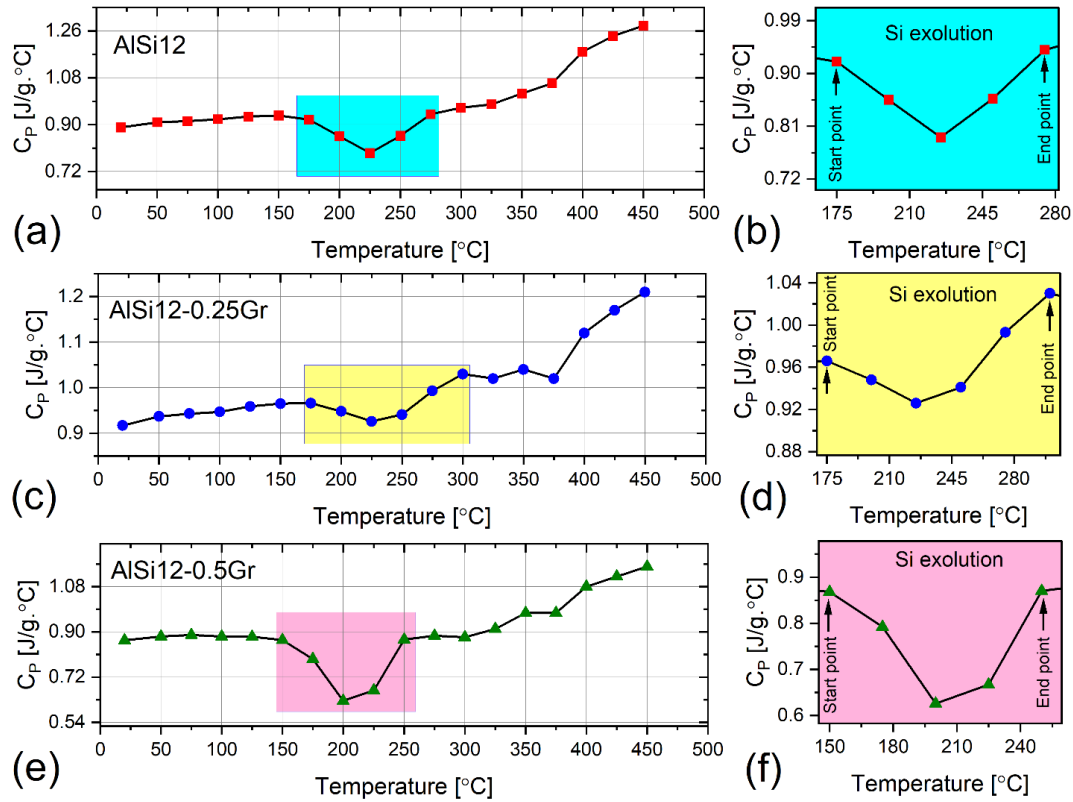


Figure 6.13. (a,c,e) C_p versus temperature for the labeled materials, and (b,d,f) higher magnification illustration of colored boxes shown in (a,c,e).

6.3.3.2 Thermal expansion and density

According to Eq. (1), the density of the optimum samples not only at room temperature but also at higher temperatures in the range of 25-450 °C was required to calculate the thermal conductivity. Accordingly, the relative change in the physical dimension ($\Delta L/L_0$) of the samples versus temperature was measured in the range of 25-450 °C (heating cycle-Figure 6.14(a-f)). By using the following equation, the density at higher temperatures ($\rho(T)$) was obtained (Figure 6.14(h)):

$$\rho(T) = \frac{\rho_{RT}}{1 + 3\frac{\Delta L}{L_0}} \quad \text{Eq. (3)}$$

in which ρ_{RT} denotes the density of the optimum sample at room temperature. As mentioned earlier, the optimum samples of AlSi12, AlSi12-0.25Gr, and AlSi12-0.5Gr possessed relative densities of 99.8, 99.5, and 99.2%, respectively. Assuming the true density of composite samples was similar to that of the AlSi12 alloy (2.67 g/cm^3), 2.665, 2.657, and 2.649 g/cm^3 were used as the ρ_{RT} for the respective samples. The density versus temperature results shown in Figure 6.14(h) suggest a less than 5% decrease in the density of samples over the measurement temperature range.

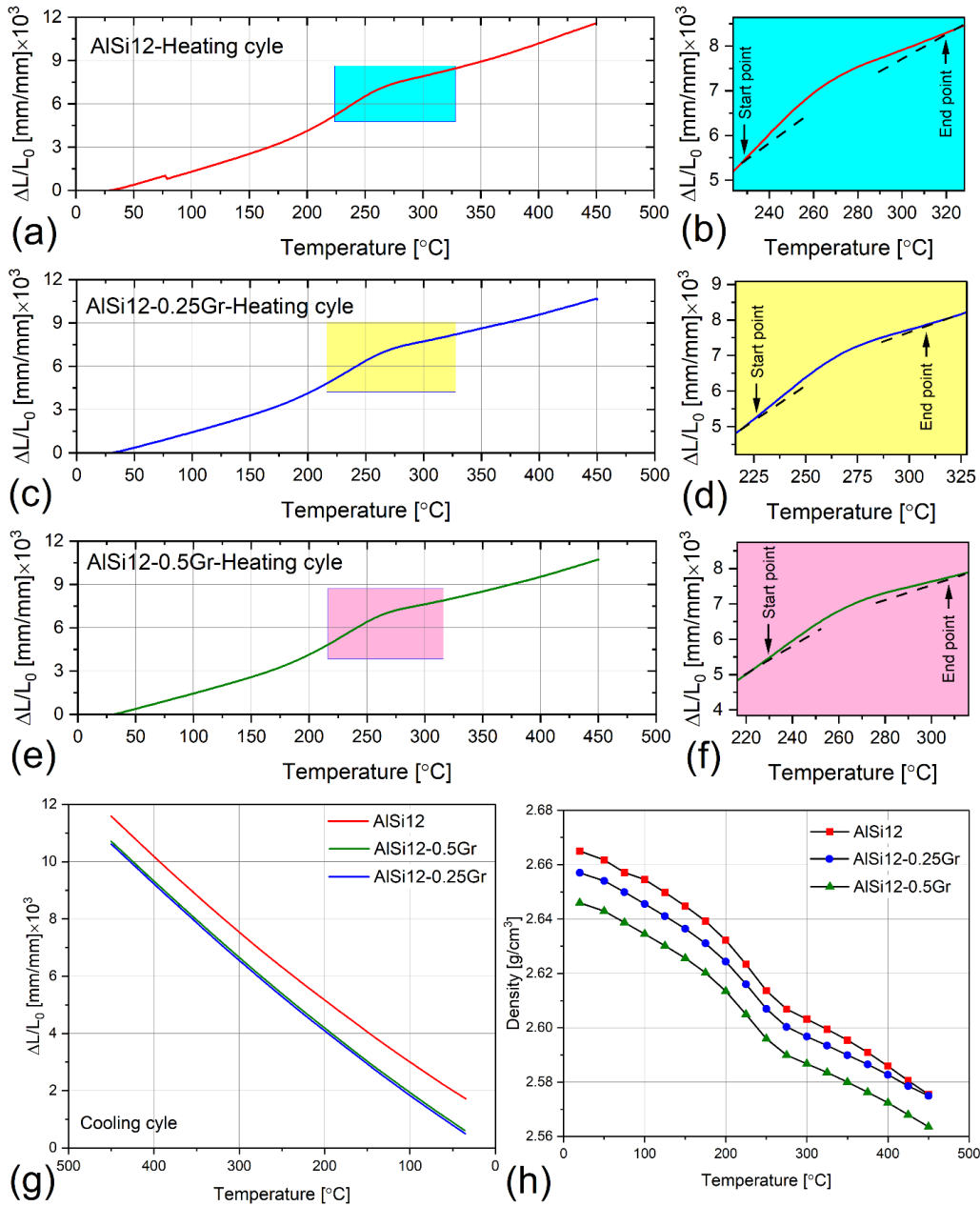


Figure 6.14. (a,c,e) relative change in physical dimensions versus temperature during heating cycle for the labeled materials, and (b,d,f) higher magnification illustration of colored boxes shown in (a,c,e). (g) relative change in physical dimensions versus temperature during cooling cycle, and (h) density versus temperature curves.

Regarding the $\Delta L/L_0$ versus temperature results in the heating cycle, an anomaly was observed in the linear thermal expansion behavior of all materials in the temperature range

of ~220-320 °C. The onset of deviation from linear expansion behavior agrees with the temperature at which the exothermic reaction peaked for all materials in the CP-T curves (Figure 6.13). The depletion of the supersaturated α -Al lattice from smaller Si atoms (radius=110 pm) is accompanied by an increase in the lattice parameter, showing itself as a relatively sharp increase in physical dimensions at the microscopic level and deviations from linear thermal expansion behavior [62]. Interestingly, deviations started with a lag when Si content had reduced significantly in the α -Al matrix. To prove the hypothesis that the observed anomaly in the heating cycle was because of the Si exolution, the change in $\Delta L/L_0$ ratio as a function of temperature was also investigated during the cooling cycle. As evident in Figure 6.14(g), the thermal contraction behavior during the cooling stage was found to be perfectly linear after the complete exolution of Si from the supersaturated α -Al matrix during the heating cycle, proving that the observed anomalies in Figure 6.14(a-f) were due to the entrapped Si solutes during the L-PBF fabrication of reinforced and unreinforced AlSi12 samples. Assuming a linear thermal expansion behavior in the heating cycle curves in the whole measured temperature range, the linear coefficient of thermal expansions of 27.5, 25.3, and 25.5 ($\times 10^{-6}/^\circ\text{C}$) were obtained for AlSi12, AlSi12-0.25Gr, and AlSi12-0.5Gr, respectively. The lower coefficient of thermal expansion of the composites is because of the low and negative coefficient of thermal expansions of Al_4C_3 ($3.5 \times 10^{-6}/^\circ\text{C}$ at 100 °C [63]) and Gr constituents ($-8.72 \times 10^{-6}/^\circ\text{C}$ at 50 °C [64]) in the composites, respectively.

6.3.3.3 Thermal diffusivity

The results of thermal diffusivity measurements along and perpendicular to the build direction are shown in Figure 6.15, from which valuable information can be obtained. First, a slight difference was observed between the thermal diffusivity of each material along and

perpendicular to the building direction; nevertheless, the relative thermal diffusivity differences reached up to ~11, 10 and 15% at specific temperatures for AlSi12, AlSi12-0.25Gr, and AlSi12-0.5Gr, respectively. This implies the slight dependency of thermal diffusivity on the orientation of the printed sample. Second, the thermal diffusivity of all materials remains relatively constant in the temperature ranges of 25-150 °C (minor change in thermal diffusivity, <5%) and above ~250 °C. This is while a sharp thermal diffusivity enhancement in the temperature range of 150-250 °C is perceptible. This temperature range is almost identical to the one found for the exothermic reaction of Si exolution from the C_p -T measurement results. This signifies that the sharp increase in the thermal diffusivity originates from the depletion of the supersaturated α -Al matrix from Si, which reduces the electron scattering frequency and consequently enhances the thermal diffusivity (see section 6.3.3.4). Finally, as opposed to what has been expected, the AlSi12-0.25Gr and AlSi12-0.5Gr composites showed either the same or slightly lower thermal diffusivity than monolithic AlSi12. This is mainly due to creating a new source of electron scattering site in the composites (Al_4C_3 -Figure 6.10), which is explained in detail in section 6.3.3.4.

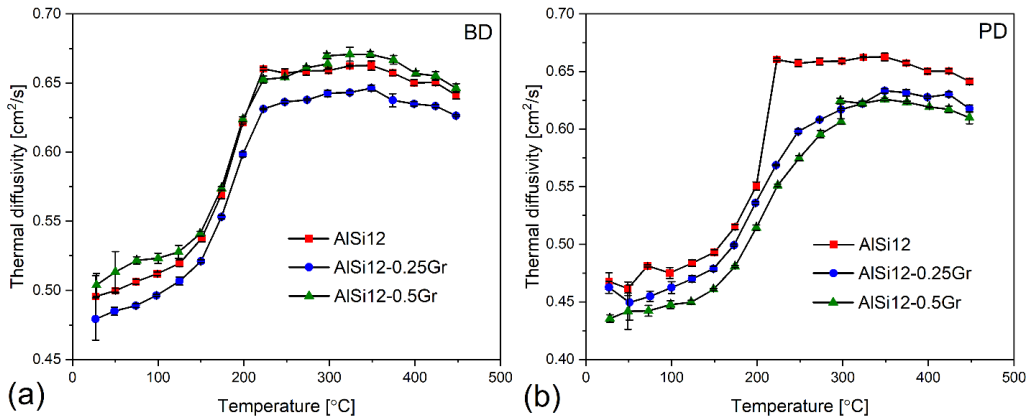


Figure 6.15. Thermal diffusivity versus temperature (a) along and (b) perpendicular to the building direction.

6.3.3.4 Thermal conductivity

By using the C_p , density, and thermal diffusivity measurement results in the temperature range of 25-450 °C, the thermal conductivity of AlSi12, AlSi12-0.25Gr, and AlSi12-0.5Gr was calculated using Eq. (1). The thermal conductivity versus temperature results are shown in Figure 6.16 along and perpendicular to the building direction. Generally speaking, the thermal conductivity of AlSi12-0.25Gr is more or less the same as that of the AlSi12 in the studied temperature range. However, the former was found to have a higher thermal conductivity in the range of 150-350 °C for the sample along the building direction (Figure 6.16(a)) and in the range of 150-250 °C for the sample perpendicular to the building direction (Figure 6.16(b)). Regarding AlSi12-0.5Gr, the thermal conductivity is always lower than that of the AlSi12 sample. Therefore, it is fair to conclude that the addition of graphene nanoplatelets/graphitic guest particles to AlSi12 host powder had no influence or deteriorated the thermal conductivity of the AlSi12 alloy. Even when the thermal conductivity of the AlSi12-0.25Gr exceeds that of the AlSi12 sample, it has nothing to do with the addition of a second constituent but a lower Si solute entrapment in the former sample, inferred from the shallower exothermic peak in the C_p -T curve (Figure 6.13) and point EDS results. Now because of having a higher C_p value in the range of the Si exsolution exothermic reaction and almost the same thermal diffusivity values as that of the AlSi12 sample (along the building direction), AlSi12-0.25Gr shows higher thermal conductivity in the range of 200-350 °C (along the building direction). The reason for having different Si solute supersaturation levels in different materials is that the optimum samples of the reinforced and unreinforced AlSi12 were obtained at different sets of process parameters. Moreover, the incorporation of Gr into AlSi12, its transformation to Al_4C_3 , and presumably

its dissolution in the molten AlSi12 during the L-PBF process are other reasons that can change the Si solute entrapment.

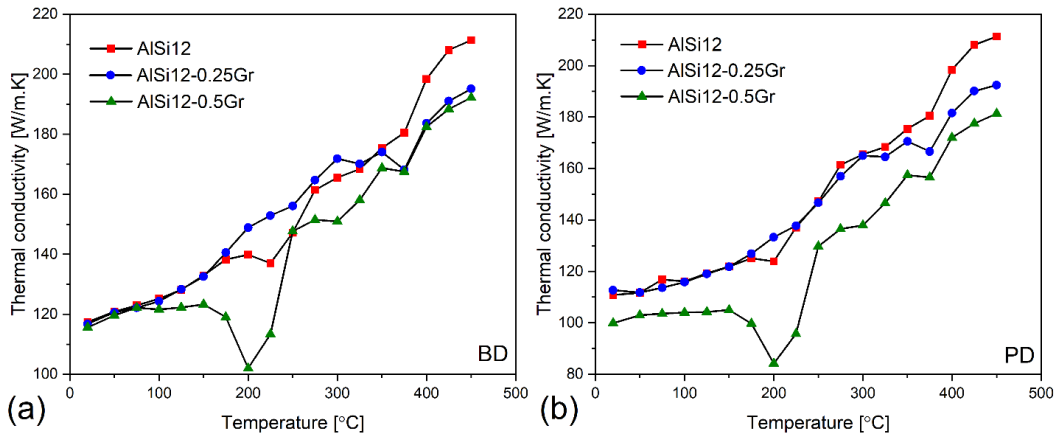


Figure 6.16. Thermal conductivity versus temperature (a) along and (b) perpendicular to the building direction.

The findings of thermal conductivity seem to contradict what has been explained in the introduction section, where graphene was introduced as a highly conductive material; then why the incorporation of Gr with higher thermal conductivity into AlSi12 failed to enhance the thermal conductivity of the material? The answer to this question can be found in the followings:

i. High degree of structural disorder in the survived carbonaceous nano-constituent:

As explained in section 6.3.2.1, carbon survives during the L-PBF process (Figure 6.8); however, due to its partial transformation to Al_4C_3 , its structural integrity is damaged significantly (Figure 6.9), meaning that the remaining carbon has not the extraordinary features and properties of the graphene.

ii. Transformation of Gr into Al_4C_3 with low thermal conductivity:

As explained in section 6.3.2.2, most carbon-containing phases detected in the L-PBF fabricated composites were found to be Al_4C_3 (Figure 6.8(c) and Figure 6.10). According to

the thermal conductivity calculation conducted by JMatPro Software, the thermal conductivity of Al_4C_3 lies in the range of 19.2-24.3 W/m.K when the temperature changes from 25 to 450 °C. The presence of a low thermal conductivity constituent in the AlSi12 matrix can be one of the main reasons behind the reduced thermal conductivity of composites. A slight reduction in thermal conductivity is expected owing to the low volume fraction of Al_4C_3 (1.14 and 2.26 vol% upon the complete transformation of Gr into Al_4C_3) in the fabricated composites.

- iii. *Presence of graphite/graphene nanoplatelets (Gr) rather than monolayer graphene*: According to Raman spectroscopy results (Figure 6.9), Gr particles with high structural integrity (low I_D/I_G) were also detected in the L-PBF fabricated parts. However, this was not monolayer graphene, as the 2D peak was not more intense than the G peak (fingerprint of monolayer graphene), meaning that even upon the survival of Gr particles, they are either graphite or graphene nanoplatelets (layers < 150). Referring to the literature [65], in monolayer graphene, the out-of-plane acoustic mode contributes significantly to conduction; however, when the number of layers increases, the interplanar interactions open new pathways for phonon scattering, reducing the conductivity. For instance, by increasing the number of layers from 1 to 4, a 30% reduction in thermal conductivity was reported [65]. The thermal conductivity of graphite is significantly lower than graphene monolayer and even lower than Al in most of the crystallographic directions [66]. On this account, the presence of Gr rather than single-layer graphene cannot contribute (or contribute slightly) to increasing the thermal conductivity of the fabricated composites.

- iv. Anisotropic conductivity in Gr: Remaining Gr possesses relatively high in-plane thermal conductivity, not out of the plane and all remaining Gr were not aligned along or perpendicular to the building direction in the L-PBF fabricated composites but have random orientations.

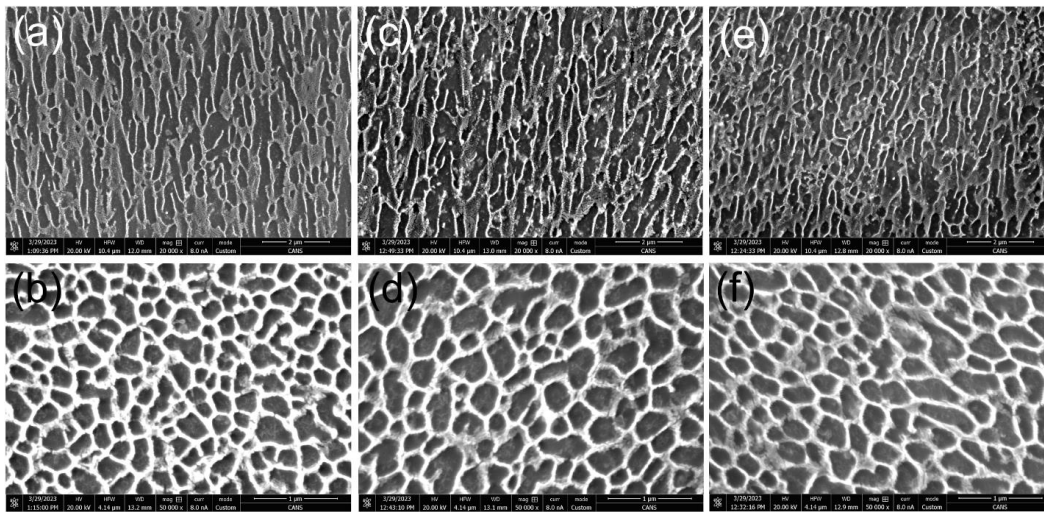


Figure 6.17. SEM micrographs of the designated materials (a,c,e) along and (b,d,f) perpendicular to the building direction.

Referring to Figure 6.16, the thermal conductivity of the L-PBF fabricated reinforced and unreinforced AlSi12 in the perpendicular direction was found to be slightly lower than building direction. According to a previous study [21] conducted by the authors on thermal conductivity of the L-PBF fabricated AlSi12 under 200 °C of preheating, it was found out that in addition to the electron-phonon intrinsic scattering event, there are other extrinsic scattering sites dictating the magnitude of overall electron mean free path and thermal conductivity, namely, (i) pores, (ii) grain boundaries, (iii) cell boundaries, (iv) dislocations, (v) vacancies, and (vi) supersaturated Si. Based on theoretical calculations, it was proved that the contribution of pores (for samples with relative densities higher than 99%) and grain boundaries were negligible compared to the rest of scattering sites. The scattering

events caused by phonons (intrinsic), supersaturated Si, cell boundaries, vacancies and dislocations accounted for 51.2, 43.3, 2.1, 1.9, and 1.5% of the total electron scattering, respectively. The main reason for slightly lower thermal conductivity in the perpendicular direction compared to the building direction is believed to be the significantly lower cell size in the former, as shown in Figure 6.17. In other words, the contribution of cell boundaries to scatter electrons increases meaningfully in the perpendicular direction due to their noticeably lower size, leading to the reduced thermal conductivity.

6.4 Conclusions

In this study, the possibility of enhancing thermal conductivity of AlSi12 alloy through the incorporation of a second constituent (i.e., graphene nanoplatelets/graphite (Gr)), with higher nominal thermal conductivity, was put into test. For this purpose, AlSi12-0.25Gr and AlSi12-0.5Gr powders were ball milled and then processed using laser powder bed fusion (L-PBF) technique. Influence of Gr addition and mixing process on laser absorptivity of powders, O/C/N content of the powders and printed parts, and densification level of the printed parts was discussed. The strategy of low laser power to scanning velocity ratio (P/V) and relative low hatch spacing (below 100 μm) was proposed to end up with highly dense composite parts with relative densities up to 99.5 and 99.2% for AlSi12-0.25Gr and AlSi12-0.5Gr, respectively. In-depth microstructural and nano-structural studies were performed on the optimum samples of reinforced and unreinforced AlSi12 using TEM, HRTEM, EBSD, EDS and Raman spectroscopy and it was found out that (i) most of Gr transforms into Al₄C₃, (ii) a part of the carbonaceous material survives, though it is more like disordered carbon than starting Gr, and (iii) neither carbonaceous phase nor Al₄C₃ could act as an inoculant for grain nucleation during the L-PBF process. The optimum samples were also investigated in terms of specific heat capacity (C_p),

coefficient of thermal expansion (CTE), thermal diffusivity, and thermal conductivity in the temperature range of 25-450 °C. The C_p -T behavior of all samples was dictated by supersaturation of Si in α -Al phase, with the highest level of Si supersaturation found to be for AlSi12-0.5Gr composite. Thermal expansion measurement results revealed that the coefficient of thermal expansion decreased from $27.5 \times 10^{-6}/^\circ\text{C}$ for AlSi12 to $25.3 \times 10^{-6}/^\circ\text{C}$, and $25.5 \times 10^{-6}/^\circ\text{C}$ for AlSi12-0.25Gr, and AlSi12-0.5Gr, respectively, due to the presence of nano-sized Al₄C₃ phase and the residual carbon with lower CTE than AlSi12. For AlSi12-0.5Gr, the thermal conductivity was either the same or lower than that of the monolithic AlSi12 in the studied temperature range. Comparing the thermal conductivities of AlSi12 and AlSi12-0.25Gr, the latter possessed higher thermal conductivity only in the temperature range of 150-350 °C. The reduced thermal conductivity for AlSi12-0.5Gr and AlSi12-0.25Gr in temperatures below 150 °C or above 350 °C was due to (i) high degree of structural disorder in the survived carbonaceous nano-constituent, (ii) transformation of Gr into Al₄C₃ with low thermal conductivity, (iii) presence of graphite/graphene nanoplatelets (Gr) rather than monolayer graphene, and (iv) anisotropic conductivity in Gr. Higher thermal conductivity of AlSi12-0.25Gr in the temperature range of 150-350 °C was because of lower Si supersaturation in this case compared to the others.

6.5 Supplementary materials

6.5.1 L-PBF Process parameters

The details of the process parameters used to print composite parts are tabulated in Table S1.

Table S1. The list of process parameter combinations used in this research study to print composite parts.

Laser power [W]	Scanning speed [mm/s]	Hatch spacing [μm]	Nominal powder layer thickness (platform displacement) [μm]
200	600, 800, 1000, 1200, 1400	100	30
	1600, 1800, 2000	70	
250	1000, 1200, 1400, 1600, 1800, 2000	100	
	1600, 1800, 2000	70	
300	1000, 1200, 1400, 1600, 1800, 2000	100	
		130	
370	1200, 1400, 1600, 1800, 2000, 2200, 2400, 2600, 2800, 3000	100	
	1200, 1400, 1600, 1800, 2000	150	
		190	

6.5.2 Powder attributes and behaviors

Figure S1(a-c) shows the cumulative distribution and relative frequency of the monolithic AlSi12, AlSi12-0.25Gr and AlSi12-0.5Gr powders, respectively. The D_{10} , D_{50} , and D_{90} of each powder is embedded in the graphs. The provided size distribution curves for the composite powders give information only about the metallic AlSi12 particles (host) not the graphene ones (guest) as their size was lower than the detection limit. The particle size measurement results prove that the ball milling parameters were selected properly as slight deviations in the size of host particles has happened during the mixing process. As evident, D_{10} , and D_{50} of composite powders are all similar to those of the unreinforced AlSi12 powder. Even D_{90} of AlSi12-0,25Gr and AlSi12-0.5Gr powders was found to be only ~9 and 13% higher than the reference sample, proving limited deformation and cold welding of host particles during the ball milling process. To quantitatively characterize the shape evolutions of the host particles before and after mixing, the sphericity (SPHT) and breadth to length ratio (b/l) were calculated from the particle projections using the following equations [67, 68]:

$$SPHT = \frac{4\pi A}{P^2} \quad \text{Eq. (S1)}$$

$$\frac{b}{l} = \frac{X_{c,min}}{X_{Fe,max}} \quad \text{Eq. (S2)}$$

where A , p , $X_{c,min}$, and $X_{Fe,max}$ denote area of a particle projection, perimeter of a particle projection, the minimum chord length and maximum Feret diameter, respectively. The chord length is basically the maximum distance between two horizontal boundary points of the particle projection. To determine $X_{c,min}$, the projection is rotated for a certain number of rotation angles and the smallest value is selected [68]. $X_{Fe,max}$ is defined as the largest distance between the two parallel planes containing the object perpendicular to that direction [69]. Figure S1(d,e) shows the mean SPHT and b/l results plus the standard deviations for different powders. Also, the percentage of particles having SPHT, and b/l values equal to or greater than 0.9 (e.g., $1-Q(\text{SPHT}=0.9)$) are shown in these figures. From the mean SPHT and $1-Q(\text{SPHT}=0.9)$ perspectives, the host powder particles of the composite samples are almost identical to the starting AlSi12 powder. Based on the b/l criterion it was found that the host particles in AlSi12-0.25Gr and AlSi12-0.5Gr powders are only 2.5 and 7.4% flatter than the starting AlSi12 particles. However, $1-Q(b/l=0.9)$ decreased from 30.5% for the AlSi12 powder to 23.2 and 14.6% for AlSi12-0.25Gr and AlSi12-0.5Gr powders, respectively. This is mainly attributed to the plastic deformation of the host particles during the ball milling process.

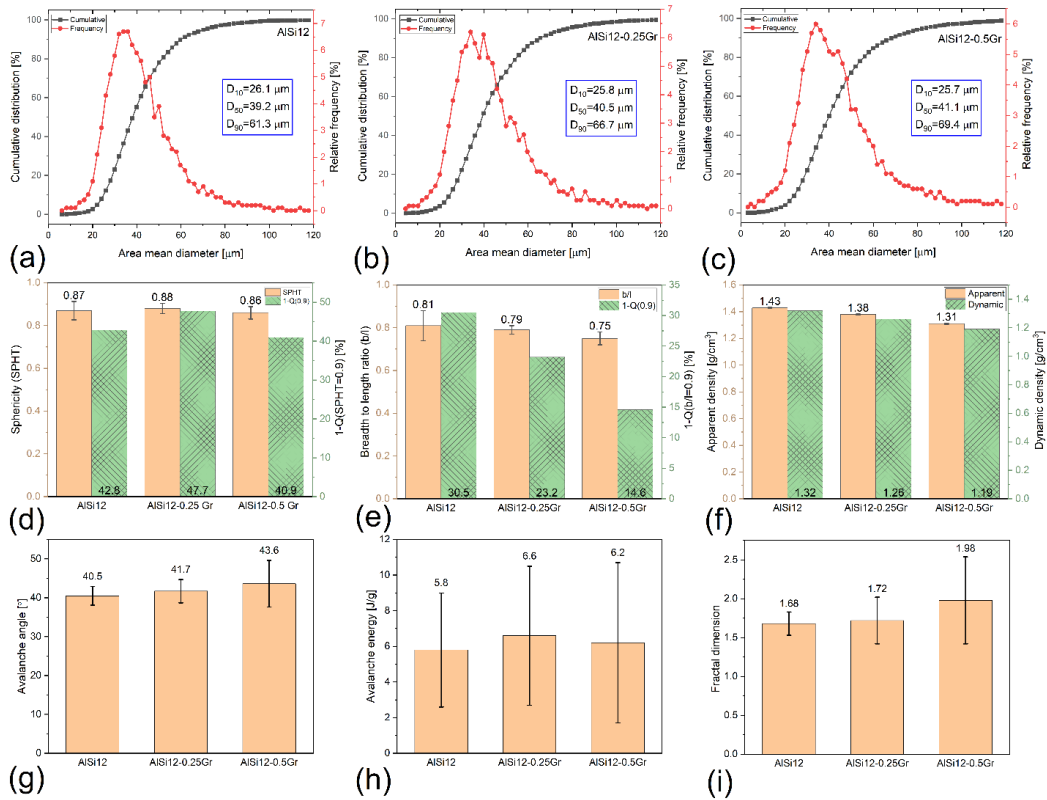


Figure S1. (a-c) cumulative distribution and relative frequency, (d) mean SPHT and 1-Q(SPHT=0.9), (e) mean b/l ratio and 1-Q(b/l=0.9), (f) mean apparent packing density and dynamic density, (g) mean avalanche angle, (h) mean avalanche energy, and (i) mean fractal dimension of AISi12 [an under review paper], AISi12-0.25Gr and AISi12-0.5Gr [an under review paper] powders. The error bars in (d-i) represent the standard deviation of the measured values.

The results of apparent packing density (Carney funnel) and dynamic density (Revolution powder analyzer) of the composite and reference powders are shown in **Error! Reference source not found.**(f). Although different values were obtained for each powder using different measurement methods, the trends are the same. According to both criteria, the densities of composite powders are less than 10% lower than that of the reference powder. The avalanche angle, avalanche energy and fractal dimension results are shown in Figure S1(g-i). The detailed definition of these parameters can be found in [70]. The lower the avalanche angle and energy, the better the flowability of the powders. According to these

two flowability criteria, the composite powders are almost identical to reference powder as the differences observed in avalanche angles and energies are insignificant. Fractal dimension is an indirect measurement of the powder cohesivity. As reported in [71], fractal dimensions in the range of 1.5-2 ensures even and smooth powder bed for the L-PBF application. Based on the abovementioned results, it is fair to conclude that the produced composite powders have attributes and behaviors close to those of the reference powder and therefore, they are suitable for the L-PBF process.

Acknowledgment

The authors would like to thank Dr J. E. Greedan and Evan Smith from the Department of Chemistry at McMaster University for the ball milling facility and Dr. Zhilin Peng at the Center for Advanced Nuclear Systems (CANS) at McMaster University for EBSD.

References

1. Tjong, S.C., *Recent progress in the development and properties of novel metal matrix nanocomposites reinforced with carbon nanotubes and graphene nanosheets*. Materials Science and Engineering: R: Reports, 2013. **74**(10): p. 281-350.
2. Lee, C., et al., *Measurement of the elastic properties and intrinsic strength of monolayer graphene*. science, 2008. **321**(5887): p. 385-388.
3. Balandin, A.A., et al., *Superior thermal conductivity of single-layer graphene*. Nano letters, 2008. **8**(3): p. 902-907.
4. Wong, E.W., P.E. Sheehan, and C.M. Lieber, *Nanobeam mechanics: elasticity, strength, and toughness of nanorods and nanotubes*. science, 1997. **277**(5334): p. 1971-1975.
5. Pop, E., et al., *Thermal conductance of an individual single-wall carbon nanotube above room temperature*. Nano letters, 2006. **6**(1): p. 96-100.

6. Saboori, A., et al., *An overview of metal matrix nanocomposites reinforced with graphene nanoplatelets; mechanical, electrical and thermophysical properties*. Metals, 2018. **8**(6): p. 423.
7. Uozumi, H., et al., *Fabrication process of carbon nanotube/light metal matrix composites by squeeze casting*. Materials Science and Engineering: A, 2008. **495**(1-2): p. 282-287.
8. Oh, S.-I., et al., *Fabrication of carbon nanofiber reinforced aluminum alloy nanocomposites by a liquid process*. Journal of Alloys and Compounds, 2012. **542**: p. 111-117.
9. Fereiduni, E., A. Ghasemi, and M. Elbestawi, *Selective laser melting of aluminum and titanium matrix composites: recent progress and potential applications in the aerospace industry*. Aerospace, 2020. **7**(6): p. 77.
10. Laha, T., et al., *Interfacial phenomena in thermally sprayed multiwalled carbon nanotube reinforced aluminum nanocomposite*. Acta Materialia, 2007. **55**(3): p. 1059-1066.
11. Hu, Z., et al., *3D printing graphene-aluminum nanocomposites*. Journal of Alloys and Compounds, 2018. **746**: p. 269-276.
12. Li, S., et al., *Enhanced mechanical behavior and fabrication of silicon carbide particles covered by in-situ carbon nanotube reinforced 6061 aluminum matrix composites*. Materials & Design, 2016. **107**: p. 130-138.
13. Yu, H., et al., *Microstructural evolution, mechanical and physical properties of graphene reinforced aluminum composites fabricated via powder metallurgy*. Materials Science and Engineering: A, 2021. **802**: p. 140669.
14. Wang, J., et al., *Reinforcement with graphene nanosheets in aluminum matrix composites*. Scripta Materialia, 2012. **66**(8): p. 594-597.
15. Choi, H., J. Shin, and D. Bae, *Grain size effect on the strengthening behavior of aluminum-based composites containing multi-walled carbon nanotubes*. Composites Science and Technology, 2011. **71**(15): p. 1699-1705.
16. Jiang, L., et al., *The use of flake powder metallurgy to produce carbon nanotube (CNT)/aluminum composites with a homogenous CNT distribution*. Carbon, 2012. **50**(5): p. 1993-1998.
17. Ibrahim, M.A., et al., *Mechanical properties of aluminium matrix composite including SiC/Al₂O₃ by powder metallurgy-a review*. GSJ, 2019. **7**(3): p. 23-38.
18. Vasanthakumar, P., K. Sekar, and K. Venkatesh, *Recent developments in powder metallurgy based aluminium alloy composite for aerospace applications*. Materials Today: Proceedings, 2019. **18**: p. 5400-5409.

19. Balbaa, M., et al., *Role of powder particle size on laser powder bed fusion processability of AlSi10Mg alloy*. Additive Manufacturing, 2021. **37**: p. 101630.
20. Ghasemi, A., et al., *Influence of alloying elements on laser powder bed fusion processability of aluminum: A new insight into the oxidation tendency*. Additive Manufacturing, 2021. **46**: p. 102145.
21. Ghasemi, A., et al., *Unraveling the low thermal conductivity of the LPBF fabricated pure Al, AlSi12, and AlSi10Mg alloys through substrate preheating*. Additive Manufacturing, 2022. **59**: p. 103148.
22. Narvan, M., et al., *Laser powder bed fusion of functionally graded bi-materials: Role of VC on functionalizing AISI H13 tool steel*. Materials & Design, 2021. **201**: p. 109503.
23. Wang, Y., et al., *Investigation of porosity and mechanical properties of graphene nanoplatelets-reinforced AlSi10 Mg by selective laser melting*. Journal of Micro and Nano-Manufacturing, 2018. **6**(1).
24. Fereiduni, E., A. Ghasemi, and M. Elbestawi, *Microstructural characterization and mechanical properties of nano-scale/sub-micron TiB-reinforced titanium matrix composites fabricated by laser powder bed fusion*. Journal of Alloys and Compounds, 2022. **896**: p. 163054.
25. Rezaeifar, H. and M. Elbestawi, *Minimizing the surface roughness in L-PBF additive manufacturing process using a combined feedforward plus feedback control system*. The International Journal of Advanced Manufacturing Technology, 2022. **121**(11-12): p. 7811-7831.
26. Hashim, J., L. Looney, and M. Hashmi, *Metal matrix composites: production by the stir casting method*. Journal of materials processing technology, 1999. **92**: p. 1-7.
27. Tiwari, J.K., et al., *Effect of graphene addition on thermal behavior of 3D printed graphene/AlSi10Mg composite*. Journal of Alloys and Compounds, 2022. **890**: p. 161725.
28. Zhao, X., et al., *Selective laser melting of carbon/AlSi10Mg composites: Microstructure, mechanical and electronical properties*. Journal of Alloys and Compounds, 2016. **665**: p. 271-281.
29. Wang, L.-z., T. Chen, and S. Wang, *Microstructural characteristics and mechanical properties of carbon nanotube reinforced AlSi10Mg composites fabricated by selective laser melting*. Optik, 2017. **143**: p. 173-179.
30. Jiang, L., et al., *Preparation and mechanical properties of CNTs-AlSi10Mg composite fabricated via selective laser melting*. Materials Science and Engineering: A, 2018. **734**: p. 171-177.

31. Zhao, Z., et al., *AlSi10Mg alloy nanocomposites reinforced with aluminum-coated graphene: Selective laser melting, interfacial microstructure and property analysis*. Journal of Alloys and Compounds, 2019. **792**: p. 203-214.
32. Jiang, L., et al., *Thermal expansion behavior of CNT reinforced AlSi10Mg composite fabricated via laser powder bed fusion*. Materials Research Express, 2020. **6**(12): p. 125806.
33. Aboulkhair, N.T., et al., *Evolution of carbon nanotubes and their metallurgical reactions in Al-based composites in response to laser irradiation during selective laser melting*. Materials Science and Engineering: A, 2019. **765**: p. 138307.
34. Gu, D., et al., *Laser additive manufacturing of carbon nanotubes (CNTs) reinforced aluminum matrix nanocomposites: Processing optimization, microstructure evolution and mechanical properties*. Additive Manufacturing, 2019. **29**: p. 100801.
35. Lee, E.R., et al., *Manufacturing aluminum/multiwalled carbon nanotube composites via laser powder bed fusion*. Materials, 2020. **13**(18): p. 3927.
36. Xi, L., et al., *In-situ synthesis of aluminum matrix nanocomposites by selective laser melting of carbon nanotubes modified Al-Mg-Sc-Zr alloys*. Journal of Alloys and Compounds, 2022. **891**: p. 162047.
37. Zhao, W., et al., *The interfacial characteristics of graphene/Al4C3 in graphene/AlSi10Mg composites prepared by selective laser melting: First principles and experimental results*. Materials, 2020. **13**(3): p. 702.
38. Qiu, J., C. Chen, and M. Zhang, *Effects of graphene on the mechanical properties of AlSi10Mg melted by SLM*. Materials Science and Technology, 2022: p. 1-11.
39. Zhang, S., et al., *Wear properties of graphene/zirconia biphasic nano-reinforced aluminium matrix composites prepared by SLM*. Materials Today Communications, 2022. **30**: p. 103009.
40. Zhang, S., et al., *Graphene/ZrO₂/aluminum alloy composite with enhanced strength and ductility fabricated by laser powder bed fusion*. Journal of Alloys and Compounds, 2022. **910**: p. 164941.
41. Bai, P., et al., *Microstructure and tribological behavior of graphene/Al composites produced by selective laser melting*. Materials Research Express, 2019. **6**(10): p. 1065c1.
42. Liu, X., et al., *CNT-reinforced AlSi10Mg composite by selective laser melting: microstructural and mechanical properties*. Materials Science and Technology, 2019. **35**(9): p. 1038-1045.
43. Tiwari, J.K., et al., *Investigation of porosity, microstructure and mechanical properties of additively manufactured graphene reinforced AlSi10Mg composite*. Additive Manufacturing, 2020. **33**: p. 101095.

44. Tiwari, J.K., et al., *Novel approach for micrographical investigation of graphene in additively manufactured graphene/AlSi10Mg composite*. Materials Letters, 2021. **284**: p. 128923.
45. Yu, T., et al., *Microstructure and wear characterization of carbon nanotubes (CNTs) reinforced aluminum matrix nanocomposites manufactured using selective laser melting*. Wear, 2021. **476**: p. 203581.
46. Wu, L., et al., *Wear resistance of graphene nano-platelets (GNPs) reinforced AlSi10Mg matrix composite prepared by SLM*. Applied Surface Science, 2020. **503**: p. 144156.
47. Zhou, W., et al., *In situ formation of uniformly dispersed Al₄C₃ nanorods during additive manufacturing of graphene oxide/Al mixed powders*. Carbon, 2019. **141**: p. 67-75.
48. Dong, M., et al., *Microstructure and mechanical property of graphene oxide/AlSi10Mg composites fabricated by laser additive manufacturing*. Materials Characterization, 2020. **170**: p. 110678.
49. Gaskell, D., *An introduction to transport phenomena in materials engineering*. 2012: Momentum Press.
50. Rezaeifar, H. and M. Elbestawi, *Porosity formation mitigation in laser powder bed fusion process using a control approach*. Optics & Laser Technology, 2022. **147**: p. 107611.
51. du Plessis, A., *Effects of process parameters on porosity in laser powder bed fusion revealed by X-ray tomography*. Additive Manufacturing, 2019. **30**: p. 100871.
52. Ellingham, H.J., *Reducibility of oxides and sulphides in metallurgical processes*. J. Soc. Chem. Ind, 1944. **63**(5): p. 125-160.
53. Balbaa, M., et al., *On selective laser melting of Inconel 718: Densification, surface roughness, and residual stresses*. Materials & Design, 2020. **193**: p. 108818.
54. Meier, C., et al., *Raman properties of silicon nanoparticles*. Physica E: Low-dimensional Systems and Nanostructures, 2006. **32**(1-2): p. 155-158.
55. Lin, R.Y. *Interface evolution in aluminum matrix composites during fabrication*. in *Key Engineering Materials*. 1995. Trans Tech Publ.
56. Bakshi, S.R., et al., *Interface in carbon nanotube reinforced aluminum silicon composites: Thermodynamic analysis and experimental verification*. Journal of Alloys and Compounds, 2009. **481**(1-2): p. 207-213.
57. Stefanescu, D.M., et al., *Behavior of ceramic particles at the solid-liquid metal interface in metal matrix composites*. Metallurgical Transactions A, 1988. **19**: p. 2847-2855.

58. Kou, S., *Welding metallurgy*. New Jersey, USA, 2003. **431**(446): p. 223-225.
59. Liu, X., et al., *Microstructure of selective laser melted AlSi10Mg alloy*. *Materials & Design*, 2019. **168**: p. 107677.
60. Hadadzadeh, A., et al., *Columnar to equiaxed transition during direct metal laser sintering of AlSi10Mg alloy: effect of building direction*. *Additive Manufacturing*, 2018. **23**: p. 121-131.
61. Marola, S., et al., *A comparison of Selective Laser Melting with bulk rapid solidification of AlSi10Mg alloy*. *Journal of Alloys and Compounds*, 2018. **742**: p. 271-279.
62. Yang, P., et al., *Microstructure evolution and thermal properties of an additively manufactured, solution treatable AlSi10Mg part*. *Journal of Materials Research*, 2018. **33**(23): p. 4040-4052.
63. Sun, L., et al., *Prediction on structural, mechanical and thermal properties of Al₄SiC₄, Al₄C₃ and 4H-SiC under high pressure by first-principles calculation*. *Modern Physics Letters B*, 2017. **31**(09): p. 1750080.
64. Abdullah, M.A., T.M.B. Albarody, and A.R. Hussein, *Graphite thermal expansion coefficient measured by in-situ X-ray diffraction*. *Nanotechnology*, 2020. **31**(28): p. 285709.
65. Singh, D., J.Y. Murthy, and T.S. Fisher, *Mechanism of thermal conductivity reduction in few-layer graphene*. *Journal of Applied Physics*, 2011. **110**(4): p. 044317.
66. Alofi, A. and G. Srivastava, *Thermal conductivity of graphene and graphite*. *Physical Review B*, 2013. **87**(11): p. 115421.
67. *Operating instructions/Manual particle size analysis system CAMSIZER*. Retsch Technology GmbH, Rheinische StraBe 43, 42781 Haan, Germany
68. Mitterlehner, M., et al., *Comparative Evaluation of Characterization Methods for Powders Used in Additive Manufacturing*. *Journal of Materials Engineering and Performance*, 2021. **30**(9): p. 7019-7034.
69. Merkus, H.G., *Particle size measurements: fundamentals, practice, quality*. Vol. 17. 2009: Springer Science & Business Media.
70. Spierings, A.B., et al., *Powder flowability characterisation methodology for powder-bed-based metal additive manufacturing*. *Progress in Additive Manufacturing*, 2016. **1**(1): p. 9-20.

71. Spurek, M.A., et al., *Influence of the particle size distribution of monomodal 316L powder on its flowability and processability in powder bed fusion*. Progress in Additive Manufacturing, 2022. **7**(4): p. 533-542.

7 Chapter 6 Summary, Application, and Future Work

7.1 Summary and Application

The overarching objective of this study was to solve a real-world problem in the field of electric vehicles in automotive industry. The objective was to come up with an innovative lightweight battery pack casing that not only holds the battery cells/modules but also acts as a heat sink to cool them down during the driving cycle to eliminate the need for active cooling of the batteries by air fans or water circulation. Since the design was complex in shape and included intricate features, it was difficult to be manufactured by any of the traditional techniques. This is where laser powder bed fusion (LPBF) process as one of the most promising additive manufacturing techniques (AM) came to play. The LPBF process has revolutionized almost all industries including aerospace, automotive, heat exchanger/heat sink and electronics by bringing to the table the possibility of manufacturing complex geometries with almost no limitations except the designer's imaginations. In terms of material, Al and Al alloys (AlSi12 and AlSi10Mg) with highest thermal conductivity to weight ratio (specific thermal conductivity), essential for the above application, were selected. However, before being able to successfully print the real battery casing, the optimum powder particle size and optimum sets of process parameters to achieve defect-free parts with negligible oxygen content needed to be known. On this account, the following steps were taken, (phase I) optimization of powder particle size by printing cubic coupons from different nominal powders, (Phase II) study of the in-situ oxidation behavior of Al/Al alloys during the L-PBF process and optimization of the process parameters to achieve highly-dense parts, both on cubic coupons, (phase III) measurement of the thermal conductivity of the optimum samples to ensure thermal conductivities comparable to those of the conventionally manufactured Al/Al alloys, and

(phase IV) possibility of enhancing thermal conductivity through incorporation of graphene to an Al alloy.

Since powder serves as the starting material in the LPBF process, powder particle size and size distribution needed to be optimized prior to the printing. There are different Al/Al alloy powder commercially available, two of which could be used for the LPBF purposes, named as fine (1-20 μm) and coarse (15-70 μm) powders in this study. In the first phase of the PhD study, the role of powder particle size on the density, top/side surface roughness, and dimensional accuracy of the LPBF fabricated AlSi10Mg (as a model) samples was studied. In terms of everything, the parts fabricated from coarse powder were superior to those of the fine powder. For instance, the highest relative density achieved using the coarse powder was 99% but 95% for the fine powder. In addition, the coarse powder led to parts with 5-73% lower surface roughness than those printed from fine powder. Therefore, for the rest of the studies on all Al-based materials, the coarse powder was utilized.

In the second phase of the study, coarse powders of pure Al, and two alloys of AlSi12, and AlSi10Mg were subjected to the LPBF process in a wide range of process parameters. It was found out that Si in AlSi12 and Si/Mg in AlSi10Mg significantly improve the processing window of Al since they noticeably enhance the laser absorptivity of pure Al from 38.6% to 58.4% (AlSi12) and 56.1% (AlSi10Mg). For all cases, almost defect-free parts with relative densities equal or greater than 99.5% were achieved. To study the possibility of in-situ oxidation during the LPBF process, the oxygen content of the starting powders and printed parts under different laser powers and scanning speeds were determined. Interestingly, regardless of the material studied and the process parameters employed it was understood that oxygen content of the printed parts were lower than the

starting powders, meaning that the rate of oxide removal was higher than any possible in-situ oxidation. The analysis of oxygen content in pure Al (2260 ppm), AlSi12 (1299 ppm), and AlSi10Mg (740 ppm) powders, as well as their printed parts at a laser power of 300 W, with oxygen levels of 90 ppm for pure Al, 220 ppm for AlSi12, and 130 ppm for AlSi10Mg, proves the above statement. The following mechanism was proposed to justify the decrease in oxygen content, (i) spallation of the nanosized oxide layer on the AlSi12 particles during the rapid heating cycle of the L-PBF process, followed by (ii) the accumulation of the nanosized oxide particles (formed during the spallation stage) on the surface of the melt pool due to the upward buoyancy forces at the center of the melt pools and outward Marangoni flow at the surface of the melt pools, and finally (iii) the evaporation of nanosized oxides due to their direct interaction with the high-intensity laser beam. This part of the study proved that through careful selection of process parameters it is not only possible to end up with almost defect-free parts but also parts with negligible oxygen content.

The aim of the third phase of the study was to determine the thermal conductivity of the LPBF fabricated pure Al, AlSi12 and AlSi10Mg (optimum samples from previous phase) in the as-built condition and to compare it to their conventionally manufactured counterparts. This stage was important to ensure that the LPBF fabricated Al/Al alloys were reliable in terms of thermal conductivity for the real battery holding structure application. After performing a preliminary test on AlSi12 alloy, it was understood that the thermal conductivity in as-built condition was noticeably lower than AlSi12 wrought/cast counterparts. Based on the existing literature, post-build heat treatment was essential to enhance the thermal conductivity of the LPBF fabricated Al alloys in as-built condition. However, heat treatments are time-consuming, cost-prohibitive; in addition,

there is a high chance of oxidation of Al/Al alloys during the heat treatment even if atmospheric control furnaces are used. In light of the foregoing, strategy of build plate preheating (200 °C) was put into test to study whether it is possible to synchronize the printing process and post-build heat treatment. The results were promising, as pure Al (~230 W/m.K), AlSi12 (~140 W/m.K), and AlSi10Mg (~160 W/m.K) optimum samples were shown to possess up to 15 %, 25 %, and 80 % higher thermal conductivity values than their non-preheated counterparts reported in the literature. By using the optimum sets of process parameters and the preheating strategy (for AlSi10Mg), the battery holding structure was finally printed.

After successfully printing a relatively complex shape battery casing with reliable performance, an important question was raised, *is it possible to further enhance the thermal conductivity of Al/Al alloys to end up with battery casings with higher cooling efficiency?* For this purpose, graphene was decided to be added to an Al alloy to end up with an Al matrix composite (AMC). The idea behind adding graphene as a second constituent to an Al alloy matrix in the fourth phase of this study was due to the fact that graphene has higher thermal/electrical conductivity than Al. To study the possibility of enhancing thermal conductivity through incorporation of graphene, AlSi12 alloy with the minimum thermal conductivity among the studied materials was selected. Mixing of the two powders was essential prior to the printing as in the LPBF process there is only one powder dispenser not multiple nozzles to feed different powders. Two dry mechanical mixing techniques were opted for mixing of graphene and AlSi12 powders with different graphene concentrations of 0.25, 0.5 and 1 wt%. The powder attributes (size, distribution, and shape), behaviors (absorptivity, packing density, and flowability), relative humidity, O/C/H content, and quality of the graphene were examined for reinforced and unreinforced cases.

It was found out that the ball-milled powders possessed remarkably higher flowability than regularly-mixed ones, meeting the requirements of the LPBF process. The ball milled powders were subjected to the LPBF process and since parts with relative densities higher than 99% could not be achieved for AlSi12-1wt%Gr, no further characterizations were carried out on this material. The strategy of low laser power to scanning velocity ratio (P/V) and relative low hatch spacing (below 100 μm) was proposed to end up with highly dense composite parts with relative densities up to 99.5 and 99.2% for AlSi12-0.25Gr and AlSi12-0.5Gr, respectively. In-depth microstructural and nano-structural studies were performed on the optimum samples of reinforced and unreinforced AlSi12 using TEM, HRTEM, EBSD, EDS and Raman spectroscopy and it was found out that (i) most of Gr transforms into Al₄C₃, (ii) a part of the carbonaceous material survives, though it is more like disordered carbon than starting Gr, and (iii) neither carbonaceous phase nor Al₄C₃ could act as an inoculant for grain nucleation during the L-PBF process. Comparing thermal conductivities of the LPBF fabricated AlSi12-0.25Gr and AlSi12-0.5Gr with that of the AlSi12 alloy it was understood that graphene incorporation caused either slight increase or slight deterioration in thermal conductivity. This was found to be due to (i) high degree of structural disorder in the survived carbonaceous nano-constituent, (ii) transformation of Gr into Al₄C₃ with low thermal conductivity, (iii) presence of graphite/graphene nanoplatelets (Gr) rather than monolayer graphene, and (iv) anisotropic conductivity in Gr.

7.2 Future work

The followings are suggested for the future work:

- In this study, for the first time, it was understood that the rate of the diminishment of the existing oxides in the starting powder was higher than any possible in-situ

oxidation during the LPBF processing of pure Al, AlSi12, and AlSi10Mg. A mechanism was proposed for the escape of oxides from the melt pool through evaporation; however, ultrahigh speed X-ray imaging of the melt pool and the use of high-speed camera to capture the melt flow direction and accumulation of the oxides on the surface of the melt pool (assumptions behind the proposed mechanism) can shed some more light on the observed phenomenon.

- In many of the research studies that targeted the challenges during the LPBF processing of Al and Al alloys, the in-situ oxidation of the molten material during this layer-wise manufacturing process has been acknowledged. They have referred to the work conducted by Louvis et al., which was published at the early stages of the LPBF process, or cited articles that were published before the emergence of the LPBF process. On the other hand, owing to the complicated physics of the LPBF process with non-equilibrium melting and solidification nature, oxidation of melt pool had received only scant attention within the literature. The reason behind becoming suspicious to the oxidation during the LPBF process was the fact that the mechanical properties of the LPBF fabricated Al/Al alloys were proved to be superior to their conventionally manufactured counterparts, and this could not happen if intensive oxidation of Al has happened during the LPBF process as suggested by Louvis et al. Although this has been proved in this study that rate of oxide diminishment for Al/Al alloys was higher than any possible reoxidation during the LPBF process, it is still an unanswered question for many other metallic materials. Whether they show the same trend or not can be the subject of future studies, especially for highly reactive metals such as Ti and Mg alloys.

- In this study, it was proved that printing under 200 °C of preheating (maximum preheating temperature of EOS M280) had profound influence on thermal conductivity improvements for pure Al, AlSi12 and AlSi10Mg in as-built condition. However, for AlSi12 and AlSi10Mg alloys, the obtained thermal conductivities were still lower than their nominal values. Based on the lessons drawn from the post-build heat treatment recommendations for thermal conductivity enhancement, preheating should be performed at 300 °C to achieve the nominal thermal conductivity values for AlSi12 and AlSi10Mg alloys. For future work it is suggested to print these materials with new generation of LPBF machines with higher preheating temperatures to prove the possibility of achieving nominal thermal conductivity values for these materials in as-built condition.
- According to the in-depth microstructural investigations by TEM, HRTEM and EDS it was found out that graphene either transformed to Al_4C_3 or significantly lost its structural integrity during the LPBF process. It seems like coating of graphene with a metallic material (i.e., Cu) or semiconductor (i.e., Si) can be an effective way to improve the wettability of these reinforcements with molten Al and decrease the interaction of Al with graphene. On the other hand, the presence of such coatings alleviates the van der Waals attraction between carbonaceous particles and their agglomeration during the powder storage or printing process.
- According to Al-C binary phase diagram, Al_4C_3 becomes stable upon addition of even a negligible carbon to Al. In AlSi12-C system, ternary compounds also exist with the general formula of $Al_xSi_yC_z$. Since the Gibbs formation energy of Al_4C_3 is significantly negative, this compound easily forms even at short melt durations of the LPBF process, Formation of Al_4C_3 destroys the structural integrity of

graphene. One of the strategies to ensure graphene remains intact during the LPBF process can be the incorporation of graphene into metallic matrices with no chance of carbide formation. For instance, incorporation of C to Cu will not be accompanied by any carbide formation since no carbide is stable in the Cu-C system based on its binary phase diagram.

- In this study, thermal properties of AlSi12-graphene composites were investigated in the temperature range of 25-450 °C. Conclusive conclusions regarding the suitability of incorporation of graphene into AlSi12 can be made after performing investigations on mechanical properties of these composites at part level. There are currently some research studies that targeted the intrinsic mechanical properties of the LPBF fabricated carbon-reinforced AMCs through microhardness or nanohardness tests. However, tensile and compression tests in a wide range of temperatures on large samples are required to comment on role that Al₄C₃ and damaged graphene can play in improvements of mechanical properties.